HEINRICH HEINE
UNIVERSITÄT
DÜSSELDORF

Triplet states in bacterial reaction centers of *Rhodobacter sphaeroides* and related systems

Inaugural-Dissertation

zur Erlangung des Doktorgrades
der Mathematisch-Naturwissenschaftlichen Fakultät
der Heinrich-Heine-Universität Düsseldorf

vorgelegt von

Aliaksandr Marchanka
aus Orechowsk

Düsseldorf, Juni 2009

Aus dem Max-Planck-Institut für Bioanorganische Chemie, Mülheim an der Ruhr

Gedruckt mit der Genehmigung der
Mathematisch-Naturwissenschaftlichen Fakultät der
Heinrich-Heine-Universität Düsseldorf

Referent: Prof. Dr. W. Lubitz
Koreferent: Prof. Dr. K. Kleinermanns

Tag der mündlichen Prüfung: 26.06.2009

No llores porque ya se terminó… sonríe, porque sucedió.

To my mother and the memory of my father

Aknowledgement

I would like to thank Dr. Maurice van Gastel, my supervisor, for his help, mentoring, support, trust and patience in leading me through secrets of science. He is also thanked for carefully reading and suggesting scientific and grammatical corrections of our publications and this thesis.

Prof. Dr. Wolfgang Lubitz is gratefully acknowledged for giving me the opportunity to perform my PhD project in his laboratory, for general supervising, and for being my first reviewer. I would like to thank Prof. Dr. Karl Kleinermanns for being my second reviewer.

Dr. Jens Niklas, Dr. Shipra Prakash, Dr. Alexey Silakov and Maria Eirini-Pandelia are gratefully acknowledged for the advices, fruitful discussions and help at various stages of this project.

I would like to thank Gabriele Schmitz, Kathrin Schwarzbach, Michael Reus and Horst Selbach for their help with preparations and purification of samples. Gudrun Klihm and Frank Reikowski are gratefully acknowledged for the maintenance of EPR spectrometers and laser systems.

Dr. M. Paddock and Prof. Dr. M. Y. Okamura are gratefully acknowledged for supplying *Rb. sphaeroides* mutant samples and for discussions about our joint publication. I would like to thank Dr. P. Gast for the *Rb. sphaeroides* quadruple mutant samples and Dr. A. Savitsky for his help with the W-band measurements on this mutant.

Prof. Dr. E. J.J. Groenen, Prof. Dr. K. Möbius, Prof. H.-J. Steinhoff and Dr. M. Engelhard are thanked for the collaboration within the DFG/NWO Teilprojekt GA1100/1-2. I would like to thank the DFG, NWO, SFB 663, TP A7 and MPG for the financial support.

I would like to thank my friends Tatyana, Iryna, and Olga for their permanent support and help. All my friends and colleagues are gratefully thanked for their help and advices.

At last but not least, I would like to express my sincerest gratitude to my dear mother for her help, support, love and belief in me.

Table of contents

Summary

In bacterial photosynthesis, the important process of light induced charge separation occurs in photosynthetic reaction center proteins and proceeds from a primary donor (a dimer of bacteriochlorophylls) predominantly along one of two nearly symmetric branches of cofactors. The relative photosynthetic activity of the two branches can be advantageously investigated by EPR and ENDOR spectroscopy of the triplet state of the primary donor. Though the triplet state occurs with low yield in native systems, it can be induced to a yield of unity by prereducing the final quinone electron acceptors. Since the paramagnetic triplet state has the same electronic configuration as the diamagnetic photoexcited singlet state from which charge separation initiates and since its polarization pattern depends on the presence or absence of light-induced charge-separated intermediate states at either branch, the triplet EPR spectrum of the primary donor contains essential information about the initial processes of photosynthetic charge separation. In this thesis, the photoexcited triplet state of the primary donor and the carotenoid in bacterial reaction centers of *Rb. sphaeroides*, in mutants, in reaction centers of *Bl. viridis* and in model systems (bacteriochlorophylls *in vitro*), have been investigated by EPR and ENDOR spectroscopy at cryogenic temperatures. The experiments have been supplemented with DFT calculations.

The triplet state is found to derive from radical pair and intersystem crossing mechanisms. The former mechanism is operative for *Rb. sphaeroides* wild type, R-26.1, mutant GD(M203)/AW(M260) and *Bl. viridis* wild type in the measured temperature range 10 K – 100 K, indicating effective A-branch separation at these temperatures. The latter mechanism is operative for bacteriochlorophylls *in vitro* and for *Rb. sphaeroides* mutants LH(M214)/AW(M260) and HL(M182)/GD(M203)/LH(M214)/AW(M260). An intersystem crossing triplet state indicates that no long-lived radical pairs are formed upon direct excitation of the primary donor and that virtually no charge separation at the B-branch occurs at low temperatures. When the temperature is raised above 30 K, B-branch charge separation is observed. Its yield is at most one percent of the A-branch charge separation. B-branch radical pair formation can be induced at 10 K with low yield by direct excitation of the bacteriopheophytin of the B-branch at 537 nm. The formation of a carotenoid triplet state is observed in *Rb. sphaeroides* wild type and in GD(M203)/AW(M260), LH(M214)/AW(M260) and HL(M182)/GD(M203)/LH(M214)/AW(M260) mutants. The thermal activation barrier varies among different mutants. Most probably, the thermally activated transfer step in the B-

branch occurs between the primary donor, P_{865}, and the accessory bacteriochlorophyll, whereas this step is barrierless down to 10 K along the A-branch.

The spin density distributions of the triplet state of bacteriochlorophyll *a* and *b in vitro* were found to be similar except for the presence of additional spin density on carbon 8^1 in bacteriochlorophyll *b*. The triplet state in bacteriochlorophylls cannot be explained *via* simple HOMO LUMO excitation. Rather, a mixture of HOMO LUMO and HOMO−1 LUMO excitations is necessary for a satisfactory explanation of the observed hyperfine interactions. The observed hyperfine couplings have been assigned to specific molecular positions and anisotropy of the interactions were found to be compatible with the orientation of the zero-field splitting tensor.

The electron spin density was found to be almost evenly delocalized over both dimer halves in the special pair of *Rb. sphaeroides* ($^3P_{865}$) and *Bl. viridis* ($^3P_{960}$). The spin density distribution found for $^3P_{865}$ and $^3P_{960}$ is essentially the same, except for the ethylidene groups in $^3P_{960}$ that carry additional spin density. In contrary to the triplet state of the bacteriochlorophyll monomer, the triplet state of the dimer can be satisfactorily explained as being a simple HOMO $\rightarrow$ LUMO excitation. The LUMO orbital of ^3P is arguably the best model for the LUMO orbital of P^*, from which the charge separation starts. The evenly delocalized spin density distribution over both dimer halves LUMO orbital indicates that asymmetry of photosynthetic charge separation with respect to the A and B branches of cofactors indeed does not stem from the internal asymmetry in the electronic structure of the bacteriochlorophyll dimer. Rather, small differences in the distances and mutual orientation of cofactors in the A- and B-branch, different site energies *e.g.* caused by variation in hydrogen bonding of cofactors and maybe differences in reorganization energies for the electron transfer in both branches, are responsible for the large asymmetry in photosynthetic activity of the two branches.

Zusammenfassung

Der wichtige Prozess der lichtinduzierten Ladungstrennung in der bakteriellen Photosynthese findet in den photosynthetischen Reaktionszentren statt und verläuft vom primären Donator (ein Bakteriochlorophyll-Dimer) hauptsächlich über einen der zwei nahezu symmetrischen Kofaktorzweigen, den A-Zweig. Die relative photosynthetische Aktivität der zwei Kofaktorzweige kann mittels EPR und ENDOR Spektroskopie an dem primären Donator untersucht werden. Obwohl der Triplettzustand in nativen Systemen nur mit kleiner Ausbeute vorkommt, kann die Effektivität der Triplettbildung durch die Reduktion der terminalen Elektronakzeptoren auf nahezu 100 % erhöht werden. Da der paramagnetische Triplettzustand die gleiche elektronische Konfiguration wie der diamagnetische photoangeregte Singlettzustand hat, von dem die Ladungstrennung ausgeht, und dessen Polarisationsmuster abhängig von der Anwesenheit oder Abwesenheit der lichtinduzierten ladungsgetrennten intermediären Zuständen in dem einen oder anderen Zweig ist, enthält das Triplettspektrum des primären Donators die wichtige Information über primäre Prozesse der photosynthetischen Ladungstrennung. In dieser Doktorarbeit wurden die photoangeregten Triplettzustände vom primären Donator und Carotinoid in den bakteriellen Reaktionszentren von *Rb. sphaeroides*, in deren Mutanten, und in Reaktionszentren des verwandten Purpurbakteriums *Bl. viridis* und in Modellsystemen (Bakteriochlorophyllen *in vitro*) mittels EPR und ENDOR Spektroskopie bei tiefen Temperaturen untersucht. Die Experimente wurden durch DFT Rechnungen gestützt.

Der Triplettzustand des primären Donators kann mittels Radikalpaar- oder Intersystem- Crossing-Mechanismen gebildet werden. Der erste Mechanismus ist wirksam für *Rb. sphaeroides* Wildtyp, R-26.1, Mutant GD(M203)/AW(M260) and *Bl. viridis* Wildtyp im gemessenen Temperaturbereich 10 K – 150 K, was auf die effektive Ladungstrennung im A-Zweig bei diesen Temperaturen hinweist. Der zweite Mechanismus ist für Bakteriochlorophylle *in vitro* und die Mutanten LH(M214)/AW(M260) und HL(M182)/GD(M203)/LH(M214)AW(M260) von *Rb. sphaeroides* wirksam. Ein Intersystem-Crossing-Triplettzustand weist darauf hin, dass keine langlebigen Radikalpaare bei einer direkten Anregung des primären Donators dieser Mutanten gebildet werden können und auch keine Ladungstrennung im B-Zweig bei niedrigeren Temperaturen stattfindet. Wenn die Temperatur auf über 30 K ansteigt, ist Ladungstrennung im B-Zweig zu beobachten. Ihre Ausbeute ist nur etwa 1 % der Ladungstrennung im A-Zweig. Die Bildung von Radikalpaaren

im B-Zweig bei 10 K kann durch direkte Anregung von Bakteriophäophytin bei 537 nm induziert werden. Die Bildung des Triplettzustandes vom Carotinoid ist in *Rb. sphaeroides* Wildtyp und den Mutanten GD(M203)/AW(M260), LH(M214)/AW(M260) und HL(M182)/GD(M203)/LH(M214)AW(M260) zu beobachten. Die thermische Aktivierungsbarriere variiert in den unterschiedlichen Mutanten. Höchstwahrscheinlich findet ein thermisch aktivierter Transferschritt im B-Zweig zwischen primären Donator, P_{865} und dem akzessorischen Bakteriochlorophyll statt, während dieser Schritt bis zu 10 K im A-Zweig barrierfrei ist.

Die Spindichteverteilung im Triplettzustand der Bakteriochlorophylle *a* und *b in vitro* ist sehr ähnlich bis auf die Präsenz zusätzlichen Spindichte am Kohlenstoffatom 8^1 in Bakteriochlorophyll *b*. Der Triplettzustand in Bakteriochlorophyllen kann nicht als einfache HOMO LUMO Anregung dargestellt werden. Stattdessen muss eine Mischung von HOMO LUMO und HOMO–1 LUMO Anregungen angenommen werden, um die gemessenen Hyperfeinkopplungen korrekt erklären zu können. Die gemessenen Hyperfeinkopplungen wurden spezifischen Positionen im Molekül zugeordnet. Es wurde gezeigt, dass die Anisotropie von Hyperfeinkopplungen mit der Orientierung des ZFS-Tensors kompatibel ist.

Die Elektronspindichte ist gleichmäßig verteilt über die zwei Dimerhälften im „Special Pair“ von *Rb. sphaeroides* ($^3P_{865}$) und *Bl. viridis* ($^3P_{960}$). Die Verteilung ist ähnlich in $^3P_{865}$ und $^3P_{960}$ - bis auf die Ethylidenegruppen in $^3P_{960}$, wo sich zusätzliche Spindichte befindet. Im Gegensatz zum Triplettzustand im Monomer von Bakteriochlorophyllen, kann der Triplettzustand des Dimers als einfache HOMO $\rightarrow$ LUMO Anregung beschrieben werden. Das LUMO Orbital von ^3P ist wahrscheinlich das beste Modell für das LUMO Orbital von P^*, von dem die Ladungstrennung beginnt. Das gleichmäßig über zwei Dimerhälften delokalisierte LUMO Orbital zeigt, dass die Asymmetrie in der photosynthetischen Ladungstrennung bezüglich der A- und B-Zweige der Kofaktoren *nicht* von der internen Asymmetrie in der elektronischer Struktur des Bakteriochlorophyll-Dimer stammt. Die Unterschiede im Wasserstoffbrücken-Netzwerk der zwei Zweige und, zusätzlich, Unterschiede in Abstand und Orientierungen der Kofaktoren in A- und B-Zweige, verursachen unterschiedliche Elektrontransfer-Matrixelementen, Standard-Gibbs-Energien und Reorganisationsenergien in beiden Zweigen, die für starke Asymmetrie der photosynthetischen Aktivität der zwei Zweige verantwortlich sind.

Abbreviations

ATP - Adenosine triphosphate
ADP - Adenosine diphosphate
B - Bacteriochlorophyll
Bl. - *Blastochloris*
BChl *a* - Bacteriochlorophyll *a*
BChl *b* - Bacteriochlorophyll *b*
BPheo - Bacteriopheophytin
bRC - Bacterial reaction center
Car - Carotenoid
cw - continuous wave (spectroscopy)
DAF - Delay After Flash
DFT - Density Functional Theory
DIIS - Direct Inversion of Iterative Subspace
EPR - Electron Paramagnetic Resonance
ESE - Electron spin echo
ESEEM - Electron spin-echo envelope modulation
ESR - Electron Spin Resonance
ENDOR - Electron Nuclear DOuble Resonance
Φ_B - genetically introduced bacteriopheophytin in B-branch
GGA - Generalized gradient approximations
GTO - Gaussian-type orbital
HOMO - Highest Occupied Molecular Orbital
H - Bacteriopheophytin
HFC - Hyperfine coupling
HPLC - High Performance Liquid Chromatography
ISC - Intersystem crossing
KS - Kohn-Sham formalism
LCAO - Linear combination of atomic orbitals
LDA - Local-density approximation
LH - Light Harvesting (antenna complexes)
LSDA - Local-spin-density approximation
LUMO - Lowest Unoccupied Molecular Orbital

MO - Molecular Orbital

MTHF - 2-MethylTetraHydroFuran

NMR - Nuclear Magnetic Resonance

OPO - Optical parametric oscillator

P - Primary donor

P_{865} - Primary donor in *Rhodobacter sphaeroides*

P_{960} - Primary donor in *Blastochloris viridis*

P_L - Bacteriochlorophyll in special pair, connected to L-protein subunit

P_M - Bacteriochlorophyll in special pair, connected to M-protein subunit

Q - quinone

Rb. - *Rhodobacter*

RC - Reaction center

RHF - Restricted Hartree-Fock approximation

RKS - Restricted Kohn-Sham formalism

RP - Radical pair

SCF - Self-Consistent Field

SDS PAGE - Sodium Dodecylsulfate Polyacrylamide Gel Electrophoresis

SO - Spin-Orbit

SS - Spin-Spin

STO - Slater-type orbital

TRIPLE - Electron-nuclear-nuclear triple resonance

Tris - Tris(hydroxymethyl)aminomethane

UHF - Unrestricted Hartree-Fock approximation

UKS - Unrestricted Kohn-Sham formalism

UQ - Ubiquinone

UV - Ultraviolet

ZFS - Zero Field Splitting

Chapter 1

Introduction

Photosynthesis is a biological process whereby light energy is captured by an organism and the stored energy is used to drive cellular processes. The most common form of photosynthesis, for example in plants, involves chlorophyll-type pigments, and operates using light-driven electron transfer processes.[1] Photosynthesis is carried out by a large variety of organisms, by some bacteria and by algae and plants.

In purple bacteria, the photosynthetic proteins are located in a specially modified portion of the inner cell membrane, called the intracytoplasmic membrane (Fig. 1.1A).[1-3] The early processes of photosynthesis are carried out by the membrane-bound proteins, later stages of the process are mediated by proteins that are diffusible in the aqueous phase. The energy storage in photosynthesis can be divided into four phases:[1]

1) light absorption and energy transfer by antenna systems
2) primary charge separation in reaction centers
3) energy stabilization of the charge separated state by secondary processes
4) synthesis and export of stable products that store the excess energy.

The first two phases are called light reactions, and the last two correspond to dark reactions. The photosynthetic apparatus of purple bacteria consist of light harvesting antenna complexes (LH), the reaction center protein (RC), an ubiquinone-cytochrome b/c oxidoreductase complex and ATP synthase (Fig. 1.1B).[4]

In short, photosynthesis proceeds along the following lines. In the first stage of photosynthesis, antenna systems absorb light. Then, a series of energy transfer processes follows with migration of electronically excited states towards the reaction center. In purple photosynthetic bacteria two types of antenna complexes are present, known as light-harvesting 1 and 2 complexes, LH1 and LH2.[5] LH1 is an integral membrane core antenna pigment-protein complex, which is physically surrounding the reaction center (Fig. 1.1A). LH2 is an accessory antenna. The number of LH2 proteins per reaction center is variable and they are not directly in contact with the reaction center complex.[5]

The energy collected by the LH complexes is transferred to the RC, where the second phase takes place. This step involves the conversion of an electronically excited state into a charge-separated state, where an electron-pair is separated. The reaction center is a protein-

pigment complex embedded in the photosynthetic membrane and performs the task of charge separation with a quantum efficiency close to 100%. Its structure and function are discussed in the next chapter below. In bacteria, only one reaction center is present, whereas the oxygen evolving photosynthetic organisms have two reaction centers. They are known as photosystems 1 and 2.

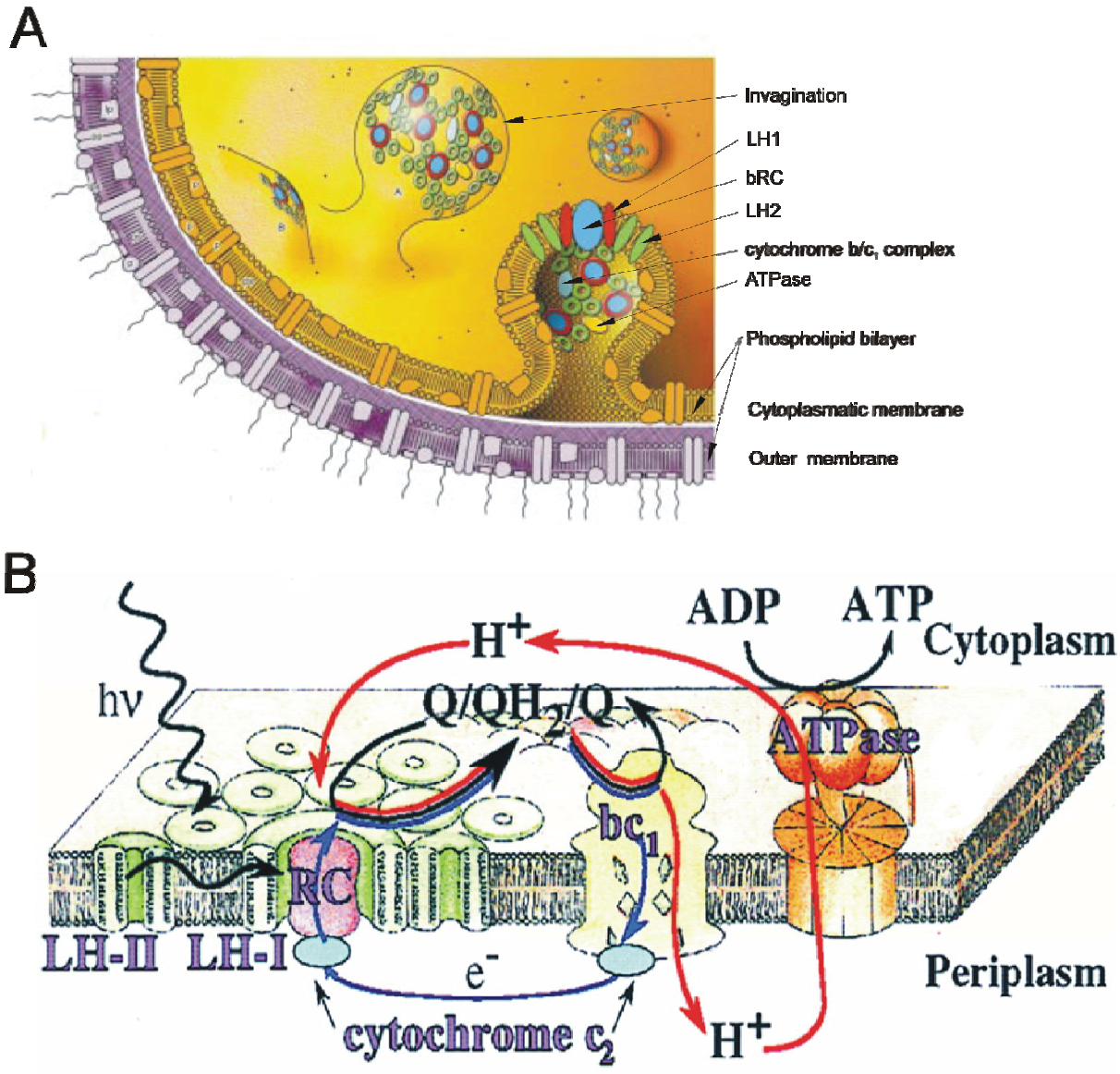

Figure 1.1. Membrane of purple photosynthetic bacteria *Rb. sphaeroides*.
(A) Representation of the intracytoplasmic membrane system formed in *Rb. sphaeroides* as a result of a reduction in the oxygen tension.[1-3] Protein-cofactor complexes and major components are depicted.
(B) Schematic representation of the photosynthetic apparatus in the intracytoplasmic membrane of purple bacteria. Pigment complexes are shown. Electron flow is depicted in blue, proton flow in red, and quinone flow in black.[4]

The cofactor arrangement in the RC is such that the charge-separated state is stabilized and charge recombination is energetically unfavourable. These structural elements constitute the third phase of photosynthesis.

The final phase of photosynthetic energy storage is the production of stable energy-carrying molecules like NADPH and ATP that are used to drive vital processes in the cell and to reduce carbon dioxide (CO_2) to sugars. In eukaryotic photosynthetic organisms phosphorylated sugars are used as the final molecules for storage of energy.

Photosynthesis also occurs in the photosynthetic prokaryotes (bacteria) and photosynthetic eukaryotes (plants and algae). In bacterial photosynthesis, five major groups of bacteria can be distinguished. Four of these are anoxygenic (the purple bacteria, the green sulfur bacteria, the green non-sulfur bacteria and the heliobacteria),[6] which means that they do not produce molecular oxygen. The only oxygen evolving bacteria are the cyanobacteria. Purple bacteria are anoxygenic phototropic organisms that are widely distributed in nature.[6] The "purple" (purpur) name comes from the color (red), found in many of the common species. Representatives of these bacteria are *Rhodobacter sphaeroides*, *Blastochloris viridis* and *Rhodobacter capsulatus*. The study presented in this thesis is focused on the bacterial reaction centers of the purple bacteria *Rb. sphaeroides* and *Bl. viridis*.

References

(1) Blankenship, R. *Molecular mechanisms of photosynthesis;* Blackwell Science: Oxford, London, 2002.

(2) Naylor, G. W.; Addlesee, H. A.; Gibson, L. C. D.; Hunter, C. N. (1999) The photosynthesis gene cluster of Rhodobacter sphaeroides, *Photosynth. Res., 62*, 121-139.

(3) Hunter, C. N.; van Grondelle, R.; Olsen, J. D. (1989) Photosynthetic Antenna Proteins - 100 Ps Before Photochemistry Starts, *Trends in Biochem. Sci., 14*, 72-75.

(4) Hu, X. C.; Damjanovic, A.; Ritz, T.; Schulten, K. (1998) Architecture and mechanism of the light-harvesting apparatus of purple bacteria, *Proc. Natl. Acad. Sci. USA, 95*, 5935-5941.

(5) Cogdell, R. J.; Isaacs, N. W.; Howard, T. D.; McLuskey, K.; Fraser, N. J.; Prince, S. M. (1999) How photosynthetic bacteria harvest solar energy, *J. Bacteriol., 181*, 3869-3879.

(6) Blankenship, B.; Madigan, M.; Bauer, C. *Anoxygenic Photosynthetic Bacteria;* Kluwer Academic Publishers: 1995.

Chapter 2

Bacterial reaction centers

2.1 Structure and function of bacterial reaction centres

The primary photochemistry of charge separation from a donor species to a series of acceptors proceeds in an integral membrane-bound pigment-protein complex, called the bacterial reaction center (bRC).[1-5] The reaction centers are oriented in such a way, that the donor species faces the periplasm of the cell. The bRC from *Rb. sphaeroides* contains three protein subunits, L, M and H (Fig 2.1A).[4] Four bacteriochlorophylls *a* (BChl, B), two bacteriopheophytins *a* (BPheo, H), two quinones (ubiquinones) (Q), a non-heme iron and a carotenoid spheroidene (Car) are present as cofactors (Fig. 2.1B). The structure of the cofactors BChl *a*, BChl *b*, BPheo *a*, ubiquinone-10 and carotenoid (spheroidene) is shown in Fig. 2.2.

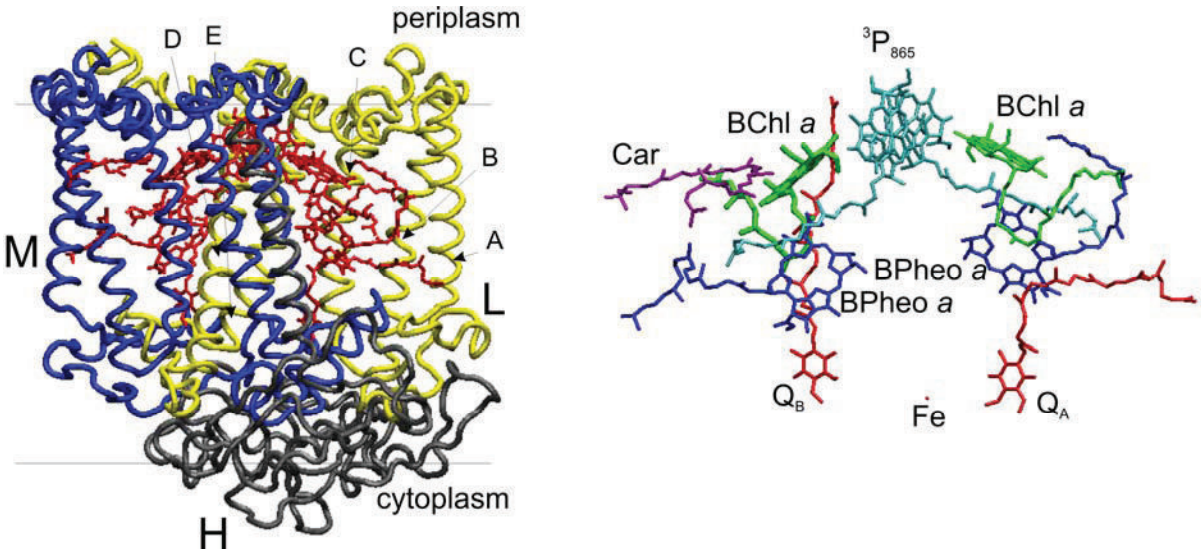

Figure 2.1. Schematic overview of the bacterial reaction center of *Rb. sphaeroides*
(A) Protein subunits L, M, H are indicated in yellow, blue and green, respectively. The α helices A-E[4] in protein subunit L are also depicted. Cofactors are indicated in red.
(B) Cofactor arrangement in the bRC of *Rb. sphaeroides*.
Figures were prepared with the VMD package.[6]

The composition of the bRC from *Bl. viridis* is slightly different. It has four protein subunits, L, M, H and tightly bound cytochrome with four heme cofactors. Moreover, it contains four bacteriochlorophyll *b* molecules, two bacteriopheophytin *b* molecules, a menaquinone, an ubiquinone, a non-heme iron atom and a carotenoid 1,2-dihydroneurosporene.

In the bRC of *Rb. sphaeroides*, the protein subunits L, M and H comprise 281, 307 and 260 amino acids, respectively.[4] The L and M subunits are firmly anchored in the photosynthetic membrane. The bulk of the H subunit is located on the cytoplasmic side. The L and M subunits are in close contact and form a cylindrical core.[1, 4] In total, five trans-membrane helices are present in both the L and M subunits and one in the H subunit. The five membrane-spanning helices in the L and M subunits are labelled A-E (Fig. 2.1A).[7] The outermost helices A and B as well as the D helices are straight. In contrast, the C and E helices are tilted, possibly due to steric constraints imposed by the steeply tilted D helices of the opposing subunits and the cofactors.[4]

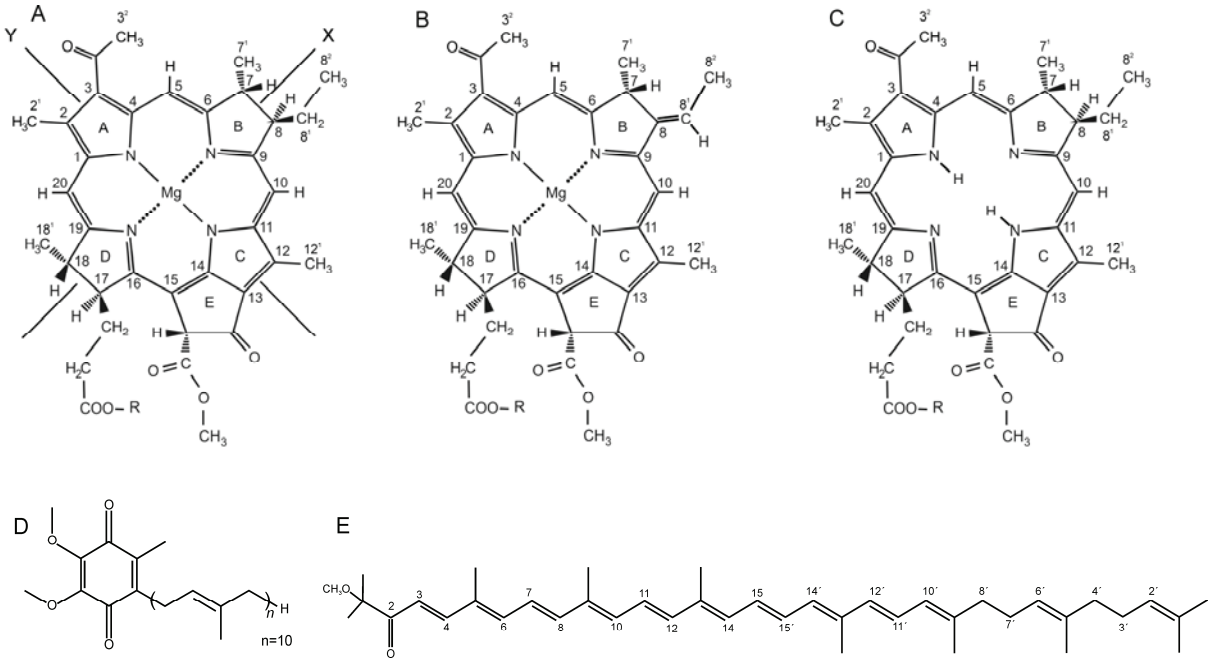

Figure 2.2. Molecular structures and IUPAC numbering scheme for (A) bacteriochlorophyll *a*, (B) bacteriochlorophyll *b*, (C) bacteriopheophytin *a*, (D) ubiquinone 10, (E) *all-trans* spheroidene. The orientation of the molecular axis of BChl *a* is shown in (A).

The cofactors are arranged along two branches, A and B, with near C_2 symmetry. The root-mean-square deviation between equivalent atoms of both branches is about 1 Å.[8] Two bacteriochlorophylls form a dimer, the so-called "special pair" ($BChl_2$, P). The special pair is located close to the C_2 symmetry axis. Each of the two branches (A and B) of cofactors extends from the special pair through the protein to the cytoplasmic side. They both consist of one "accessory" bacteriochlorophyll (B_A, B_B), one bacteriopheophytin ($BPheo_A$, $BPheo_B$), and one quinone (Q_A, Q_B). Both quinones are connected by a non-heme iron atom that is further coordinated by nitrogen atoms of four histidine residues and two oxygens of a glutamic acid. The carotenoid is located near B_B.

The pigments present in the bRC give rise to an overall red color (blue in the carotenoidless mutant R-26.1). The absorption spectra of each cofactor and a description of Q_x and Q_y transitions are given in the upcoming section. Here the UV/VIS spectrum of the bRC, shown in Fig. 2.3 is discussed.

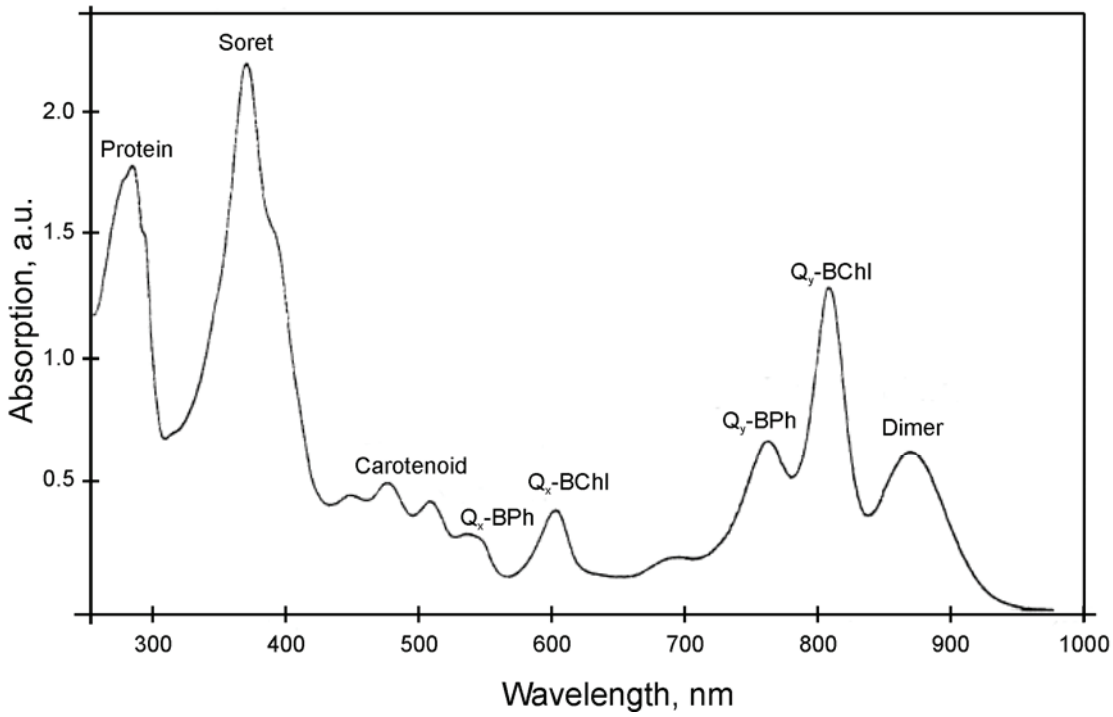

Figure 2.3. UV-VIS absorption spectrum of detergent solubilized bRC of *Rb. sphaeroides* 2.4.1 (wild type).[9]

The band at 280 nm corresponds to an absorption of the amino acids, in particular tryptophan and tyrosine present in the protein. The strong band at about 400 nm is a Soret band (see below) of all bacteriochlorophylls and bacteriopheophytins present in the bRC. The bands at 460 nm and 500 nm stem from the carotenoid cofactor. The band at 537 nm

corresponds to the Q_x transition of bacteriopheophytin, the band at 590 nm belongs to the Q_x transition of the accessory bacteriochlorophyll *a*. The one at 780 nm corresponds to the Q_y transition of bacteriopheophytins, at 800 nm to the Q_y transition of the accessory bacteriochlorophylls. The absorption at 865 nm corresponds to the low-energy band of the Q_y transition of the bacteriochlorophyll dimer (P_{865}).[10] The monomeric bands are red shifted in comparison to the corresponding band in the pigments measured *in vitro* due to interaction with the protein surrounding. The bands of the bacteriochlorophyll dimer are red shifted due to dimerization.[10] The bands of the primary donor shift to longer wavelengths and becomes more narrow upon lowering the temperature. This seems to be a particular property of the bacteriochlorophyll dimer, and may be due to a small temperature-induced change in the dimer configuration.[11, 12]

Upon absorption of a photon or energy transfer from the light-harvesting complexes to the bRC, an electron is excited at the special pair. The processes that follow are summarized in an energy level diagram given in Fig. 2.4 (green pathway). The singlet excited special pair

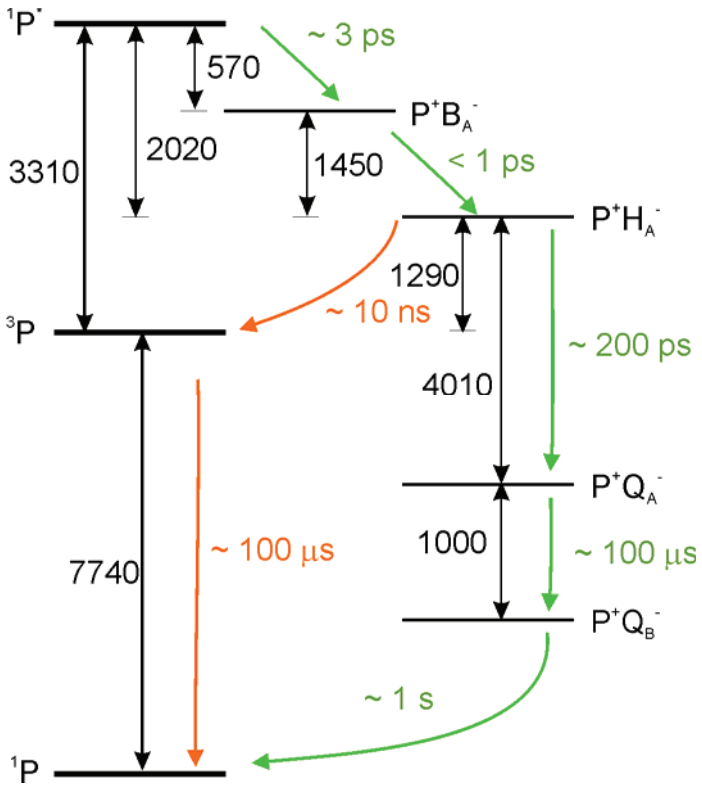

Figure 2.4. Energy levels and time constants for the energy transfer in bacterial reaction centers of *Rb. sphaeroides*.[1, 13, 14] Electron transfer in the native system is shown with green arrows, electron transfer in the system with blocked primary acceptor Q_A and formation of the triplet state are shown with orange arrows. Energy differences are given in [cm^{-1}].

(P) first donates an electron to B_A. The exited electron subsequently travels to H_A, Q_A and the final electron acceptor, the quinone of the B-branch (Q_B).[1, 15] The electron transfer from the special pair to bacteriopheophytin occurs in about 3 ps. The radical pair $P^{\bullet+}B_A^{\bullet-}$ has been observed only *via* subpicosecond absorption spectroscopy,[16, 17] due to very short lifetime of this state.[13, 14, 16, 17]

Though the two A and B branches are geometrically similar, they are strikingly different in their photosynthetic activity, as was elegantly demonstrated by optical measurements at low temperature.[14, 18, 19] At low temperature, the bacteriopheophytin Q_x band splits into two bands with absorption maxima 532 nm and 545 nm.[14] From linear dichroism studies, the longer-wavelength band has been assigned to the bacteriopheophytin of the A-branch.[14] Picosecond measurements at 5 K and 76 K have shown that only the band at 545 nm is bleached, thus indicating that only H_A participates in the electron transfer. In the subsequent step, Q_A receives an electron from H_A. The electron transfer from bacteriopheophytin to the primary acceptor Q_A is independent of temperature with a time constant of about 200 ps in bacterial reaction centers of *Rb. sphaeroides*.[14] The structure suggests that Trp M252 may be involved in the electron transfer process. The residue Trp M252 is conserved in *Bl. viridis*, although the distances (and angles) to the cofactors differ somewhat. The electron transfer from Q_A to Q_B occurs in about 100 μs. This step occurs parallel to the membrane and close to the cytoplasmic surface. During or after a second electron transfer to Q_B this cofactor binds two protons. Electron transfer from the primary donor towards the primary acceptor Q_A has been fully optimized by nature and occurs *via* the A-branch with zero activation energy. The $Q_A \rightarrow Q_B$ electron transfer is, however, an activated process. Similar asymmetries and similar electron transfer kinetics are present in the bRC of *Bl. viridis*, which contains BChl *b* and BPheo *b* cofactors.[11]

Q_A can be chemically reduced (*e.g.*, with $Na_2S_2O_4$)[20] such that electron transfer from H_A to Q_A will not occur. Electron transfer to Q_A can also be blocked by introducing site-directed mutations of amino acids around the binding pocket of Q_A such that it cannot bind in its native position.[21] If electron transfer to Q_A is blocked, the singlet radical pair $P^{\bullet+}H_A^{\bullet-}$ lives then long enough (~ 10 ns) to form the triplet radical pair that recombines to the triplet state of the donor (orange pathway in Fig. 2.4).[22]

The rate of electron transfer is found to be at least 20 times smaller along the B-branch,[15] which is still not fully understood. This special feature arises probably from a breaking of the two-fold symmetry at several places in the structure of the bacterial reaction center. Most notably, subtle differences exist in the position and hydrogen bonding network

of the two accessory BChls. In bRC of *Rb. sphaeroides* the distance between H_A and B_A is 1.5 Å smaller than that between corresponding cofactors in the B-branch. The overlap matrix elements, which couple the electronic states of reactants (singlet excited primary donor) with the electronic states of products (radical pairs) are also different due to slightly different mutual orientations of cofactors and their electronic structure in both branches.[15, 23] Furthermore, the distribution of charged amino acids is asymmetric. Whereas in the A-branch the free-energy change in the reaction ΔG^0 and reorganization energy λ are precisely tuned, so that $-\Delta G^0 = \lambda$ to obtain the maximal electron transfer rate,[24] the corresponding parameters in the B-branch are probably not tuned, resulting in low-rate electron transfer in the B-branch.

2.2 The photosynthetic cofactors

Bacteriochlorophylls and bacteriopheophytins

The bacteriochlorophylls are derived from cyclic tetrapyrroles of the porphyrin, chlorin or bacteriochlorin family, which are characterised by a fifth, isocyclic ring (see Fig. 2.2(A-B). All bacteriochlorophylls contain a central magnesium atom. The bacteriopheophytins slightly differ from the BChls in that they lack the central magnesium ion replaced by two protons (see Fig. 2.2C).[25]

The bacteriochlorophylls display in general two major absorption bands, one in the near UV region (the B band) and one in the near IR region (the Q band) (Fig. 2.5A).[26-29] These absorption bands are ascribed to a set of π - π transitions, involving the electrons of the chlorophyll macrocycle. The strong B band (also called Soret band) usually occurs at about 400 nm and corresponds to the two higher-energy $S_0 \rightarrow S_2$ transitions, the weak absorption of the Q band corresponds to the two lower-energy $S_0 \rightarrow S_1$ transitions and typically occurs at 600-700 nm. Since these absorptions belong to the chlorin base, they are similar for many porphyrins. The electronic transitions are associated with transition dipole moments. The longest-wavelength transition is invariably polarized along the y-axis of the molecule and is therefore known as the Q_y transition. This means that this absorption will be strongest if the electric field vector of linearly polarized light is parallel to the y molecular axis of the pigment. The weaker Q_x transition in bacteriochlorophyll *a* is also polarized but along the x molecular axis.[30] The molecular axe of bacteriochlorophyll is depicted in Fig. 2.2A.

BChl *a* (Fig. 2.2A) is the most widely distributed bacteriochlorin pigment, which occurs in the majority of photosynthetic bacteria. In a few species, *e.g. Bl. viridis*, it is

replaced by BChl *b* (Fig. 2.2B).[31, 32] BChl *b* differs from BChl *a* by the presence of a C-8 ethylidene group in ring B. (Fig. 2.2B). Bacteriochlorophyll *b* has the longest-wavelength absorbance of any known chlorophyll-type pigment, with an absorbance maximum of Q_y band at 800 nm.[26] Bacteriochlorophylls *c*, *d*, and *e* are found only in green photosynthetic bacteria. They are unusual among chlorophylls in that they are chlorins with only one reduced pyrrole ring (D), whereas the classic bacteriochlorins have two such rings. Accordingly, their absorptions are intermediate between the plant chlorophylls and the BChl *a* or *b*.[25] BChl *g* is found only in the anoxygenic heliobacteria.[26, 27] It is essentially a molecular hybrid of chlorophyll *a* and bacteriochlorophyll *b* and is very labile.[25]

The metal-free chlorophylls are known as pheophytins. In these compounds, two protons replace the central Mg^{2+}.[25, 33] Both bacteriopheophytins *a* and *b* occur in reaction centers from photosynthetic bacteria, where they are situated nearby bacteriochlorophylls. Bacteriochlorophylls and bacteriopheophytins differ significantly in the absorption spectra, *e.g.* the maximum of Q_x band for BChl is at 590 nm and for BPheo at 537 nm. In bacterial reaction centers the identity of coordinating amino acids determines whether an Mg-containing BChl or a Mg-free BPheo is incorporated.[25, 26]

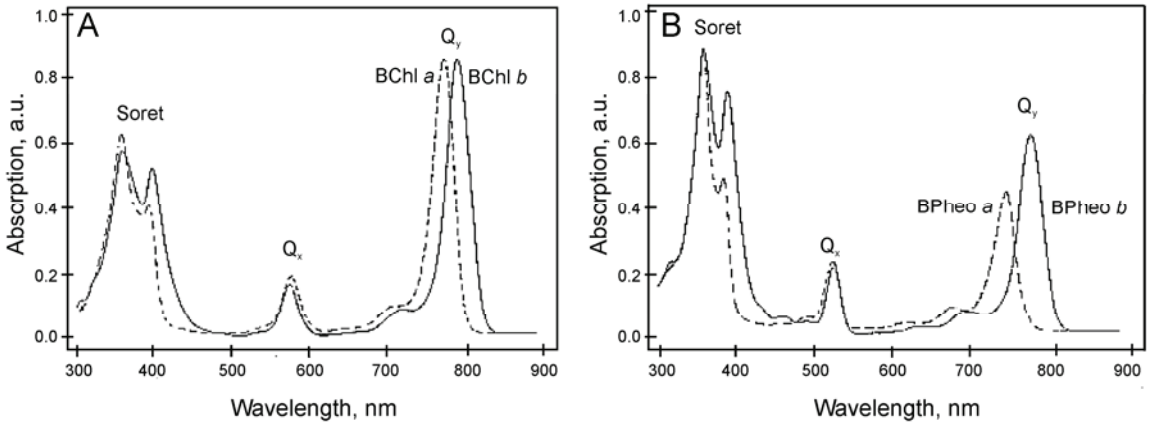

Figure 2.5. UV/Vis absorption spectra of the photosynthetic cofactors:[9]
(A) BChl *a* (dashed) and BChl *b* (solid)
(B) BPheo *a* (dashed) and BPheo *b* (solid).

For bacteriochlorophyll *a*, the Q_x and Q_y bands occur at 577 and 773 nm, respectively (Fig. 2.5A).[9] For bacteriopheophytin *a* Q_x and Q_y bands are present at 525 and 749 nm (Fig. 2.5B). The Soret band occurs at 358 nm in BChl *a* and at 357, 385 nm in BPheo *a*.[26, 34] All bands in bacteriochlorophyll *b* and bacteriopheophytin *b* are slightly red shifted in comparison

to BChl *a* and BPheo *a*. The absorption maxima of the Q_x and Q_y bands of BChl *b* are found at 580 nm and 794 nm, respectively. Those of BPheo *b* are found at 528 nm and 776 nm (Fig. 2.5 B). The Soret band is also slightly red-shifted and found at 368 nm for BChl *b* and at 368, 398 nm for BPheo *b*.[34]

The paramagnetic radical cation,[35, 36] radical anion [37] and metastable triplet state[38] of bacteriochlorophylls have been extensively investigated with EPR spectroscopy. In the radical cation one unpaired electron is present in the HOMO orbital, in the radical anion one electron is present in the LUMO orbital. The triplet state would have two unpaired electrons, one in the HOMO and one in the LUMO orbital and allows a simultaneous study of these orbitals.[36, 39] Triplet EPR spectra of ^{3}BChl *a*, ^{3}BChl *b*, ^{3}BPheo *a*, ^{3}BPheo *b* have been measured and zero field splitting constants have been obtained.[40] An overview of spectroscopic EPR parameters *D* and *E* measured at 5 K in 15 % pyridine/85 % toluene[41] is given in table 1.1.

Table 1.1. Zero field splitting parameters *D* and *E* for BChl *a*/*b* and BPheo *a*/*b* cofactors.[40, 41]

	BChl *a*	BChl *b*	BPheo *a*	BPheo *b*
$D \cdot 10^{-4}$, cm^{-1}	224	212	259	249
$E \cdot 10^{-4}$, cm^{-1}	53	55	46	50

Carotenoids

Carotenoids are a class of unsaturated hydrocarbons and their unsaturated derivatives, which consist of several isoprenoid units. Carotenoids are essentially hydrophobic molecules and are typically found in photosynthetic proteins. Although, many chemically distinct carotenoids exist, some consistent structural features are common to most photosynthetic carotenoids. They are extended molecules with a conjugated π–electron system. Carotenoids from oxygenic organisms usually contain ring structures at each end, and many carotenoids contain oxygen atoms, usually as part of hydroxyl or epoxide groups (Fig. 2.2E). Carotenoids perform two major functions in photosynthesis: photoprotection and light harvesting.[42] An arguably essential function of carotenoids is to prevent harmful photo-oxidative reactions. Carotenoids can interact with singlet oxygen directly and quench it or they can quench the triplet states of chlorophylls before they interact with molecular oxygen.[42] In the quenching process the carotenoid takes over the triplet excitation from the chlorophyll by Dexter energy transfer.[43] Since the lifetime of the carotenoid triplet state is short, typically 10 μs,[44, 45] the excess energy is quickly disposed of as heat by radiationless decay processes. If the carotenoid interacts with singlet oxygen directly, the Dexter mechanism for triplet transfer is

also active.[43] In bacterial reaction centers of *Rb. sphaeroides* and *Bl. viridis* a carotenoid is situated close to B_B. In the former organism it acts as an effective scavenger of triplet states of BChls.[42, 44, 46] A protective functionality of the carotenoid in bacterial reaction centers of *Bl. viridis* has not been reported so far.

The second function of carotenoids in the light-harvesting proteins is to act as accessory light harvesting pigments. They absorb light-energy in the region between 450 and 570 nm, where the chlorophyll pigments do not, and they transfer this energy to the chlorophylls. By using carotenoids as photosynthetic pigments, this wavelength region also becomes available for the photosynthetic process, thus increasing its efficiency.

2.3 References

(1) Feher, G., Allen, J. P., Okamura, M. Y., Rees, D. C. (1989) Structure and Function of Bacterial Photosynthetic Reaction Centers, *Nature, 339*, 111-116.

(2) Feher, G.; Okamura, M. Y. Chemical composition and properties of reaction centers. In *The Photosynthetic Bacteria*; Clayton, R. and Sistrom, Eds.;Plenum Press: New York, 1978; pp 349-386.

(3) Allen, J. P., Feher, G., Yeates, T. O., Komiya, H., Rees, D. C. (1987) Structure of the Reaction Center from *Rhodobacter sphaeroides* R-26 - the Cofactors, *Proc. Natl. Acad. Sci. USA, 84*, 5730-5734.

(4) Allen, J. P., Feher, G., Yeates, T. O., Komiya, H., Rees, D. C. (1987) Structure of the Reaction Center from *Rhodobacter sphaeroides* R-26 - the Protein Subunits, *Proc. Natl. Acad. Sci. USA, 84*, 6162-6166.

(5) Allen, J. P., Feher, G., Yeates, T. O., Komiya, H., Rees, D. C. (1988) Structure of the Reaction Center from *Rhodobacter sphaeroides* R-26 - Protein Cofactor (Quinones and Fe-2+) Interactions, *Proc. Natl. Acad. Sci. USA, 85*, 8487-8491.

(6) Humphrey, W., Dalke, A., Schulten, K. (1996) VMD: Visual molecular dynamics, *J. Mol. Graphics, 14*, 33-38.

(7) Deisenhofer, J., Epp, O., Miki, K., Huber, R., Michel, H. (1985) Structure of the Protein Subunits in the Photosynthetic Reaction Center of Rhodopseudomonas-Viridis at 3A Resolution, *Nature, 318*, 618-624.

(8) Ermler, U., Fritzsch, G., Buchanan, S. K., Michel, H. (1994) Structure of the Photosynthetic Reaction-Center from *Rhodobacter sphaeroides* at 2.65-Angstrom Resolution - Cofactors and Protein-Cofactor Interactions, *Structure, 2*, 925-936.

(9) Bönigk, B. (1994) PhD Thesis, Technische Universität Berlin.

(10) Cantor, C. R.; Schimmel, P. R. Absorption Spectroscopy. In *Biophysical Chemistry*; Bartlett, A. C., Vapnek, and McCombs, Eds.;W.H. Freeman and Company: San Francisco, 1980; pp 349-409.

(11) Hoff, A. J., Deisenhofer, J. (1997) Photophysics of photosynthesis. Structure and spectroscopy of reaction centers of purple bacteria, *J. Phys. Rep., 287*, 2-247.

(12) Allen, J. P.; Yeates, T. O.; Komiya, H.; Rees, D. C. Structure of the Reaction Center from Rhodobacter sphaeroides R-26 and 2.4.1. In *The Photosynthetic Bacterial Reaction Center*; Breton, J. and Vermeglio, Eds.;Plenum Press: 1988; pp 5-11.

(13) Volk, M., Aumeier, G., Langenbacher, T., Feick, R., Ogrodnik, A., Michel-Beyerle, M. E. (1998) Energetics and mechanism of primary charge separation in bacterial photosynthesis. A comparative study on reaction centers of *Rhodobacter sphaeroides* and *Chloroflexus aurantiacus*, *J. Phys. Chem. B, 102*, 735-751.

(14) Kirmaier, C., Holten, D. (1987) Primary Photochemistry of Reaction Centers from the Photosynthetic Purple Bacteria, *Photosynth. Res., 13*, 225-260.

(15) Michel-Beyerle, M. E., Plato, M., Deisenhofer, J., Michel, H., Bixon, M., Jortner, J. (1988) Unidirectionality of Charge Separation in Reaction Centers of Photosynthetic Bacteria, *Biochim. Biophys. Acta, 932*, 52-70.

(16) Arlt, T., Schmidt, S., Kaiser, W., Lauterwasser, C., Meyer, M., Scheer, H., Zinth, W. (1993) The Accessory Bacteriochlorophyll - A Real Electron Carrier in Primary Photosynthesis, *Proc. Natl. Acad. Sci. USA, 90*, 11757-11761.

(17) Holzapfel, W., Finkele, U., Kaiser, W., Oesterhelt, D., Scheer, H., Stilz, H. U., Zinth, W. (1989) Observation of A Bacteriochlorophyll Anion Radical During the Primary Charge Separation in A Reaction Center, *Chem. Phys. Let., 160*, 1-7.

(18) Kirmaier, C., Holten, D., Parson, W. W. (1985) Temperature and Detection-Wavelength Dependence of the Picosecond Electron-Transfer Kinetics Measured in Rhodopseudomonas-Sphaeroides Reaction Centers - Resolution of New Spectral and Kinetic Components in the Primary Charge-Separation Process, *Biochim. Biophys. Acta, 810*, 33-48.

(19) Kirmaier, C., Holten, D., Parson, W. W. (1985) Picosecond-Photodichroism Studies of the Transient States in Rhodopseudomonas-Sphaeroides Reaction Centers at 5-K - Effects of Electron-Transfer on the 6 Bacteriochlorin Pigments, *Biochim. Biophys. Acta, 810*, 49-61.

(20) Lendzian, F., Bittl, R., Lubitz, W. (1998) Pulsed ENDOR of the photoexcited triplet states of bacteriochlorophyll a and of the primary donor P-865 in reaction centers of *Rhodobacter sphaeroides* R-26, *Photosynth. Res., 55*, 189-197.

(21) Paddock, M. L., Chang, C., Xu, Q., Abresch, E. C., Axelrod, H. L., Feher, G., Okamura, M. Y. (2005) Quinone (Q(B)) reduction by B-branch electron transfer in mutant bacterial reaction centers from *Rhodobacter sphaeroides*: Quantum efficiency and X-ray structure, *Biochemistry, 44*, 6920-6928.

(22) Frank, H. A., Friesner, R., Nairn, J. A., Dismukes, G. C., Sauer, K. (1979) Orientation of the Primary Donor in Bacterial Photosynthesis, *Biochim. Biophys. Acta, 547*, 484-501.

(23) Plato, M., Möbius, K., Michel-Beyerle, M. E., Bixon, M., Jortner, J. (1988) Intermolecular Electronic Interactions in the Primary Charge Separation in Bacterial Photosynthesis, *J. Am. Chem. Soc., 110*, 7279-7285.

(24) Marcus, R. A., Sutin, N. (1985) Electron Transfers in Chemistry and Biology, *Biochim. Biophys. Acta, 811*, 265-322.

(25) Scheer, H. Structure and occurence of chlorophylls. In *The Chlorophylls*; Scheer, H., Ed.;CRC Press: Boca Raton, 1991; pp 4-31.

(26) Hoff, A. J.; Amesz, J. Visible absorption spectroscopy of chlorophylls. In *The Chlorophylls*; Scheer, H., Ed.;CRC Press: Boca Raton FL, 1991; pp 723-738.

(27) Amesz, J. (1995) The Heliobacteria, A New Group of Photosynthetic Bacteria, *J. Photochem. Photobiol. B, 30*, 89-96.

(28) Gouterman, M. (1959) Study of the Effects of Substitution on the Absorption Spectra of Porphin, *J. Chem. Phys., 30*, 1139-1161.

(29) Longuet-Higgins, H. C., Rector, C. W., Platt, J. R. (1950) Molecular Orbital Calculations on Porphine and Tetrahydroporphine, *J. Chem. Phys., 18*, 1174-1181.

(30) Gouterman, M. (1961) Spectra of Porphyrins, *J. Mol. Spectrosc., 6*, 138-163.

(31) Michel, H. (1982) 3-Dimensional Crystals of A Membrane-Protein Complex - the Photosynthetic Reaction Center from *Rhodopseudomonas viridis*, *J. Mol. Biol., 158*, 567-572.

(32) Deisenhofer, J., Epp, O., Miki, K., Huber, R., Michel, H. (1984) X-Ray Structure-Analysis of A Membrane-Protein Complex - Electron-Density Map at 3A Resolution and A Model of the Chromophores of the Photosynthetic Reaction Center from *Rhodopseudomonas viridis*, *J. Mol. Biol., 180*, 385-398.

(33) Blankenship, R. *Molecular mechanisms of photosynthesis;* Blackwell Science: Oxford, London, 2002.

(34) Oelze, J. Analysis of Bacteriochlorophylls. In *Methods in Microbiology*; Gottschalk, G., Ed.;Academic Press: London, 1985; pp 257-283.

(35) Lubitz, W., Lendzian, F., Plato, M., Scheer, H., Möbius, K. (1997) The bacteriochlorophyll a cation radical revisited. An ENDOR and TRIPLE resonance study, *Appl. Magn. Reson, 13*, 531-551.

(36) Lubitz, W. EPR and ENDOR studies of chlorophyll cation and anion radicals. In *The Chlorophylls*; Scheer, H., Ed.;CRC Press: Boca Raton, 1991; pp 903-944.

(37) Lubitz, W., Lendzian, F., Möbius, K. (1981) N-14 and H-1 Electron Nuclear Multiple Resonance Experiments on Bacteriochlorophyll-A Anion Radicals in Solution, *Chem. Phys. Let., 81*, 235-241.

(38) Budil, D. E., Thurnauer, M. C. (1991) The Chlorophyll Triplet-State As A Probe of Structure and Function in Photosynthesis, *Biochim. Biophys. Acta, 1057*, 1-41.

(39) Angerhofer, A. Chlorophyll triplets and radical pairs. In *Chlorophylls*; Scheer, H., Ed.;CRC Press: Boca Raton FL, 1991; pp 945-991.

(40) Thurnauer, M. C. (1979) ESR study of the photoexcited triplet state in photosynthetic bacteria, *Rev. Chem. Int., 100*, 197-231.

(41) Thurnauer, M. C., Norris, J. R. (1977) Ordering of Zero-Field Triplet Spin Sub-Levels in Chlorophylls - Magneto-Photoselection Study, *Chem. Phys. Let., 47*, 100-105.

(42) Frank, H. A., Cogdell, R. J. (1996) Carotenoids in photosynthesis, *Photochem. Photobiol., 63*, 257-264.

(43) Dexter, D. L. (1953) A Theory of Sensitized Luminescence in Solids, *J. Chem. Phys., 21*, 836-850.

(44) Frank, H. A., Bolt, J. D., Costa, S. M. D. B., Sauer, K. (1980) Electron-Paramagnetic Resonance Detection of Carotenoid Triplet-States, *J. Am. Chem. Soc., 102*, 4893-4898.

(45) Frank, H. A., Chynwat, V., Hartwich, G., Meyer, M., Katheder, I., Scheer, H. (1993) Carotenoid Triplet-State Formation in *Rhodobacter sphaeroides* R-26 Reaction Centers Exchanged with Modified Bacteriochlorophyll Pigments and Reconstituted with Spheroidene, *Photosynth. Res., 37*, 193-203.

(46) McGann, W. J., Frank, H. A. (1985) Transient Electron-Spin Resonance Spectroscopy of the Carotenoid Triplet-State in *Rhodopseudomonas sphaeroides* Wild-Type, *Chem. Phys. Let., 121*, 253-261.

Chapter 3

Theory and methodology

3.1 Theory

3.1.1 EPR Spectroscopy

Electron spin resonance spectroscopy (ESR), also known as electron paramagnetic resonance (EPR) was invented by Zavoisky in 1944. The subject matter of EPR is the interaction of spins with applied magnetic fields and with each other.[1] Most commonly, EPR spectroscopy is used to obtain information of the electronic structure of the species under investigation. The hyperfine coupling pattern provides information about the number and identity of magnetic nuclei with which the unpaired electron interacts. Additionally, like all forms of spectroscopy, EPR intensities, through the dependence on the number of spins, can be used analytically to determine the concentration of a paramagnetic species. Also, EPR spectroscopy can be used to determine rate constants of a chemical reaction or the rate of a conformation change.

3.1.2 Spin Hamiltonian

Zeeman interaction

The EPR spectrum of a free radical or coordination complex with one unpaired electron (S = ½) gives rise to a simple Lorentzian resonance signal. When an electron is placed in a magnetic field, the degeneracy of the electron levels is lifted and described by the spin Hamiltonian:

$$H_{Ze} = g_e \mu_B \vec{B} \cdot \vec{S} \qquad (1)$$

The electron spin energy levels are then:

$$E_{\pm} = \pm(\tfrac{1}{2}) g_e \mu_B B \qquad (2)$$

The energy levels are depicted in Fig. 3.1 together with their eigenfunctions.

The difference in energy between two levels equals:

$$\Delta E = g_e \mu_B B \qquad (3)$$

Application of an oscillating field perpendicular to H induces transitions of the electron spin provided the frequency ν such that the electronic paramagnetic resonance condition

$$h\nu = g_e \mu_B B \tag{4}$$

is satisfied.

The same considerations are valid for nuclear spins described by the nuclear Zeeman Hamiltonian:

$$H_{Zn} = -g_n \mu_N \vec{B} \cdot \vec{I} \tag{5}$$

The nuclear energy is much smaller than the electronic energy.

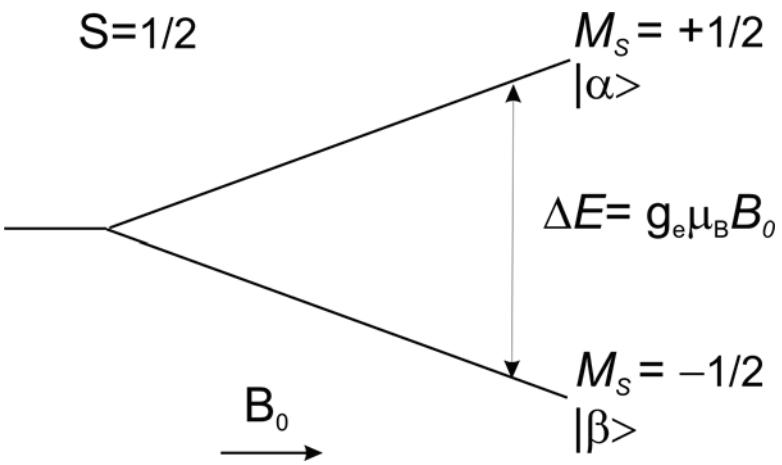

Figure 3.1. Energy levels for an electron spin (S=1/2) in the presence of a magnetic field B_0.

Hyperfine coupling

The Hamiltonian that describes the magnetic interaction between the electron spin and a nuclear spin consists of two parts:

$$H = H_1 + H_2 \tag{6}$$

where H_1 represents the isotropic part and H_2 is the anisotropic part of the hyperfine interaction.

Because of a finite density of the unpaired electron at the nucleus, the magnetic moments of the unpaired electron and the nucleus are coupled via the so-called Fermi contact interaction. It has the form

$$H_1 = a\vec{I} \cdot \vec{S} \tag{7}$$

The coupling constant a is proportional to the squared amplitude of the wave function of the unpaired electron at the nucleus.

$$a = \frac{8\pi}{3} g_e \mu_B g_n \mu_N \left|\psi(0)\right|^2 \tag{8}$$

There is also a coupling between the magnetic moments of the electron and nucleus, which is entirely analogous to the classical dipolar coupling between two bar magnets. This dipolar hyperfine interaction is described by the following Hamiltonian:

$$H_2 = -g_e \mu_B g_n \mu_N \left\{ \frac{\vec{I} \cdot \vec{S}}{r^3} - \frac{3(\vec{I} \cdot \vec{r})(\vec{S} \cdot \vec{r})}{r^5} \right\} \tag{9}$$

The dipolar interaction is anisotropic. It averages to zero if the electron cloud is spherical.

Quadrupole interaction

Nuclei with $I \geq 1$ can have a non-spherical charge distribution so that they have a quadrupole moment.[1] The charge distribution can either be oblate or prolate. The Hamiltonian can then be written as a tensor coupling of the nuclear spin with itself,

$$H_Q = \vec{I} \cdot \vec{\vec{P}} \cdot \vec{I}\,, \tag{10}$$

where $\vec{\vec{P}}$ is the quadrupole coupling tensor.

The elements of the traceless tensor $\vec{\vec{P}}$ are:

$$P_{\alpha\beta} = \frac{eQ}{2I(2I-1)} V_{\alpha\beta} \tag{11}$$

where $V_{\alpha\beta}$ is the electric field gradient at the nucleus (α,β = x,y,z).

Multiple electrons. The triplet state

A molecule in which the total spin of the electrons is equal or more than one ($S \geq 1$) has split electron spin energy levels even without the external magnetic field. In the case of a triplet state the energy level scheme consists of three distinct sublevels or states with almost the same energy. In the triplet state an even number of electrons is present.

The spin Hamiltonian that describes the magnetic dipole interaction between the two electrons with spins $\vec{s}_1$ and $\vec{s}_2$ is:

$$H_{ZFS} = \frac{\mu_0}{4\pi} g_e^2 \mu_B^2 \left\{ \frac{\vec{s}_1 \cdot \vec{s}_2}{r^3} - \frac{3(\vec{s}_1 \cdot \vec{r})(\vec{s}_2 \cdot \vec{r})}{r^5} \right\} \tag{12}$$

Expressed entirely in terms of the total spin $\vec{S}$ it has the form:

$$H_{ZFS} = \vec{S} \cdot \vec{\vec{D}} \cdot \vec{S} \tag{13}$$

$\vec{\vec{D}}$ is a symmetric tensor called the zero-field splitting tensor, which has elements:

$$D_{\alpha\beta} = \frac{1}{2}\frac{\mu_0}{4\pi} g_e^2 \mu_B^2 \left\langle \frac{r^2 \delta_{\alpha\beta} - 3\alpha\beta}{r^5} \right\rangle \tag{14}$$

The zero field splitting tensor $\vec{\vec{D}}$ is symmetric and traceless and can always be cast into diagonal form by a suitable choice of axes. For this principal axis system the Hamiltonian is:

$$H_{ZFS} = D_{XX} S_X^2 + D_{YY} S_Y^2 + D_{ZZ} S_Z^2, \tag{15}$$

where D_{XX}, D_{YY}, D_{ZZ} are the principal values of $\vec{\vec{D}}$.

Since $\vec{\vec{D}}$ is traceless, the Hamiltonian can be expressed by two new parameters:

$$D = D_{ZZ} - \frac{1}{2}\left(D_{XX} + D_{YY}\right) \tag{16}$$

$$E = \frac{1}{2}\left(D_{XX} - D_{YY}\right) \tag{17}$$

and

$$H_{ZFS} = D\left\{ S_Z^2 - \frac{1}{3} S(S+1) \right\} + E\left(S_X^2 - S_Y^2\right) \tag{18}$$

The eigenvalues of the ZFS Hamiltonian are:

$$\begin{aligned} E_X &= \frac{1}{3} D + E \\ E_Y &= \frac{1}{3} D - E \\ E_Z &= -\frac{2}{3} D \end{aligned} \tag{19}$$

Combining all components, the full spin Hamiltonian is written as:

$$\begin{aligned} &H = H_{Ze} + H_{Zn} + H_{HF} + H_{ZFS} + H_Q = \\ &g_e \mu_B \vec{B} \cdot \vec{S} - g_n \mu_N \vec{B} \cdot \vec{I} + \vec{S} \cdot \vec{\vec{A}} \cdot \vec{I} + \vec{S} \cdot \vec{\vec{D}} \cdot \vec{S} + \vec{I} \cdot \vec{\vec{P}} \cdot \vec{I} \end{aligned} \tag{20}$$

Under the assumption that the terms involving the nuclear spin operator are much smaller than the other terms (strong field approximation), the electronic spin Hamiltonian is comprised of the following terms

$$H_T = g_e \mu_B \vec{B} \cdot \vec{S} + \vec{S} \cdot \vec{\vec{D}} \cdot \vec{S} \tag{21}$$

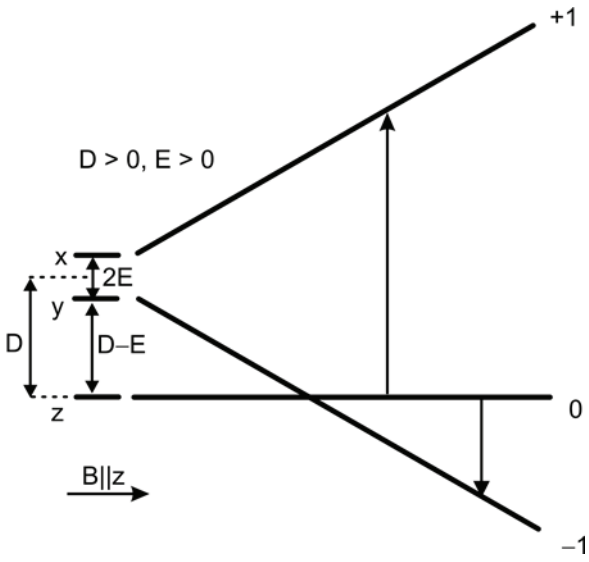

Figure 3.2. Energy level scheme of the triplet sublevels with the magnetic field direction parallel to the *Z* principal axis of the ZFS tensor. The zero-field-splitting parameters *D* and *E* are depicted in the figure.

The zero-field splitting of organic molecules in triplet states is dominated by the dipole-dipole interaction of the unpaired electrons. The ZFS parameters *D* and *E* are useful to characterize the electronic spin density distribution of these molecules in the triplet state. The energy level scheme for the magnetic field oriented parallel to Z is depicted in Fig. 3.2. Whether an EPR transition becomes absorptive or emissive depends on the relative populations of the energy levels, which in turn is determined by the mechanism of triplet formation.

The full spin Hamiltonian for the triplet state with hyperfine interaction to one I = ½ nucleus is:

$$H_T = g_e \mu_B \vec{B} \cdot \vec{S} - g_N \mu_n \vec{B} \cdot \vec{I} + \vec{S} \cdot \vec{\vec{A}} \cdot \vec{I} + \vec{S} \cdot \vec{\vec{D}} \cdot \vec{S} \qquad (22)$$

This Hamiltonian is used to describe the ENDOR experiments, where a proton spin interacts with the triplet electron spin.

3.1.3 Formation of the triplet state

In a simple molecular orbital picture the molecule in the ground state have two electrons in the HOMO and no electrons in the LUMO, the molecule in the triplet state would have an unpaired electron in both the HOMO and the LUMO orbitals.[2] Investigation of the triplet state will allow simultaneously study of the HOMO and LUMO orbital. The energy

levels in an excited triplet state are usually not populated according to the Boltzmann-law. Transitions between energy levels 0, +1 and 0, −1 may occur (Fig. 3.2). This means that two EPR lines for one canonical orientation may be observable. The polarization pattern (the order of absorptive/emissive transitions observed through at all 6 canonical orientations) contains general information about the mechanism of formation of the triplet state.

Four different mechanisms of the triplet formation are possible, of which the last two are direct triplet formation mechanisms:

1) Triplet-triplet energy transfer (sensibilisation), that occurs in bacterial reaction centers, *e.g.* special pair – carotenoid transfer.[3, 4] In this mechanism one molecule already resides in the triplet state. The excitation is then transferred to another molecule with a triplet state lower in energy than the first molecule and the first molecule reverts back to the ground state.

2) The triplet pair mechanism is possible under high-energy excitation. Two molecules are necessary for this process (triplet fission). Exciton fission is the isoenergetic intermolecular transitions, through which a high singlet excitation on one molecule is converted into a pair of lower triplet excitations located on two different molecules.[5] This process has been observed in athracene, stilbene, teracene and perylene crystals and has been investigated using magnetic field dependence effects.[6, 7] The transition to the triplet pair state energetically is only possible if the vibronic singlet levels are higher in energy by twice the lowest electronic triplet state energy.[5]

3) Intersystem crossing (ISC)

In the intersystem crossing mechanism the formation of the triplet state occurs on one molecule. Spin-dependent processes, most notably spin-orbit (SO) coupling,[8] flip the spin of one of the unpaired electrons in the excited singlet state to form the triplet state of the molecule. This mechanism is dominant for porphyrins (*e.g.* chlorophylls and bacteriochlorophylls in solutions). For monomeric BChl, a polarization pattern EEEAAA is observed in the EPR spectra, which points to an ISC mechanism of the triplet formation.[9-11]

4) Radical pair mechanism (RP)

In the radical pair formation mechanism, after excitation, the excited electron leaves the molecule and a radical pair state of the donor and acceptor is initially present as a singlet state. Since the unpaired electrons are located on different molecules, they feel a different effective magnetic field and their spins are no longer correlated.[12] Because the singlet state remains virtually degenerate with the T_0 sublevel of the triplet radical pair state, a significant mixing of the S and T_0 levels occurs, in which the radical pair state oscillates back and forth between S and T_0. The T_0 radical pair state can then recombine to form the triplet state of the

molecule that was excited. This mechanism is also called the S-T_0 mechanism.[13] In the radical pair mechanism the $M_S = 0$ sublevel of the molecule is exclusively populated. This implies that shortly after the laser flash and before decay processes play a role, all $T_0 \rightarrow T_{+1}$ transitions are absorptive and $T_0 \rightarrow T_{-1}$ are emissive and it also implies that the amplitudes of the absorptive and emissive signals are identical.[i]

3.2 Methodology

3.2.1 cw EPR spectroscopy

The Electron Paramagnetic Resonance effect occurs when the energy of the microwave field matches the energy difference between two electron spin levels. The first EPR experiment employed continuous microwave irradiation. The magnitude of the EPR signal depends on the difference in the population of these levels. The EPR sensitivity (net absorption) increases with the total number of spins, with decreasing temperature and with increasing magnetic field strength.[14] The basic requirement of an EPR spectrometer is a source of frequency-stable radiation and a magnet providing a field, which can be slowly swept to record the spectrum. The microwave radiation is provided by a klystron, a Gunn diode or a digitizer and is transported to the sample along a waveguide. The sample itself is located in a resonant cavity, whose dimensions match the wavelength of the radiation so that a standing wave appears.[1] The exact frequency of the cavity with sample inside depends on the sample character and temperature, which means that the frequency of microwave radiation has to be slightly tuned. The radiation passes from the waveguide into the cavity through the small hole, the iris. In condition of perfect matching all the microwave power entering the cavity is stored therein and there is no power reflecting from the cavity. If the applied magnetic field is varied to bring the sample to resonance, microwaves are absorbed by the sample, which causes a reduction in the reflected radiation. Thus, the absorption of microwaves by the sample can be detected by measuring of reflected microwave power. Such a measurement would detect also noise at all frequencies and signal-to-noise ration will be very poor. A small amplitude field modulation has been introduced to solve this problem. This small oscillating component is superimposed on the applied magnetic field. The applied magnetic field is swept slowly, that means that at any time at the detector microwave power will contain this oscillating component, whose amplitude will be proportional to the slope of

[i] A detailed explanation of the RP and ISC mechanisms of the triplet formation in the bRC is given in the "Discussion" section of the chapter 5.

the absorption line. This component can be ampflied and the EPR signal is detected as the first derivative of the absorption curve.[1, 14]

3.2.2 Pulsed EPR spectroscopy

A more extended technique is based on pulsed EPR methodology, where short and intense microwave pulses are applied to sample and a fast response is detected *via* the free-induction decay method[15] or echo method.[16] A radiation pulse contains a range of frequencies. A pulse, which rotates the magnetization by 90 degrees, such that the magnetization lies along the y-axis is called a π/2-pulse. A π-pulse flips magnetization completely such that it is aligned along *–z*.[1] Pulses of short duration and high microwave field are known as "hard" pulses. "Soft" pulses have a smaller excitation bandwidth and a longer duration. Pulsed EPR experiments can be elegantly analyzed using Bloch equations and the density matrix formalism.[1, 17]

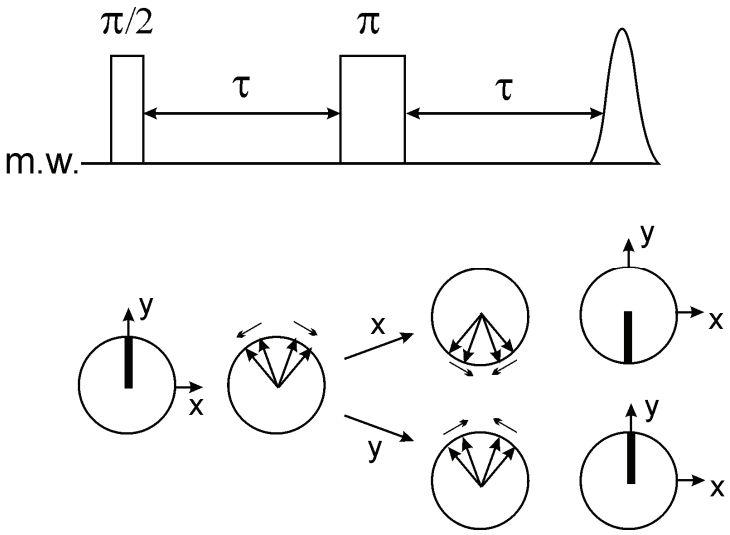

Figure 3.3. Pulse sequence for the ESE detected EPR experiment. The formation of an echo is shown below.[1]

A field-swept EPR spectrum can be recorded by measuring an echo signal created by a sequence of microwave pulses with fixed time intervals and variable external magnetic fields. This method measures the absorption signal directly. The most commonly used pulse schemes to record a field-swept EPR are the two-pulse Hahn echo and the three-pulse stimulated echo sequences.[15]

The phenomenon of the echo is based on the non-linear behaviour of an ensemble of spins with different Larmor frequencies.[16] For a Hahn echo sequence this is shown in Fig. 3.3.

At thermal equilibrium, the magnetization vector is oriented along the *z*-axis. The π/2 pulse along the *x*-axis rotates the magnetization to the *–y*-axis. After the pulse, the different spin packets begin to precess with their individual Larmor frequencies around the *z*-axis, resulting in a defocusing of the transverse magnetization. After time τ, a π pulse again along the *x*-axis turns all the magnetization vectors 180° about this axis and after another time τ, all the vectors are aligned along the *y*-axis. The resulting net *y* magnetization is called an *electron spin echo.*[15]

In this study, light-induced EPR spectra have been measured and a laser pulse has been used for excitation. The time between the laser pulse and the first microwave pulse in the Hahn echo sequence is called the Delay after flash time (DAF), and this type of EPR spectroscopy is known as DAF EPR. If the DAF time is varied, the time evolution of the EPR signal can be investigated. Using pulsed EPR spectroscopy, zero field splitting constants of the EPR spectrum can be obtained, which gives information about the effective distance between the triplet electrons. Information of the origin of the triplet state is obtained from the polarization pattern of the EPR spectrum. DAF EPR measurements and temperature dependent measurements deliver information about dynamics of the triplet states in bacterial reaction centers and possible triplet-triplet transfer pathways, *e.g.* special pair-carotenoid transfer.

ENDOR Spectroscopy

Electron Nuclear Double Resonance (ENDOR) spectroscopy is a hybrid EPR/NMR method in which microwave pulses and RF pulses are applied to induce electron spin (EPR) and nuclear spin (NMR) transitions. ENDOR works by partially saturating an EPR transition at a fixed field. Saturation makes the population of two EPR levels equal, which makes electron resonance signal very weak and broad.

The RF pulse inverts the nuclear spins and an interchange of the populations of the two nuclear states occurs. The experiment is performed by sweeping the NMR frequency to induce nuclear spin transitions. When the RF frequency matches the appropriate NMR transition frequency the EPR absorption reappers.[14] In a polarization-transfer pulsed ENDOR experiment, the ENDOR effect is based on the transfer of polarization between electron and nuclear transitions.[15] The first pulsed ENDOR methodology was proposed by Mims,[18] a more recent method was invented by Davies.[19] The Davies ENDOR scheme used in this study is based on selective microwave pulses and is presented in Fig. 3.4 together with the populations of the energy levels.[19] A first microwave pulse inverts the polarization of the EPR transition.

During the subsequent mixing period, the nuclear polarization is changed by a selective RF pulse. If the RF pulse is resonant with one of the nuclear frequencies, the polarization of this

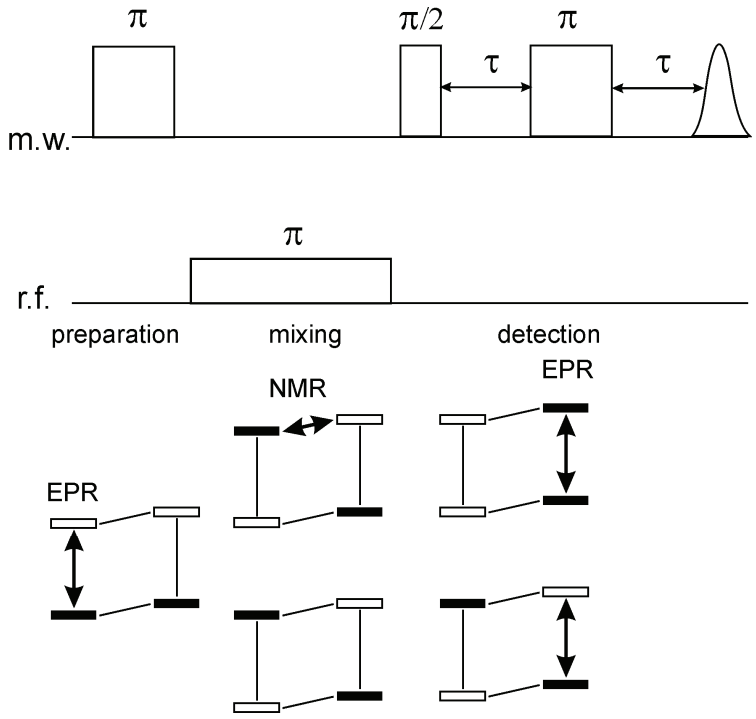

Figure 3.4. Pulse sequence for the Davies-ENDOR experiment. Populations of the energy levels at different stages of the pulse sequence are also depicted.[15]

transition changes accordingly. During the detection period, the nuclear polarization is transferred to electron coherence and measured *via* the electron spin echo (Fig. 3.4).

In the strong field approximation for the molecule in the triplet state the spin Hamiltonian (22) gives the frequency of the nuclear transitions:[1, 20]

$$\nu_{ENDOR}^{T} = \nu_n - M_S A_T \qquad (23)$$

where ν_n is the nuclear Zeeman frequency, A_T represents the hyperfine interaction in the triplet state.[i]

In this study, light-induced ENDOR spectra have been measured and a laser pulse has been used for *in situ* excitation. Pulsed ENDOR spectroscopy resolves hyperfine structure of the molecule and delivers information about the electronic structure of the investigated system on an atomic level or nuclear level. Detailed information about the electron spin density distribution of the molecule in the triplet state allows the determination of the degree of delocalization of the wavefunction.

[i] An energy level diagram for the ENDOR experiment and explanation of the signs of the hyperfine couplings obtained *via* ENDOR spectroscopy on the triplet state can be found in the"Theory" section of chapter 6.

3.2.3 Quantum Chemistry

Quantum chemistry is the research field related to solving the non-relativistic Schrödinger equation for electrons in molecules. Quantum chemistry thus mathematically describes the electronic properties of atoms and molecules. The Schrödinger equation (or Dirac equation for the relativistic case) can be solved analytically only for simple systems, *e.g.* for a harmonic oscillator or for a one-electron system. The Schrödinger-equation for many electron systems can not be solved analytically and approximations are necessary, *e.g.* the Born-Oppenheimer approximation and Hartree-Fock approximation. These approximations are incorporated in quantum chemical methods of which Density Functional Theory is widely used.[21, 22] Quantum chemical calculations deliver information about the electronic structure of the species on the atomic or nuclear level and can be used as a complementary method to experimental techniques like EPR/ENDOR spectroscopy. Calculated electron spin densities, zero field splitting constants and hyperfine couplings can be compared with experimental values derived from EPR/ENDOR techniques and different models of the spin density distribution can be verified.

Hartree-Fock approximation

The simplest antisymmetric wave function, which can describe the ground state of an N-electron system, is a single Slater determinant,

$$\left|\Psi_0\right\rangle = \left|\chi_1\chi_2\cdots\chi_N\right\rangle \tag{24}$$

The best wave function of this functional form is the one which gives the lowest possible energy

$$E_0 = \left\langle\Psi_0\left|H\right|\Psi_0\right\rangle, \tag{25}$$

where H is the full electronic Hamiltonian. By minimizing E_0 with respect to the spin orbitals, one can derive an equation, called the Hartree-Fock equation, which determines the optimal spin orbitals. The Hartree-Fock equation is an eigenvalue equation of the form

$$f(i)\chi(x_i) = \varepsilon\chi(x_i) \tag{26}$$

where *f(i)* is an effective one-electron operator, called the Fock operator. It has the form

$$f(i) = -\frac{1}{2}\nabla_i^2 - \sum_{A=1}^{M}\frac{Z_A}{r_{iA}} + v^{HF}(i) \tag{27}$$

where v^{HF}(i) is the average potential experienced by the *i*-th electron due to the presence of the other electrons. The Hartree-Fock approximation is a replacement for the complicated many electron problem by a one-electron problem with a treatment of electron-electron

repulsion in an average way.[22] The Hartree-Fock equation is non-linear due to the dependence of the Hartree-Fock potential on the spin orbitals of other electrons and thus has to be solved iteratively.

A system with an even number of electrons, which are all paired to give an overall singlet, is called a *closed-shell* system. In these systems, Hartree-Fock solutions have doubly occupied spatial orbitals, i.e. two spin orbitals share the same spatial orbital and have the same orbital energy. This is called the spin-restricted Hartree-Fock approximation (RHF). If a system contains an odd number of electrons, the RHF picture frequently becomes inadequate and it is necessary to deal with open shell scheme. In the restricted open-shell Hartree-Fock approximation the doubly occupied spatial orbitals are still equal and only a few singly occupied orbitals are present. In the unrestricted Hartree Fock approximation (UHF), each spatial orbital can be different.[21]

DFT

Density functional theory rests on the theorems of Hohenberg and Kohn, which showed that external potential of a system *v(r)* is a functional of the electron spin density *ρ(r)*.

$$\rho(r_1) = N \int ... \int |\Psi(x)|^2 \, dx_2 ... dx_N \tag{28}$$

According to the second Hohenberg-Kohn theorem, the variational principle can be used for the ground state to obtain the correct ground state energy.

The electronic energy can be written as

$$E_{elec}[\rho] = T[\rho] + E_{ne}[\rho] + J[\rho] + E_{ncl}[\rho], \tag{29}$$

Where $T[\rho]$ is the kinetic energy, $E_{ne}[\rho]$ the nuclei-electron attraction, $J[\rho]$ the classical Coulomb interaction, and $E_{ncl}[\rho]$ contains non-classical contributions like electron exchange and correlation.

Expanding equation (26) the following equation is obtained:

$$E_{elec}[\rho] = \frac{\hbar}{2m_e} \sum_{i=1}^{n} \int \psi_i^*(r_1) \nabla_1^2 \psi_i(r_1) dr_1 - \sum_{I=1}^{N} \frac{Z_I e^2}{4\pi\varepsilon_0 r_{I1}} \rho(r_1) dr_1 + \frac{1}{2} \int \frac{\rho(r_1)\rho(r_2)e^2}{4\pi\varepsilon_0 r_{12}} dr_1 dr_2 + E_{XC}[\rho] \tag{30}$$

A variational treatment leads to the one-electron Kohn-Sham equations:

$$-\frac{\hbar}{2m_e}\nabla_1^2\psi_i-\left(\sum_{I=1}^{N}\frac{Z_I e^2}{4\pi\varepsilon_0 r_{I1}}\int\frac{\rho(r_2)e^2}{4\pi\varepsilon_0 r_{12}}dr_2-V_{XC}(r_1)\right)\psi_i(r_1)$$
$$=\left(-\frac{\hbar}{2m_e}\nabla_1^2+V_{eff}(r_1)\right)\psi_i(r_1)=\varepsilon\psi_i(r_1) \qquad (31)$$

where ε_I are the orbital energies; exchange-correlation potential V_{XC} can be obtained as:

$$V_{XC}=\frac{\delta E_{XC}[\rho]}{\delta\rho} \qquad (32)$$

The Kohn-Sham equations (31) are non-linear because they depend on the wavefunctions of the other electrons and have to be solved self-consistently. An initial guess of the electron density is inserted into equation (31) from which a set of orbitals is obtained, which in turn leads to an improved electron density. The procedure is repeated until self-consistency is reached.

The effective potential of KS equations V_{eff} contains no reference to the spins of the electrons. Similar considerations as for RHF and UHF schemes for Hartree-Fock approximation are also valid for KS equation, resulting in RKS and UKS spin formalisms.

The exchange-correlation functional V_{XC} is unknown in density functional theory. It can be described *via* different approximation functions. The exchange-correlation energy is separated in two parts, an exchange part E_X and a correlation part E_C.

$$E_{XC}[\rho]=E_X[\rho]+E_C[\rho] \qquad (33)$$

The simplest approximations are the local density approximation (LDA), where the potential depends only on the electron density at the coordinate and the local spin density approximations (LSDA), which includes the electron spin additionally to the LDA.

The exchange-correlation energy in the LSDA model can be estimated as

$$E_{XC}^{LSDA}=\int\varepsilon_{XC}\left[\rho_\alpha(r),\rho_\beta(r)\right]d^3r \qquad (34)$$

A better approximation of exchange-correlation energy would be to use not only information about the density $\rho(\vec{r})$ at a particular point *r* but also information about gradient of the charge density $\nabla\rho(\vec{r})$ in order to account for the inhomogeneity of the true electron density.

The generalized gradient approximations (GGA) are the mostly used functionals in DFT. They include gradients of the charge densities, have special hole constraints and can be generally written as

$$E_{XC}^{GGA}=\int f\left[\rho_\alpha(r),\rho_\beta(r),\nabla\rho_\alpha(r),\nabla\rho_\beta(r)\right]d^3r \qquad (35)$$

Popular functionals in DFT are BLYP, B3LYP, BP86.

Almost all applications of KS density functional theory make use of the *Linear combination of atomic orbitals* expansion (LCAO expansion) of expansion of Kohn-Sham (KS) orbitals introduced by Roothaan in the framework of the Hartree-Fock method. In the LCAO approach a set of L predefined basic functions $\{\eta_\mu\}$ is introduced and the KS orbitals are linearly expanded as

$$\psi_i = \sum_{\mu=1}^{L} c_{\mu i}\eta_\mu \tag{36}$$

In real applications L is finite and it is of crucial importance to choose $\{\eta_\mu\}$ such that the linear combination provides an approximation of the exact Kohn-Sham orbitals as accurately as possible. The LCAO expansion translates the non-linear optimization problem into a linear one, which can be solved with standard linear algebra methods.

In conventional wave functions based approach, such as the Hartree-Fock and configuration-interaction schemes, the set $\{\eta_\mu\}$ is almost universally chosen to consist of so called Cartesian Gaussian-type orbitals (GTO). From a physical point of view, Slater-type orbitals (STO) are a better choice for basic functions, but integrals using STO basis sets are difficult to compute. In the so-called contracted GTO basis sets several primitive Gaussian functions are combined in a fixed linear combination to give one contracted Gaussian function (CGF).

The simplest and least accurate expansion of the molecular orbitals (*minimal* sets) utilize only one basis function (or only one contracted basis function) for each atomic orbital up to and including the valence orbital. The next level of sophistication is the *double-zeta* basis sets, where the set of functions is doubled. In *split-valence* type sets the double set of functions is limited only to the valence orbitals, while the chemically mostly inert core electrons are still treated in a minimal set. Basis sets can be augmented by polarization functions, *i.e.* functions of higher angular momentum than those occupied in the atom, which allows the orbitals to better adapt to the molecular environment. The polarized double-zeta and split valence basis sets are the most frequently used basis sets in routine quantum chemistry applications nowadays.

3.3 References

(1) Atherton, N. *Principles of Electron Spin Resonance;* Ellis Horwood PTR Prentice Hall: New York, 1993.

(2) Budil, D. E., Thurnauer, M. C. (1991) The Chlorophyll Triplet-State As A Probe of Structure and Function in Photosynthesis, *Biochim. Biophys. Acta, 1057*, 1-41.

(3) Frank, H. A., Bolt, J. D., Costa, S. M. D. B., Sauer, K. (1980) Electron-Paramagnetic Resonance Detection of Carotenoid Triplet-States, *J. Am. Chem. Soc., 102*, 4893-4898.

(4) Frank, H. A., Cogdell, R. J. (1996) Carotenoids in photosynthesis, *Photochem. Photobiol., 63*, 257-264.

(5) Klein, G., Voltz, R. (1975) Formation and Decay of Superexcited States in Dense Organic-Matter Under High-Energy Radiation, *Intern. J. Radiat. Phys. Chem., 7*, 155-174.

(6) Klein, G. (1983) Production of Pairs of Singlet Excitons and Triplet Excitons in Anthracene-Crystals, *Chem. Phys. Let., 97*, 114-118.

(7) Swenberg, C. E., Stacy, W. T. (1968) Bimolecular radiationless transitions in crystalline tetracene, *Chem. Phys. Let., 2*, 327-328.

(8) Neese, F. (2006) Importance of direct spin-spin coupling and spin-flip excitations for the zero-field splittings of transition metal complexes: A case study, *J. Am. Chem. Soc., 128*, 10213-10222.

(9) Thurnauer, M. C. (1979) ESR study of the photoexcited triplet state in photosynthetic bacteria, *Rev. Chem. Int., 100*, 197-231.

(10) Lubitz, W., Lendzian, F., Bittl, R. (2002) Radicals, radical pairs and triplet states in photosynthesis, *Acc. Chem. Res., 35*, 313-320.

(11) Lendzian, F., Bittl, R., Lubitz, W. (1998) Pulsed ENDOR of the photoexcited triplet states of bacteriochlorophyll a and of the primary donor P-865 in reaction centers of *Rhodobacter sphaeroides* R-26, *Photosynth. Res., 55*, 189-197.

(12) Hore, P.J. Analysis of polarized EPR spectra. In *Advanced EPR in biology and biochemistry*; Hoff, A., Ed.;Elsevier: Amsterdam, 1990; pp 405-440.

(13) Frank, H. A., Friesner, R., Nairn, J. A., Dismukes, G. C., Sauer, K. (1979) Orientation of the Primary Donor in Bacterial Photosynthesis, *Biochim. Biophys. Acta, 547*, 484-501.

(14) Rieger, P. H. *Electron Spin Resonance: Analysis and Interpretation;* The Royal Society of Chemistry: Cambridge, 2007.

(15) Schweiger, A.; Jeschke, G. *Principles of Pulse Electron Paramagnetic Resonance;* Oxford University Press: 2001.

(16) Hahn, E. L. (1950) Spin Echoes, *Phys. Rev., 80*, 580-594.

(17) Bloch, F. (1946) Nuclear Induction, *Phys. Rev., 70*, 460-474.

(18) Mims, W. B. (1965) Pulsed Endor Experiments, *Proc. R. Soc. London, 283*, 452-457.

(19) Davies, E. R. (1974) New Pulse Endor Technique, *Phys. Let. A., A 47*, 1-2.

(20) Carrington, A.; McLachlan, A.D. *Introduction to magnetic resonance;* Harper & Row; John Weatherhill Inc.: New York, Evanston, London, Tokyo, 1967.

(21) Koch, W.; Holthausen, M.C. *A Chemist's Guide to Density Functional Theory;* Wiley-VCH: Weinheim-New York-Torronto, 1999.

(22) Szabo, A.; Ostlund, N.S. *Modern Quantum Chemistry;* Duver Publications, Inc.: New York, 1996.

Chapter 4

Aims of the thesis

Bacterial reaction centers of *Rb. sphaeroides* and free cofactors have been investigated by many groups using different techniques like optical spectroscopy, X-Ray, ADMR, EPR, and significant progress in the knowledge of the structure and function of the bacterial reaction centers has been achived.[1-12] However, a detailed picture of the electronic structure of the excited singlet state of primary donor from which the photosynthetic charge separation starts is still lacking. The excitation of the primary donor concerns a promotion of an electron from the HOMO to the LUMO orbital, and though the excited singlet state is diamagnetic, information about both the HOMO and LUMO orbitals can still be obtained by performing ENDOR measurements on the excited triplet state, which essentially concerns the same electronic excitation. The molecule in the excited triplet state would have two unpaired electrons, one in the HOMO orbital and one in the LUMO orbital. Knowledge of these two orbitals is essential for understanding the primary photosynthetic charge separation steps,[13] since these two orbitals largely determine the chemical and spectroscopic properties of the molecule.[13-15] Furthermore, EPR spectroscopy will deliver information about origin and evolution of the triplet states and the primary radical states of the photosynthetic charge separation.[16-20] The main topic of this thesis concerns the investigation of the triplet states of bacterial reaction centers of *Rb. sphaeroides* with the aim of understanding electron transfer and energy transfer processes. This topic can be split in several parts:

- Investigation of the mechanism of the formation of the triplet state in native and mutated bacterial reaction centers of *Rb. sphaeroides* at different experimental conditions, (*e.g.* different temperature and different excitation wavelengths).
- Investigation of the degree of the uni-directionality of electron transfer and quantitative measurement of the yield of B-branch electron transfer in mutated bacterial reaction centers of *Rb. sphaeroides*. Examination of the optimal conditions for improvement of B-branch electron transfer and identification of the possibilities to manipulate the B-branch transfer and the cofactors that are responsible for the low efficiency of B-branch electron transfer in native bRC.
- Study of triplet-triplet energy transfer from the primary donor to the carotenoid in native and mutated bacterial reaction centers of *Rb. sphaeroides* at different temperatures and

different excitation wavelengths; investigation of the mechanisms involved in this process.

- Study of the electronic structure of the primary donor both of *Rb. sphaeroides* and *Bl. viridis* in the triplet state, investigation of the electron spin density distribution and elucidation of the degree of delocalization of the wavefunction of the primary donor in the triplet state. Investigation how the wavefunction correlates with the uni-directionality of charge separation in the bRC. Study of similarities and differences in the two bRCs of *Rb. sphaeroides* and *Bl. viridis*.
- Investigation of the electronic structure of the cofactors, which constitute the primary donor – BChl *a* and BChl *b* for *Rb. sphaeroides* and *Bl. viridis*, respectively. Elucidation of the electronic configuration of the bacteriochlorophyll monomer and correlation with the electronic configuration of the bacteriochlorophyll dimer.

This PhD thesis is written in a cumulative way; here a short overview of the different chapters is given.

In Chapter 5 the triplet state of the special pair of the bacterial reaction center of *Rb. sphaeroides* and two mutants is investigated using EPR spectroscopy. The mutants contain altered amino acids in the A-branch to make charge separation energetically less favorable. The uni-directionality of electron transfer and triplet quenching *via* the carotenoid is investigated at cryogenic temperatures. From measurements at different temperatures with varying time between the exciting laser flash and detection or with varying excitation wavelength, the dynamics of triplet formation *via* two mechanisms, the radical-pair and intersystem crossing mechanisms, have been investigated.

In Chapter 6, the HOMO and LUMO orbitals of BChl *a* and *b* in the excited triplet state have been investigated *in vitro* using ENDOR spectroscopy and DFT calculations. Hyperfine coupling constants for many protons have been determined from ENDOR experiments at 34 GHz. An assignment was possible based on comparison with DFT calculations and taking full advantage of the fact that BChl *a* and BChl *b* only exhibit a minor structural difference. The knowledge about the electronic structure of monomeric BChls obtained in this chapter is a prerequisite for the investigation of the electronic structure of the special pair.

In Chapter 7 the special pair of the bRC of *Rb. sphaeroides* and *Bl. viridis* has been studied in the triplet state by ENDOR spectroscopy at 34 GHz. The bRC of *Bl. viridis* is similar to that of *Rb. sphaeroides*. The obtained hyperfine coupling constants have been assigned to specific molecular positions. The degree of delocalization of the triplet

wavefunction over both dimer halves has been elucidated and the electronic structure of the primary donor both in the bRC of *Rb. sphaeroides* and *Bl. viridis* has been investigated.

In Chapter 8 a quadruple mutant of the bacterial reaction center of *Rb. sphaeroides* with improved B-branch electron transfer has been investigated and possible mechanisms of B-branch charge separation and of triplet quenching *via* the carotenoid are discussed.

References

(1) Breton, J.; Vermeglio, A. *The Photosynthetic Bacterial Reaction Center – Structure and Dynamics;* Plenum Press: New York, 1988.

(2) Michel-Beyerle, M. E. *Reaction Centers of Photosynthetic Bacteria;* Springer Verlag: Berlin, 1990.

(3) Hoff, A. J. *Advanced EPR in biology and biochemistry;* Elsevier: Amsterdam, 1990.

(4) Scheer, H. *The Chlorophylls;* CRC Press: Boca Raton, 1991.

(5) Breton, J.; Vermeglio, A. *The Photosynthetic Bacterial Reaction Center II;* Plenum Press: New York, 1992.

(6) Blankenship, B.; Madigan, M.; Bauer, C. *Anoxygenic Photosynthetic Bacteria;* Kluwer Academic Publishers: 1995.

(7) Michel-Beyerle, M. E. *Reaction Centers of Photosynthetic Bacteria - Structure and Dynamics;* Springer Verlag: Berlin, 1996.

(8) Hoff, A. J.; Deisenhofer, J. (1997) Photophysics of photosynthesis. Structure and spectroscopy of reaction centers of purple bacteria, *J. Phys. Rep., 287*, 2-247.

(9) Frank, H. A.; Young, A.J.; Britton, G.; Cogdell, R.J. *The photochemistry of carotenoids;* Springer Verlag: Berlin, 1999.

(10) Weber, S. Recent EPR studies on the bacterial photosynthetic reaction center. In *Electron Paramagnetic Resonance*; Gilbert, B. C., Davies, and McLauchlan, Eds.;Royal Society of Chemistry: Cambridge, 2000; pp 43-77, and references therein.

(11) Blankenship, R. *Molecular mechanisms of photosynthesis;* Blackwell Science: Oxford, London, 2002.

(12) Grimm, B.; Porra, R.J.; Rüdiger, W.; Scheer, H. *Chlorophylls and bacteriochlorophylls;* Springer: Heidelberg, 2006.

(13) Plato, M.; Möbius, K.; Michel-Beyerle, M. E.; Bixon, M.; Jortner, J. (1988) Intermolecular Electronic Interactions in the Primary Charge Separation in Bacterial Photosynthesis, *J. Am. Chem. Soc., 110*, 7279-7285.

(14) Frank, H. A.; Chynwat, V.; Posteraro, A.; Hartwich, G.; Simonin, I.; Scheer, H. (1996) Triplet state energy transfer between the primary donor and the carotenoid in *Rhodobacter sphaeroides* R-26.1 reaction centers exchanged with modified

bacteriochlorophyll pigments and reconstituted with spheroidene, *Photochem. Photobiol., 64*, 823-831.

(15) Frank, H. A.; Cogdell, R. J. (1996) Carotenoids in photosynthesis, *Photochem. Photobiol., 63*, 257-264.

(16) Levanon, H.; Norris, J. R. (1978) Photoexcited Triplet-State and Photosynthesis, *Chem. Rev., 78*, 185-198.

(17) Thurnauer, M. C.; Katz, J. J.; Norris, J. R. (1975) Triplet-State in Bacterial Photosynthesis - Possible Mechanisms of Primary Photo-Act, *Proc. Natl. Acad. Sci. USA, 72*, 3270-3274.

(18) Thurnauer, M. C. (1979) ESR study of the photoexcited triplet state in photosynthetic bacteria, *Rev. Chem. Int., 100*, 197-231.

(19) Hoff, A. J. (1976) Kinetics of Populating and Depopulating of Components of Photoinduced Triplet-State of Photosynthetic Bacteria *Rhodospirillum rubrum*, *Rhodopseudomonas spheroides* (Wild-Type), and Its Mutant R-26 As Measured by ESR in Zero-Field, *Biochim. Biophys. Acta, 440*, 765-771.

(20) Hore, P.J. Analysis of polarized EPR spectra. In *Advanced EPR in biology and biochemistry*; Hoff, A., Ed.;Elsevier: Amsterdam, 1990; pp 405-440.

Chapter 5

Triplet state in bRC of *Rhodobacter sphaeroides* and mutants studied by EPR*

Abstract

The photosynthetic charge separation in bacterial reaction centers occurs predominantly along one of two nearly symmetric branches of cofactors. Low temperature EPR spectra of the triplet states of the chlorophyll and carotenoid pigments in the reaction center of *Rb. sphaeroides* R-26.1, 2.4.1 and two double mutants GD(M203)/AW(M260) and LH(M214)/AW(M260) have been recorded at 34 GHz to investigate the relative activities of the 'A' and 'B' branches. The triplet states are found to derive from radical pair and intersystem crossing mechanisms. The former mechanism is operative for *Rb. sphaeroides* R-26.1, 2.4.1 and mutant GD(M203)/AW(M260) and indicates that A-branch charge separation proceeds at temperatures down to 10 K. The latter mechanism, operative for mutant LH(M214)/AW(M260) indicates that no long-lived radical pairs are formed upon direct excitation of the primary donor and that virtually no charge separation at the B-branch occurs at low temperatures. When the temperature is raised above 30 K, B-branch charge separation is observed, which is at most 1% of A-branch charge separation. B-branch radical pair formation can be induced at 10 K with low yield by direct excitation of the bacteriopheophytin of the B-branch at 537 nm. The formation of a carotenoid triplet state is observed. The rate of formation depends on the orientation of the reaction center in the magnetic field and is caused by a magnetic field dependence of the oscillation frequency by which the singlet and triplet radical pair precursor states interchange. Combination of these findings with literature data provides strong evidence that the thermally activated transfer step on the B-branch occurs between the primary donor, P_{865}, and the accessory bacteriochlorophyll, whereas this step is barrierless down to 10 K along the A-branch.

* This chapter is based on the publication "Low temperature pulsed EPR study at 34 GHz of the triplet states of the primary electron donor P_{865} and the carotenoid in native and mutant bacterial reaction centers of *Rhodobacter sphaeroides"* by Marchanka, A., Paddock, M., Lubitz, W., van Gastel, M. *Biochemistry* (2007), 46, 14782-14794.

5.1 Introduction

Photosynthesis is of vital importance for life on earth. In photosynthesis, large protein-cofactor complexes function as light-driven switches. These complexes catalyze a light-induced electron and proton transport across the photosynthetic membrane and have been optimized by nature to perform this task with a quantum efficiency close to unity. The prototype bacterial reaction centers (bRCs) have been studied by many groups and significant progress in the knowledge of the structure and function of the bRCs has been achieved.[1-8] The first crystal structure of a bRC was determined in the 1980s.[3, 9-11] The prototypical reaction center from *Rb. sphaeroides* is composed of three protein subunits, L, M, and H, with a molecular weight of 31, 34 and 28 kDa.[12] The reaction center contains as cofactors four bacteriochlorophyll molecules (B, BChl), two bacteriopheophytins (H, BPheo), two ubiquinones, one carotenoid (spheroidene) and one non-heme iron.[3] Two bacteriochlorophylls form a dimer, or special pair called P_{865}, where the subscript denotes the wavelength of maximum absorption in the UV-VIS spectrum. The other cofactors are arranged in two branches, denoted A-branch and B-branch, that show a pseudo C_2 symmetry (see Fig. 5.1).

Upon absorption of a photon from (sun)light at about 865 nm, an electron is excited at P_{865}. The exited electron subsequently travels to the final electron acceptor, the quinone on the B-branch (Q_B) by passing through a series of intermediate states. In the final charge-separated state, P_{865} is oxidized and Q_B is reduced. Earlier results derived mostly from optical spectroscopy of the native system showed that only the A-branch is active in charge separation with an efficiency of close to 100 %[5, 13, 14] and that in the intermediate states the excited electron resides on one of the cofactors of the A-branch. After reaching Q_A, the electron then travels to the final acceptor, Q_B. Electron transfer along the B-branch is found to be below 1 %.[5, 15, 16] According to Feher, Allen *et al*[5] this arises from the breaking of the two-fold symmetry at several places in the structure of the reaction centre. Furthermore, inherent asymmetries in the dimer structure exist. The distance of the special pair with B_A is smaller than with B_B, bacteriopheophytin H_A is closer to B_A than H_B to B_B and the detailed binding of the cofactors to the protein backbone is different in the two branches. It has been recently proposed that protein dynamics control the kinetics of the initial steps in the charge separation processs.[17]

Differences between A-branch and B-branch charge separation have so far been studied by optical spectroscopy.[18-20] Upon excitation at 390 nm of *Rb. sphaeroides* reaction centers, a radical pair $B^{\bullet+}H^{\bullet-}$ is formed on the B-branch that decays in picoseconds.[21] This

radical pair state has also been observed in mutated reaction centers upon excitation of the singlet excited states at different wavelengths[21] and B-branch electron transfer becomes possible by excitation to higher excited states of the reaction center.[22] The largest B-branch radical pair formation in *Rb. sphaeroides* with efficiency of 35%-45% has been found for a quadruple mutant in which a BPheo is introduced in place of B_B and a BChl *a* in place of H_A.[23] In a *Rb. capsulatus* mutant the presently largest B-branch charge separation of 70% has been reported.[24]

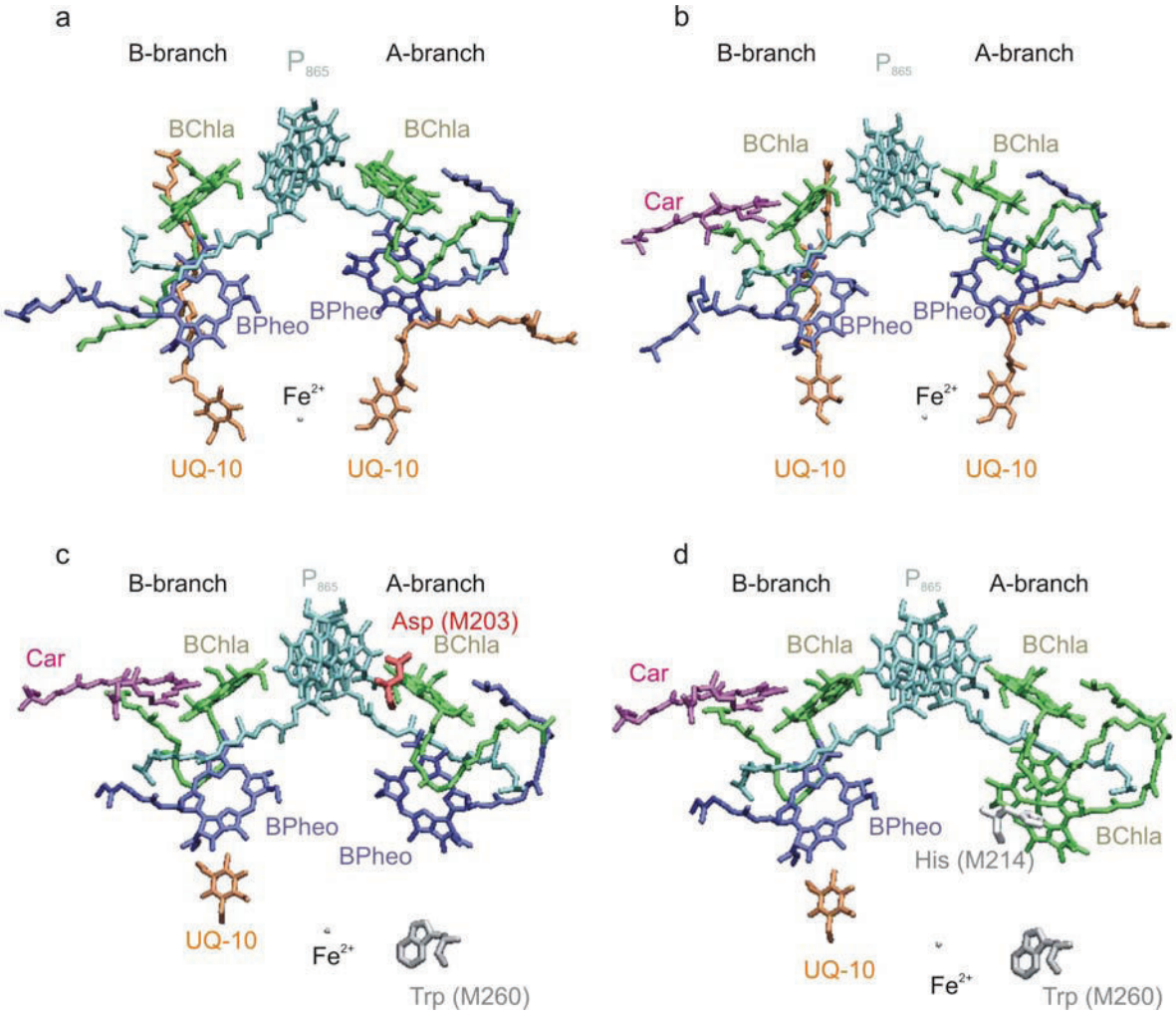

Figure 5.1. Cofactor arrangement in the bacterial reaction centers of (a) *Rb. sphaeroides* R-26.1 (PDB code: 1pcr), (b) *Rb. sphaeroides* 2.4.1 (PDB code: 4rcr), (c) *Rb. sphaeroides* double mutant GD(M203)/AW(M260) and (d) *Rb. sphaeroides* double mutant LH(M214)/AW(M260). The mutants are modeled after the structure of a quintuple mutant that contains all these mutations (PDB code: 1yf6).[15]

In this study, the triplet states of bacterial reaction centers and mutants thereof are investigated by EPR spectroscopy, to better understand the charge separation process and the directionality of charge separation with respect to the A and B branches. The triplet state is well suited for this, because the polarization pattern of the triplet state is determined by the precursor states directly after light excitation.[25] Thus, by measuring the polarization pattern, information is obtained about whether or not the triplet state is derived from a long-lived radical pair state on either branch, or whether other triplet-forming mechanisms are operative. Moreover, the rates of formation and decay of the paramagnetic species can be studied on a timescale of nanoseconds or longer. A disadvantage of the EPR technique is that singlet states cannot be detected. Therefore, the initial charge separation process, in which singlet radical pair states are involved, cannot be addressed directly by this method. Nevertheless, the EPR spectrum contains information about paramagnetic intermediates complementary to spectra obtained by fast optical techniques. In this respect, EPR spectroscopy can be used parallel with optical methods for the study of charge separation along the two branches.

In native reaction centers, the formation of the triplet state cannot compete with forward electron transfer. However, when the quinone acceptors are pre-reduced, an EPR spectrum of P_{865} in the triplet state ($^3P_{865}$) with a characteristic AEEAAE (A – absorptive, E - emissive) polarization is observed, which derives from a $P_{865}^{\bullet+}H_A^{\bullet-}$ radical pair.[2] In case of different radical pair precursors, or other triplet forming mechanisms, the polarization pattern of the observed $^3P_{865}$ triplet state is expected to be different. In our study we investigated triplet states of bacterial reaction centers for 4 species at Q-band microwave frequencies: first, *Rb. sphaeroides* R-26.1, which lacks the carotenoid spheroidene (Fig. 5.1a). The second species is *Rb. sphaeroides* 2.4.1, used as a reference (Fig. 5.1b). The third is the *Rb. sphaeroides* double mutant GD(M203)/AW(M260), where the first mutation changes the H-bonding network near the accessory bacteriochlorophyll and makes the electron transport over the A-branch energetically less favorable (Fig. 5.1c). The second mutation introduces a tryptophan in the binding pocket for Q_A, which blocks the access for the quinone at this position.[15, 26] The fourth species is the double mutant *Rb. sphaeroides* LH(M214)/AW(M260), which introduces a histidine near the BPheo in the A-branch (Fig. 5.1d), whereby a magnesium is incorporated into the BPheo which thus converts to BChl *a*.

The LH(M214) mutation has been extensively studied by Kirmaier and Holten using fast optical techniques.[18-20] The introduction of BChl *a* in the A-branch, also denoted as "β mutant" in literature, yields a short-lived radical pair state $P_{865}^{\bullet+}I^{\bullet-}$ upon excitation, where $I^{\bullet-}$ is most likely a BChl *a* species.[18] Depending on the presence of additional mutations or the

temperature, the lifetime of this radical pair state is ≤ 1 ns.[19] The main effect of the LH(M214) mutation seems to be an increased charge recombination rate by a factor of about 20, which reduces the amount of $P_{865}^{\bullet+}Q_A^{\bullet-}$ to 60 % as compared to 100% in native reaction centers.

For carotenoid-less reaction centers of *Rb. sphaeroides* R-26.1 the triplet state $^3P_{865}$ was studied, for the other three systems the triplet states of $^3P_{865}$ *and* ^{3}Car. Carotenoids protect the photosynthetic apparatus from photo-induced damage by either trapping chlorophyll triplet states or quenching the excited singlet state of molecular oxygen.[27] Spectroscopic and kinetic parameters are already available for carotenoids in bacterial reaction centers from earlier studies.[28-30]

A requirement for a detectable EPR signal from $^3P_{865}$ that derives from a radical pair precursor is that the radical pair lives long enough to change from the singlet to the triplet state. A typical lifetime required for this process is 15 ns.[31] Shorter lived radical pair states, *e.g.* as observed for LH(M214) mutants[19] remain in the singlet state and decay too fast to produce EPR detectable signals. The presence of short-lived singlet radical pairs, can therefore not be detected by EPR spectroscopy and can thus at no stage be excluded from EPR measurements. In this study it is found that two triplet forming mechanisms are operative and that charge separation along the A and B branches can be strongly influenced by mutations of amino acids near either of the branches.

5.2 Materials and Methods

Experimental

Rb. sphaeroides R-26.1 was isolated and purified as described by Feher and Okamura[32] and those from *Rb. sphaeroides* 2.4.1 as described by Frank *et al.*[33] The quinones Q_A and Q_B were reduced as described in reference[34] by addition of sodium dithionite solution (0.5 M in 1 M Tris-HCl, pH 8.0) to yield a final dithionite concentration of 50 mM in the sample. *Rb. sphaeroides* mutants GD(M203)/AW(M260) and LH(M214)/AW(M260) were expressed and purified according to Paddock *et al*.[15] The mutants were not reduced with dithionite. Test measurements on mutants in which the quinones were reduced with dithionite gave the same results as those without dithionite reduction. The samples were frozen in liquid nitrogen in the dark. The quality of the samples was checked by UV/VIS, SDS PAGE and Special TRIPLE EPR[35, 36] measurements at room temperature.

Elecron Spin Echo (ESE) detected and transient EPR spectra were recorded on a Bruker Q-band Elexsys E580 FT pulse EPR spectrometer equipped with a home-built EPR/ENDOR resonator,[37] and an Oxford CF935 helium gas-flow cryostat for temperature control. Samples were excited with an Opotek OPO laser at variable wavelength, pumped by a Vibrant Nd:YAG laser at 10 Hz repetition rate. Excitation at 865 nm was performed with 5 mJ/pulse, at 537 nm and 590 nm with 6 mJ/pulse. The EPR measurements were performed in the temperature range of 10 K to 130 K. The microwave frequency was typically 33.9 GHz, with variations of 0.2 GHz, depending on the identity of the sample and the temperature.

In the two-pulse EPR, delay-after-flash (DAF)-EPR and two-pulse Electron Spin Echo Envelope Modulation (ESEEM) experiments[38] shown in scheme 1. It consists of a laser pulse followed by two microwave pulses and detection by a Hahn echo. In the ESE-detected EPR experiments the magnetic field is swept, in DAF-EPR the magnetic field is fixed and the time t_{DAF} is swept, in two-pulse ESEEM, the time τ is swept. The length of the $\pi/2$ pulse was 40 ns, that of the π pulse was 80 ns. The delay between the two pulses was 440 ns and the microwave power was 20 mW. The value for the delay was the minimum possble, taking into account the spectrometer dead time of about 400 ns. Some triplet EPR spectra recorded at larger delays times can be found in Appendix A (Fig. A1). The accumulation time was typically 30 minutes for an EPR spectrum, except for mutant LH(M214)/AW(M260), which gave rise to much weaker signals. For this mutant the signal was accumulated for 8 to 12 hours. With two-pulse EPR spectroscopy, the polarization pattern of the triplet state were

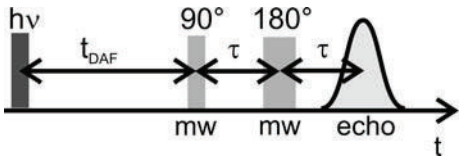

Scheme 1.

measured, DAF-EPR was used to obtain information about kinetic parameters, like growth and decay rates of EPR signals and with ESEEM spectroscopy, the hyperfine and quadrupole interaction of the pyrrole nitrogens can be investigated.

Transient EPR measurements were performed on the same spectrometer by using the Bruker "Specjet" oscilloscope as a transient recorder. The microwave power was 40 μW. The spectrum was accumulated with 200 averages. A spectrum took about 7 hours of measurement time. Simulations of the triplet EPR spectra were performed with a self-written

program based on the formalism described in reference.[39] For a more detailed description see Appendix A.

5.3 Results

The Q-band transient EPR spectrum of *Rb. sphaeroides* R-26.1 is shown in Fig. 5.2. The spectrum is comprised of absorptive (A) and emissive (E) signals. The width of the spectrum is determined by the zero field splitting (ZFS) parameters *D* and *E* and the observed polarization pattern AEEAAE is consistent with that reported earlier.[2] The three canonical orientations, for which a molecule is oriented either with its X, Y or Z axis of the ZFS tensor parallel to the magnetic field direction are indicated in the figure. They will be used as labels in the text. ESE-detected EPR spectra of *Rb. sphaeroides* R-26.1, 2.4.1, mutants GD(M203)/AW(M260) and LH(M214)/AW(M260) and BChl *a* in pyridine recorded at T = 10 K and T = 50 K are shown in Fig. 5.3. The spectra at T = 10 K of *Rb. sphaeroides* R-26.1, 2.4.1 and GD(M203)/AW(M260) are similar. Strikingly, the EPR spectrum of *Rb. sphaeroides* LH(M214)/AW(M260) is completely different, and more similar to that of BChl *a* in pyridine. At T = 50 K, the polarization patterns of all spectra are different.

In the subsequent paragraphs, the EPR spectra, the polarization (A/E) patterns and the time and temperature dependences are described for each species.

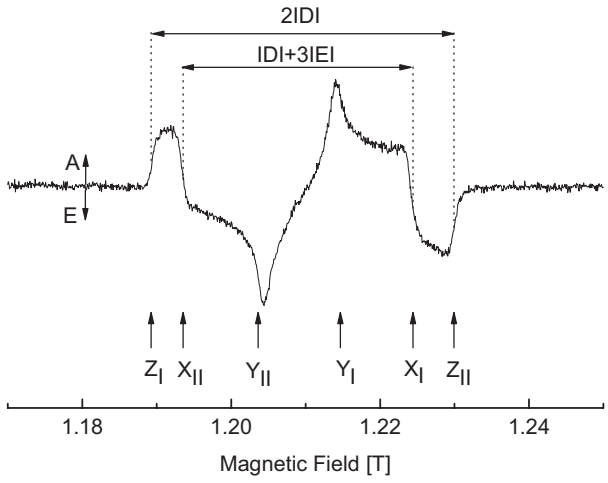

Figure 5.2. Q-band transient EPR spectrum of the bRC of *Rb. sphaeroides* R-26.1 at T=10 K.

***Rb. sphaeroides* R-26.1**

The ESE-detected EPR spectrum of $^3P_{865}$ in *Rb. sphaeroides* R-26.1 at T = 10 K excited with a wavelength of 865 nm is characterized by the well-known polarization pattern AEEAAE.[2] A narrow signal, marked with an asterisk, is present in the center of the spectrum, which belongs to a radical. A striking feature of the spectrum is that the emissive signals are systematically more intense than the corresponding absorptive signals, which contrasts with earlier measurements carried out at X-band frequencies using cw EPR[2] or transient EPR techniques. This is caused by a strong Electron Spin Echo Envelope Modulation (ESEEM) effect at Q-band for the pyrrole nitrogens detected dominantly on the $M_S = 0 \leftrightarrow +1$ transition (*vide infra*).

The ZFS parameters *D* and *E* have been read from the spectrum and amount to $|D| = 0.0188\ cm^{-1}$, $|E| = 0.0031\ cm^{-1}$. They are given in table 5.1 and agree well with those reported earlier.[2, 34] When the temperature is increased from 10 K to 50 K, the shape of the EPR spectrum remains virtually the same and the amplitude decreases. The observation that the *D* and *E* parameters do not change indicates that the triplet state remains localized at $^3P_{865}$.

Information about the decay of the triplet sublevels of $^3P_{865}$ can be obtained by decay-after-flash (DAF)-EPR measurements. In this experiment, EPR spectra are recorded as a function of the time between the laser flash and the Hahn echo. The two-dimensional spectrum at T = 10 K is given as in Appendix A (Fig. A2) and is characterized by a slow decay with a time constant of 250 μs at the low- and high-field edges of the spectrum ($B \parallel Z_I$ and $B \parallel Z_{II}$) and faster decays with time constants of both 80 μs for $B \parallel X_I, Y_I$ and $B \parallel X_{II}, Y_{II}$. At both 10 K and 50 K the decay behavior was found to be adequately described by a set of three time constants as given in equation A3 (appendix A).

***Rb. sphaeroides* 2.4.1**

The ESE-detected EPR spectrum of $^3P_{865}$ in *Rb. sphaeroides* 2.4.1, recorded at T = 10 K is shown in Fig. 5.3b. The spectrum is essentially the same as that recorded at 10 K for *Rb. sphaeroides* R-26.1. However, the EPR spectrum changes drastically when the temperature is increased to 50 K. Such a change in polarization pattern has been observed earlier[28, 29] and was attributed to a triplet transfer to the carotenoid – spheroidene,[12, 40] hereafter referred to as carotenoid. At temperatures above 30K, the polarization pattern changes significantly, which indicates a temperature activated triplet transfer. The carotenoid triplet spectrum is broader and is characterized by different *D* and *E* parameters than that of $^3P_{865}$ (see table 5.1). The EPR spectrum of the carotenoid is highly symmetric with respect to the relative intensity of

the absorptive and emissive signals in the polarization patterns, and no ESEEM effects are observed. The carotenoid signal has a polarization pattern EAAEEA.

The triplet transfer from P_{865} to Car and the time evolution of both triplet signals has

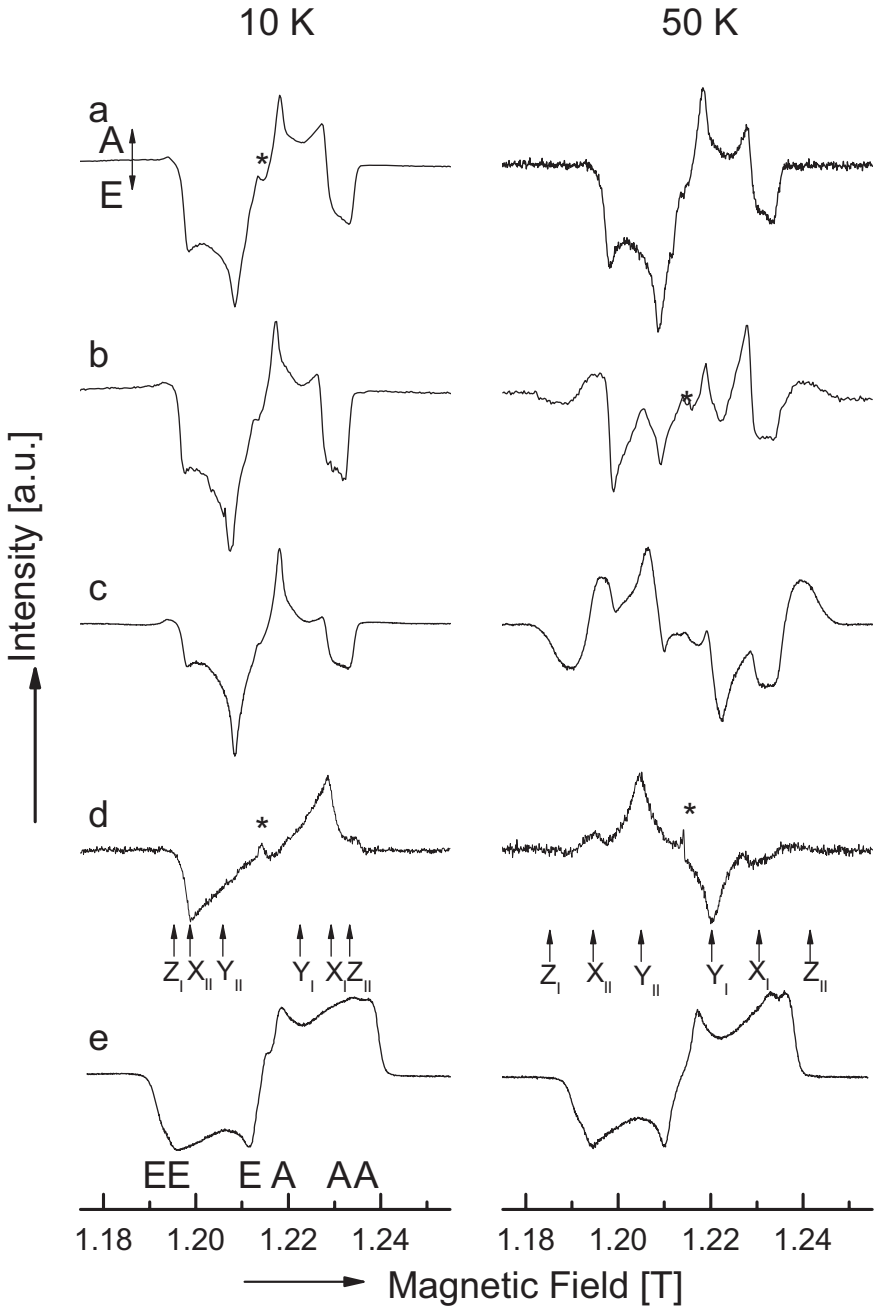

Figure 5.3. Q-band ESE-detected triplet EPR spectra in bRCs in *Rb. sphaeroides* at T = 10 K (left) and T = 50 K (right). (a) *Rb. sphaeroides* R-26.1, (b) *Rb. sphaeroides* 2.4.1, (c) *Rb. sphaeroides* GD(M203)/AW(M260), (d) *Rb. sphaeroides* LH(M214)/AW(M260). (e) ^{3}BChl *a* in pyridine. The signal marked with (*) is assigned to a radical signal. The microwave frequency was typically 33.9 GHz with a variation of 0.2 GHz depending on the sample.

been measured by DAF-EPR at T = 50 K and is shown in Fig. 5.4a. The $^3P_{865}$ signal is quenched quickly and anisotropically by the carotenoid with time constants of about 1 μs (B || Y, Z) and 4 μs (B || X) and the ^{3}Car signal decays to the ground state with time constants of 6 μs (B || Y, Z) and 14 μs (B || X). Two time traces recorded with B || X_{II} and B || Z_I are given in Fig. 5.4b. A small fraction of the $^3P_{865}$ signal is not taken over by carotenoid, and the $^3P_{865}$ polarization can still be recognized at 8 μs after the laser flash. This residual $^3P_{865}$ signal decays to the ground state with a time constant of about 40 μs.

Table 5.1. ZFS parameters for $^3P_{865}$ and ^{3}Car in *Rb. sphaeroides* R-26.1 and LH(M214)/AW(M260). Those for *Rb. sphaeroides* 2.4.1 and the double mutant GD(M203)/AW(M260) are the same within the error limits as those of R-26.1. Triplet decay rates are temperature dependent and given in Fig. 5.4(c-f). The error margins are: *D* and *E* [±0.0002 cm^{-1}], p_x, p_y and p_z [±0.05] with constraint that $p_x + p_y + p_z = 1$, g_x, g_y and g_z [±0.0003], linewidth [±0.2 mT].

	R-26.1		LH(M214)/AW(M260)	
	$^3P_{865}$	^{3}Car	$^3P_{865}$	^{3}Car
D [cm^{-1}]	0.0188	–0.0280	0.0188	–0.0280
E [cm^{-1}]	0.0031	0.0040	0.0039	0.0040
p_x			0.7	0.7
p_y			0.3	0.3
p_z			0.0	0.0
g_x	2.0033	2.0023	2.0033	2.0023
g_y	2.0038	2.0023	2.0042	2.0023
g_z	2.0023	2.0023	2.0023	2.0023
linewidth [mT]	0.8	0.8	0.8	1.0

The temperature dependence of the time constants for formation and decay of the ^{3}Car signal is given in Fig. 5.4c and 5.4d. All time constants decrease with temperature. The time constant for B || X is about a factor of 3 larger than the time constants for B || Y, Z for both the formation and decay of the ^{3}Car signal.

***Rb. sphaeroides* GD(M203)/AW(M260)**

The third system under investigation is the *Rb. sphaeroides* double mutant GD(M203)/AW(M260).[15] The EPR spectra at T = 10 K and T = 50 K are shown in Fig. 5.3c. The spectrum at T = 10 K again looks similar to those of *Rb. sphaeroides* R-26.1 and *Rb.*

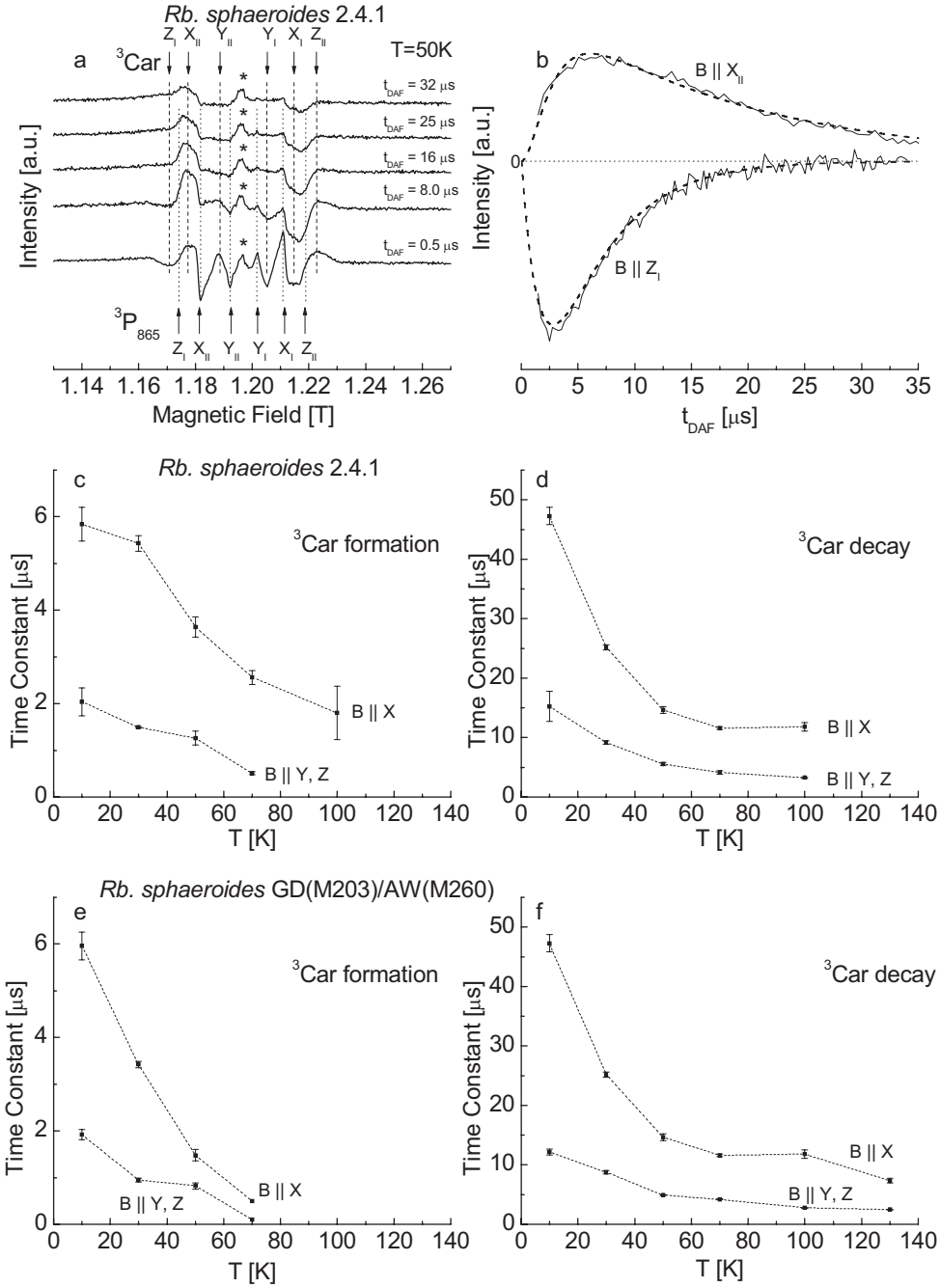

Figure 5.4. (a) ESE-detected EPR spectra of the $^3P_{865}$ and ^{3}Car triplet signals in *Rb. sphaeroides* 2.4.1 at 50K recorded at different times after the laser flash. Dotted lines indicate the canonical orientations of $^3P_{865}$, dashed lines those of ^{3}Car; (b) Time traces of the EPR signal recorded at B || X_{II} and B || Z_I and simulations (dashed lines) using the model described in Appendix A; (c,d) Temperature dependence of time constants for ³Car formation and decay in *Rb. sphaeroides* 2.4.1; (e,f) Temperature dependence of time constants for ³Car formation and decay in *Rb. sphaeroides* GD(M203)/AW(M260).

sphaeroides 2.4.1 with minor changes, *e.g.*, the intensities of the X_I and X_{II} transitions decrease so that the intensity of X_I becomes almost zero. This shows that also in this mutant the triplet state remains at $^3P_{865}$ at T = 10 K. At T = 50 K, the spectrum changes and the P_{865} triplet is again transferred to Car. By comparison with the spectrum of *Rb. sphaeroides* 2.4.1, it is seen that more ^{3}Car is present for mutant GD(M203)/AW(M260).[i] In this mutant the triplet state is taken over faster by Car than in *Rb. sphaeroides* 2.4.1 and the signal is so large that it is possible to observe ^{3}Car signals with pulsed EPR methodology in our spectrometer up to 130K. Above 130K the relaxation processes reduce the signal below the noise level, hampering detection. The temperature dependence of the decay and growth constants is shown in Fig. 5.4e and 5.4f. The growth constant for B || X decreases faster with higher temperatures in mutant GD(M203)/AW(M260) than in *Rb. sphaeroides* 2.4.1 (Fig. 5.4d). The time constants for the decay of the ^{3}Car signal have the same temperature dependence in *Rb. sphaeroides* 2.4.1 and mutant GD(M203)/AW(M260).

In Fig. 5.5, two-pulse ESEEM spectra and modulation patterns recorded at B || Z_I and B || Z_{II} are depicted. At these field positions, the same set of molecules is selected - those that are oriented with the principal Z axis of the ZFS tensor parallel to the magnetic field. At the latter magnetic field setting, only shallow modulations are observed, whereas at B || Z_I, deep modulations are visible, explaining the observed asymmetry of the Q-band ESE-detected EPR spectra. The modulations are caused by the presence of nuclei with I > 0, in this case the four pyrrole nitrogens (I(^{14}N) = 1), whose hyperfine interaction is of the same order as the nuclear Zeeman interaction, which is known as the "exact cancellation" condition.[41] Large modulations are observed when the exact-cancellation condition is fulfilled.[41] In this case it is fulfilled better at B || Z_I than B || Z_{II}, and the implications will be discussed further in the discussion.

The frequencies at 3.2 MHz, 4.6 MHz and 7.8 MHz are observed in both ESEEM spectra with only a small difference of ±0.2 MHz. Also, the latter frequency is the sum of the former two frequencies, which shows that 7.8 MHz concerns the double quantum transition and that all frequencies stem from the M_S = 0 manifold (see Fig. 5.5a). Taking advantage of the fact that no hyperfine interaction is present in the M_S = 0 level, an estimate of the size of the quadrupole interaction for the pyrrole nitrogens can be made by using the formula[38]

$$\nu_{dq} = 2\sqrt{\nu_Z^2 + \frac{e^2qQ}{4h}\left(3+\eta^2\right)} \qquad (1)$$

[i] In this mutant was possible to measure the first ENDOR spectra of the triplet state of carotenoid, see Appendix A and Fig. A3 there for details.

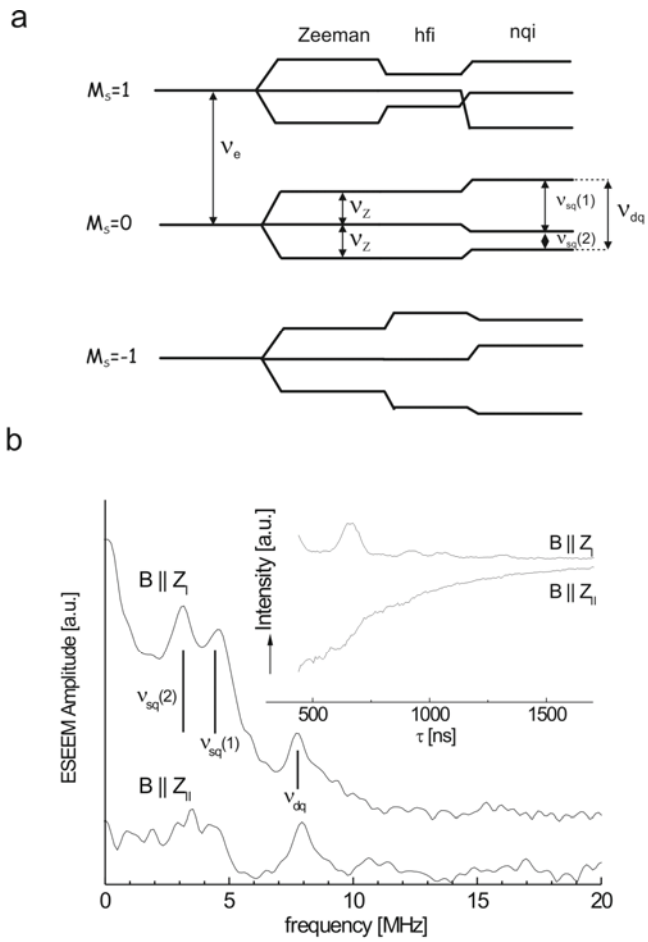

Figure 5.5. (a) Schematic energy level diagram for a nuclear spin I = 1 and electron spin S = 1 in a magnetic field, including nuclear Zeeman, hyperfine (hfi) and nuclear quadrupole (nqi) interactions. The three frequencies $\nu_{sq}(1)$, $\nu_{sq}(2)$ and ν_{dq} of the $M_S = 0$ manifold dominate the ESEEM spectrum. (b) Two-pulse ESEEM spectra and modulation patterns (inset) of $^3P_{865}$ recorded for *Rb. sphaeroides* GD(M203)/AW(M260) at the Z_I (low field) and Z_{II} (high field) canonical orientations (see Fig. 5.2a). The modulation depth at Z_I is about four times larger than at Z_{II}. The temperature is 10 K and no contribution of carotenoid was detected in the EPR spectrum.

where ν_Z is the Zeeman frequency for ^{14}N, e^2qQ/h and η are the nuclear quadrupole coupling parameters [42]. The asymmetry parameter η is defined as

$$\eta = \frac{Q_{xx} - Q_{yy}}{Q_{zz}} \qquad (2)$$

where Q_{xx}, Q_{yy} and Q_{zz} are electric field gradients at the nitrogen. The asymmetry parameter ranges between 0 and 1 and its exact value only influences that of e^2qQ/h by about 0.4 MHz. By using equation (4), a value of $e^2qQ/h = 3.2 \pm 0.3$ MHz is found.

***Rb. sphaeroides* LH(M214)/AW(M260)**

Fig. 5.3d shows the ESE-detected EPR spectrum of $^3P_{865}$ in *Rb. sphaeroides* LH(M214)/AW(M260) in frozen solution. The spectrum has a polarization pattern EEEAAA, which is completely different from those of the triplet spectra of $^3P_{865}$ in *Rb. sphaeroides* R-26.1, 2.4.1 and GD(M203)/AW(M260). The signal in mutant LH(M214)/AW(M260) is weaker by a factor of about 300 in comparison to the triplet signals in the other three systems, nevertheless, the *D* value for mutant LH(M214)/AW(M260) remains the same and the *E* value

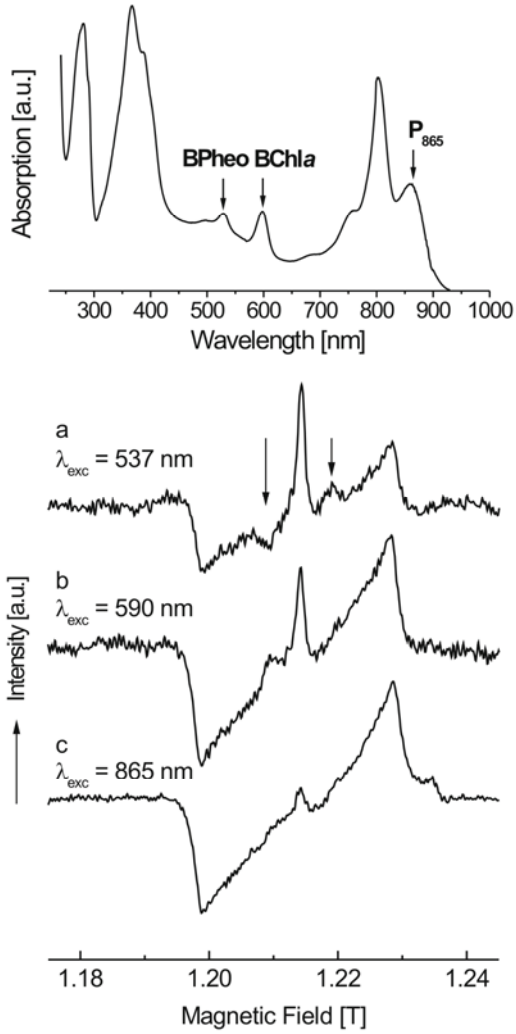

Figure 5.6. (top) UV-VIS spectrum and ESE-detected EPR spectra of $^3P_{865}$ in *Rb. sphaeroides* LH(M214)/AW(M260) at T = 10 K. (bottom) EPR spectra recorded with laser excitation of wavelength (a) 537 nm, (b) 590 nm and (c) 865 nm. The labels in the UV-VIS spectrum indicate absorbing cofactors. The arrows at the spectrum with (a) λ_{exc} = 537 nm and T = 10 K indicate additional signals of low intensity which correspond to the RP triplet state of $^3P_{865}$.

(0.0039 cm^{-1}) is only slightly increased. Therefore, this triplet state is most likely also stems from P_{865}. The EEEAAA polarization pattern in this mutant is similar to that of a BChl *a* monomer *in vitro*, shown in Fig. 5.3e, which is formed by an intersystem crossing rather than a radical pair mechanism. The signal at Z_I is further attenuated by the ESEEM effect and can barely be seen.

At T = 50 K, the EPR signal changes as compared to T = 10 K. The polarization pattern becomes EAAEEA and the Z_I and Z_{II} transitions are very weak. Strikingly, the D and E parameters read from the spectrum at T = 50 K agree with those of ^{3}Car observed in the other three systems, but again the polarization pattern is different. Almost no contribution of $^3P_{865}$ signal is observed in the spectrum at T = 50 K anymore, which indicates that the time constants for quenching of $^3P_{865}$ by the carotenoid are even shorter here than in mutant GD(M203)/AW(M260), but the temperature threshold remains about 30 K.

Additional EPR experiments have been performed with excitation wavelength λ = 537 nm and λ = 590 nm. The motivation for these experiments is that at 537 nm the remaining BPheo in the B-branch is excited and at 590 nm all BChl *a* molecules are excited. At the former wavelength B-branch charge separation can therefore be selectively studied. In both cases, the absolute signal is decreased as compared to excitation at 865 nm, indicating less efficient triplet formation. The spectra at T = 10 K are shown in Fig. 5.6. Excitation at 537 nm introduces small but important changes in the polarization pattern, marked with arrows in Fig. 5.6b, whereas excitation at 590 nm does not alter the spectrum as compared to excitation at 865 nm. The changes occur exactly at the Y_I and Y_{II} canonical orientations of $^3P_{865}$ and show an emissive signal at low-field and an absorptive signal at high-field. The polarization of these additional signals is the same as that of the Y_I and Y_{II} orientations for *Rb. sphaeroides* R-26.1, 2.4.1 and GD(M203)/AW(M260).

Simulations

Simulations of the EPR spectra for all four systems are shown in Fig. 5.7. They are simulated by either a radical pair or intersystem crossing mechanism and concern simulations for $^3P_{865}$ (left column) and ^{3}Car (right column). The simulations reproduce the positions of s essentially all bands in the spectra and the overall line shape. Some mismatches with respect to the line shape occur because of the presence of a large ESEEM effect in the pulsed EPR spectra at Q-band (*vide infra*), for example at the low-field side in Fig. 5.7b, the simulation shows an emissive feature that is suppressed in the experimental spectrum by the ESEEM effect. The parameters used in the simulation are shown in table 5.1. The ZFS parameters *D*

and *E* for $^3P_{865}$ are essentially the same in all four systems under investigation, as are those for ^{3}Car. Also, for $^3P_{865}$ the effect of anisotropy of the g tensor ($g_x \neq g_y \neq g_z$) can be observed in the EPR spectrum. For example, the width of the low-field signal in the EPR spectrum of $^3P_{865}$ is smaller than that of the high-field signal. This effect can only be simulated by inclusion of an anisotropic g tensor. In the EPR spectra for ^{3}Car, the signals at low-field and high-field have the same width and no g tensor anisotropy can be observed.

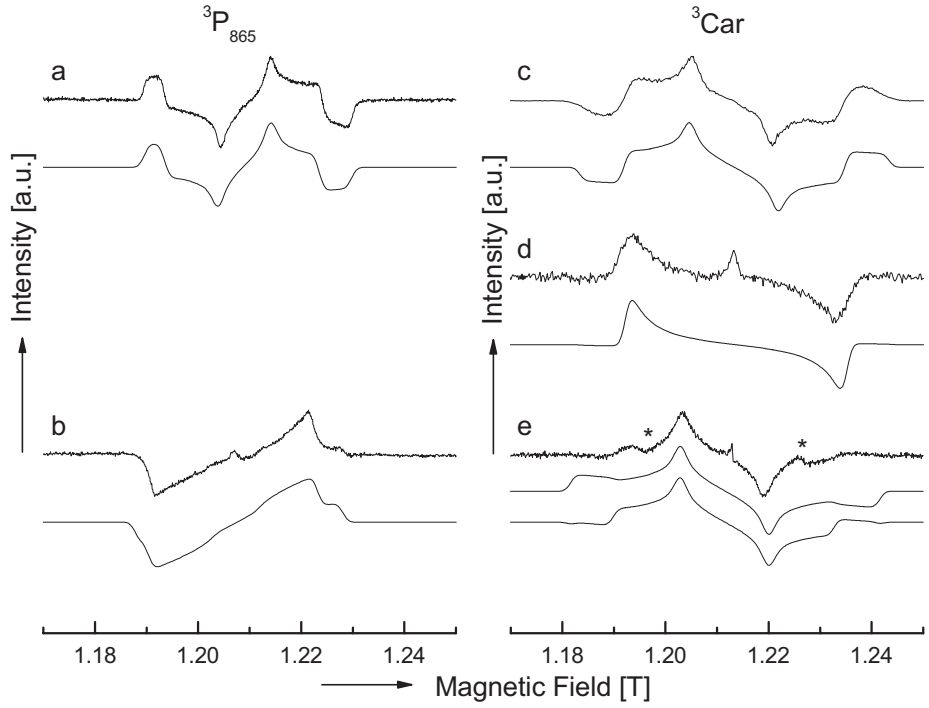

Figure 5.7. EPR spectra (upper trace) and simulations (lower traces) of the $^3P_{865}$ and ^{3}Car triplet states in bacterial reaction centers of *Rb. sphaeroides*. (a) transient EPR, $^3P_{865}$ in *Rb sphaeroides* R-26.1, T = 10 K; (b) ESE-detected EPR, $^3P_{865}$ in *Rb. sphaeroides* LH(M214)/AW(M260), T = 10 K, t_{DAF} = 500 ns; (c) ESE-detected EPR, ^{3}Car in *Rb. sphaeroides* GD(M203)/AW(M260), T=70K, t_{DAF}=500 ns; (d) ESE-detected EPR, ^{3}Car in *Rb. sphaeroides* GD(M203)/AW(M260), T=70K, t_{DAF}=25 μs; (e) ESE-detected EPR, ^{3}Car in *Rb. sphaeroides* LH(M214)/AW(M260), T = 50K, t_{DAF} = 500 ns. The signals marked with * belong to a small contribution of $^3P_{865}$, which has not yet fully decayed. The middle trace in (e) is a simulation assuming a pure ISC mechanism, in the lower trace 50% ISC and 50% RP mechanism efficiency was used.

5.4. Discussion

The Q-band ESE-detected EPR spectra of *Rb. sphaeroides* R-26.1, 2.4.1 and the mutants GD(M203)/AW(M260) and LH(M214)/AW(M260) shown in Fig. 5.3 display different polarization patterns and temperature behavior. Though some of these observations are already known from earlier studies at different microwave frequencies, several new observations related to A- and B-branch charge separation are made here. In the discussion, these new observations are interpreted and discussed, and a comparison is made with existing literature data where possible. First, the polarization patterns of the EPR spectra are discussed. They are related to the mechanism by which the triplet state of $^3P_{865}$ is formed and thereby give information about radical pair precursor states on either the A- or B-branch and the charge separation processes of both branches. Second, the dynamics and temperature dependence of triplet-triplet energy transfer from $^3P_{865}$ to ^{3}Car is discussed. An interesting observation here is that the triplet-triplet transfer is found to be anisotropic; it depends on the orientation of the bRC in the magnetic field. Lastly, the additional signals in mutant LH(M214)/AW(M260) upon excitation at 537 nm are discussed. This mutant has only one remaining bacteriopheophytin in the B-branch, and B-branch charge separation can thus be selectively investigated by excitation at 537 nm.

Polarization pattern, intersystem crossing and radical pair mechanisms

In *Rb. sphaeroides* 2.4.1, R-26.1 and mutant GD(M203)/AW(M260), the triplet state is formed after light excitation by a radical pair mechanism (Fig. 5.8a). In this mechanism, the excited electron is transferred from P_{865} to bacteriopheophytin (H) on the A-branch and forms a radical pair $P_{865}^{\bullet+}H_A^{\bullet-}$ [2, 4, 6, 13] The radical pair state is initially present as a singlet state. However, since the unpaired electrons are located on different molecules, they feel a different effective magnetic field.[31] Because the singlet state remains virtually degenerate with the T_0 sublevel of the triplet radical pair state, a significant mixing of the S and T_0 levels occurs, in which the radical pair states oscillate back and forth between S and T_0. The T_0 radical pair state can then recombine to form $^3P_{865}$. This mechanism is also called the S-T_0 mechanism [33]. In the radical pair mechanism the $M_S = 0$ sublevel of $^3P_{865}$ is exclusively populated. This implies that shortly after the laser flash and before decay processes play a role, all $T_0 \rightarrow T_{+1}$ transitions are absorptive and $T_0 \rightarrow T_{-1}$ are emissive, as is explained in Fig. 5.8a. A polarization pattern AEEAAE is observed, which means that the zero-field parameter D is positive, consistent with previous results.[2, 4, 6, 34] The quantum yield of $^3P_{865}$ formation in

reduced reaction centers at temperatures below 50 K is found to be close to unity, at 300 K it is about 15%.[13, 28]

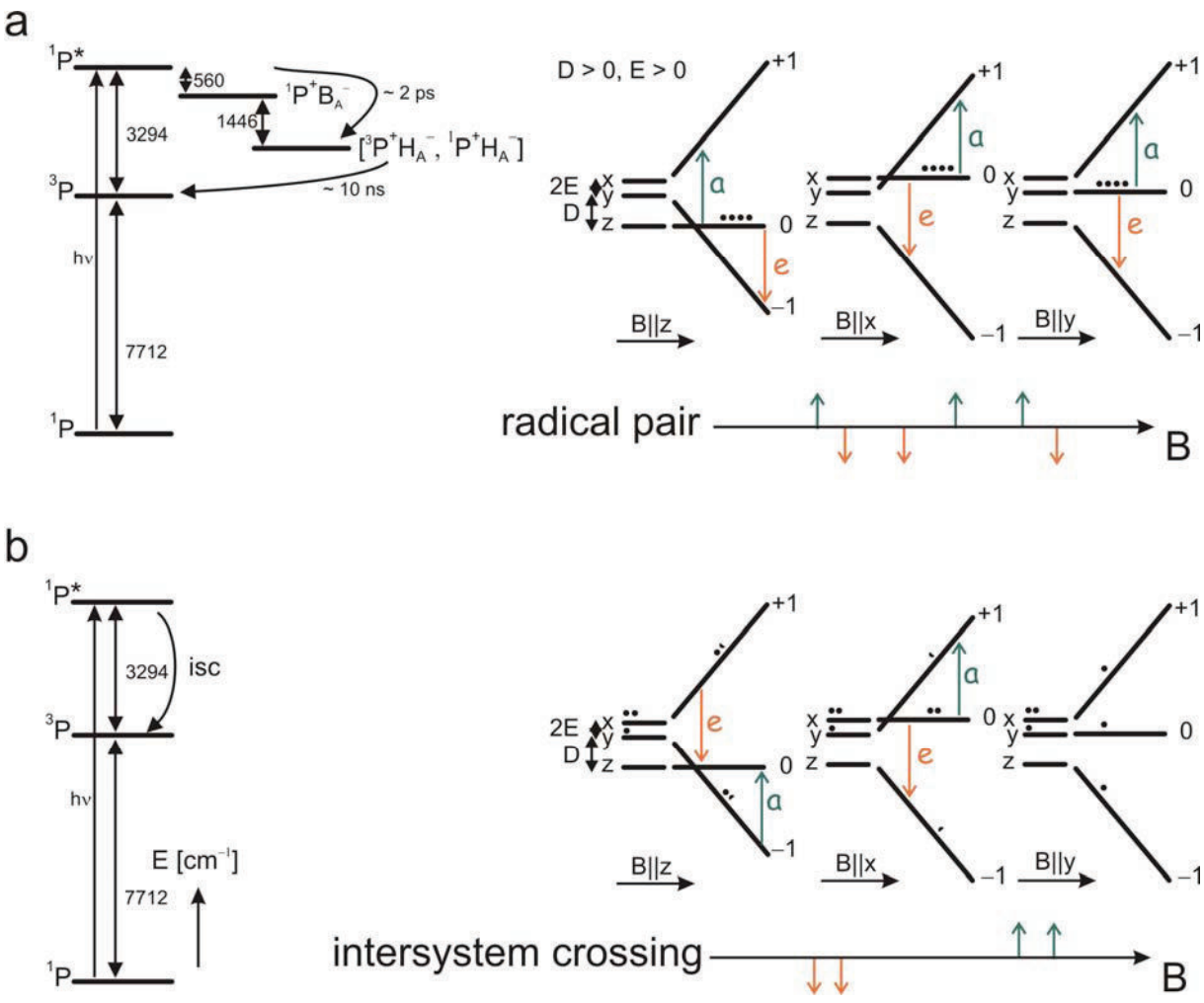

Figure 5.8. (a) Triplet formation in bacterial reaction centers of *Rb. sphaeroides* R-26.1, 2.4.1 and GD(M203)/AW(M260) by the radical pair mechanism. Energies are in [cm^{-1}] and reproduced from references.[5, 13] Also indicated is the splitting for the triplet sublevels for the magnetic field direction parallel to the X, Y or Z principal axis of the ZFS tensor. All population is located in the M_S = 0 sublevel. The resulting polarization pattern of the ESE-detected EPR spectrum; (b) Triplet formation in the bacterial reaction center of *Rb. sphaeroides* LH(M214)/AW(M260) by the intersystem crossing mechanism. The splitting of the triplet sublevels is identical to (a), but the population is distributed as described by equation A1 (Appendix A), resulting in a different polarization pattern. P: special pair (bacteriochlorophyll dimer), B_A: accessory bacteriochlorophyll, H_A: bacteriopheophytin (both in the A-branch).

The triplet radical pair mechanism also implies that the amplitudes of the absorptive and emissive signals are identical. This is indeed observed in transient EPR spectra (see Fig. 5.2 and reference[28]). However, the Electron Spin Echo Envelope Modulation (ESEEM)

effect[43-46] may introduce a modulation of the ESE amplitude in pulsed EPR spectroscopy. For nuclei with I > 0, in this case the four pyrrole nitrogens, whose hyperfine interaction is of the same order as the nuclear Zeeman interaction,[41] deep modulations can be observed. This phenomenon is known as the "exact cancellation" condition[41] and essentially means that in one of the M_S manifolds, the nuclear Zeeman and hyperfine splitting virtually cancel each other and cause a large mixing of the nuclear spin sublevels. Though normally applied to doublet (S = ½) states, the exact cancellation condition works similarly for triplet states. For triplet states, the $M_S = 0$ manifold is not split further by nuclear hyperfine interaction (see Fig. 5.5a). Depending on the sign of the hyperfine interaction, cancellation occurs either in the $M_S = +1$ or $M_S = -1$ manifold. Therefore, out of the two possible EPR transitions ($M_S = 0 \leftrightarrow +1$ and $M_S = 0 \leftrightarrow -1$) the ESEEM effect will be large only for the EPR transition that involves the "cancelled" M_S level, and small for the other EPR transition.

The behavior described in the previous paragraph is exactly what is observed in the two-pulse ESEEM experiments on $^3P_{865}$. A strong ^{14}N (I = 1) modulation for B || Z_I, which with positive *D* corresponds to the $M_S = 0 \leftrightarrow +1$ transition and a shallow modulation for B || Z_{II}, which is the $M_S = 0 \leftrightarrow -1$ transition. This allows the identification of the relative sign of the hyperfine interaction with respect to that of *D*. Since *D* is known to be positive[4, 6] it means that the $M_S = +1$ manifold is cancelled and the sign of the hyperfine interaction of the pyrrole nitrogens must thus also be positive.

Another attractive feature unique to triplet states is that the ^{14}N quadrupole interaction can be directly determined from the frequencies of the $M_S = 0$ manifold. Since no hyperfine interaction is present in this M_S manifold, the nuclear frequencies are well separated from those of the cancelled $M_S = +1$ manifold. The latter are close to 0 MHz and give rise to the intense band close to 0 MHz in the ESEEM spectrum at B || Z_I (*cf.* Fig. 5.5). The frequencies of the $M_S = 0$ manifold are expected around the ^{14}N Zeeman frequency (3.6 MHz at B || Z_I) and the double of this frequency. Under the assumption that the four pyrrole nitrogens have a very similar quadrupole splitting, the quadrupole parameter $e^2qQ/h = 3.2 \pm 0.3$ MHz has been read from the spectrum (*cf.* results), which is of similar magnitude to that observed in experiments at X-band (3.76 MHz[47]). The discrepancy may stem from the fact that at X-band frequency the quadrupole splitting is large enough to cause significant mixing of the nuclear spin sublevels even without hyperfine interaction in the $M_S = 0$ manifold and therefore the X-band spectra are significantly more difficult to interpret.

A simulation based on the radical pair mechanism of a transient EPR spectrum recorded at T = 10 K shortly after the laser flash is shown in Fig. 5.7a for *Rb. sphaeroides* R-

26.1. In the transient EPR spectrum, no ESEEM effects are present and the spectrum displays absorptive and emissive signals of equal intensity. The spectrum is also representative for *Rb. sphaeroides* 2.4.1 and mutant GD(M203)/AW(M260) at T = 10 K. All features of the experimental spectrum are reproduced and the simulation parameters are included in table 5.1. The *D* parameter is 0.0188 cm^{-1}, identical to the one read directly from the spectrum. The different widths of the low-field and high-field signals are attributed to a small anisotropy of the g tensor of $^3P_{865}$.[48, 49] In the simulation in reference,[48] the g tensor was assumed to be collinear with the ZFS tensor. We also use this approximation and the three g values amount to 2.0033, 2.0038 and 2.0023, respectively. These numbers are similar, but not identical to the ones found in measurements at 130 and 95 GHz,[48, 49] which are also not identical. The discrepancies, which stem from differences of only a few Gauss, likely come from the contribution of ^{14}N hyperfine couplings to the width of the EPR spectrum, that become less important at high microwave frequencies.

The ESE-detected EPR spectrum of mutant LH(M214)/AW(M260) does not display a polarization pattern typical for a radical-pair based triplet state. Rather the pattern is similar to that recorded for ^{3}BChl *a in vitro* (*cf.* Fig. 5.3d and 5.3e), which is formed by an intersystem crossing (ISC) mechanism. In this mechanism, depicted in Fig. 5.7b, the excited electron does not leave P_{865}. Spin-dependent processes, most notably spin-orbit (SO) coupling and spin-spin (SS) interaction,[50] then flip the spin of one of the unpaired electrons to form $^3P_{865}$. This triplet state is identical to the one formed by the radical pair mechanism in the other three systems, but because of the different precursor state (*i.e.* P^*_{865}), the relative populations of the triplet sublevels and hence the polarization pattern differs completely. The populations for an ISC triplet are given by formula A2 (Appendix A). By using this formula, the ESE-detected EPR spectrum at T = 10 K for mutant LH(M214)/AW(M260) can indeed be simulated by using virtually identical parameters used for the simulation – only g_y has changed to 2.0042 - of the radical-pair triplet, and a population distribution of the ZFS levels p_x, p_y and p_z of 0.7, 0.3 and 0.0, respectively. The only discrepancy concerns a difference in amplitude at the low-field side, which stems from the ESEEM effect that is not included in the simulation. The simulation is given in Fig. 5.7b.

The observation of an ISC triplet and not a RP triplet in mutant LH(M214)/AW(M260) has two important consequences for the charge separation process. First, the LH(M214) mutation completely inhibits long-lived radical pair formation at the A-branch. Second, also no long-lived radical pair is formed at T = 10 K in the B-branch. This is in-line with the observations that the lifetime of a transient radical pair is so short[19] that the

spin state remains a singlet [31]. Since no mutation has been introduced at the B-branch in this mutant, the second observation is likely valid for all systems. In the wild type case, the A-branch electron transfer proceeds at temperatures down to 10K, the B-branch transfer has a thermal activation barrier of 30 K.[51]

Anisotropy of triplet-triplet transfer dynamics and relaxation processes

After formation of $^3P_{865}$, spin-dependent interactions convert the triplet state back into the ground state. The decay rates are in general temperature dependent. When a carotenoid is present, the triplet state is taken over by ^{3}Car from $^3P_{865}$ via a Dexter energy transfer mechanism, since ^{3}Car is lower in energy than $^3P_{865}$.[30, 51-53] The energy transfer from P_{865} to Car occurs via the accessory BChl *a* in the B-branch and the rate of the transfer is determined by the activation barrier between P_{865} and BChl *a*.[30, 54] The triplet state of the accessory BChl *a* in the B-branch of wild type *Rb. sphaeroides* has never been observed, which indicates that the subsequent transfer to carotenoid is essentially activationless and very fast.[30] If the carotenoid is not present, *e.g.* in *Rb. sphaeroides* R-26.1, $^3P_{865}$ decays back to the ground state, and also a monomeric bacteriochlorophyll triplet was observed by ODMR experiments.[55, 56] In triplet-triplet transfer, as well as the decay of ^{3}Car to the ground state, again a spin-crossover has to take place. The same interactions that are responsible for the formation of the ISC triplet are also responsible for this spin crossover, and the decay rates k_i are described by equation A3 (Appendix A).

For *Rb. sphaeroides* R-26.1 decay times of 80 μs were observed in the DAF-EPR measurements at T = 10 K for the X and Y transitions and 250 μs for the Z transition. These results agree with those from transient EPR spectroscopy on *Rb. sphaeroides*.[27, 57] Indeed, it is already known that the X and Y sublevels are mainly responsible for deactivation of the triplet state of chlorophylls and derivatives.[58] Metz *et al* have shown that for planar aromatic systems one would expect that in calculating the spin vibronic coupling term, the spin sublevels corresponding to the in-plane molecular axes (X and Y) associated with a ππ* triplet state derive their intersystem crossing activity from first order, one-center spin-orbit coupling with singlet σπ* and nπ* levels, whereas the Z spin sublevel must utilize higher order one-center terms to gain appreciable activity;[59] therefore the population and depopulation rates for the Z level will always be smaller than those for the X and Y levels.[27, 28, 58]

For *Rb. sphaeroides* 2.4.1 and mutant GD(M203)/AW(M260) large changes in the triplet EPR spectra are observed upon increase of the temperature to 50 K (*cf.* Fig. 5.3). The shape of the spectrum changes because above 30 K the triplet state is taken over by carotenoid.[28] Monger *et al*[60] concluded that the carotenoid triplet was formed by energy

transfer from $^3P_{865}$. Since the energy transfer rate from the donor to the acceptor triplet occurs on a time scale which above 30 K becomes fast compared with spin-lattice relaxation, the acceptor triplet spectrum will also display a radical pair polarization pattern.[29] The carotenoid triplet has a polarization pattern EAAEEA, which is opposite to the polarization pattern AEEAAE of $^3P_{865}$.[28] The difference can be explained if the *D* value of ^{3}Car is opposite to that of the donor ($^3P_{865}$), *i.e.* negative.[28] In mutant GD(M203)/AW(M260), the pure ^{3}Car signal could be measured by pulsed EPR shortly after the laser flash before decay processes could take place. The simulation using a RP mechanism is shown in Fig. 5.7c, the simulation parameters are given in table 5.1. The DAF-EPR spectra of ^{3}Car at 70K can be simulated satisfactorily with three time constants, $k_y = k_z = 4$ μs, $k_x = 13$ μs. As an example, the ^{3}Car signal at $t_{DAF} = 25$ μs is simulated in Fig. 5.7d, where it is indeed seen that only intensity at the X orientations remains present. The temperature dependence of these numbers is given in Fig. 5.4f. The same temperature dependence is found for *Rb. sphaeroides* 2.4.1 (Fig. 5.4d) and the numbers agree with previous studies.[27, 57]

So far unreported observations concern the anisotropic triplet-triplet transfer described by three growth constants for the ^{3}Car signal and the process responsible for ^{3}Car formation in mutant LH(M214)/AW(M260). These will be discussed next.

Essentially over the temperature range from 10 K to 70 K, the ^{3}Car signal does not grow isotropically for both *Rb. sphaeroides* 2.4.1 and mutant GD(M203)/AW(M260). At B || X, the rate constant for growth is a factor of three faster than at B || Y and B || Z (Fig. 5.4). The initially puzzling result can be rationalized if all precursor states including the radical pair states are considered and it also gives a clue as to why the ratio of three between the growth constants is remarkably constant over the examined temperature range: as reported by Frank, the energy transfer from the donor to the acceptor triplet occurs on a fast time scale compared to spin-lattice relaxation.[30, 51] However, the oscillation frequency ν_{S-T_0} between the singlet and triplet radical pair states is on the order of 15 MHz,[61] which is similar to the Dexter energy transfer rate. The frequency ν_{S-T_0} depends on the orientation of the molecule in the magnetic field and since other rate constants are of similar magnitude, this dependence of ν_{S-T_0} is mirrored into the growth rates of the ^{3}Car signal.

An anisotropic, orientation-dependent quantum yield of $^3P_{865}$ has been reported at 130 GHz owing to this effect, which is expected to become negligible at lower microwave frequencies.[48] Though anisotropy in quantum yield is indeed not observed at 34 GHz, the anisotropy of the dynamics and associated rate constants *are* detectable at Q-band microwave

frequencies. The anisotropy of ω_{S-T_0} can be detected on the ^{3}Car signal if the other time constants, *e.g.*, for radical pair recombination to $^3P_{865}$, are faster or of similar magnitude. Most likely, the anisotropy of ω_{S-T_0} is also visible in the growth constants of $^3P_{865}$, the latter could unfortunately not be detected due to the spectrometer dead time.

The growth curves for the ^{3}Car signal have been fitted using the model described in Appendix A, and fits are included in Fig. 5.4b as an example. At T = 50 K, the experimentally observed formation behavior of the ^{3}Car signal in *Rb. sphaeroides* 2.4.1 can be understood by assuming that ω_{S-T_0} is equal to 100 MHz for B || Y, Z and 13 MHz for B || X (see next paragraph). In the model, the time constant for radical pair recombination was taken to be 10 ns, the isotropic Dexter energy transfer constant 1.7 μs. Thus, the slow inter-conversion of the singlet and triplet radical pairs at B || X leads to a slower buildup of the ^{3}Car signal at B || X as compared to B || Y or Z, even when the Dexter energy transfer rate is isotropic, i.e. not dependent on the orientation of the bRC in the magnetic field.

The spread in ω_{S-T_0} of one order of magnitude used in the model is large. However, the frequency of the radical pair oscillation indeed seems to be very orientation dependent if measured on the triplet radical pair state directly. This is confirmed by transient EPR measurements reported in reference,[61] particular in Fig. 5.3, where a large variation of ω_{S-T_0} with selected orientation is observed. An alternative model that includes the possibility of carotenoid in two or even more conformations[40, 52, 53, 62] was found insufficient to explain the observed anisotropy of the ^{3}Car growth constants, since the presence of multiple conformations would just lead to multiple, but isotropic growth constants (though the employed model does not rule out the presence of multiple conformations of the carotenoid). Also, a three-spin model described in literature,[31] which includes a third electron spin on Q_A has been tested, but was found to be inadequate, since the mutant GD(M203)/AW(M260) effectively has no Q_A and still displays virtually identical behavior as *Rb. sphaeroides* 2.4.1. As noted in reference[48] the anisotropy of triplet formation introduced by that of ω_{S-T_0} depends strongly on the relative orientations of the g tensors of the radical pair constituents. An even more sophisticated model that explicitly includes these quantities and their relative orientations to the ZFS and g tensor of ^{3}Car would lead to too many parameters in the simulation and has therefore not been attempted.

Now the double mutant LH(M214)/AW(M260) is considered, which displays a $^3P_{865}$ signal at T = 10 K formed by ISC (Fig. 5.8b). Since Dexter energy transfer is a spin-

conserving process, the polarization pattern of $^3P_{865}$ is expected to be taken over by ^{3}Car under conservation of the spin polarization. This is indeed the case. At T = 50 K, the EPR spectrum can be simulated by using the *D* and *E* parameters for ^{3}Car and using the same population distribution that was required to simulate $^3P_{865}$ in this mutant. The simulation is shown in the center trace of Fig. 5.7e and the parameters are included in table 5.1.

At the low-field (Z_I) and high-field (Z_{II}) edges, the simulation does not agree with the experimental spectrum, for which the signal is close to zero. It can be shown that if only the ISC mechanism populates the triplet state, an intensity of zero along Z would mean equal intensities at the X and Y canonical orientations. This is not observed experimentally. Thus the experimental spectrum at T = 50 K can not result solely from an ISC mechanism. A more plausible explanation for the mismatch at the low-field and high-field sides is that at T = 50 K, also the RP mechanism becomes operative in populating the triplet state. For the RP mechanism the simulation is shown in Fig. 5.7c. If 50% efficiency for both the ISC and RP mechanisms is assumed, the experiment and simulation agree very well, as seen in Fig. 5.7e. This has important consequences for the charge separation process, as the RP mechanism implies the formation of a radical pair species. Because mutant LH(M214)/AW(M260) does not have a BPheo in the A-branch owing to the LH(M214) mutation, the radical pair must have formed on the B-branch and it seems that at temperatures of 50 K and above, the B-branch becomes active in radical pair formation. From the signal-to-noise ratio, the B-branch charge separation amounts to at most 1% as compared to A-branch charge separation in the native system, which is much more efficient.[15, 16, 63, 64]

Wavelength dependence of $^3P_{865}$ formation

In mutant LH(M214)/AW(M260), $^3P_{865}$ at T = 10 K is formed by an ISC mechanism upon direct excitation at 865 nm. This mutant contains only one remaining BPheo in the B-branch. This system is therefore ideally suited to investigate the B-branch charge separation process since it allows a selected excitation of the BPheo at 537 nm, where no other pigments absorb. Upon excitation at 537 nm, the absolute signal becomes smaller and acquisition of the triplet ESE-detected EPR spectrum with a signal-to-noise ratio of about five requires averaging of close to twelve hours. However, the shape of the EPR spectrum displays minor changes as compared to that with excitation at 865 nm.

The *D* and *E* parameters of the spectrum at 865 nm excitation are identical to the ones observed for $^3P_{865}$ in Fig. 5.3(a-d). Thus, the spectrum recorded after excitation at 537 nm is also assigned to $^3P_{865}$. A possibility that the spectrum contains part of a BPheo triplet is

unlikely, since the spectrum does not agree with the ZFS parameters for BPheo *in vitro*. It is known that the BPheo ISC triplet EPR spectrum has polarization E at Y_{II} and A at Y_I,[2] instead of the A, E polarizations observed here. An A and E polarization seems to be quite unique to the RP mechanism for triplet formation, see Fig. 5.3.

The question then is how does the triplet state end up at P_{865} after excitation of BPheo and by which mechanism are the two additional "RP-like" signals at the Y canonical orientations formed? Formally, these processes occur on a faster timescale than that of the EPR experiment, an answer fully substantiated by EPR spectroscopy can therefore not be given. The EPR spectra, however, indicate the following. Most likely, most of the excitation

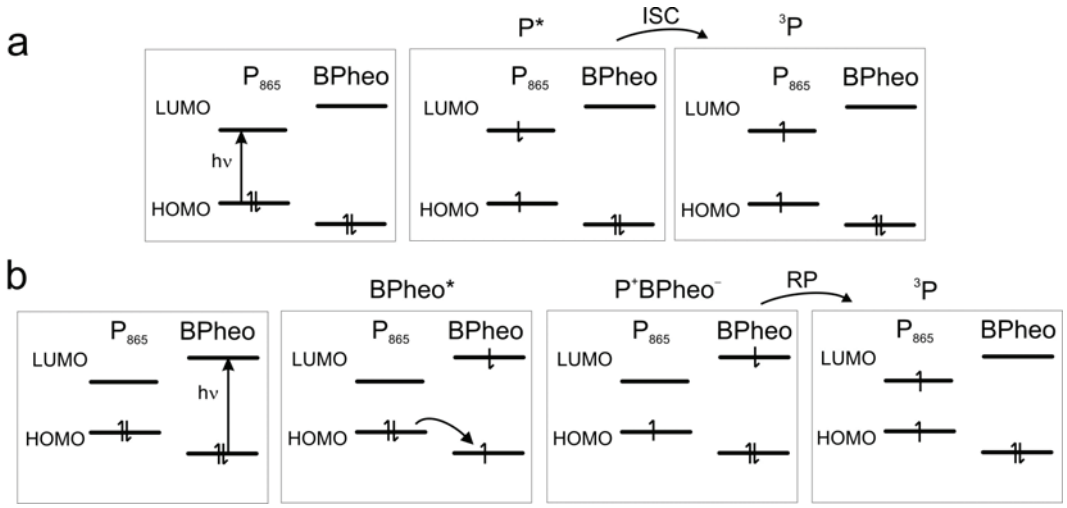

Figure 5.9. (a) Formation of $^3P_{865}$ at T = 10 K in *Rb. sphaeroides* LH(M214)/AW(M260) by the intersystem crossing mechanism at excitation of 865 nm; (b) possible HOMO-based formation of $^3P_{865}$ by the radical pair mechanism at excitation of 537 nm.

energy is transferred from H to P_{865}: $(P_{865}H^*) \rightarrow (P^*_{865}H)$ and then the ISC triplet on P_{865} is formed. This would yield the same spectrum as that after excitation at 865 nm. Additionally, and with low efficiency, it can be possible that an electron is transferred from P_{865} to BPheo* by HOMO-based electron transfer, or equivalently HOMO-base hole transfer in the other direction,[65-68] as is indicated in Fig. 5.9b. This would then lead to a B-branch RP, $P^{\bullet+}_{865}H^{\bullet-}_B$ that can recombine to $^3P_{865}$ by the RP mechanism (see Fig. 5.9b). The net result is that $^3P_{865}$ is formed after 537 nm excitation by a dominant ISC mechanism and a minor contribution from a HOMO-based RP mechanism, the latter contribution is most prominently visible at the Y orientations. The latter mechanism implies charge separation in the HOMO instead of the LUMO, or "hole transfer", whereby the created hole in HOMO of the BPheo is filled by an

electron from the donor. It is interesting to speculate whether both LUMO and HOMO based charge separation processes may occur under illumination by white (sun)light at room temperature under physiological conditions.

5.5 Conclusions

The observed polarization pattern at low temperature in the electron spin echo detected EPR spectra of *Rb. sphaeroides* R-26.1, 2.4.1 and mutant GD(M203)/AW(M260) indicates that the triplet state of $^3P_{865}$ is formed via the radical pair mechanism. In mutant LH(M214)/AW(M260), the polarization pattern is completely different and the triplet formation is explained by the intersystem crossing mechanism. The observation of a $^3P_{865}$ signal formed by intersystem crossing indicates the absence of long-lived radical-pair precursor states along the A-branch. Also the native B-branch is not active in charge separation at T = 10 K. The situation changes when the temperature is raised to about 30 K. In the bRCs with carotenoid, triplet-triplet transfer $P_{865} \rightarrow$ Car is observed. Moreover, a contribution to the spectrum by the radical pair mechanism is observed in mutant LH(M214)/AW(M260), indicating that the B-branch is "switching on" at these temperatures. The observation that both the triplet-triplet energy transfer as well as the B-branch radical pair formation become active at the same temperature above about 30 K, and the observation that accessory bacteriochlorophyll on the B-branch is involved in both processes, we conclude that an energy barrier between the accessory bacteriochlorophyll and P_{865} exists that is overcome at temperatures above 30 K. The A-branch is operative even at 10 K in the native system, indicating that no thermal barrier exists for A-branch charge separation down to this temperature.

Secondly, a triplet carotenoid EPR signal has been observed above 30 K. The growth rate of this signal depends on the orientation of the reaction center in the magnetic field. The observed anisotropy of the growth rate can be traced back to that of the frequency associated with the radical pair precursor state $[P_{865}^{\bullet+}H^{\bullet-}]$ that oscillates between the singlet and triplet states with a frequency that depends on the orientation of the bRC in the magnetic field. This behavior is observed for both *Rb. sphaeroides* 2.4.1 and mutant GD(M203)/AW(M260), for which the quinone on the A-branch cannot occupy its normal binding pocket. It therefore seems that the presence of an additional spin on Q_A does not significantly influence the spin dynamics involved in the initial steps of charge separation.

Finally, small but significant changes in the electron-spin-echo detected EPR spectrum of mutant LH(M214)/AW(M260) at 10 K have been observed upon change of the excitation wavelength to 537 nm. At this wavelength the remaining bacteriopheophytin in the B-branch is directly excited. The observed additional signals seem to stem from $^3P_{865}$ that is induced by a radical pair mechanism. A possible explanation for this observation is the existence of HOMO-based electron transfer, or hole-transfer, in which the created hole on bacteriopheophytin is filled by an electron from P_{865} with concomitant formation of the B-branch [$P_{865}^{\bullet+}H_B^{\bullet-}$] radical pair. All B-branch related processes observed in the EPR spectra at low temperature occur with an efficiency that is at most 1% of that of the corresponding processes of the A-branch. By the observations made here with EPR spectroscopy we conclude that this difference likely stems from a temperature activated process between P_{865} and the accessory bacteriochlorophyll on the B-branch. A theoretical investigation as to what causes the difference between the rates of A and B-branch radical pair formation, *e. g.* with respect to the distance between P_{865} and the accessory bacteriochlorophylls of the A and B-branches is in progress.

5.6 References

(1) Blankenship, B.; Madigan, M.; Bauer, C. *Anoxygenic Photosynthetic Bacteria;* Kluwer Academic Publishers: 1995.

(2) Thurnauer, M. C. (1979) ESR study of the photoexcited triplet state in photosynthetic bacteria, *Rev. Chem. Int., 100*, 197-231.

(3) Allen, J. P., Feher, G., Yeates, T. O., Komiya, H., Rees, D. C. (1987) Structure of the Reaction Center from Rhodobacter-Sphaeroides R-26 - the Cofactors .1, *Proc. Natl. Acad. Sci. USA, 84*, 5730-5734.

(4) Angerhofer, A. Chlorophyll triplets and radical pairs. In *Chlorophylls*; Scheer, H., Ed.;CRC Press: Boca Raton FL, 1991; pp 945-991.

(5) Feher, G., Allen, J. P., Okamura, M. Y., Rees, D. C. (1989) Structure and Function of Bacterial Photosynthetic Reaction Centers, *Nature, 339*, 111-116.

(6) Levanon, H., Norris, J. R. (1978) Photoexcited Triplet-State and Photosynthesis, *Chem. Rev., 78*, 185-198.

(7) Budil, D. E., Thurnauer, M. C. (1991) The Chlorophyll Triplet-State As A Probe of Structure and Function in Photosynthesis, *Biochim. Biophys. Acta, 1057*, 1-41.

(8) Deisenhofer, J., Epp, O., Miki, K., Huber, R., Michel, H. (1984) X-Ray Structure-Analysis of A Membrane-Protein Complex - Electron-Density Map at 3A Resolution

and A Model of the Chromophores of the Photosynthetic Reaction Center from *Rhodopseudomonas viridis*, *J. Mol. Biol., 180*, 385-398.

(9) Michel, H. (1982) 3-Dimensional Crystals of A Membrane-Protein Complex - the Photosynthetic Reaction Center from *Rhodopseudomonas viridis*, *J. Mol. Biol., 158*, 567-572.

(10) Allen, J. P., Feher, G., Yeates, T. O., Komiya, H., Rees, D. C. (1987) Structure of the Reaction Center from *Rhodobacter sphaeroides* R-26 - the Protein Subunits, *Proc. Natl. Acad. Sci. USA, 84*, 6162-6166.

(11) Allen, J. P., Feher, G., Yeates, T. O., Komiya, H., Rees, D. C. (1988) Structure of the Reaction Center from Rhodobacter-Sphaeroides R-26 - Protein Cofactor (Quinones and Fe-2+) Interactions .5, *Proc. Natl. Acad. Sci. USA, 85*, 8487-8491.

(12) Yeates, T. O., Komiya, H., Chirino, A., Rees, D. C., Allen, J. P., Feher, G. (1988) Structure of the Reaction Center from *Rhodobacter sphaeroides* R-26 and 2.4.1-Protein-Cofactor (Bacteriochlorophyll, Bacteriopheophytin, and Carotenoid) Interactions, *Proc. Natl. Acad. Sci. USA, 85*, 7993-7997.

(13) Volk, M., Aumeier, G., Langenbacher, T., Feick, R., Ogrodnik, A., Michel-Beyerle, M. E. (1998) Energetics and mechanism of primary charge separation in bacterial photosynthesis. A comparative study on reaction centers of *Rhodobacter sphaeroides* and *Chloroflexus aurantiacus*, *J. Phys. Chem. B, 102*, 735-751.

(14) Borovykh, I. V., Proskuryakov, I. I., Klenina, I. B., Gast, P., Hoff, A. J. (2000) Magnetophotoselection study of the lowest excited triplet state of the primary donor in photosynthetic bacteria, *J. Phys. Chem. B, 104*, 4222-4228.

(15) Paddock, M. L., Chang, C., Xu, Q., Abresch, E. C., Axelrod, H. L., Feher, G., Okamura, M. Y. (2005) Quinone (Q(B)) reduction by B-branch electron transfer in mutant bacterial reaction centers from *Rhodobacter sphaeroides*: Quantum efficiency and X-ray structure, *Biochemistry, 44*, 6920-6928.

(16) de Boer, A. L., Neerken, S., de Wijn, R., Permentier, H. P., Gast, P., Vijgenboom, E., Hoff, A. J. (2002) B-branch electron transfer in reaction centers of *Rhodobacter sphaeroides* assessed with site-directed mutagenesis, *Photosynth. Res., 71*, 221-239.

(17) Wang, H. Y., Lin, S., Allen, J. P., Williams, J. C., Blankert, S., Laser, C., Woodbury, N. W. (2007) Protein dynamics control the kinetics of initial electron transfer in photosynthesis, *Science, 316*, 747-750.

(18) Kirmaier, C., Laporte, L., Schenck, C. C., Holten, D. (1995) The Nature and Dynamics of the Charge-Separated Intermediate in Reaction Centers in Which Bacteriochlorophyll Replaces the Photoactive Bacteriopheophytin .1. Spectral Characterization of the Transient State, *J. Phys. Chem., 99*, 8903-8909.

(19) Kirmaier, C., Laporte, L., Schenck, C. C., Holten, D. (1995) The Nature and Dynamics of the Charge-Separated Intermediate in Reaction Centers in Which Bacteriochlorophyll Replaces the Photoactive Bacteriopheophytin .2. the Rates and Yields of Charge Separation and Recombination, *J. Phys. Chem., 99*, 8910-8917.

(20) Heller, B. A., Holten, D., Kirmaier, C. (1995) Control of Electron-Transfer Between the L-Side and M-Side of Photosynthetic Reaction Centers, *Science, 269*, 940-945.

(21) Haffa, A. L. M., Lin, S., Williams, J. C., Taguchi, A. K. W., Allen, J. P., Woodbury, N. W. (2003) High yield of long-lived B-side charge separation at room temperature in mutant bacterial reaction centers, *J. Phys. Chem. B, 107*, 12503-12510.

(22) Lin, S., Katilius, E., Haffa, A. L. M., Taguchi, A. K. W., Woodbury, N. W. (2001) Blue light drives B-side electron transfer in bacterial photosynthetic reaction centers, *Biochemistry, 40*, 13767-13773.

(23) de Boer, A. L., Neerken, S., de Wijn, R., Permentier, H. P., Gast, P., Vijgenboom, E., Hoff, A. J. (2002) High yield of B-branch electron transfer in a quadruple reaction center mutant of the photosynthetic bacterium *Rhodobacter sphaeroides*, *Biochemistry, 41*, 3081-3088.

(24) Chuang, J. I., Boxer, S. G., Holten, D., Kirmaier, C. (2006) High yield of M-side electron transfer in mutants of *Rhodobacter capsulatus* reaction centers lacking the L-side bacteriopheophytin, *Biochemistry, 45*, 3845-3851.

(25) Lubitz, W., Lendzian, F., Bittl, R. (2002) Radicals, radical pairs and triplet states in photosynthesis, *Acc. Chem. Res., 35*, 313-320.

(26) Ridge, J. P., van Brederode, M. E., Goodwin, M. G., van Grondelle, R., Jones, M. R. (1999) Mutations that modify or exclude binding of the QA ubiquinone and carotenoid in the reaction center from *Rhodobacter sphaeroides*, *Photosynth. Res., 59*, 9-26.

(27) McGann, W. J., Frank, H. A. (1985) Transient Electron-Spin Resonance Spectroscopy of the Carotenoid Triplet-State in *Rhodopseudomonas sphaeroides* Wild-Type, *Chem. Phys. Let., 121*, 253-261.

(28) Hoff, A. J., Proskuryakov, I. I. (1985) Triplet Electron-Paramagnetic-Res Spectra of the Primary Electron-Donor in Bacterial Photosynthesis at Temperatures Between 15-K and 296-K, *Chem. Phys. Let., 115*, 303-310.

(29) Frank, H. A., Bolt, J. D., Costa, S. M. D. B., Sauer, K. (1980) Electron-Paramagnetic Resonance Detection of Carotenoid Triplet-States, *J. Am. Chem. Soc., 102*, 4893-4898.

(30) Frank, H. A., Chynwat, V., Hartwich, G., Meyer, M., Katheder, I., Scheer, H. (1993) Carotenoid Triplet-State Formation in *Rhodobacter sphaeroides* R-26 Reaction Centers Exchanged with Modified Bacteriochlorophyll Pigments and Reconstituted with Spheroidene, *Photosynth. Res., 37*, 193-203.

(31) Hore, P.J. Analysis of polarized EPR spectra. In *Advanced EPR in biology and biochemistry*; Hoff, A., Ed.;Elsevier: Amsterdam, 1990; pp 405-440.

(32) Feher, G.; Okamura, M. Y. Chemical composition and properties of reaction centers. In *The Photosynthetic Bacteria*; Clayton, R. and Sistrom, Eds.;Plenum Press: New York, 1978; pp 349-386.

(33) Frank, H. A., Friesner, R., Nairn, J. A., Dismukes, G. C., Sauer, K. (1979) Orientation of the Primary Donor in Bacterial Photosynthesis, *Biochim. Biophys. Acta, 547*, 484-501.

(34) Lendzian, F., Bittl, R., Lubitz, W. (1998) Pulsed ENDOR of the photoexcited triplet states of bacteriochlorophyll a and of the primary donor P-865 in reaction centers of *Rhodobacter sphaeroides* R-26, *Photosynth. Res., 55*, 189-197.

(35) Plato, M.; Möbius, K.; Lubitz, W.; Allen, J. P.; Feher, G. Magnetic resonance and molecular orbital studies of the primary donor states in bacterial reaction centers. In *Perspectives in Photosynthesis*; Jortner, J. and Pullman, Eds.;Kluwer Academic Publishers: 1990; pp 423-434.

(36) Lendzian, F.; Endeward, B.; Plato, M.; Bumann, D.; Lubitz, W.; Möbius, K. ENDOR and TRIPLE Resonance Investigation of the Primary Donor Cation Radical P865 in Single Crystals of *Rhodobacter sphaeroides* R-26 Reaction Centers. In *Reaction Centers of Photosynthetic Bacteria*; Michel-Beyerle, M. E., Ed.;Springer Verlag: 1990; pp 57-68.

(37) Sinnecker, S., Reijerse, E., Neese, F., Lubitz, W. (2004) Hydrogen bond geometries from electron paramagnetic resonance and electron-nuclear double resonance parameters: Density functional study of quinone radical anion-solvent interactions, *J. Am. Chem. Soc., 126*, 3280-3290.

(38) Schweiger, A.; Jeschke, G. *Principles of Pulse Electron Paramagnetic Resonance;* Oxford University Press: 2001.

(39) Dauw, X. L. R., Poluektov, O. G., Warntjes, J. B. M., Bronsveld, M. V., Groenen, E. J. J. (1998) Triplet-state dynamics of C-70, *J. Phys. Chem. A, 102*, 3078-3082.

(40) Ermler, U., Fritzsch, G., Buchanan, S. K., Michel, H. (1994) Structure of the Photosynthetic Reaction-Center from *Rhodobacter sphaeroides* at 2.65-Angstrom Resolution - Cofactors and Protein-Cofactor Interactions, *Structure, 2*, 925-936.

(41) Flanagan, H. L., Singel, D. J. (1987) Analysis of N-14 Eseem Patterns of Randomly Oriented Solids, *J. Chem. Phys., 87*, 5606-5616.

(42) Lucken, E. A. C. *Nuclear Quadrupole Coupling Constants*; Academic Press: London and New York, 1969.

(43) Kosman, D. J., Peisach, J., Mims, W. B. (1980) Pulsed Electron-Paramagnetic Resonance Studies of the Copper(II) Site in Galactose-Oxidase, *Biochemistry, 19*, 1304-1308.

(44) Mims, W. B., Peisach, J., Shaw, R. W., Beinert, H. (1980) Electron-Spin Echo Studies of Cytochrome-C Oxidase, *J. Bio. Chem., 255*, 6843-6846.

(45) Mims, W. B., Peisach, J. (1976) Assignment of A Ligand in Stellacyanin by A Pulsed Electron-Paramagnetic Resonance Method, *Biochemistry, 15*, 3863-3869.

(46) Mondovi, B., Graziani, M. T., Mims, W. B., Oltzik, R., Peisach, J. (1977) Pulsed Electron-Paramagnetic Resonance Studies of Types-I and Type-Ii Copper of *Rhus-Vernicifera* Laccase and Porcine Ceruloplasmin, *Biochemistry, 16*, 4198-4202.

(47) de Groot, A., Evelo, R., Hoff, A. J., de Beer, R., Scheer, H. (1985) Electron-Spin Echo Envelope Modulation (Eseem) Spectroscopy of the Triplet-State of the Primary Donor of N-14 and N-15 Bacterial Photosynthetic Reaction Centers and of N-14 and N-15 Bacteriochlorophyll-A, *Chem. Phys. Let., 118*, 48-54.

(48) Paschenko, S. V., Gast, P., Hoff, A. J. (2001) A D-Band (130 GHz) EPR study of the primary electron donor triplet state in photosynthetic reaction Centers of *Rhodobacter sphaeroides* R26, *Appl. Magn. Reson, 21*, 325-334.

(49) Labahn, A., Huber, M. (2001) The g-tensor anisotropy of the triplet state of the primary electron donor in the photosynthetic bacterium *Rhodobacter sphaeroides* by high-field (95 GHz) EPR, *Appl. Magn. Reson, 21*, 381-387.

(50) Neese, F. (2006) Importance of direct spin-spin coupling and spin-flip excitations for the zero-field splittings of transition metal complexes: A case study, *J. Am. Chem. Soc., 128*, 10213-10222.

(51) Frank, H. A., Chynwat, V., Posteraro, A., Hartwich, G., Simonin, I., Scheer, H. (1996) Triplet state energy transfer between the primary donor and the carotenoid in *Rhodobacter sphaeroides* R-26.1 reaction centers exchanged with modified bacteriochlorophyll pigments and reconstituted with spheroidene, *Photochem. Photobiol., 64*, 823-831.

(52) Kakitani, Y., Fujii, R., Koyama, Y., Nagae, H., Walker, L., Salter, B., Angerhofer, A. (2006) Triplet-state conformational changes in 15-cis-spheroidene bound to the reaction center from *Rhodobacter sphaeroides* 2.4.1 as revealed by time-resolved EPR spectroscopy: Strengthened hypothetical mechanism of triplet-energy dissipation, *Biochemistry, 45*, 2053-2062.

(53) Angerhofer, A., Bornhauser, F., Aust, V., Hartwich, G., Scheer, H. (1998) Triplet energy transfer in bacterial photosynthetic reaction centres, *Biochim. Biophys. Acta, 1365*, 404-420.

(54) Laible, P. D., Chynwat, V., Thurnauer, M. C., Schiffer, M., Hanson, D. K., Frank, H. A. (1998) Protein modifications affecting triplet energy transfer in bacterial photosynthetic reaction centers, *Biophys. J., 74*, 2623-2637.

(55) Angerhofer, A., Aust, V. (1993) A Monomeric Bacteriochlorophyll Triplet-State ((3)B) in Reaction Centers of *Rhodobacter-Sphaeroides* R26, Studied by Absorption-Detected Magnetic-Resonance, *J. Photochem. Photobiol. B, 20*, 127-132.

(56) Hartwich, G., Scheer, H., Aust, V., Angerhofer, A. (1995) Absorption and Admr Studies on Bacterial Photosynthetic Reaction Centers with Modified Pigments, *Biochim. Biophys. Acta, 1230*, 97-113.

(57) Hoff, A. J. (1976) Kinetics of Populating and Depopulating of Components of Photoinduced Triplet-State of Photosynthetic Bacteria *Rhodospirillum rubrum*, *Rhodopseudomonas spheroides* (Wild-Type), and Its Mutant R-26 As Measured by ESR in Zero-Field, *Biochim. Biophys. Acta, 440*, 765-771.

(58) Clarke, R. H., Connors, R. E., Schaafsma, T. J., Kleibeuker, J. F., Platenkamp, R. J. (1976) Triplet-State of Chlorophylls, *J. Am. Chem. Soc., 98*, 3674-3677.

(59) Metz, F. (1973) Position-Dependent Deuterium Effect on Relative Rate Constants for Isc Processes in Aromatic-Hydrocarbons, *Chem. Phys. Let., 22*, 186-190.

(60) Monger, T. G., Cogdell, R. J., Parson, W. W. (1976) Triplet-States of Bacteriochlorophyll and Carotenoids in Chromatophores of Photosynthetic Bacteria, *Biochim. Biophys. Acta, 449*, 136-153.

(61) Bittl, R., van der Est, A., Kamlowski, A., Lubitz, W., Stehlik, D. (1994) Time-Resolved Epr of the Radical Pair P(865)(+)Q(A)(-) in Bacterial Reaction Centers - Observation of Transient Nutations, Quantum Beats and Envelope Modulation Effects, *Chem. Phys. Let., 226*, 349-358.

(62) Arnoux, B., Ducruix, A., Reisshusson, F., Lutz, M., Norris, J., Schiffer, M., Chang, C. H. (1989) Structure of Spheroidene in the Photosynthetic Reaction Center from Y-*Rhodobacter-Sphaeroides*, *Febs Lett., 258*, 47-50.

(63) Woodbury, N.; Allen, J. *Anoxygenic photosynthetic bacteria*; Blankenship, R., Madigan, and Bauer, Eds.;Kluwer Academic Publishers: Dordrecht, Netherlands, 1995.

(64) Bixon, M., Jortner, J., Michel-Beyerle, M. E., Ogrodnik, A. (1989) A Superexchange Mechanism for the Primary Charge Separation in Photosynthetic Reaction Centers, *Biochim. Biophys. Acta, 977*, 273-286.

(65) Allen, G. C., Hush, N. S. (1967) Reflectance Spectrum and Electronic States of CuCl Ion in A Number of Crystal Lattices, *Inorg. Chem., 6*, 4-15.

(66) Osuka, A., Mataga, N., Okada, T. (1997) A chemical approach towards the photosynthetic reaction center, *Pure Appl. Chem., 69*, 797-802.

(67) Reimers, J. R., Hush, N. S. (2004) Unified description of the electrochemical, charge distribution, and spectroscopic properties of the special-pair radical cation in bacterial photosynthesis, *J. Am. Chem. Soc., 126*, 4132-4144.

(68) Breton, J., Nabedryk, E., Parson, W. W. (1992) A New Infrared Electronic-Transition of the Oxidized Primary Electron-Donor in Bacterial Reaction Centers - A Way to Assess Resonance Interactions Between the Bacteriochlorophylls, *Biochemistry, 31*, 7503-7510.

Chapter 6

Spin density distribution of the triplet state of bacteriochlorophylls*

Abstract

The photoexcited triplet states of bacteriochlorophyll *a* and bacteriochlorophyll *b* have been investigated by ENDOR spectroscopy at 34 GHz in frozen solution and by DFT calculations. The spin density distribution in the triplet state is found to be similar for bacteriochlorophyll *a* and bacteriochlorophyll *b* except for the presence of spin density on carbon 8^1 in bacteriochlorophyll *b*. Based on a comparison with ENDOR experiments for the radical cation and anion, the triplet state in bacteriochlorophylls could not be explained as being a simple HOMO $\rightarrow$ LUMO excitation of Gouterman orbitals. Rather, it has to be described by a mixture of HOMO $\rightarrow$ LUMO and HOMO−1 $\rightarrow$ LUMO excitations for a satisfactory explanation of the observed hyperfine interactions. The observed hyperfine couplings in the ENDOR spectra have been assigned and the field-dependence of the signals is found to be fully compatible with the orientation of the zero field splitting tensor determined from magnetophotoselection studies.

* This chapter is based on the publication "Spin density distribution of the triplet state of bacteriochlorophylls. Triplet ENDOR and DFT Studies" by Marchanka, A., Lubitz, W., van Gastel, M. *J. Phys. Chem. B*, (2009), 113, 6917-6927.

6.1 Introduction

Bacteriochlorophylls are cofactors of crucial importance in bacterial photosynthesis. They are involved in light absorption in antenna complexes and in excitation transfer to the reaction center, where they participate in charge separation both as electron donors and electron acceptors. Up to now, twelve different chlorophylls have been found in bacteria.[1, 2] Their structural differences, however, are minor and are believed to originate from enzymes that act late in the biosynthetic pathway.[2] The bacterial reaction centers of most bacteria, *e.g.*, of *Rhodobacter* (*Rb.) sphaeroides*, contain BChl *a*.[3-5] The reaction centers of heliobacteria contain BChl *g*,[6] and those of *Blastochloris (Bl.)* – previously *Rhodopseudomonas* - *viridis* BChl *b*.[7-10] In chlorosomes of some green bacteria, BChl *c* is found.[11]

In the photosynthetic bacterial reaction center the cofactors are arranged into two branches, called A and B, with pseudo two-fold symmetry.[3, 7, 9] The charge separation process starts at a dimer of bacteriochlorophylls called the primary donor (P). The excited electron then undergoes a series of electron-transfer steps over bacteriochlorophyll and bacteriopheophytin cofactors to the primary acceptor (ubiquinone-10 in *Rb. sphaeroides*), all in the A-branch. The final electron acceptor is a loosely bound second ubiquinone-10 molecule, located at the B-branch on the cytoplasmic side. In all species investigated up to now by optical[12-15] and magnetic resonance[14, 16-20] studies, the A-branch is photosynthetically active, and less than one per cent of charge separation occurs *via* the B branch.[5, 13, 15, 21]

In order to better understand the processes associated with light-induced charge separation in the bacterial reaction center on a molecular basis, a detailed knowledge of the spatial and electronic structure of all pigments is required. For bacteriochlorophylls, the paramagnetic states, including the radical cation and anion states ($S = ½$)[22, 23] and the metastable triplet state ($S = 1$)[22, 24] are ideal tools for this purpose. In a simple molecular orbital (MO) picture, the neutral molecule comprises two electrons in the highest-occupied-molecular-orbital (HOMO) followed by an empty lowest-unoccupied-molecular-orbital (LUMO). Studies of the radical cation allow investigation of the spin density distribution of the HOMO[25-28] and studies of the radical anion give information about the LUMO.[29-31] The triplet state would have an unpaired electron in both the HOMO and LUMO in this simple MO picture, and thus allows a simultaneous study of both orbitals. For each paramagnetic state, a determination of the atoms at which large electron spin density is located is essential, *e.g.*, to identify electron transfer pathways in which overlap of HOMO and LUMO orbitals of the donor and acceptor molecules plays a crucial role.

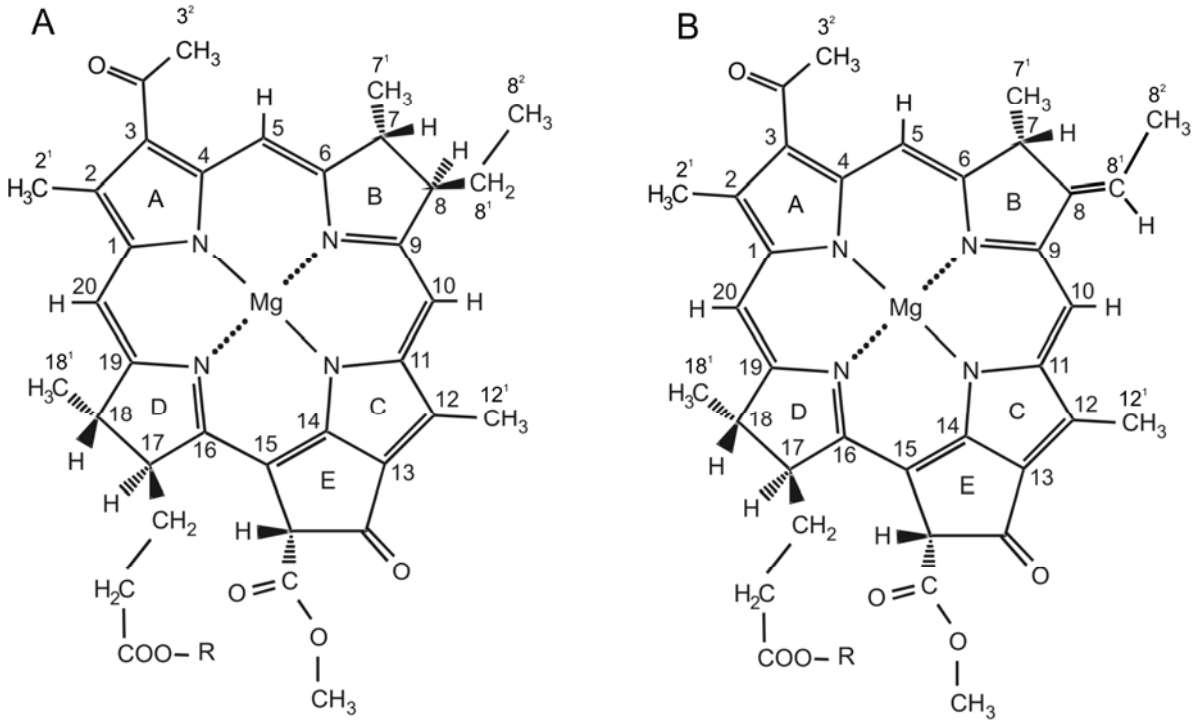

Figure 6.1. Resonance structures and IUPAC numbering scheme for (A) BChl *a* and (B) BChl *b*.[32] The two molecules differ at position 8, where an ethyl group is present in BChl *a* and an ethylidene group is present in BChl *b*. R indicates the phytyl chain in BChl *a* and BChl *b*.

The electronic structure of the excited singlet state from which electron transfer reactions start is not accessible by EPR techniques due to its diamagnetic character. However, both the HOMO and LUMO orbitals can be investigated simultaneously *via* the energetically nearby triplet state. In the simple MO picture, the primary forward electron transfer step in bacterial reaction centers proceeds from the then singly occupied LUMO orbital of the donor P^* and the charge recombination step proceeds back into the HOMO orbital of $P^{\bullet+}$.[33, 34]

The structures of BChl *a* and BChl *b* are shown in Fig. 6.1. They both comprise a bacteriochlorin base harboring a Mg^{2+} ion and only differ at position 8, where BChl *a* has an ethyl group and BChl *b* has an ethylidene group; thus the π system is slightly extended for BChl *b*.[22, 32] The bacteriochlorophylls belong to the family of porphyrins and display two major absorption bands, one in the near UV region (the B band) and one in the near IR region (the Q band).[32, 35-37] These absorption bands are ascribed to a set of π - π transitions, involving the electrons of the chlorophyll macrocycle.[37, 38] The strong B band usually occurs at about 400 nm and corresponds to the $S_0 \rightarrow S_2$ transition, the weak absorption of the Q band corresponds to the $S_0 \rightarrow S_1$ transition and typically absorbs above 600 nm.

The radical cation and anion of BChl *a* have been extensively studied by EPR and ENDOR spectroscopy.[25-31] Isotropic proton hyperfine coupling constants have been measured and assigned to specific molecular positions, and the assignments were corroborated by quantum chemical calculations.[34, 39-41] Less information is available for the triplet state. The triplet state in bacteriochlorophylls is formed after optical excitation *via* the intersystem crossing mechanism.[22, 42] Though bacteriochlorophyll triplet states have been investigated using EPR spectroscopy by many groups[18, 22, 24, 43-45] and polarization patterns and zero field splitting parameters have been obtained,[18, 43] only one ENDOR study has been reported so far for triplet BChl *a* at 9 GHz *in vitro*.[46] In that study, two signals have been observed, one has been assigned to methyl group protons and another to methine protons. The number of observed signals is much smaller than that observed in the cation and anion radicals. The difficulty with ENDOR experiments of the triplet state is related to the small spin polarization after intersystem crossing, which gives rise to weak signals.[47]

ENDOR spectroscopy has advantages in comparison to EPR spectroscopy; unresolved hyperfine structure of the triplet EPR spectrum is accessible in ENDOR experiments and the detailed electronic structure of the molecule on the atomic level can be investigated experimentally. In this work, we extend the triplet ENDOR studies of *in vitro* bacteriochlorophyll and present a systematic low-temperature study of ^{3}BChl *a* and ^{3}BChl *b* at 34 GHz. The advantage of 34 GHz over 9 GHz is the increased sensitivity inherent with larger microwave frequencies, which results in improved signal-to-noise ratios and the observation of an increased number of signals. The experiments are complemented with DFT calculations and are compared to previous results obtained for the radical cation and anion.[23, 25, 28, 29, 31] The most remarkable result found here is that a simple HOMO $\rightarrow$ LUMO electronic excitation is not compatible with the experimentally derived electronic structure of the bacteriochlorophyll triplet state, *i.e.* the spin density distribution of the triplet state is not just the "average" of that of radical cation and anion. Rather, also a HOMO−1 $\rightarrow$ LUMO excitation plays an important role in the wave function of the first excited triplet state.

6.2 Theory

"Gouterman four orbital" model

The Q and B bands in the absorption spectra of bacteriochlorophylls belong to the bacteriochlorin base and they are similar for many porphyrins. They can be described theore-

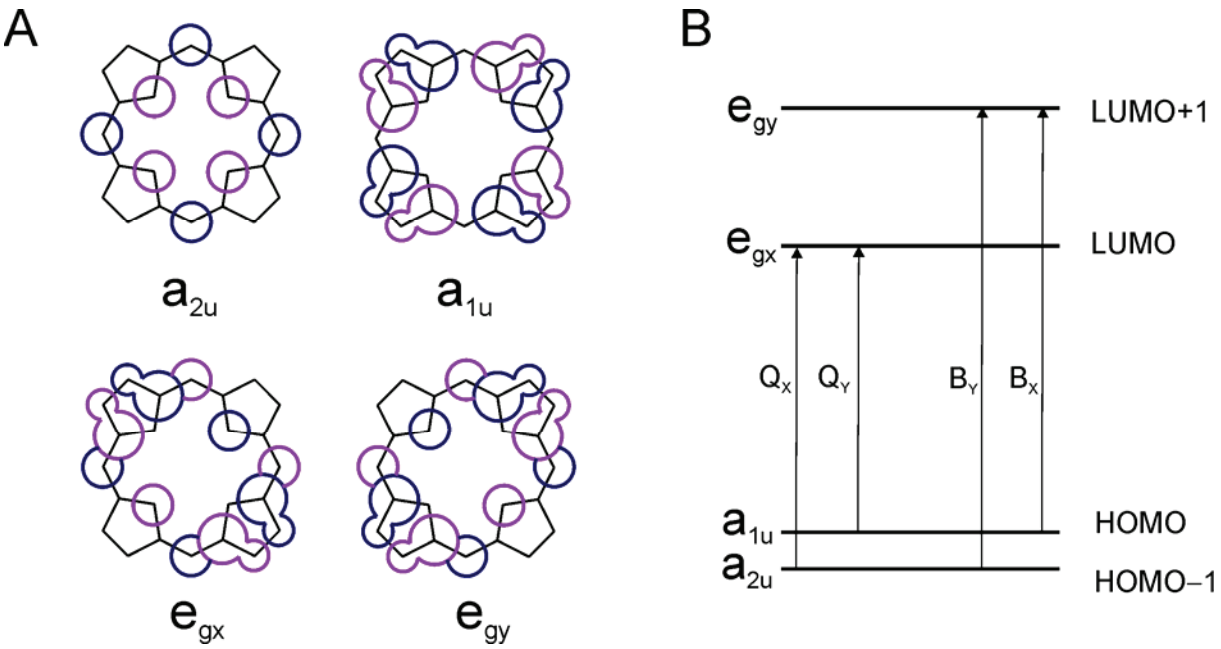

Figure 6.2. (A) Schematic representation of the four Gouterman orbitals in porphyrins.[38] The irreducible representations in case of D_{4h} symmetry are included in the figure. (B) Schematic drawing of the energy levels of the four Gouterman orbitals upon symmetry lowering from D_{4h} to C_{2v}. The set of e_g orbitals becomes non-degenerate and gives rise to Q and B bands.

tically in a simple way by only four orbitals as originally proposed in a model by Gouterman.[37, 38] The four MOs that are principally involved in these transitions are the two highest occupied MOs (HOMO−1, HOMO) and the two lowest unoccupied MOs (LUMO, LUMO+1) in the ground state molecule. The Gouterman orbitals are shown in Fig. 6.2A and an energy level scheme is shown in Fig. 6.2B. In D_{4h} symmetry, valid for protoporphyrin without ring substituents, the HOMO orbitals have symmetry a_{1u} and a_{2u} and the LUMO orbitals have symmetry e_g. Upon symmetry lowering towards approximate C_{2v} symmetry, the orbitals a_{1u} and a_{2u} transform as a_2 and b_1 and by taking appropriate linear combinations of the e_g orbitals, two new unoccupied orbitals are constructed that also transform as a_2 and b_1. Especially the two LUMO orbitals become non-degenerate and thus give rise to the B band and Q band in the visible absorption spectrum.[35, 36, 38]

Electron spin density distribution and hyperfine couplings in the triplet state

The triplet state in a simple model is described via HOMO → LUMO excitation and one unpaired electron is present in the HOMO and the LUMO orbital each. However, also the HOMO−1 orbital is nearby in energy, and the triplet state may in part comprise a HOMO−1

→ LUMO excitation. Because of the near-degeneracy of the HOMO and HOMO−1 orbitals, DFT cannot be expected to reproduce the mixing to these orbitals. In order to theoretically investigate the triplet wavefunction with respect to participation of the HOMO, HOMO−1 and LUMO, unpaired electrons have been redistributed over the set of frontier orbitals (HOMO−1, HOMO, LUMO, LUMO+1). The spin density ρ_π for any combination of HOMO → LUMO and HOMO−1 → LUMO excitation can be then calculated using the equation

$$\rho_\pi = \cos^2 \varphi \rho_{H,L} + \sin^2 \varphi \rho_{H-1,L} \quad (1)$$

where $\rho_{H,L}$ and $\rho_{H-1,L}$ are the spin densities from calculations with pure HOMO → LUMO and HOMO−1 → LUMO excitation, respectively, and φ determines the amount of mixing; $\varphi = 0^\circ$ corresponds exclusively to HOMO → LUMO excitation, $\varphi = 90^\circ$ to a HOMO−1 → LUMO excitation. Due to the proportionality of isotropic hyperfine coupling constants of methyl group protons and β protons to the electron spin density on the adjacent carbon atom,[48] the calculation of hyperfine coupling constants for any combination of HOMO → LUMO and HOMO−1 → LUMO excitation is performed using a similar equation

$$A\left({}^1H\right) = \cos^2 \varphi A_{H,L}\left({}^1H\right) + \sin^2 \varphi A_{H-1,L}\left({}^1H\right) \quad (2)$$

For the in-plane methine protons, spin polarization is responsible for the isotropic hyperfine coupling constants. It also plays a minor role for the hyperfine couplings of the other protons, but it is the dominant effect for the methine (*meso*) protons. Since spin polarization involves the polarization of the orbitals of an electron pair in a doubly occupied orbital of lower energy, it is not taken into account correctly in calculations upon mixing of the frontier orbitals. In order to calculate the isotropic couplings for the methine protons, additional calculations have been performed using spin-unpolarized orbitals derived from a calculation of the singlet ground state. The triplet π spin density for HOMO → LUMO and HOMO−1 → LUMO excitation was then recalculated from the spin-unpolarized molecular orbitals by computing the spin densities based on the unpolarized orbitals. Subsequently, equation (1) was used to obtain the unpolarized triplet spin density for an arbitrary mixture of HOMO → LUMO and HOMO−1 → LUMO excitation. Finally, isotropic hyperfine coupling constants for the methine protons, a_H, were calculated using McConnell's relation[48, 49]

$$a_H = Q\rho_\pi \quad (3)$$

where Q is a proportionality factor and has a value of −63 MHz,[48, 49] and ρ_π is the spin density on the adjacent carbon atom.

ENDOR and hyperfine interaction

The spin Hamiltonian for the triplet state has the form

$$H = g_e \mu_B \vec{B} \cdot \vec{S} - g_n \mu_N \vec{B} \cdot \vec{I} + \vec{S} \cdot \vec{\vec{A}} \cdot \vec{I} + \vec{S} \cdot \vec{\vec{D}} \cdot \vec{S} \qquad (4)$$

where μ_B and μ_N are the Bohr and nuclear magnetons, g_e and g_n are the g-values of the electron und nucleus, $\vec{S}$ is the total electron spin, $\vec{I}$ is the nuclear spin, $\vec{\vec{A}}$ is the nuclear hyperfine tensor, $\vec{\vec{D}}$ is the zero field tensor.

Under the assumption that the terms involving the nuclear spin operator are much smaller than the other terms (strong field approximation), the nuclear spin transitions for a nuclear spin, *e.g.* that of a proton ($I = ½$), coupled to the triplet electron spin ($S=1$) are determined by nuclear Zeeman and hyperfine terms of the spin Hamiltonian. For the molecule in the triplet state they occur at

$$\nu_{ENDOR}^{T} = \nu_n - M_S A_T \qquad (5)$$

where ν_n is the nuclear Zeeman frequency, A_T represents the hyperfine interaction in the triplet state. The energy level diagram for a proton (I = ½) coupled to the triplet electron spin S = 1 is shown in scheme 1. The frequencies of the nuclear transitions observed in ENDOR spectroscopy in the presence of hyperfine interaction with respect to nuclear Zeeman frequen-

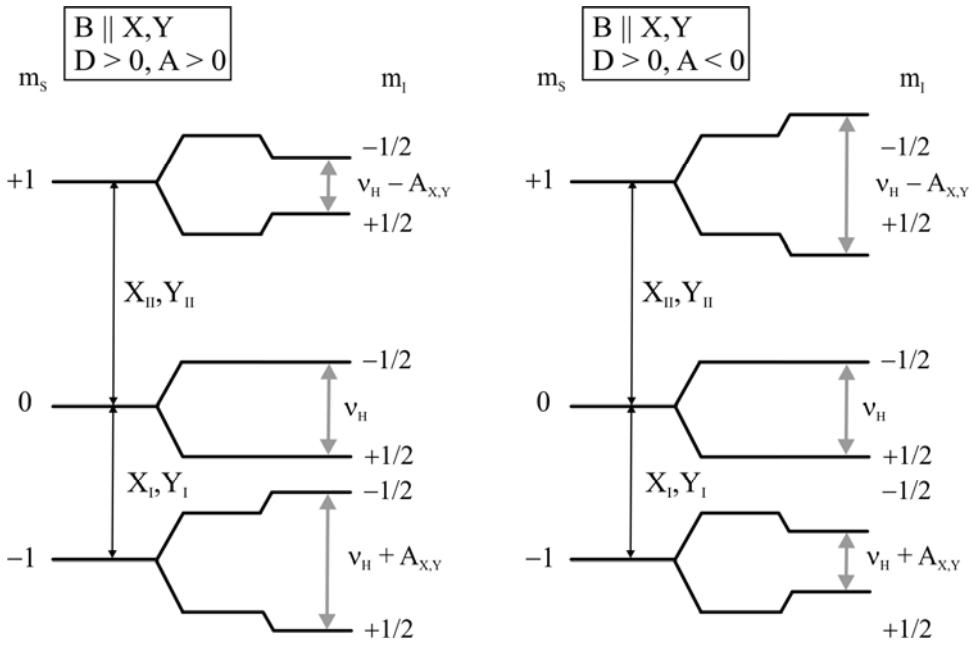

Scheme 1.

cy can be read from the spectra according to equation (5). For example, if $A_T > 0$, the larger nuclear transition frequency occurs in the $M_S = -1$ triplet sublevel and the smaller in the $M_S = +1$ (see scheme 2). In the $M_S = 0$ triplet sublevel, no hyperfine interaction is present and the ENDOR frequency occurs at the nuclear Zeeman frequency $\nu_n(^1H)$. For triplet ENDOR measurements with a magnetic field resonant with the $M_S = 0 \leftrightarrow -1$ transition a sharp band from the $M_S = -1$ manifold is thus expected at $\nu_n(^1H) + A_T$ for $A_T > 0$ and *vice versa* for $A_T < 0$.[46] The opposite hyperfine shift is observed for $M_S = +1$ manifold (scheme 1). The sign of the hyperfine coupling A_T with respect to that of the zero field splitting parameter D is thus directly obtained from the ENDOR spectrum.[18, 46, 50] The reading of the frequency was performed without a simulation procedure.

6.3 Materials and Methods

Sample preparation

BChl *a* and BChl *b* were isolated from *Rb. sphaeroides* and *Bl. viridis*, respectively, by extraction with deoxygenated cold acetone and 2-diethylether in the dark.[51] After phase separation, the ether part contained the bacteriochlorophylls. Further purification was performed by reversed phase HPLC with S1/S2 columns from Waters 2695, 996. As a solid phase Waters Novapak RP-18 was used. First, a washing step with 24% acetonitrile, 20% ethylacetate, 47% methanol and 9% 100 mM Tris-HCl, pH 8.0 as the liquid phase has been performed. Fraction with high amount of BChl has been purified further in a second HPLC step. For this, the sample has been diluted in acetone and 10% 1 M ammonium acetate has been added. A linear gradient of 52 minutes has subsequently been run from 29.1% acetonitrile, 9% ethylacetate 44.4% methanol and 17.5% 10 mM Tris-HCl to 20% acetonitrile, 30% ethylacetate and 50% methanol, followed by a 6 minute washing step with the final buffer. Then, a two-minute linear gradient to 29.1% acetonitrile, 9% ethylacetate, 44.4% methanol and 17.5% 10 mM Tris-HCl has been run followed by a 5 minutes elution phase. Immediately after purification, the bacteriochlorophylls were lyophilized and dissolved in purified deoxygenated MTHF. The solution was then transferred to the EPR tube and quickly frozen in liquid nitrogen to form an optically transparent glass. All steps of the purification were performed in dim green light.

EPR/ENDOR

Electron Spin Echo (ESE) detected EPR and ENDOR spectra were recorded on a Bruker Q-band Elexsys E580 FT pulse EPR spectrometer equipped with a home-built EPR/ENDOR resonator,[52] and an Oxford CF935 helium gas-flow cryostat. Samples were excited with an Opotek OPO laser at variable wavelength, pumped by a Vibrant Nd:YAG laser at 10 Hz repetition rate. Excitation at 590 nm (for BChl *a*) and 600 nm (BChl *b*) was performed with 8 mJ/pulse. The EPR measurements were carried out in the temperature range of 10 K to 50 K. For BChl *a*, the microwave frequency was 33.829 GHz, for BChl *b* the frequency was 33.632 GHz. The ENDOR measurements were performed at 10 K. The microwave frequency was typically 33.9 GHz, with variations of 0.2 GHz, depending on the sample and the temperature.

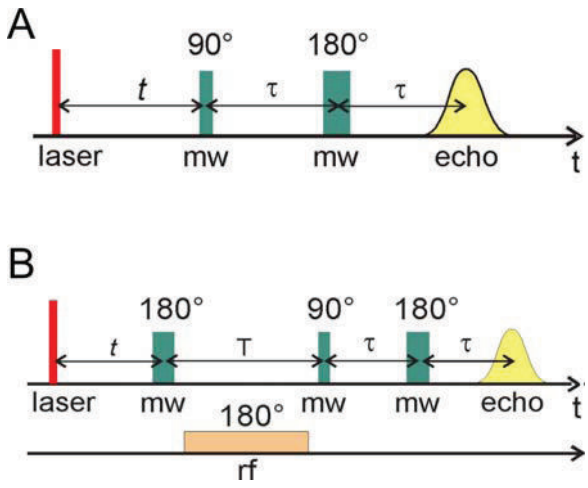

Scheme 2.

The Delay after Flash (DAF) EPR experiment pulse sequence[53] is shown in scheme 2A. It consists of a laser pulse followed by two microwave pulses and detection by a Hahn echo. The pulse lengths were 40 ns and 80 ns, respectively, the delay between the two pulses was 440 ns and the microwave power was 20 mW. Pulsed ENDOR measurements were performed according to the Davies ENDOR pulse sequence (scheme 2B).[46, 53] A weak selective microwave pulse was used for preparation (pulse length 300 ns, t = 1 µs) and a standard Hahn echo scheme was used for detection (pulse sequence π/2 - π with pulse lengths 150 and 300 ns, τ = 440 ns). The detection pulses were applied 2 µs after the end of the radio frequency π pulse of 20 µs length. The accumulation time was typically 30 minutes for an EPR spectrum and 6-12 hours for an ENDOR spectrum depending on the sample and the magnetic field setting, at which the ENDOR measurements were performed.

DFT calculations

DFT calculations of the BChl *a* and BChl *b* triplet state were performed with the *ab initio*, DFT and semi-empirical SCF-MO package ORCA.[54-57] All calculations were performed using the BP86 functional, TZVP[58] basis set and TZV/C[59] auxiliary basis set. The convergence criteria for the SCF procedure were 10^{-7} Hartree for the change in total energy and 10^{-4} for the DIIS error. The model geometry of BChl *a* was taken from the PDB entry 1RG5.[60] That of BChl *b* was constructed from the BChl *a* geometry by modification of the ethyl group at position 8 to an ethylidene group. All protons and methyl groups were geometry optimized using the program package Gaussian[61] to improve the calculation of the ^{1}H hyperfine couplings.[48] Calculations have been performed with and without an axial ligand (modelled as either pyridine or water, instead of MTHF, since it is only a very weak coordinating solvent). In all cases, the axial ligand was found not to contribute to any of the four orbitals (HOMO−1, HOMO, LUMO, LUMO+1) and less than 0.2 % spin density has been found on the axial ligand. The results presented in the tables are obtained in a series of calculations without an axial ligand.

The hyperfine coupling constants for the methyl groups and β protons in the triplet calculation DFT I were calculated by response theory using a spin-unrestricted Kohn-Sham formalism (UKS).[62] The accuracy of such calculations for reproduction of hyperfine coupling constants is typically 25 %.[62] The three proton hyperfine coupling tensors of the methyl groups were averaged and diagonalized to obtain mean hyperfine coupling constants for a rotating methyl group. In order to accurately take into account spin-polarization effects, isotropic hyperfine coupling constants for the methine protons have been calculated using spin-unpolarized orbitals from an additional calculation of the singlet ground state, followed by artificial promotion of an electron from HOMO to LUMO without performing additional SCF iterations. This calculation yields spin densities at the carbon atoms adjacent to the methine protons. The carbon spin densities have subsequently been inserted into the McConnell equation to compute the isotropic hyperfine couplings (see Theory section).

Hyperfine coupling constants from DFT calculations with a different distribution of unpaired electrons over the set of four Gouterman orbitals have been calculated (DFT II) have been calculated in the following way. For the methyl groups and β protons, an additional triplet calculation was performed by artificially rearranging the unpaired electrons such that one unpaired electron resides in the HOMO−1 and one in the LUMO and not performing additional SCF iterations. Hyperfine coupling constants for this HOMO−1 → LUMO triplet state have subsequently been calculated in ORCA by using response theory. The hyperfine

coupling constants for an arbitrary mixture of HOMO → LUMO and HOMO−1 → LUMO excitation have then been calculated according to equation (2). For the methine protons, again a singlet ground state calculation is performed, followed by two triplet calculations without additional SCF iterations in which the unpaired electrons have been redistributed either according to HOMO → LUMO or to HOMO−1 → LUMO excitation. The carbon spin densities from these two calculations have then been used to calculate carbon spin densities for a triplet state of mixed HOMO → LUMO and HOMO−1 → LUMO character by using equation (1). Subsequently, the McConnell equation (3) is used to calculate isotropic couplings.

Lastly, a set of calculations with bent BChl *a* and BChl *b* geometries within the DFT II framework was performed to investigate a possible structural heterogeneity of the bacteriochlorin macrocycle. In this set of calculations, either one of the pyrrole rings A-D or two, three or all four pyrrole rings were tilted up or down by 5 or 10 degrees. From this large set of calculations, the average value and the standard deviation of the isotropic proton hyperfine coupling constants have been obtained (see Appendix B for details).

6.4 Results

EPR

The ESE-detected triplet EPR spectra of ^{3}BChl *a* and ^{3}BChl *b* in MTHF are shown in Fig. 6.3a and 6.3b, respectively. The width and rhombicity of the triplet EPR spectrum are determined by the zero field splitting parameters (ZFS) *D* and *E*.[18, 50] The spectra are similar and are characterized by the ZFS parameters, $D = 0.0231(4)$ cm^{-1} and $E = 0.0061(4)$ cm^{-1} for ^{3}BChl *a* and $D = 0.0222(4)$ cm^{-1} and $E = 0.0053(4)$ cm^{-1} for ^{3}BChl *b*. The parameters are the same as those obtained by other groups.[18, 46] The slightly smaller *D* parameter for BChl *b* indicates a larger effective electron-electron distance and can be rationalized on the basis of an extended π system owing to the ethylidene group. The polarization patterns of the triplet EPR spectra of ^{3}BChl *a* and ^{3}BChl *b* are both EEEAAA (E = emissive, A = absorptive). The polarization pattern remains the same in the temperature range from 10 to 50 K and the EPR signal decreases at higher temperature. The enumeration of the canonical orientations (X, Y, Z) is chosen such that $|D_{ZZ}| > |D_{YY}| > |D_{XX}|$. The amplitude of the EPR signal at the low-field and high-field (Z, Y) sides of the spectrum is slightly larger for BChl *b*, whereas the signal is

largest in the center (X) of the EPR spectrum for BChl *a*. The g-tensor anisotropy is unresolved at 34 GHz.

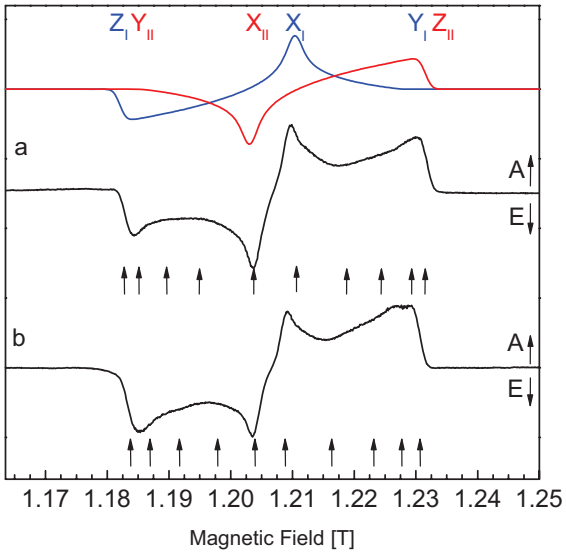

Figure 6.3. ESE-detected triplet EPR spectra at Q-band of (a) ^{3}BChl *a* and (b) ^{3}BChl *b*, both in MTHF, T = 10 K. The spectrum of ^{3}BChl *b* is moved by +7 mT to align the two spectra. The magnetic field settings of the canonical orientations (X, Y, Z) as well as the field positions, where ENDOR spectra are recorded (arrows), are indicated in the figure. A = absorption, E = emission. For bacteriochlorophyll *a*, a simulation with separate 0 → 1 (blue) and 0 → $^-$1 (red) transitions is shown.

ENDOR

As discussed in the Theory section, the signs of hyperfine couplings were directly obtained from the ENDOR spectrum with respect to that of *D* as follows. In practice, the X and Z canonical orientations dominate the EPR spectra of ^{3}BChl *a* and ^{3}BChl *b* (*cf.* Fig. 6.3). For $D > 0$[18, 44] and taking into account the change of the EPR signals of transitions $0 \leftrightarrow 1$ (I) and $0 \leftrightarrow -1$ (II), see Fig. 6.3, the bands in the spectra have been assigned to either transition I or II.[18, 46] The signs then follow from Eq (5) and they are indicated in Fig 6.4.

Fig. 6.4A shows orientation-selected Davies ENDOR spectra of ^{3}BChl *a* recorded at the canonical orientations and some intermediate magnetic field settings. The spectra for ^{3}BChl *b* are shown in Fig. 6.4B. The frequency axis is displayed as a $\nu_{ENDOR} - \nu_n(^1H)$ axis, such that the narrow signal corresponding to $\nu_n(^1\mathrm{H})$ has been set to 0 MHz to facilitate the determination and comparison of hyperfine coupling constants. Up to three bands with negative couplings and four bands with positive couplings are discerned. As is seen, the

ENDOR spectra for ^{3}BChl *a* and ^{3}BChl *b* are largely similar. Differences are also present; in the ENDOR spectra of ^{3}BChl *b* one additional band with negative coupling, enumerated as

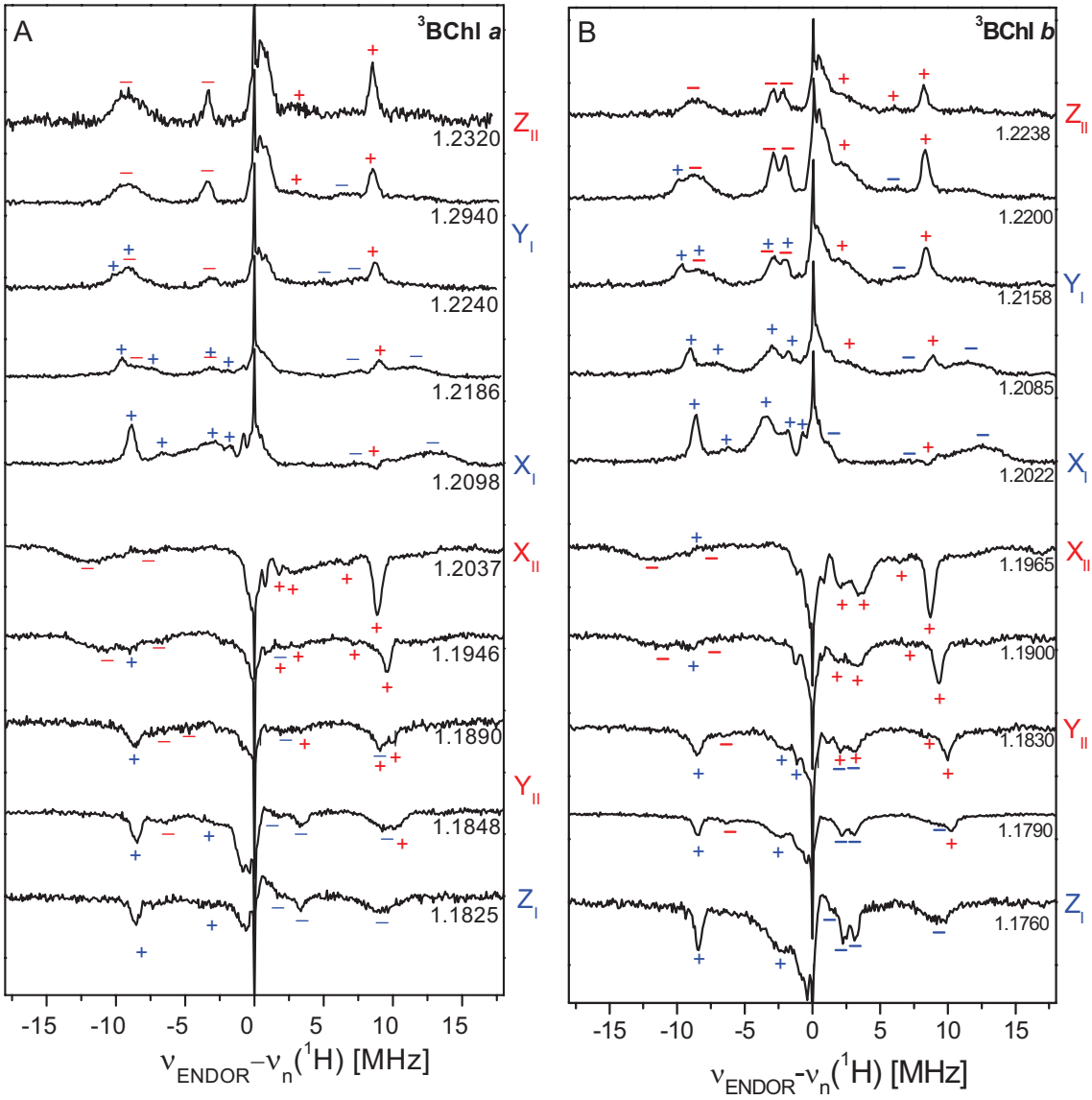

Figure 6.4. Triplet Davies ENDOR spectra of (A) ^{3}BChl *a* and (B) ^{3}BChl *b* at ν_{mw} = 34 GHz, T = 10 K. The magnetic field settings (in Tesla) and signs of hyperfine coupling constants (+, –) from the 0 → 1 (blue) and 0 → –1 (red) transitions are included in the figure. In most ENDOR spectra, less than six bands are observed. The spectra are shown relative to the free proton frequency $\nu_n(^1H)$.

band [3], is observed. The narrow band [6] is present only in the ENDOR spectra for ^{3}BChl *b* whereas the broad and less pronounced band [5] is only present in the ENDOR spectra of ^{3}BChl *a*. The frequencies of the observed signals vary with magnetic field setting.

An overview of the variation of the bands in the ENDOR spectra for ^{3}BChl *a* and ^{3}BChl *b* with the magnetic field setting is shown in the field-frequency plot in Fig. 6.5. The hyperfine coupling constants read at the canonical orientations are collected in table 6.1 for each band. A complete data set is given in Appendix B. Isotropic hyperfine coupling constants are presented in tables 6.2 and 6.3.

Table 6.1. Hyperfine couplings constants [MHz] of signals observed at the canonical orientations of the orientation-selected Davies ENDOR spectra of ^{3}BChl *a* and ^{3}BChl *b*. The uncertainties in hyperfine coupling constants are about 0.1 MHz. The signals are grouped into 8 bands that could be traced over a large part of the magnetic field range spanned by the EPR spectrum.

	EPR position					
BChl *a*	Z_I	X_I	Y_I	Z_{II}	X_{II}	Y_{II}
1	–9.2	–12.6/–7.2	–6.3	–9.3	–12.1/–7.5	–6.4
2	–3.4		–5.2	–3.4		–5.2
4		+1.7			+1.7	
5	+3.4	+3.0		+3.3	+3.2	
7		+6.7	+9.0	+6.7	+9.0	
8	+8.5	+8.9	+10.2	+8.5	+8.9	+10.3
BChl *b*						
1	–9.5	–12.5/–7.1	–6.1	–8.8	–12.1/–7.6	–6.3
2	–3.1			–3.0		
3	–2.3	–2.4		–2.1		
4		+1.8	+2.0		+1.9	+2.0
6	+2.5	+3.5	+2.9	+2.4	+3.5	+3.1
7		+6.4	+8.5	+6.0	+6.5	+8.4
8	+8.4	+8.6	+10.0	+8.3	+8.7	+10.2

Bands [1] and [8] are observable both for ^{3}BChl *a* and ^{3}BChl *b* at almost all measured field settings, except in center of EPR spectrum and at the Y-canonical orientation, where the intensity of EPR transition approaches zero (see simulation in Fig. 6.3a); additionally in BChl *a* bands [2], [5] and [7] and in BChl *b* bands [2], [3], [6] and [7] are visible at most measured fields. Band [4] is only visible in a few ENDOR spectra and a complete field-frequency pattern is lacking. For some signals near $\nu_n(^1\mathrm{H})$ in the ENDOR spectra of ^{3}BChl *a* and ^{3}BChl *b*, no field-frequency pattern could be determined. Band [1] displays an anisotropy with maximum coupling at a field setting that corresponds to the center of the EPR spectra (X_I, X_{II}). Bands [7] and [8] also have similar anisotropy and the hyperfine couplings are maximal at magnetic field settings that correspond to the Y orientations of the triplet EPR spectrum. Bands [4] and [5] in the ENDOR spectra of ^{3}BChl *a* and band [4] in the ENDOR spectra of

^{3}BChl *b* are almost constant at all measured field settings with variations of less than 0.5 MHz. Maximum couplings are observed at field settings that correspond to the Z orientations of the triplet EPR spectrum. Band [6] for ^{3}BChl *b* has maximum coupling constants at field settings that correspond to the X orientations of the triplet EPR spectrum.

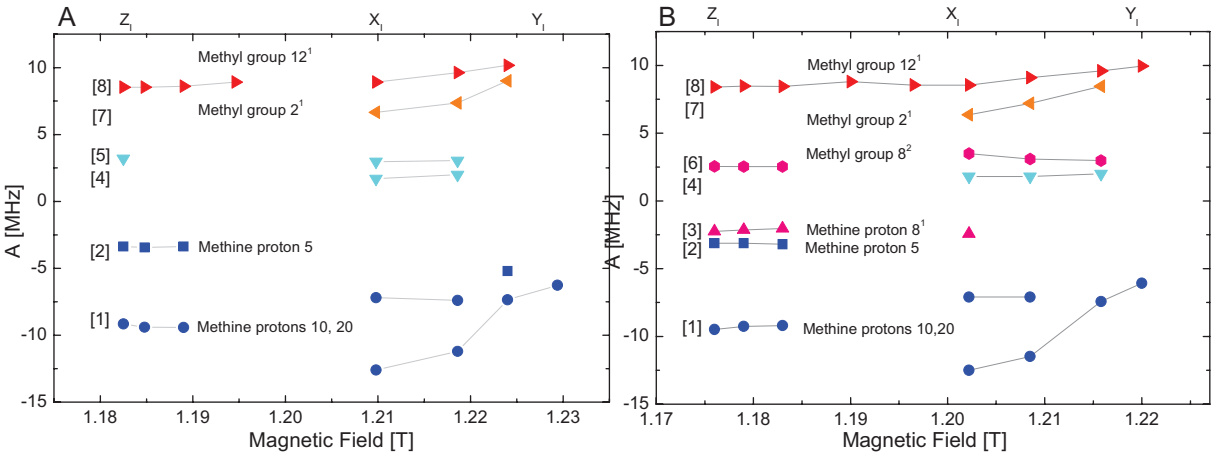

Figure 6.5. Field-frequency plot for bands [1] to [8] observed in the ENDOR measurements of (A) ^{3}BChl *a* and (B) ^{3}BChl *b*. A tentative assignment based on comparison with the DFT calculations is included in the figure.

DFT

The sets of orbitals (HOMO–1, HOMO, LUMO, LUMO+1) from the DFT calculations for ^{3}BChl *a* and ^{3}BChl *b* are shown in Fig. 6.6 and 6.7, respectively. The orbitals are similar to the ones used by Gouterman to explain the spectroscopic properties of porphyrins (see Fig. 6.2). The HOMO–1 (a_{2u}) approximately has a four-fold symmetry axis perpendicular to the bacteriochlorin plane, and large wavefunction coefficients are present at the nitrogen atoms and *meso* carbons. The HOMO is distributed evenly over the four pyrrole rings and is very similar to the a_{1u} Gouterman orbital shown in Fig. 6.2. For BChl *b*, significant electron density is found at carbon atom 8^1 of the ethylidene group, which gives rise to observable hyperfine couplings for methyl group 8^2 and methine proton 8^1. The LUMO of both BChls is essentially a Gouterman e_g orbital and only two nitrogen atoms carry electron density. The LUMO+1 differs between ^{3}BChl *a* and ^{3}BChl *b*. The second e_g Gouterman orbital can still be clearly recognized in both cases, but the orbital for BChl *b* is more localized near pyrrole ring B than that for BChl *a*.

In the first set of triplet calculations, one electron is present in the HOMO and one in the LUMO. The calculated ^{1}H isotropic hyperfine coupling constants are included in tables

6.2 and 6.3 (DFT I). For a methyl group, an average isotropic hyperfine coupling constant is given under the assumption that the methyl group can rotate freely. As expected, methyl

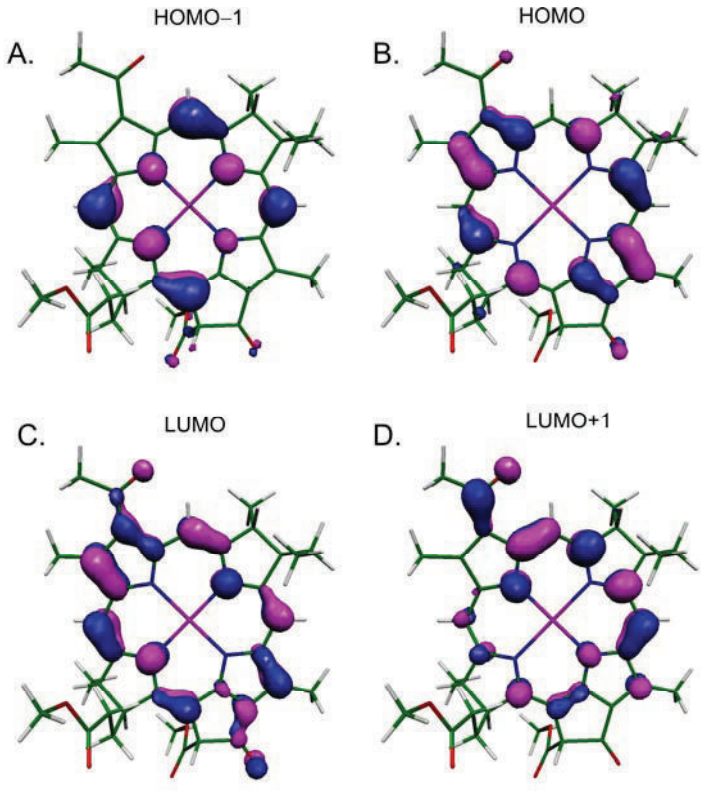

Figure 6.6. (A) HOMO–1, (B) HOMO, (C) LUMO and (D) LUMO+1 molecular orbitals from the DFT calculation of ^{3}BChl *a*.

groups 2^1 and 12^1 have large hyperfine coupling constants (for ^{3}BChl *a* +7.9 MHz and +8.9 MHz, respectively), which are derived from both the HOMO and LUMO. The β protons 7, 8, 17, 18 have large isotropic hyperfine coupling constants (+7.8 MHz, +8.5 MHz, +5.1 MHz and +4.3 MHz, respectively) which also stem from both the HOMO and LUMO. The methine protons are characterized by negative hyperfine couplings.[48] They stem from LUMO-based spin density at the *meso* carbon atoms and amount to –4.0, –5.4 and –4.8 MHz for ^{3}BChl *a*. Similar hyperfine couplings constants were obtained in calculations for ^{3}BChl *b* (table 6.3). The methyl groups 2^1 and 12^1 have hyperfine coupling constants +7.6 MHz and +8.3 MHz, β protons 7, 17, 18 have isotropic hyperfine coupling constants +6.6 MHz, +3.3 MHz and +3.1 MHz, respectively. The methine protons are characterized by calculated isotropic hyperfine couplings –4.0 MHz, –6.0 MHz, and –4.6 MHz. Additionally, the hyperfine interaction at methine proton 8^1 and methyl group 8^2 amounts to –5.9 MHz and +5.7 MHz owing to density at C(8^1) in the HOMO.

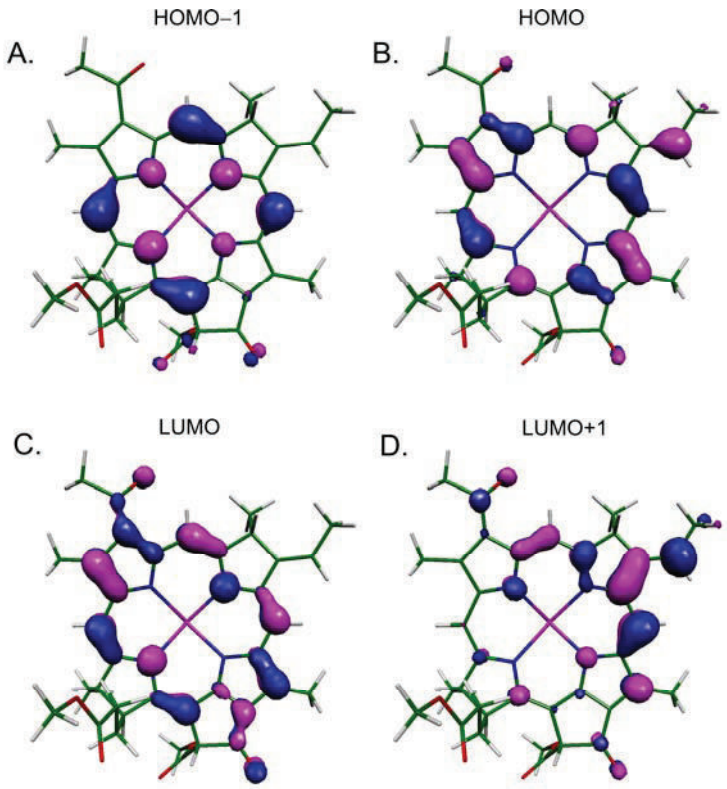

Figure 6.7. (A) HOMO−1, (B) HOMO, (C) LUMO and (D) LUMO+1 molecular orbitals from the DFT calculation of ^{3}BChl *b*.

Additional to these calculations, a triplet excitation derived to 50% by a promotion of an electron from HOMO to LUMO and to 50% from HOMO−1 to LUMO has been considered. The electron spin density on the *meso* carbons and the hyperfine coupling constants of β protons and methyl group protons have been determined from calculations with pure HOMO → LUMO and HOMO−1 → LUMO excitation according to equations (1) and (2) of the Theory section. A correct description of spin polarization, responsible for the isotropic hyperfine interaction of the methine protons, would require re-optimization of polarization effects in lower-lying doubly occupied orbitals. Re-optimization of these effects is technically not feasible; it would also re-optimize the frontier orbitals and bring them back to a HOMO → LUMO excitation. The isotropic hyperfine interaction at the methine protons has therefore been calculated by McConnell's relation (3) using a spin-unpolarized wavefunction (see Theory section for details).

The isotropic hyperfine coupling constants for this set of calculations are included in tables 6.2 and 6.3 (DFT II). As compared to the previous set, the triplet state is now to 25% derived from the HOMO−1. The spin density at the *meso* carbons has increased owing to the

presence of density at these atoms in the HOMO–1 and the isotropic hyperfine interaction of

Table 6.2. Isotropic hyperfine couplings [MHz] of BChl *a* from radical cation[28] (a_c) and anion[31] (a_a) ENDOR measurements and their average value and isotropic values from ENDOR experiments of ^{3}BChl *a* (a_T). The error margin for a_T is ±0.3 MHz. Also included are calculated isotropic couplings from DFT calculations with HOMO → LUMO excitation (I) and 50% HOMO–1 → LUMO and 50% HOMO → LUMO excitation (II). The hyperfine coupling constants for the methine protons in case of DFT I and II are calculated using McConnell's equation (3). The enumeration of the bands observed in the ENDOR spectra for ^{3}BChl *a* is included in parentheses.

	Experiment				Theory	
	a_c	a_a	½(a_c + a_a)	a_T	DFT I	DFT II
Methine protons						
5	+2.35	–9.65	–3.65	–4.3 [2]	–4.0	–8.2
10	+1.30	–6.91	–2.81	–9.3 [1]	–5.4	–8.0
20	+1.30	–6.23	–2.47		–4.8	–8.2
Methyl groups						
2^1	+4.93	+7.63	+6.28	+7.7 [7]	+7.9	+6.5
12^1	+9.62	+9.19	+9.41	+9.2 [8]	+8.9	+7.1
7^1					+0.2	+0.4
18^1					+0.4	+0.4
β protons						
7	+13.47	+0.95	+7.21	+1.8 [4]	+7.8	+5.8
8	+16.35	+0.95	+8.65	+3.2 [5]	+8.5	+5.3
17	+13.11	+0.95	+7.03		+5.1	+3.4
18	+11.76	+0.95	+6.36		+4.3	+3.0

the methine protons has increased proportionally by almost a factor of 2. The positive couplings of the methyl groups and β protons decreased somewhat, but still remain large owing to the fact that these couplings derive in part from LUMO-based spin density. The hyperfine coupling constants of the β protons have decreased systematically, since the HOMO–1 does not have significant density near any of these protons. A similar behaviour of hyperfine coupling constants was observed in the calculations for ^{3}BChl *b*. The couplings of the methyl 8^2 and methine 8^1 protons decrease owing to the presence of only 25% HOMO character instead of 50% HOMO character in the triplet state.

Lastly, the effect of bending of the bacteriochlorophyll plane was investigated. For this purpose, a large set of calculations has been performed, whereby each pyrrole ring is either tilted by plus or minus 5 or 10 degrees from the equatorial plane. All possible combinations of bending of one, two, three or all four pyrrole rings have been considered and average isotropic

hyperfine constants $\langle a_{iso} \rangle$ and standard deviations σ_d have been calculated. The

Table 6.3. Isotropic hyperfine couplings [MHz] of BChl *b* from radical cation[23] (a_c) and anion[63] (a_a) ENDOR measurements and their average value, and isotropic values from ENDOR experiments of ^{3}BChl *b* (a_T). The error margin for a_T is ±0.3 MHz. Also included are calculated isotropic couplings from DFT calculations with HOMO → LUMO (I) excitation and 50% HOMO−1 → LUMO and 50% HOMO → LUMO excitation (II). The hyperfine coupling constants for the methine protons in case of DFT I and II are calculated using McConnell's equation (3). The enumeration of the bands observed in the ENDOR spectra of ^{3}BChl *b* is included in parentheses.

	Experiment				Theory	
	a_c	a_a	$\frac{1}{2}(a_c + a_a)$	a_T	DFT I	DFT II
Methine protons						
5	+2.50	–7.28	–2.39	–3.0 [2]	–4.0	–8.1
10	+1.20	–6.72	–2.76	–9.2 [1]	–6.0	–8.3
20	+1.20	–5.32	–2.06		–4.6	–7.7
Methyl groups						
2^1	+4.70	+8.68	+6.69	+7.0 [7]	+7.6	+6.3
12^1	+8.95	+8.68	+8.82	+9.0 [8]	+8.3	+6.7
7^1					+0.2	+0.3
18^1					+0.3	+0.1
β protons						
7	+12.45				+6.6	+4.2
17	+11.60			+1.9 [4]	+3.3	+2.3
18	+10.55				+3.1	+2.1
Ethylidene group						
Methine 8	–0.40			–2.1 [3]	–5.9	–3.3
Methyl 8^2	+9.70			+3.0 [6]	+5.7	+4.0

value of $2\sigma_d$ can be considered a theoretical linewidth caused by bending, associated with each hyperfine coupling constant. The numbers are included in table 6.4 for a triplet state derived from a (50% HOMO−1, 50% HOMO) → LUMO excitation. The average isotropic hyperfine coupling constants $\langle a_{iso} \rangle$ are slightly smaller than those calculated for a geometry-optimized BChl molecule. The standard deviation σ_d amounts to 0.2-0.4 MHz for a tilt of 5 degrees and 0.4-0.9 MHz for a tilt of 10 degrees. Noteworthy is that the value of the theoretical linewidth $2\sigma_d$ can vary by up to a factor of 2 and that the β protons 7 and 8 have larger linewidths than any other proton. The value of $2\sigma_d$ for a tilt angle of 5 degrees is equal to the linewidth of the narrow bands in the ENDOR spectra, thus suggesting an upper limit of 5 degrees for bending of the bacteriochlorin macrocycle.

Table 6.4. Average value $\langle a_{iso} \rangle$ and standard deviation σ_a (linewidth) of the isotropic hyperfine couplings constants [MHz] for the methyl groups and β protons upon bending by 5 degrees or 10 degrees of the porphyrin plane and upon 50% HOMO–1 → LUMO and 50% HOMO → LUMO excitation.

	BChl *a*				BChl *b*			
	5 deg		10 deg		5 deg		10 deg	
	$\langle a_{iso} \rangle$	σ_a	$\langle a_{iso} \rangle$	σ_a	$\langle a_{iso} \rangle$	σ_a	$\langle a_{iso} \rangle$	σ_a
Methyl groups								
2^1	6.4	0.3	6.7	0.5	6.1	0.3	6.1	0.4
12^1	6.8	0.3	6.9	0.5	6.4	0.3	6.5	0.6
7^1	0.5	0.2	0.9	0.6	0.5	0.2	0.6	0.4
18^1	0.6	0.3	0.9	0.7	0.4	0.3	0.7	0.6
8^2					3.9	0.5	3.5	0.9
β protons								
7	5.4	0.4	5.0	0.7	3.7	0.5	3.2	0.7
8	5.3	0.4	4.8	0.8				
17	3.2	0.2	3.0	0.4	2.2	0.2	2.1	0.3

6.5 Discussion

First the observed signals obtained from ENDOR spectroscopy for the radical cation, anion and triplet states of BChl *a* will be compared on a purely experimental basis. Then, the calculated hyperfine coupling constants are compared with the experimentally obtained ones, and the electronic structure of the triplet state in terms of HOMO → LUMO and HOMO–1 → LUMO excitation is deduced. The anisotropy of the zero-field tensor known already from magnetophotoselection studies[45] is then compared with the observed anisotropy of the ENDOR signals, and lastly, a tentative assignment of the signals observed in the triplet ENDOR spectra to protons of the bacteriochlorin macrocycle is presented.

Comparison of ENDOR experiments for $BChl^{\bullet+}$, $BChl^{\bullet-}$ and ^3BChl

ENDOR measurements performed for the BChl *a* radical cation and anion and an assignment of signals to protons of the bacteriochlorin macrocycle have been presented elsewhere.[25, 27-29, 31] As compared to the neutral molecule, an unpaired electron is present in the HOMO for the radical cation, and in the LUMO for the radical anion. For the triplet state, in the simplest approximation of HOMO → LUMO excitation, an unpaired electron would be present in the HOMO as well as in the LUMO. The normalized π-spin electron density in the

triplet state ρ_T would be given as the average of the electron spin density of cation (ρ_{cation}) and anion (ρ_{anion}) radicals [46, 48]

$$\rho_T = \frac{1}{2}[\rho_{cation} + \rho_{anion}] \quad (6)$$

Since the isotropic hyperfine couplings constants are proportional to the spin density,[48, 64] the same relation is also valid for isotropic hyperfine coupling constants for the case where the spin polarization is neglected

$$a_T = \frac{1}{2}[a_{cation} + a_{anion}] \quad (7)$$

As opposed to the simple theory described by equation (6), a significant discrepancy is observed between the experimental mean of the cation and anion couplings for the three methine protons included in tables 6.2 and 6.3 and the couplings in the triplet state, which differ by more than a factor of 2. The isotropic couplings for the methine protons in the triplet state and the anion state are essentially equal. Of the methyl groups for BChl *a*, those at positions 2^1 and 12^1 have the largest average cation and anion coupling of +6.28 MHz and +9.40 MHz, respectively. The largest positive couplings observed in the triplet ENDOR spectra (see Fig. 6.5) are +7.7 MHz and +9.2 MHz. These sets agree reasonably well. The β protons with the largest couplings are those at positions 7, 8, 17 and 18. The average couplings for the cation and anion are typically +7 MHz and may depend on the orientation of the substituent group that contains the proton. Such couplings are not observed for the triplet state. Rather, signals with couplings on the order of +1.9 MHz and +3.2 MHz are observed.

The mismatch between several of the isotropic hyperfine couplings of the triplet state and the average of radical cation and anion has been observed before[46] and indicates that equations (6) and (7) are not obeyed by BChl *a* and *b*. Already from these experimental considerations, it becomes clear that the bacteriochlorophyll triplet state is not adequately described by a HOMO → LUMO excitation involving only the Gouterman a_{1u} and e_g orbitals.

DFT calculations for ^{3}BChl

DFT calculations have been performed complementary to the ENDOR experiments in order to gain deeper insight into the electronic structure. The calculated isotropic hyperfine couplings for BChl *a* and BChl *b* in the triplet state, included in the "DFT I" column of tables 6.2 and 6.3, are in good agreement with the average couplings for the radical cation and anion for all protons. Thus, the DFT calculations provide an accurate description of the HOMO and LUMO orbitals probed by the ENDOR experiments of the radical cation and anion. However,

the calculated couplings do not agree with the observed couplings of the methine protons in the triplet state, which differ by about a factor of two.

Obviously, a HOMO → LUMO excitation results in too little spin density at the *meso* carbons, and thereby too small hyperfine couplings for the methine protons. Upon inspection of the orbitals for BChl *a* and BChl *b* (see Fig. 6.2, 6.6 and 6.7), the HOMO−1 orbital does have large wavefunction coefficients at the *meso* carbons. The energy difference between HOMO and HOMO−1 is only 4000 cm^{-1}, calculated from the UV/VIS spectrum.[32] Since the energy gap is small and equivalent to a weak hydrogen bond of about 3 kcal/mol,[65] the HOMO−1 may actually significantly contribute to the triplet wavefunction, *e.g.*, through configurational mixing, bending of the bacteriochlorin macrocycle or fluctuations of the hydrogen bonding network.

The DFT calculations with 50% HOMO → LUMO and 50% HOMO−1 → LUMO excitation presented in the column DFT II of tables 6.2 and 6.3 improve the agreement and minimize the observed discrepancies between theory and experiment. Since the HOMO−1 has significant density on the *meso* carbons, the isotropic hyperfine coupling constant of the three methine protons increases to about −8 MHz. The hyperfine couplings of the methine protons from the triplet ENDOR experiments and theoretical calculations for the triplet state are then in good agreement. For the methyl groups, the agreement can be considered good given the accuracy of the DFT method.[62] The couplings of β protons 7, 8, 17 and 18 decrease and also come closer to the experimental values. Note that the couplings of the β protons are more susceptible to bending of the bacteriochlorin macrocycle than the methyl and methine protons and it is therefore doubtful whether they are observable in the ENDOR spectra (*vide infra*). For the ethylidene group of BChl *b* (see table 6.3), the isotropic hyperfine coupling of methine proton 8^1 has become smaller in magnitude from −5.9 MHz to −3.3 MHz, which also brings it close to the experimental value of −2.1 MHz. The calculated coupling for the methyl group 8^2 decreases from +5.7 MHz to +4.0 MHz, now also close to the measured value of +3.0 MHz.

Bending of the bacteriochlorin macrocycle has been theoretically investigated with a large set of calculations to obtain average hyperfine coupling constants and standard deviations. The average hyperfine coupling constants are found to be slightly smaller than those taken from a DFT calculation with optimized structure. The standard deviation for a bending of 5 degrees amounts to 0.4 MHz and for 10 degrees bending to 0.9 MHz. Comparing the theoretical linewidth (double value of standard deviation) with the linewidth

of the resolved bands in the ENDOR spectra, it can be concluded that bending of the bacteriochlorin macrocycle in BChl *a* and BChl *b* can occur to about 5 degrees.

Orientation of the zero-field tensor and assignment of the ^{1}H hyperfine tensors

Knowledge of the directions of the principal axes of the ZFS tensor is required for analysis of the anisotropy of the hyperfine couplings observed in the orientation-selected ENDOR spectra and the field-frequency plot (Fig. 6.5). Unfortunately, the methods available for the calculation of ZFS parameters, though reliable for the calculation of *D*, still have a significant inaccuracy for *E* and the directions of the associated in-plane principal axes.[66, 67] Experimentally, the directions of the principal ZFS axes have been determined by magnetophotoselection measurements for ^{3}BChl *a*.[45] The principal directions of the ZFS tensor are shown in Fig. 6.8, the principal directions of the hyperfine tensor for the methyl group protons and the methine protons taken from DFT calculations are also depicted.

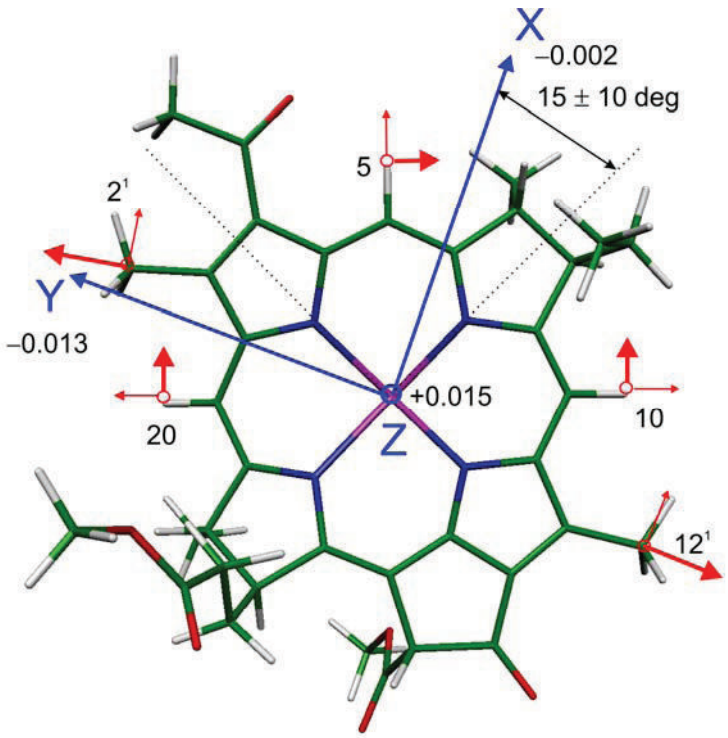

Figure 6.8. Principal values [cm^{-1}] and orientation of the principal axes of the ZFS tensor for ^{3}BChl *a* taken from magnetophotoselection studies.[45] The orientation of the principal axes of the hyperfine tensor is shown for the methyl groups 2^{1} and 12^{1} and the three methine protons in red. The directions of maximum hyperfine coupling are indicated in bold.

The orientation-selective ENDOR studies allow a determination of the principal directions of the hyperfine tensor of the protons with respect to the zero field splitting tensor.

It has to be stressed that the present dataset is not complete enough to come to a full assignment of all observed signals. However, the observed field-dependence of the majority of bands is still sufficient for an assignment to molecular positions; they also support an electronic structure that is described by a mixed HOMO → LUMO and HOMO−1 → LUMO character.

For methyl groups 2^1 and 12^1, the direction that corresponds to the maximum absolute hyperfine interaction points along the C(pyrrole)-C(methyl) bond. This direction is almost parallel to the Y principal ZFS axis (with principal value −0.013 cm^{-1}) and thus the maximum coupling for the methyl groups 2^1 and 12^1 is expected to occur close to the Y direction. Bands [7] and [8] are assigned to methyl groups 2^1 and 12^1, respectively. For the methine protons, the maximum coupling is expected tangential to the bacteriochlorin macrocycle and the smallest coupling is along the C-H direction (see Fig. 6.8).[68]

For protons 10 and 20, this direction is closest to the principal ZFS axis with the smallest absolute eigenvalue (X, −0.002 cm^{-1}), which corresponds to the canonical orientation in the center of EPR spectrum. For methine proton 5, this direction would be closest to the Y principal axis. The broad band [1] in the ENDOR spectra and methine protons 10 and 20 in the DFT calculations have similar hyperfine couplings and the field-frequency plot indeed shows a maximum absolute coupling for the center (X) of the EPR spectrum. We thus assign band [1] to methine protons 10 and 20.

Band [5] in the ENDOR spectra of ^{3}BChl *a* is broad. In the ENDOR spectra of ^{3}BChl *b* band [5] is lacking and another band, [6], with a different anisotropy is observed. Moreover, band [3], which has a pronounced negative isotropic coupling of −2.5 MHz is observable only for ^{3}BChl *b*. These differences between the observed signals of ^{3}BChl *a* and ^{3}BChl *b* are in-line with the structural differences observed for pyrrole ring B (see Fig. 6.1). Band [6] acquires its maximum hyperfine coupling at the X canonical orientation, in agreement with what is expected for methyl group 8^2 when the directions of the principal axes of the ZFS tensor are considered. We thus assign bands [5] to β proton 8 in ^{3}BChl *a*, and bands [3] and [6] to the methine proton 8^1 and methyl group 8^2 in ^{3}BChl *b*.

Bands [4] does not display a strong anisotropy in the field-frequency plot, and their isotropic hyperfine interaction is small. This band probably stems from a proton that is located further away from the bulk spin density and an assignment is not feasible at present.

A band with a large negative hyperfine coupling, which would correspond to methine proton 5, was not observed for either BChl *a* or BChl *b*. It is conceivable that the signals of this proton may belong to band [2] or are of low intensity in this region of the spectrum. Since

it is expected that the signals of this proton have a maximum absolute hyperfine coupling near Y, as opposed to those of protons 10 and 20, measurements on single crystals would be necessary to obtain increased resolution in this region of the spectrum.

6.6 Conclusion

In this work a systematic study of the triplet state of bacteriochlorophyll *a* and bacteriochlorophyll *b* is presented. Using ENDOR spectroscopy at 34 GHz with laser excitation on frozen solutions and complementary DFT calculations, a set of proton hyperfine couplings has been obtained and assigned to protons of the bacteriochlorin macrocycle. The electron spin density distribution in the triplet state for BChl *a* and BChl *b* is found to be similar. Spectral differences are present for position 8, where an ethyl group is present in BChl *a* and an ethylidene group in BChl *b*. One additional signal with negative coupling and one with positive coupling have been observed for ^{3}BChl *b*, which indicates the presence of electron spin density on the carbon atom 8^1. The additional negative hyperfine coupling is assigned to methine proton at 8^1 and the positive hyperfine coupling to methyl group at 8^2.

Bending of the bacteriochlorin macrocycle has been investigated theoretically. These calculations indicate a change in the hyperfine couplings of the methyl and β protons of about ±0.4 MHz for an angle of 5 degrees and ±0.8 MHz for 10 degrees. The value for tilts of 5 degrees is about equal to the linewidth of the narrow ENDOR signals, thus indicating an upper limit for the bending of the bacteriochlorin macrocycle of about 5 degrees.

Based on a comparison of the experimental and calculated hyperfine couplings of the triplet state with those for the radical cation and anion,[28, 31] the bacteriochlorophyll triplet was found to result not from a simple HOMO → LUMO excitation. Rather, a combination of HOMO → LUMO and HOMO–1 → LUMO excitation is required to satisfactorily explain all observed hyperfine couplings. Moreover, this electronic configuration is compatible with the experimentally determined directions of the principal axes of the zero-field-splitting tensor from magnetophotoselection studies.[45]

Knowledge of the triplet electron spin density distribution of monomeric ^{3}BChl is necessary for an understanding of the triplet state of the "special pair" P in bacterial reaction centers.[69] P is a dimer of bacteriochlorophylls and acts as a primary donor in the electron transfer process. Triplet ENDOR methodology is the only experimental method that allows a characterization of the electron spin density distribution in both frontier orbitals (HOMO *and*

LUMO). Since the LUMO orbital of P is the orbital from which photosynthetic charge separation starts, and since the LUMO orbital is not nearly degenerate like the HOMO/HOMO−1 pair, the LUMO orbital of P* in the singlet state can be accurately probed by ENDOR measurements of ^{3}P. However, in order to fully interpret spectra of the BChl dimer, it is necessary to first investigate the BChl monomer.

Knowledge of the LUMO orbital on an atomic level[70] is necessary to understand the primary steps of charge separation, *i.e.* upon computation of forward electron transfer matrix elements associated with the excited singlet state of P and its acceptor.[33] Moreover, knowledge of the electronic structure of the triplet states of bacteriochlorophylls might lead to a more detailed understanding of the quenching mechanism of reactive triplet states of the donor *via* B-branch triplet-triplet energy transfer to a nearby carotenoid.[71-73] The triplet state of the primary donor - both in *Rb. sphaeroides* and *Bl. viridis* - has been reinvestigated in our laboratories; the analysis of these data will be presented in a forthcoming publication.

6.7 References

(1) Scheer, H. Structure and occurence of chlorophylls. In *The Chlorophylls*; Scheer, H., Ed.;CRC Press: Boca Raton, 1991; pp 4-31.

(2) Maqueo Chew, A. G., Bryant, D. A. (2007) Chlorophyll biosynthesis in bacteria: The origins of structural and functional diversity, *Annu. Rev. Microbiol., 61*, 113-129.

(3) Allen, J. P., Feher, G., Yeates, T. O., Komiya, H., Rees, D. C. (1987) Structure of the Reaction Center from *Rhodobacter sphaeroides* R-26 - the Cofactors, *Proc. Natl. Acad. Sci. USA, 84*, 5730-5734.

(4) Yeates, T. O., Komiya, H., Chirino, A., Rees, D. C., Allen, J. P., Feher, G. (1988) Structure of the Reaction Center from *Rhodobacter sphaeroides* R-26 and 2.4.1-Protein-Cofactor (Bacteriochlorophyll, Bacteriopheophytin, and Carotenoid) Interactions, *Proc. Natl. Acad. Sci. USA, 85*, 7993-7997.

(5) Feher, G., Allen, J. P., Okamura, M. Y., Rees, D. C. (1989) Structure and Function of Bacterial Photosynthetic Reaction Centers, *Nature, 339*, 111-116.

(6) Amesz, J. (1995) The Heliobacteria, A New Group of Photosynthetic Bacteria, *J. Photochem. Photobiol. B, 30*, 89-96.

(7) Michel, H. (1982) 3-Dimensional Crystals of A Membrane-Protein Complex - the Photosynthetic Reaction Center from *Rhodopseudomonas viridis*, *J. Mol. Biol., 158*, 567-572.

(8) Deisenhofer, J., Epp, O., Miki, K., Huber, R., Michel, H. (1984) X-Ray Structure-Analysis of A Membrane-Protein Complex - Electron-Density Map at 3A Resolution and A Model of the Chromophores of the Photosynthetic Reaction Center from *Rhodopseudomonas viridis*, *J. Mol. Biol., 180*, 385-398.

(9) Deisenhofer, J., Epp, O., Miki, K., Huber, R., Michel, H. (1985) Structure of the Protein Subunits in the Photosynthetic Reaction Center of Rhodopseudomonas-Viridis at 3A Resolution, *Nature, 318*, 618-624.

(10) Cogdell, R. J., Gall, A., Kohler, J. (2006) The architecture and function of the light-harvesting apparatus of purple bacteria: from single molecules to in vivo membranes, *Q. Rev. Biophys., 39*, 227-324.

(11) Carbonera, D., Burzomato, V., Bordignon, E., Giacometti, G., Agostini, G., Heathcote, P., Leech, H. K. (2002) Fluorescence and absorption detected magnetic resonance of membranes from the green sulfur bacterium Chlorobium limicola. Full assignment of detected triplet states, *J. Phys. Chem. B, 106*, 7560-7568.

(12) Kirmaier, C., Holten, D., Parson, W. W. (1985) Picosecond-Photodichroism Studies of the Transient States in Rhodopseudomonas-Sphaeroides Reaction Centers at 5-K - Effects of Electron-Transfer on the 6 Bacteriochlorin Pigments, *Biochim. Biophys. Acta, 810*, 49-61.

(13) Kirmaier, C., Holten, D. (1987) Primary Photochemistry of Reaction Centers from the Photosynthetic Purple Bacteria, *Photosynth. Res., 13*, 225-260.

(14) Hoff, A. J., Deisenhofer, J. (1997) Photophysics of photosynthesis. Structure and spectroscopy of reaction centers of purple bacteria, *J. Phys. Rep., 287*, 2-247.

(15) Volk, M., Aumeier, G., Langenbacher, T., Feick, R., Ogrodnik, A., Michel-Beyerle, M. E. (1998) Energetics and mechanism of primary charge separation in bacterial photosynthesis. A comparative study on reaction centers of *Rhodobacter sphaeroides* and *Chloroflexus aurantiacus*, *J. Phys. Chem. B, 102*, 735-751.

(16) Thurnauer, M. C., Katz, J. J., Norris, J. R. (1975) Triplet-State in Bacterial Photosynthesis - Possible Mechanisms of Primary Photo-Act, *Proc. Natl. Acad. Sci. USA, 72*, 3270-3274.

(17) Hoff, A. J. (1976) Kinetics of Populating and Depopulating of Components of Photoinduced Triplet-State of Photosynthetic Bacteria *Rhodospirillum rubrum*, *Rhodopseudomonas spheroides* (Wild-Type), and Its Mutant R-26 As Measured by ESR in Zero-Field, *Biochim. Biophys. Acta, 440*, 765-771.

(18) Thurnauer, M. C. (1979) ESR study of the photoexcited triplet state in photosynthetic bacteria, *Rev. Chem. Int., 100*, 197-231.

(19) Hoff, A. J., Proskuryakov, I. I. (1985) Triplet Electron-Paramagnetic-Res Spectra of the Primary Electron-Donor in Bacterial Photosynthesis at Temperatures Between 15-K and 296-K, *Chem. Phys. Let., 115*, 303-310.

(20) Marchanka, A., Paddock, M., Lubitz, W., van Gastel, M. (2007) Low-temperature pulsed EPR study at 34 GHz of the Triplet states of the primary electron donor P-865 and the carotenoid in native and mutant bacterial reaction centers of Rhodobacter sphaeroides, *Biochemistry, 46*, 14782-14794.

(21) Michel-Beyerle, M. E., Plato, M., Deisenhofer, J., Michel, H., Bixon, M., Jortner, J. (1988) Unidirectionality of Charge Separation in Reaction Centers of Photosynthetic Bacteria, *Biochim. Biophys. Acta, 932*, 52-70.

(22) Angerhofer, A. Chlorophyll triplets and radical pairs. In *Chlorophylls*; Scheer, H., Ed.;CRC Press: Boca Raton FL, 1991; pp 945-991.

(23) Lubitz, W. EPR and ENDOR studies of chlorophyll cation and anion radicals. In *The Chlorophylls*; Scheer, H., Ed.;CRC Press: Boca Raton, 1991; pp 903-944.

(24) Budil, D. E., Thurnauer, M. C. (1991) The Chlorophyll Triplet-State As A Probe of Structure and Function in Photosynthesis, *Biochim. Biophys. Acta, 1057*, 1-41.

(25) Feher, G., Hoff, A. J., Isaacson, R. A., Ackerson, L. C. (1975) Endor Experiments on Chlorophyll and Bacteriochlorophyll Invitro and in Photosynthetic Unit, *Ann. N. Y. Acad. Sci., 244*, 239-259.

(26) Norris, J. R., Scheer, H., Katz, J. J. (1975) Models for Antenna and Reaction Center Chlorophylls, *Ann. N. Y. Acad. Sci., 244*, 260-280.

(27) Borg, D. C., Forman, A., Fajer, J. (1976) ESR and ENDOR Studies of Pi-Cation Radical of Bacteriochlorophyll, *J. Am. Chem. Soc., 98*, 6889-6893.

(28) Lubitz, W., Lendzian, F., Plato, M., Scheer, H., Möbius, K. (1997) The bacteriochlorophyll a cation radical revisited. An ENDOR and TRIPLE resonance study, *Appl. Magn. Reson, 13*, 531-551.

(29) Fajer, J., Borg, D. C., Forman, A., Dolphin, D., Felton, R. H. (1973) Anion Radical of Bacteriochlorophyll, *J. Am. Chem. Soc., 95*, 2739-2741.

(30) Okamura, M. Y., Isaacson, R. A., Feher, G. (1979) Spectroscopic and Kinetic-Properties of the Transient Intermediate Acceptor in Reaction Centers of Rhodopseudomonas-Sphaeroides, *Biochim. Biophys. Acta, 546*, 394-417.

(31) Lubitz, W., Lendzian, F., Möbius, K. (1981) N-14 and H-1 Electron Nuclear Multiple Resonance Experiments on Bacteriochlorophyll-A Anion Radicals in Solution, *Chem. Phys. Let., 81*, 235-241.

(32) Hoff, A. J.; Amesz, J. Visible absorption spectroscopy of chlorophylls. In *The Chlorophylls*; Scheer, H., Ed.;CRC Press: Boca Raton FL, 1991; pp 723-738.

(33) Plato, M., Möbius, K., Michel-Beyerle, M. E., Bixon, M., Jortner, J. (1988) Intermolecular Electronic Interactions in the Primary Charge Separation in Bacterial Photosynthesis, *J. Am. Chem. Soc., 110*, 7279-7285.

(34) Plato, M.; Möbius, K.; Lubitz, W.; Allen, J. P.; Feher, G. Magnetic resonance and molecular orbital studies of the primary donor states in bacterial reaction centers. In *Perspectives in Photosynthesis*; Jortner, J. and Pullman, Eds.;Kluwer Academic Publishers: 1990; pp 423-434.

(35) Longuet-Higgins, H. C., Rector, C. W., Platt, J. R. (1950) Molecular Orbital Calculations on Porphine and Tetrahydroporphine, *J. Chem. Phys., 18*, 1174-1181.

(36) Platt, J. Electronic structure and excitation of polyens and porphyrins. In *Radiation Biology*; Hollaender, A., Ed.;McGraw Hill: New York, 1956; pp 71-124.

(37) Gouterman, M. (1959) Study of the Effects of Substitution on the Absorption Spectra of Porphin, *J. Chem. Phys., 30*, 1139-1161.

(38) Gouterman, M. (1961) Spectra of Porphyrins, *J. Mol. Spectrosc., 6*, 138-163.

(39) Plato, M.; Lendzian, F.; Lubitz, W.; Tränkle, E.; Möbius, K. Molecular orbital studies on the primary donor P_{960} in reaction centers of *Rps*. *viridis*. In *The Photosynthetic Bacterial Reaction Center – Structure and Dynamics*; Breton, J. and Vermeglio, Eds.;Plenum Press: New York, 1988; pp 379-388.

(40) Plato, M.; Möbius, K.; Lubitz, W. Molecular orbitals calculations on chlorophyll radical ions. In *The Chlorophylls*; Scheer, H., Ed.;CRC Press: Boca Raton, 1991; pp 1015-1046.

(41) Plato, M.; Lendzian, F.; Lubitz, W.; Möbius, K. Molecular orbital study of electronic asymmetry in primary donors of bacterial reaction centers. In *The Photosynthetic Bacterial Reaction Center II*; Breton, J. and Vermeglio, Eds.;Plenum Press: New York, 1992; pp 109-118.

(42) Dauw, X. L. R., Poluektov, O. G., Warntjes, J. B. M., Bronsveld, M. V., Groenen, E. J. J. (1998) Triplet-state dynamics of C-70, *J. Phys. Chem. A, 102*, 3078-3082.

(43) Levanon, H., Scherz, A. (1975) Epr Study of Electron-Spin Polarization in Photoexcited Triplet-State of Chlorophyll-A and Chlorophyll-B, *Chem. Phys. Let., 31*, 119-124.

(44) Levanon, H., Norris, J. R. (1978) Photoexcited Triplet-State and Photosynthesis, *Chem. Rev., 78*, 185-198.

(45) Vrieze, J., Hoff, A. J. (1995) The Orientation of the Triplet Axes with Respect to the Optical-Transition Moments in (Bacterio)Chlorophylls, *Chem. Phys. Let., 237*, 493-501.

(46) Lendzian, F., Bittl, R., Lubitz, W. (1998) Pulsed ENDOR of the photoexcited triplet states of bacteriochlorophyll a and of the primary donor P-865 in reaction centers of *Rhodobacter sphaeroides* R-26, *Photosynth. Res., 55*, 189-197.

(47) Schadee, R. A., Schmidt, J., van der Waals, J. H. (1976) Intersystem Crossing Into A Superposition of Spin States - System Tetramethylpyrazine in Durene, *Chem. Phys. Let., 41*, 435-439.

(48) Carrington, A.; McLachlan, A.D. *Introduction to magnetic resonance;* Harper & Row; John Weatherhill Inc.: New York, Evanston, London, Tokyo, 1967.

(49) McConnell, H. M., Chesnut, D. B. (1958) Theory of Isotropic Hyperfine Interactions in Pi-Electron Radicals, *J. Chem. Phys., 28*, 107-117.

(50) Atherton, N. *Principles of Electron Spin Resonance;* Ellis Horwood PTR Prentice Hall: New York, 1993.

(51) Omata, T., Murata, N. (1983) Preparation of Chlorophyll-A, Chlorophyll-B and Bacteriochlorophyll-A by Column Chromatography with Deae-Sepharose Cl-6B and Sepharose Cl-6B, *Plant Cell Physiol., 24*, 1093-1100.

(52) Sinnecker, S., Reijerse, E., Neese, F., Lubitz, W. (2004) Hydrogen bond geometries from electron paramagnetic resonance and electron-nuclear double resonance parameters: Density functional study of quinone radical anion-solvent interactions, *J. Am. Chem. Soc., 126*, 3280-3290.

(53) Schweiger, A.; Jeschke, G. *Principles of Pulse Electron Paramagnetic Resonance;* Oxford University Press: 2001.

(54) Neese, F., Solomon, E. I. (1998) Calculation of zero-field splittings, g-values, and the relativistic nephelauxetic effect in transition metal complexes. Application to high-spin ferric complexes, *Inorg. Chem., 37*, 6568-6582.

(55) Neese, F. (2006) Importance of direct spin-spin coupling and spin-flip excitations for the zero-field splittings of transition metal complexes: A case study, *J. Am. Chem. Soc., 128*, 10213-10222.

(56) Neese, F. ORCA – An *ab initio,* Density Functional and Semiempirical program package, Version 2.6, revision 63, 2008, Universität Bonn., 2008.

(57) Ganyushin, D., Neese, F. (2006) First-principles calculations of zero-field splitting parameters, *J. Chem. Phys., 125*, 024103-

(58) Schafer, A., Horn, H., Ahlrichs, R. (1992) Fully Optimized Contracted Gaussian-Basis Sets for Atoms Li to Kr, *J. Chem. Phys., 97*, 2571-2577.

(59) Weigend, F., Haser, M. (1997) RI-MP2: first derivatives and global consistency, *Theor. Chem. Acc., 97*, 331-340.

(60) Roszak, A. W., McKendrick, K., Gardiner, A. T., Mitchell, I. A., Isaacs, N. W., Cogdell, R. J., Hashimoto, H., Frank, H. A. (2004) Protein regulation of carotenoid binding: Gatekeeper and locking amino acid residues in reaction centers of Rhodobacter sphaeroides, *Structure, 12*, 765-773.

(61) Frisch, M. J.; Trucks, G. W.; Schlegel, H. B.; Scuseria, G. E.; Robb, M. A.; Cheeseman, J. R.; Montgomery, Jr. J. A.; Vreven, T.; Kudin, K. N.; Burant, J. C.; Millam, J. M.; Iyengar, S. S.; Tomasi, J.; Barone, V.; Mennucci, B.; Cossi, M.; Scalmani, G.; Rega, N.; Petersson, G. A.; Nakatsuji, H.; Hada, M.; Ehara, M.; Toyota, K.; Fukuda, R.; Hasegawa, J.; Ishida, M.; Nakajima, T.; Honda, Y.; Kitao, O.; Nakai, H.; Klene, M.; Li, X.; Knox, J. E.; Hratchian, H. P.; Cross, J. B.; Bakken, V.; Adamo, C.; Jaramillo, J.; Gomperts, R.; Stratmann, R. E.; Yazyev, O.; Austin, A. J.; Cammi, R.; Pomelli, C.; Ochterski, J. W.; Ayala, P. Y.; Morokuma, K.; Voth, G. A.; Salvador, P.; Dannenberg, J. J.; Zakrzewski, V. G.; Dapprich, S.; Daniels, A. D.; Strain, M. C.; Farkas, O.; Malick, D. K.; Rabuck, A. D.; Raghavachari, K.; Foresman, J. B.; Ortiz, J. V.; Cui, Q.; Baboul, A. G.; Clifford, S.; Cioslowski, J.; Stefanov, B. B.; Liu, G.; Liashenko, A.; Piskorz, P.; Komaromi, I.; Martin, R. L.; Fox, D. J.; Keith, T.; Al-Laham, M. A.; Peng, C. Y.; Nanayakkara, A.; Challacombe, M.; Gill, P. M. W.; Johnson, B.; Chen, W.; Wong, M. W.; Gonzalez, C.; Pople, J. A. Gaussian 03, Gaussian Inc., 2004.

(62) Neese, F. (2003) Metal and ligand hyperfine couplings in transition metal complexes: The effect of spin-orbit coupling as studied by coupled perturbed Kohn-Sham theory, *J. Chem. Phys., 118*, 3939-3948.

(63) Davis, M. S., Forman, A., Hanson, L. K., Thornber, J. P., Fajer, J. (1979) Anion and Cation Radicals of Bacteriochlorophyll and Bacteriopheophytin-B - Their Role in the Primary Charge Separation of Rhodopseudomonas-Viridis, *J. Phys. Chem., 83*, 3325-3332.

(64) McLachlan, A. D., Dearman, H. H., Lefebvre, R. (1960) Theory of Hyperfine Interactions in Aromatic Radicals, *J. Chem. Phys., 33*, 65-70.

(65) Steiner, T. (2002) The hydrogen bond in the solid state, *Angew. Chem. Int. Ed., 41*, 48-76.

(66) Sinnecker, S., Neese, F. (2006) Spin-spin contributions to the zero-field splitting tensor in organic triplets, carbenes and biradicalss - A density functional and ab initio study, *J. Phys. Chem. A, 110*, 12267-12275.

(67) van der Waals, J. H., ter Maten, G. (1964) Zero-Field Splitting of Lowest Triplet State of Some Aromatic Hydrocarbons - Calculation + Comparison with Experiment, *Mol. Phys., 8*, 301-318.

(68) Lendzian, F., Bittl, R., Telfer, A., Lubitz, W. (2003) Hyperfine structure of the photoexcited triplet state (3)P680 in plant PSII reaction centres as detennined by pulse ENDOR spectroscopy, *Biochim. Biophys. Acta, 1605*, 35-46.

(69) Lendzian, F., Huber, M., Isaacson, R. A., Endeward, B., Plato, M., Bönigk, B., Möbius, K., Lubitz, W., Feher, G. (1993) The Electronic-Structure of the Primary Donor Cation-Radical in Rhodobacter-Sphaeroides R-26 - Endor and Triple-Resonance Studies in Single-Crystals of Reaction Centers, *Biochim. Biophys. Acta, 1183*, 139-160.

(70) Huber, M., Doubinskii, A. A., Kay, C. W. M., Möbius, K. (1997) ENDOR on the triplet state of the primary electron donor in the photosynthetic bacterium Rhodobacter sphaeroides - One step forward in a still unfinished story, *Appl. Magn. Reson, 13*, 473-485.

(71) Frank, H. A., Cogdell, R. J. (1996) Carotenoids in photosynthesis, *Photochem. Photobiol., 63*, 257-264.

(72) Di Valentin, M., Ceola, S., Agostini, G., Giacometti, G. M., Angerhofer, A., Crescenzi, O., Barone, V., Carbonera, D. (2008) Pulse ENDOR and density functional theory on the peridinin triplet state involved in the photo-protective mechanism in the peridinin-chlorophyll a-protein from Amphidinium carterae, *Biochim. Biophys. Acta, 1777*, 295-307.

(73) Di Valentin, M., Ceola, S., Salvadori, E., Agostini, G., Giacornetti, G. M., Carbonera, D. (2008) Spectroscopic properties of the peridinins involved in chlorophyll triplet quenching in high-salt peridinin-chlorophyll a-protein from Amphidinium carterae as revealed by optically detected magnetic resonance, pulse EPR and pulse ENDOR spectroscopies, *Biochim. Biophys. Acta, 1777*, 1355-1363.

Chapter 7

Spin density distribution of the triplet state of the primary donor*

Abstract

The primary electron donor (P) in the photosynthetic bacterial reaction center of *Rhodobacter sphaeroides* and *Blastochloris viridi*s consists of a dimer of bacteriochlorophyll cofactors. Its photoexcited triplet state in frozen solution has been investigated by time resolved ENDOR spectroscopy at 34 GHz. The electron spin density was found to be evenly delocalized over both dimer halves in the special pair of *Rb. sphaeroides* ($^3P_{865}$) and *Bl. viridis* ($^3P_{960}$), which contrasts with previous findings of a strongly asymmetric delocalization of the spin density in the radical cation states $P_{865}^{\bullet+}$ [Lendzian *et al*, *BBA*, 1993] and $P_{960}^{\bullet+}$ [Lendzian *et al*, *Chem. Phys. Let*, 1988]. The spin density distribution found for $^3P_{865}$ and $^3P_{960}$ is essentially the same, except for the ethylidene groups in $^3P_{960}$ that carry additional spin density. As opposed to the triplet state of the bacteriochlorophyll monomer [Marchanka *et al*, *J. Phys. Chem. B*, 2009], the triplet state of the dimer can be better explained as a simple HOMO → LUMO excitation. These findings are discussed in light of the large difference in photosynthetic activity of the two branches of cofactors present in the bacterial reaction center proteins.

* This chapter is based on publication „ Comparative 34 GHz ENDOR Study of the Triplet State of the Primary Donor in Bacterial Reaction Centers of *Rb. sphaeroides* and *Bl. viridis*" by Marchanka, A., Lubitz, W., van Gastel, M. (2009), *in preparation for J. Phys. Chem. B.*

7.1 Introduction

Photosynthesis is a process of vital importance on earth.[1-3] In photosynthesis, large protein cofactor complexes catalyze a light-driven electron and proton transport across the photosynthetic membrane. These proteins utilize sunlight and convert it into chemical energy, which is then used to drive ATP synthesis. [2-7] Since photosynthesis is the only known biological process able to convert sunlight directly into chemical energy, knowledge of its function may help to design biologically inspired systems that may be used for storage and utilization of solar energy. Many groups have accordingly studied the photosynthetic proteins with different techniques. For bacterial photosynthesis, significant progress in the understanding of both the structure and function of the proteins, which are called bacterial reaction centers (bRCs), has been obtained.[2-6, 8, 9]

The crystallographic structure of the bRC of the purple photosynthetic bacteria *Rhodobacter (Rb.) sphaeroides*[10-18] and *Blastochlorus (Bl.) viridis*[19-22] - previously called *Rhodopseudomonas viridis* - has been determined by X-ray crystallography. Both bRCs consists of three protein subunits, L, M and H. In the bRC of *Bl. viridis* a fourth protein subunit, a tightly attached cytochrome is present, which contains four hemes.[19, 23] Two subunits (L, M) are located in the photosynthetic membrane and harbor the cofactors of the electron transfer chain. The third subunit does not bind any cofactor, it is largely situated on the periplasmic side.[12, 13, 15, 18]

The bacterial reaction center contains as cofactors four bacteriochlorophylls, two bacteriopheophytins, two quinones, non-heme iron and a carotenoid.[2, 3, 6, 18] Photosynthetic charge separation starts from a dimer of bacteriochlorophylls called the primary donor (P).[3, 5] The other cofactors form two nearly identical branches called A and B, and each branch consists of an accessory bacteriochlorophyll, a bacteriopheophytin and a quinone.[12, 19-21] In the bRC of *Rb. sphaeroides*, BChl *a* and BPheo *a* are present as cofactors and in the bRC of *Bl. viridis*, BChl *b* and BPheo *b* are present. The molecular structures of BChl *a* and BChl *b* are shown in Fig. 7.1. They differ at position 8^1 where BChl *b* has an ethylidene group, thus slightly extending the π system of the bacteriochlorin macrocycle as compared to BChl *a*.

Low-temperature optical measurements have shown that electron transfer in native bacterial reaction centers occurs only *via* the A-branch, starting from the special pair *via* the accessory bacteriochlorophyll, bacteriopheophytin and quinone Q_A to the quinone Q_B in the B-branch, which acts as the final electron acceptor.[12, 13, 15, 18, 24, 25] This asymmetry in activity of the two very similar A and B branches is still not fully understood. Differences have been

observed in the hydrogen-bonding network of both branches.[18] These differences may induce an asymmetry in the electronic structure or in the midpoint potential of the cofactors and thereby influence their relative photosynthetic activity. Alternatively, the asymmetry may also be inherent with the cofactor arrangement itself.[26] It might be that the photoexcited electron, which resides in the lowest unoccupied molecular orbital (LUMO) at the chlorophyll dimer, is not equally distributed over both dimer halves, thus favoring a particular branch for electron transfer.[24] Knowledge of the LUMO is thus essential to understand the primary processes of photosynthesis. In particular, forward electron-transfer matrix elements can be calculated

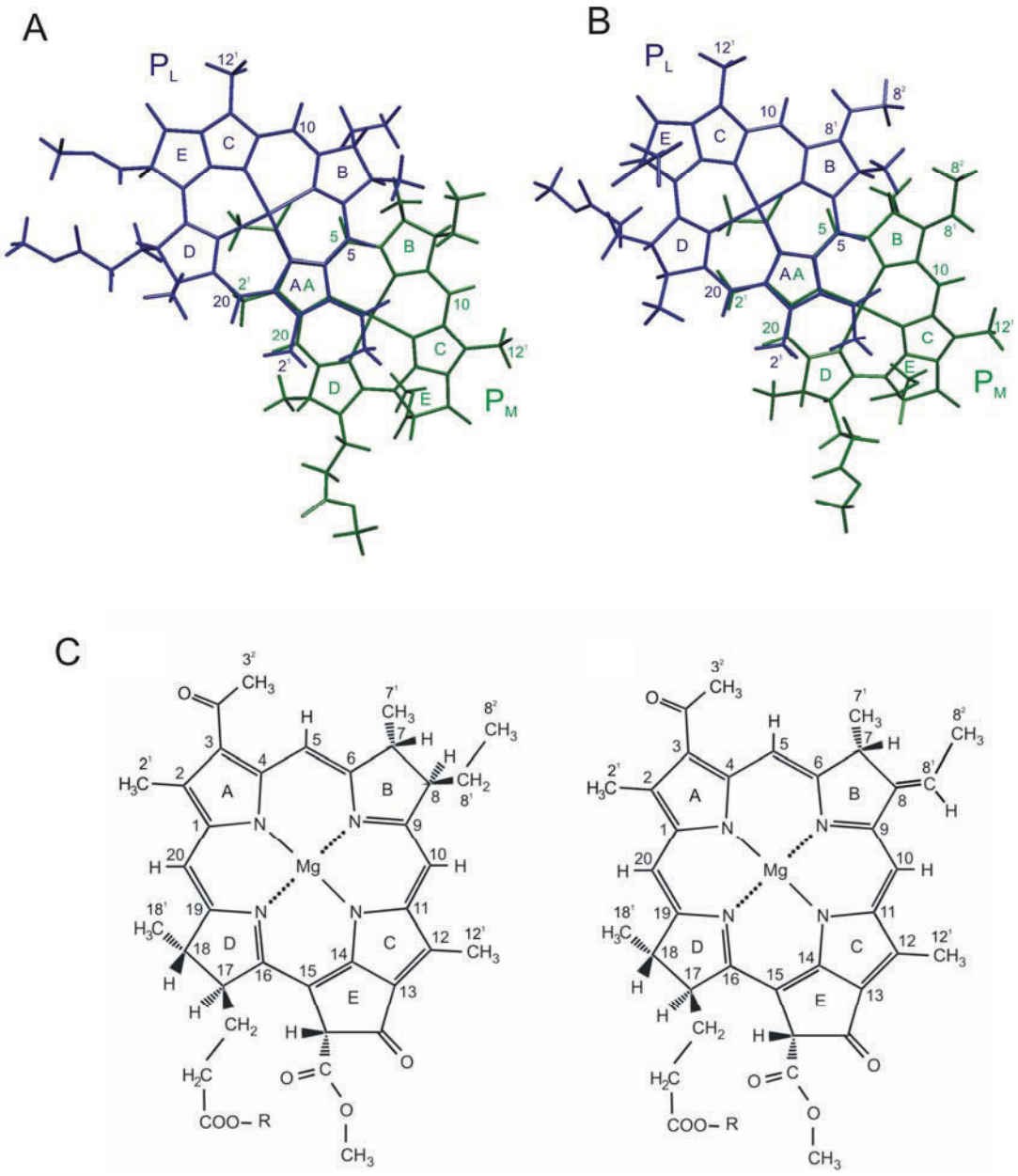

Figure 7.1. The primary donor (A) P_{865} in the bacterial reaction center of *Rb. sphaeroides* and (B) P_{960} in *Bl. viridis*. The dimer halves P_L (A-branch), P_M (B-branch) and relevant atoms are depicted. (C) Resonance structures and IUPAC numbering scheme for BChl *a* (left) and BChl *b* (right).

when the LUMO orbital of P and the acceptor orbital are known. The LUMO orbital itself gives information about the presence of internal asymmetry in the electronic structure of the bacteriochlorophyll dimer, from which electron transfer originates. Information about the LUMO orbital can in principle be obtained from electron paramagnetic resonance (EPR) and electron nuclear double resonance (ENDOR) spectroscopy.[24, 27]

Though the singlet excited state P^* is diamagnetic and can therefore not be studied by EPR techniques, information about the lowest unoccupied orbital (LUMO) of P – which would be singly occupied in P^* - can still be obtained by studying the photoexcited triplet state, ^3P. In the triplet state, two unpaired electrons are present, one in the HOMO and one in the LUMO orbital. In the simple model of HOMO $\rightarrow$ LUMO excitation, ^3P and the photosynthetically relevant state P^* actually have the same electronic configuration and only differ in their exchange interaction. Thus, by performing EPR and ENDOR measurements for ^3P, detailed information is obtained about both the HOMO and LUMO orbitals. The set of important frontier orbitals (HOMO–1, HOMO, LUMO, LUMO+1) belonging to the macrocycle, is in the case of (bacterio)chlorophylls and porphyrins usually represented in terms of a four-orbital model introduced by Gouterman.[28, 29]

Though the triplet state of the BChl dimer has been extensively studied by EPR spectroscopy,[30-35] only two studies by time resolved EPR and ENDOR spectroscopy at 9 GHz have been undertaken on the triplet state of bRC of *Rb. sphaeroides* so far.[33, 35] In these studies, two hyperfine couplings have been observed and assigned to the methyl groups and the in-plane methine protons of the bacteriochlorin base.[33]

In a recent contribution, we have investigated the difference in photosynthetic activity of the A and B branches by pulse EPR spectroscopy at 34 GHz of the triplet state ^3P in native and mutated bRCs.[36] The higher microwave frequency allowed for increased spectral resolution and sensitivity. The measurements indicated that the B-branch charge separation remains inactive up to temperatures of 50 K, even when A-branch charge separation is inhibited by site directed mutations in the A-branch.[36] Moreover, the triplet states of the monomeric cofactors BChl *a* and BChl *b* *in vitro* have recently been characterized by ENDOR spectroscopy at 34 GHz.[37] It has been found that the monomeric triplet state cannot be described as a simple HOMO $\rightarrow$ LUMO excitation in terms of Gouterman orbitals. Rather a mixture of HOMO $\rightarrow$ LUMO and HOMO–1 $\rightarrow$ LUMO excitation more accurately describes the monomeric BChl triplet state.[37] The knowledge of the spin density distribution of the monomeric ^{3}BChl *a* and ^{3}BChl *b* is an essential prerequisite for the interpretation of the ENDOR data of the BChl dimer presented in this study.

In order to investigate whether the asymmetry of photosynthetic charge separation with respect to the A and B branches is inherent with the electronic structure of the BChl dimer, or related to other differences of the two branches, *e.g.* the hydrogen bonding network and/or different electronic configuration of the other cofactors in both branches, we here present a systematic ENDOR study at 34 GHz of the triplet states of $^3P_{865}$ and $^3P_{960}$ at cryogenic temperatures. The dimer triplet state is also compared to the triplet state and radical cation[38, 39] and radical anion[40-42] states of the monomeric bacteriochlorophylls *in vitro*, which are paramagnetic and have been characterized by EPR and ENDOR spectroscopy. Since the DFT methodology, which was useful for the study of the triplet state of monomeric BChl, is not expected to correctly address the π interaction of the two monomers in the special pair, the experimentally derived data are compared additionally with theoretical results obtained from DFT calculations of the BChl monomer.[37] The emphasis of our study is to clarify whether the LUMO orbital of P, from which charge separation in P^* starts is symmetrically or asymmetrically delocalized over both dimer halves. Though an asymmetric spin density distribution over the two dimer halves has been found in the charged radical state for both $P_{865}^{\bullet+}$ in *Rb. sphaeroides*[43] and $P_{960}^{\bullet+}$ in *Bl. viridis*,[44] the spin density in the neutral triplet state seems to be more evenly delocalized over the special pair.

7.2 Materials and methods

Sample preparation

Carotenoidless *Rb. sphaeroides* R-26.1 bacterial reaction centers were isolated and purified as described by Feher and Okamura.[45] The reaction centers from *Bl. viridis* wild type were purified as described by Trosper *et al.*[46] The quinones Q_A and Q_B were reduced by addition of sodium dithionite solution[33] (0.5 M in 1 M Tris-HCl, pH 8.0) to yield a final dithionite concentration of 50 mM in the sample. Then the samples were quickly frozen in the Q-band EPR tube in liquid nitrogen in the dark.[33] The optical density of the samples was about 50 at 865 nm and 960 nm for the bRC of *Rb. sphaeroides* and *Bl. viridis*, respectively.

EPR/ENDOR spectroscopy

Electron Spin Echo (ESE) detected EPR and ENDOR spectra were recorded on a Bruker Q-band Elexsys E580 FT pulse EPR spectrometer with laser excitation as described previously.[37] Excitation at 865 nm and 960 nm was performed with 5 mJ/pulse and 4

mJ/pulse, respectively. Since the absorption maximum of the dimer band depends on the temperature, the excitation wavelengths were slightly tuned around 865 nm and 960 nm for the bRC of *Rb. sphaeroides* and *Bl. viridis*, respectively, to obtain a maximum EPR signal. The EPR measurements were performed in the temperature range 10 K – 100 K, the ENDOR measurements were performed at 10 K.

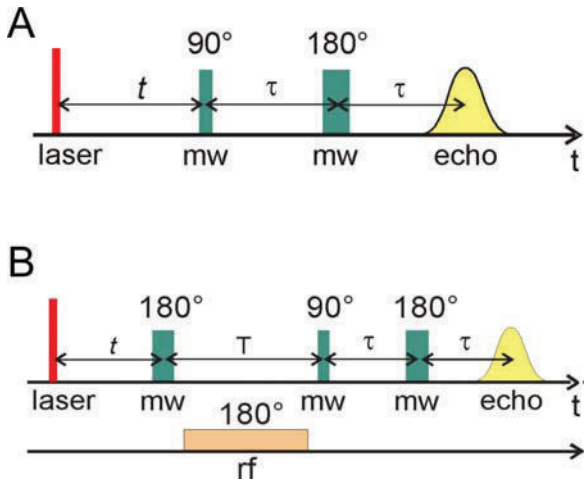

Scheme 1.

The EPR pulse sequence is shown in scheme 1A.[33, 47] It consists of a laser pulse followed by a Hahn echo microwave pulse sequence for detection. The pulse lengths and delays are identical to those used previously for such systems.[36] Pulse ENDOR measurements were performed according to the Davies ENDOR sequence (scheme 1B).[33, 47] Pulse lengths and delays were the same as in a recent ENDOR study of BChl *a* and BChl *b in vitro*.[37] The accumulation time was typically 30 minutes for an EPR spectrum and 6–12 hours for an ENDOR spectrum depending on the magnetic field, at which the measurements were performed.

7.3 Results

EPR

The ESE detected EPR spectra of $^3P_{865}$ in the bRC of *Rb. sphaeroides* R26.1 and of $^3P_{960}$ in the bRC of *Bl. viridis* at 10 K are shown in Fig. 7.2. The shape of the spectra is determined by the zero field splitting parameters (ZFS) *D* and *E*.[30, 33, 36] The ZFS parameter *D* for *Bl. viridis* is slightly smaller than that for *Rb. sphaeroides* (0.0161(3) cm^{-1} and 0.0188(3) cm^{-1}). The *E* parameter is larger for *Bl. viridis* (*E* = 0.0041(3) cm^{-1}) than for *Rb. sphaeroides*

(E = 0.0031(3) cm^{-1}). The ZFS parameters found in the triplet EPR measurements are similar to those obtained by other groups.[30, 33, 48, 49] The polarization patterns (AEEAAE) of the triplet EPR spectra of $^3P_{865}$ and $^3P_{960}$ are identical at 10 K and indicative of a radical pair mechanism of triplet formation.[31, 32, 49, 50] The polarization pattern of the triplet EPR spectrum of the bRC of *Bl. viridis* has been found to be temperature independent up to T = 100 K. Also, the polarization pattern of the EPR spectrum of *Rb. sphaeroides* R26.1 is temperature independent. This contrasts to the bRC of wild type *Rb. sphaeroides*, where the triplet state of $^3P_{865}$ is taken over by the carotenoid at temperatures above 30 K, which has a different polarization pattern EAAEEA.[36, 51, 52] The triplet state in the bRC of *Bl. viridis* is not quenched by carotenoid since the energy level of the ^{3}Car (1,2-dyhydroneurosporene) in *Bl. viridis* lies above that of $^3P_{960}$ and thus no triplet-triplet transfer is possible.[23, 53]

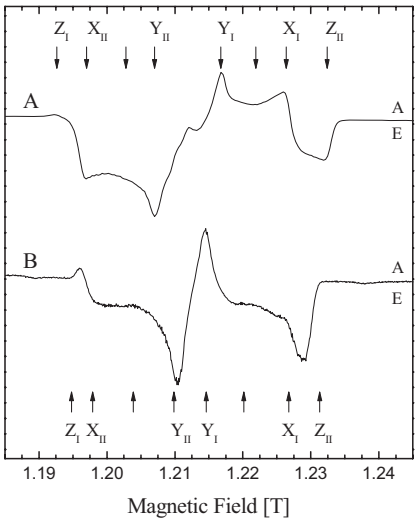

Figure 7.2. ESE-detected EPR spectra for (A) $^3P_{865}$ in *Rb. sphaeroides* and (B) $^3P_{960}$ in *Bl. viridis* at 34 GHz.

ENDOR

Orientation-selected triplet ENDOR spectra have been recorded at 34 GHz for both $^3P_{865}$ and $^3P_{960}$ at 10 K for different magnetic field settings, indicated by arrows in Fig. 7.2. Fig. 7.3A shows Davies ENDOR spectra of $^3P_{865}$ in the bRC of *Rb. sphaeroides*, Fig. 7.3B that of $^3P_{960}$ in the bRC of *Bl. viridis*. The frequency axis is displayed as $\nu_{ENDOR}-\nu_n(^1H)$ axis; the narrow signal corresponds to $\nu_n(^1H)$ and has been set to 0 MHz. Accordingly to triplet ENDOR resonance condition[37, 54]

$$\nu_{ENDOR}^{T} = \nu_n - M_S A_T \qquad (1)$$

where ν_n is the nuclear Zeeman frequency, the hyperfine coupling A_T can directly be obtained from the frequency shift ν^T_{ENDOR}. Furthermore, with the knowledge that D is positive,[30, 33, 36] the sign of the hyperfine coupling constant can be also directly obtained from the frequency shift of the corresponding ENDOR signal.[33, 37, 54] The absolute sign of the hyperfine shift is included in Fig. 7.3 for the absorptive and emissive signals.

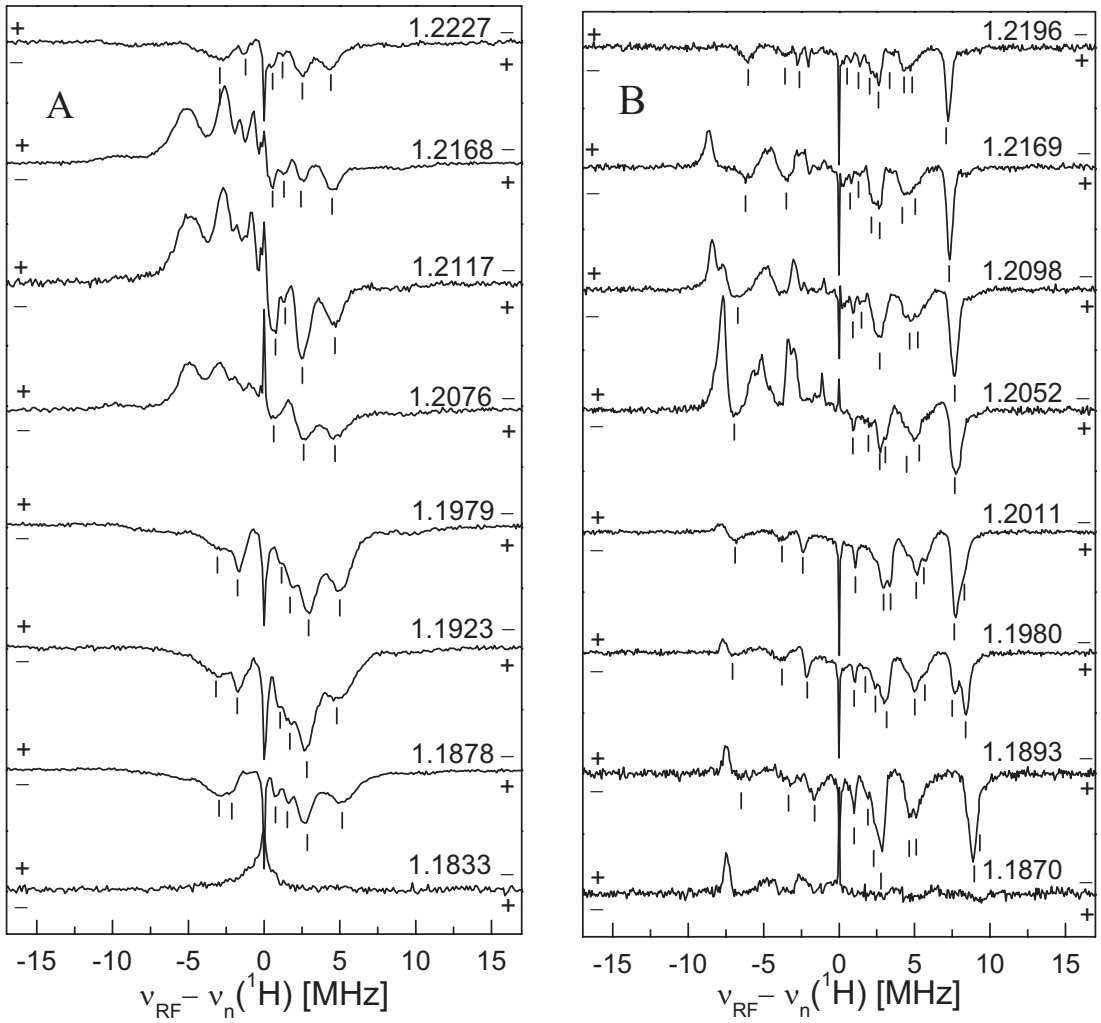

Figure 7.3. Davies ENDOR spectra of $^3P_{865}$ in *Rb. sphaeroides* (A) and $^3P_{960}$ in *Bl. viridis* (B). Magnetic field settings and signs of hyperfine coupling constants are indicated. The signs above and below each ENDOR spectrum are valid for the absorptive and emissive signals, respectively.

As is seen, the ENDOR spectra are rich in structure. Moreover, it is obvious that the signals observed in the spectra for $^3P_{865}$ are also present in the spectra for $^3P_{960}$ measured at corresponding magnetic field settings. However, differences are also present. In the ENDOR

spectra of $^3P_{960}$, two additional signals are observed at all magnetic field settings, one with a negative frequency shift of about −6 MHz and another with a positive frequency shift of +8.0 MHz. These signals are absent in the ENDOR spectra of $^3P_{865}$.

Table 7.1. Hyperfine couplings constants [MHz] of the emissive signals observed at the canonical orientations in the Davies ENDOR spectra of $^3P_{865}$ and $^3P_{960}$. The uncertainties in hyperfine coupling constants are about 0.1 MHz. The signals are grouped into 8 bands that have been traced over a large part of the magnetic field range spanned by the EPR spectrum. Two values for some bands of $^3P_{960}$ are given that indicate the splitting of hyperfine coupling constants.

$^3P_{865}$	Z_I	X_{II}	Y_{II}	Y_I	X_I	Z_{II}
2		−3.1	−3.1			−2.8
3		−2.2	−1.6	−1.6		−1.2
4		+0.7	+1.2	+0.8	+0.6	+0.6
5		+1.6	+2.0		+1.4	+1.2
6		+2.7	+3.0	+2.5	+2.5	+2.6
7		+5.0	+5.0	+4.7	+4.5	+4.3
$^3P_{960}$						
1		−7.1	−7.0	−7.0	−6.8	−6.2
2		−3.3	−3.8		−3.6	−3.6
3		−1.6	−2.4			−2.0
4		+1.0	+1.1	+1.1	+0.8	+0.8
5		+1.9	+2.4	+1.8	+1.5	+1.4
6.1		+2.4	+2.9	+2.6	+2.3	+2.1
6.2		+2.9	+3.4	+3.1	+2.7	+2.6
7.1		+4.6	+5.1	+5.0	+4.5	+4.2
7.2		+5.1	+5.7	+5.3	+5.2	+4.8
8.1		+8.9	+7.7	+7.7	+7.3	+7.2
8.2			+8.3			

Single-crystal-like ENDOR signals are only observed at the Z_I and Z_{II} canonical orientations, at the edges of the EPR spectrum. In the ENDOR spectra measured at the X and Y canonical orientations and at intermediate magnetic field settings, both the $M_S = 0 \leftrightarrow -1$ and $M_S = 0 \leftrightarrow +1$ transitions contribute. In all spectra, the emissive signals are more intense than the absorptive signals. The emissive signals are observable at all magnetic field settings, except at the Z_I orientation, where the $M_S = 0 \leftrightarrow -1$ EPR transition does not contribute. The observed hyperfine coupling constants for the emissive EPR transition at the canonical orientations are summarized in table 7.1. A complete dataset measured at 8 fields is given in

appendix C. Isotropic hyperfine coupling constants for each band are derived as an averaging of hfcs over all measured magnetic field orientations and are presented in table 7.2.

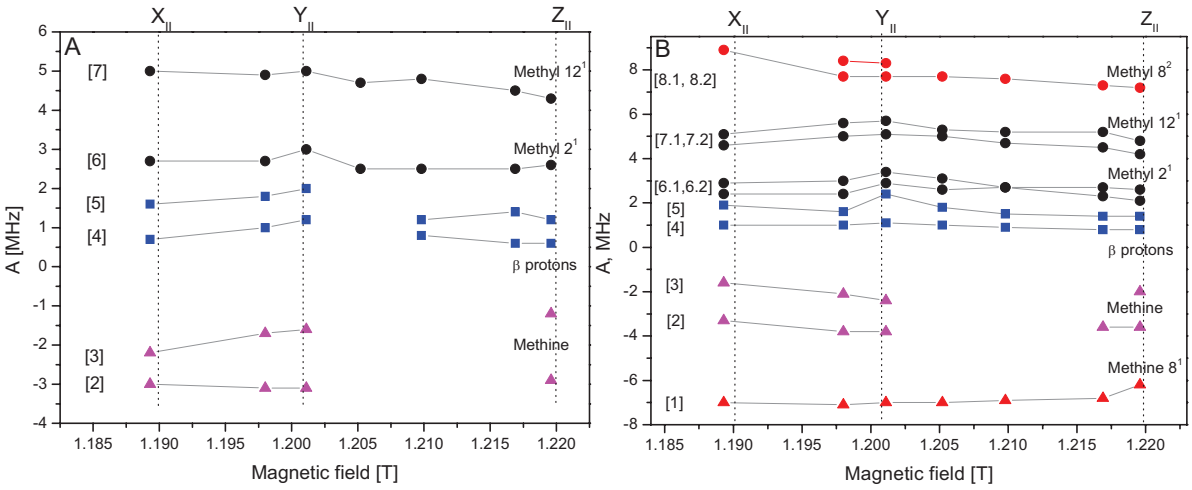

Figure 7.4. Field-frequency plots for the band observed in the triplet ENDOR spectra of $^3P_{865}$ of *Rb. sphaeroides* (A) and $^3P_{960}$ of *Bl. viridis* (B). An assignment based on comparison with monomer data[37] is included in the figure. Splitting of hyperfine coupling constants is observable for methyl groups 2^1, 12^1 and 8^2 in $^3P_{960}$.

All observed signals vary with different field settings. Field-frequency plots have been constructed for the emissive signals and are shown in Fig. 7.4A and 7.4B. Bands [6] and [7] are observable at all orientations and are similar in the triplet ENDOR spectra of $^3P_{865}$ and $^3P_{960}$. The anisotropy can be followed through all magnetic field positions. The maximum hyperfine coupling occurs at the field setting that corresponds to Y_{II} orientation. Bands [2] and [3] have negative hyperfine shifts and are visible only at some orientations both in $^3P_{865}$ and in $^3P_{960}$. The maximum couplings of bands [2] and [3] occur at magnetic field settings that correspond to the center region of the EPR spectrum. In $^3P_{865}$ their maximum couplings occur closer to the X_{II} canonical orientation, in $^3P_{960}$ closer to the Y_{II} canonical orientation. The maximum couplings of bands [4] and [5] occur at the Y_{II} canonical orientation. They are characterized by an isotropic hyperfine coupling constant of +1.0 MHz and +1.7 MHz in both $^3P_{865}$ and $^3P_{960}$.

Band [1] has an isotropic hyperfine coupling of –6.6 MHz and is only present in the triplet ENDOR spectra of $^3P_{960}$. Its maximum coupling occurs at a field position that is intermediate between the X_{II} and Y_{II} orientations. The intense band [8] is also only present for $^3P_{960}$. It has an isotropic coupling constant of +8.0 MHz. The maximum coupling is attained at the X_{II} orientation.

Bands [6], [7] and [8] for $^3P_{960}$ are split into two signals. They are enumerated [6.1] and [6.2], [7.1] and [7.2], [8.1] and [8.2]. The corresponding bands have very similar isotropic hyperfine coupling constants and display the same field-frequency behaviour. Such a splitting is not observable within the line width of the bands for $^3P_{865}$, which is indeed broader than that in $^3P_{960}$.

7.4 Discussion

First the extent of delocalization of the triplet wavefunction in a dimeric supermolecule will be addressed as obtained directly from the experimental data. The spin density could either be localized only on one dimer half, asymmetrically delocalized or symmetrically delocalized over both halves.

In case of localized spin density one would expect the same ZFS parameter *D* and hyperfine coupling constants as in the monomer with some minor variations. In case of a symmetrical distribution, the ZFS parameter *D* would be significantly smaller and values of the hfc's would be halved without any splitting. If the distribution would be asymmetric, a splitting of hfc's with various values in between these of the monomer and dimer values is expected.[i]

A comparison of the zero-field splitting parameter *D* of monomeric BChl with that of the special pair has been used for the determination of the delocalization of the triplet wavefunction over the dimer halves. Since the ZFS parameter *D* in organic triplet states depends on the effective electron-electron distance of the triplet electrons, a more delocalized wavefunction decreases the *D* parameter.[54, 55] The *D* parameters of $^3P_{865}$ (0.0188 cm^{-1}) and $^3P_{960}$ (0.0161 cm^{-1}) are significantly smaller than those of ^{3}BChl *a* (0.0231 cm^{-1}) and ^{3}BChl *b* (0.0222 cm^{-1}). This points to a significant delocalization of the triplet wavefunction over the dimer halves. However, due to possible charge transfer contribution in the triplet wavefunction, a final conclusion about the degree of delocalization is difficult to obtain from the EPR data alone.[30, 31]

[i] In an alternate description the triplet state of the primary donor can be presented as a combination of two local excitations $^3P_LP_M$, $P_L{}^3P_M$ and charge transfer states $P_L^+P_M^-$ and $P_L^-P_M^+$; however the weight contribution of individual terms in the wavefunction is unknown.[30, 33]

The ENDOR spectra of $^3P_{865}$ and $^3P_{960}$ look very similar with almost the same average values and field-frequency dependence. This similarity points to a similar delocalization of the triplet wavefunction in $^3P_{865}$ and $^3P_{960}$.

Next, the number of observed signals is considered. No splitting of ENDOR signals is present in $^3P_{865}$ within the experimental linewidth of 1 MHz. Only a minor splitting of the ENDOR signals of less than 10 % is observed in $^3P_{960}$. In the ENDOR spectra of $^3P_{865}$ six hyperfine couplings are present. In the ENDOR spectra of $^3P_{960}$ eight hyperfine couplings are observable, whereas in the ENDOR spectra of ^{3}BChl *a* and ^{3}BChl *b* six and seven hyperfine couplings are observed, respectively. The number of bands observed in the spectra of the dimer is thus essentially equal to the number of bands observed for the respective monomers, not double.[37]. Furthermore, the hfcs's in the dimer are on the average smaller than in the monomer. These finding exclude an asymmetrically delocalized wavefunction, which would give rise to a large number of signals as compared to the monomer. Thus, it looks as if the triplet state is essentially evenly delocalized. A symmetrically delocalized triplet state of $^3P_{865}$ has been also postulated from single crystal EPR studies on bRCs of *Rb. sphaeroides*.[56, 57]

In $^3P_{960}$, two additional large couplings are present as compared to $^3P_{865}$, which could only stem from the structural difference at position 8 where P_{960} has an the ethylidene group. The positive coupling is derived from the methyl group (8^2) and the negative coupling from the methine proton (8^1).[37] Since only one additional positive hyperfine coupling with minor splitting and only one additional negative coupling are present in $^3P_{960}$, it also supports an almost even spin distribution over the dimer halves.

Assignment of experimental hyperfine couplings of $^3P_{865}$ and $^3P_{960}$ based on comparison between experimental dimer, monomer and theoretical monomer hyperfine coupling constants.

Since the triplet wavefunction is essentially symmetrically ($^3P_{865}$) or almost symmetrically ($^3P_{960}$) delocalized over the dimer halves P_L and P_M, the hyperfine coupling constants of $^3P_{865}$ and $^3P_{960}$ should be half of those of the BChl *a* and BChl *b* monomer. The coupling constants for ^{3}BChl *a* and ^{3}BChl *b in vitro* determined from a recent ENDOR study and from DFT calculations[37] are included in table 7.2. For both monomeric ^{3}BChl *a* and ^{3}BChl *b in vitro*, it was recently found that the triplet state is best described by a multireference excitation that involves 50% HOMO $\rightarrow$ LUMO excitation and 50% HOMO–1 $\rightarrow$ LUMO excitation.[37] Since the triplet state in $^3P_{865}$ and $^3P_{960}$ is not necessarily described by the same multirefence excitation, direct comparison of experimental dimer hfc constants and half of the experimental

Table 7.2. Average isotropic hyperfine couplings constants [MHz] for $^3P_{865}$ and $^3P_{960}$ derived from the experiments. Additionally, for comparison also included are the hyperfine coupling constants $a_T^{(M)}/2$ for the BChl monomer *in vitro*,[37] theoretically derived hfc's $a_{DFT}^{(M)}/2$ from DFT I calculations on the triplet state of the BChl monomer performed as a simple HOMO → LUMO excitation[37] and hfc's from cation and anion measurements ¼(a_c+a_a).[38, 40-42]

$^3P_{865}$				
	¼(a_c+a_a)	$a_T^{(M)}/2$	$a_{DFT}^{(M)}/2$	Exp[i]
Methine protons				
5	–1.8	–2.1	–2.0	–1.7 [3]
10	–1.4	–4.6	–2.7	–3.0 [2]
20	–1.2		–2.4	
Methyl groups				
2^1	+3.1	+3.8	+4.0	+2.8 [6]
12^1	+4.7	+4.6	+4.5	+4.9 [7]
β protons				
7	+3.6		+3.9	
8	+4.3	+0.9	+4.3	+1.0 [4]
17	+3.5	+1.6	+2.6	+1.7 [5]
18	+3.2		+2.2	

$^3P_{960}$				
	¼(a_c+a_a)	$a_T^{(M)}/2$	$a_{DFT}^{(M)}/2$	Exp
Methine protons				
5	–1.2		–2.0	–2.0 [3]
10	–1.4	–1.5	–3.0	–3.6 [2]
20	–1.0	–4.6	–2.3	
Methyl groups				
2^1	+3.3	+3.5	+3.8	+2.8 [6]
12^1	+4.4	+4.5	+4.2	+5.0 [7]
β protons				
7			+3.3	+1.8 [5]
17		+1.0	+1.7	+1.0 [4]
18			+1.6	
Ethylidene group				
8^1		–1.1	–3.0	–6.6 [1]
8^2		+1.5	+2.9	+8.2 [8]

[i] Assignment only of „types of protons" for α protons (methine) and β protons have been performed

monomer hfc constants may not give rise to quantitative agreement. It is nevertheless still insightful to compare the experimental hfc constants for each band with half of the hfc constants of the monomeric bacteriochlorophyll triplet states *in vitro* and with half of the hyperfine couplings from DFT I calculations of the BChl monomer, performed as a simple HOMO → LUMO excitation.[37]

Bands [2] and [3] are slightly more shifted in $^3P_{960}$ than in $^3P_{865}$. They are characterized by negative hyperfine coupling constants *via* spin polarization and therefore correspond to in-plane methine protons.[55] The only candidates are the protons at the *meso* positions 5, 10, 20 of the bacteriochlorin macrocycle. Only two signals are observed, whereas each BChl has three methine protons. However, the methine protons 5, 10 and 20 have significantly larger hyperfine coupling contants in the BChl *a* monomer ($a_T^{(M)}/2$ = –4.6 MHz and –2.1 MHz) than in the dimer $^3P_{865}$ (–3.0 MHz and –1.7 MHz). The DFT deduced values of –2.7 MHz, –2.4 MHz and –2.0 MHz are closer to the experimental couplings. Since a third signal is not observed, a complete assignment does not seem feasible at present. The same holds for $^3P_{960}$.

Bands [6] and [7] in $^3P_{865}$ have the largest positive hyperfine coupling constants of +2.8 MHz and +4.9 MHz. Upon comparison with half of the hfc constants for ^{3}BChl *a in vitro* and DFT-deduced hfc constants, these values are close to those of methyl groups 2^1 and 12^1 (+3.8 MHz and +4.0 MHz for methyl group 2^1 and +4.6 MHz and +4.5 MHz for methyl group 12^1). Band [6] and [7] can be thus assigned to methyl groups 2^1 and 12^1. The less good agreement for methyl group 2^1 can be rationalized, since methyl groups 2^1 are located at a position where the π stacking in rings A occurs (see Fig. 7.1). Similarly, comparison of the hyperfine coupling constants of ^{3}BChl *b* with those of $^3P_{960}$ reveals good agreement for the methyl group 12^1 and slightly worse agreement for methyl group 2^1, probably also due to the π stacking.

Bands [4] and [5] are characterized by comparatively small positive hyperfine coupling constants of +1.0 MHz and +1.7 MHz for $^3P_{865}$, respectively. These values are similar to those found for the β protons 7, 8, 17 and 18 derived from monomeric BChl experiments ($a_T^{(M)}/2$ =+0.9 MHz and +1.6 MHz) but are significantly smaller than those found in DFT calculations. The small coupling constants indicate that the bands [4] and [5] could correspond to β protons or to protons located far away from the bulk spin density. It cannot be excluded that they belong to the surrounding of the bacteriochlorophyll dimer (matrix).

Band [1] and band [8] are exclusively present in $^3P_{960}$. Band [1] displays a negative hyperfine shift of about −6 MHz, band [8] a positive one with a positive frequency shift of +8.0 MHz. Thus, band [1] belongs to an in-plane proton and band [8] to a β proton or methyl group. The presence of these bands correlates well with the structural differences between BChl *a* and BChl *b* at position 8. The ethylidene group of BChl *b* has one in-plane proton 8^1 and a methyl group 8^2, to which bands [1] and [8] are assigned. Especially band [8] has a rather narrow linewidth and displays only a minor splitting at some magnetic field settings (*cf.* Fig. 7.3B). The experimental hyperfine couplings, −6.6 MHz and +8.2 MHz are, however, significantly larger than either monomer derived experimental couplings (−1.1 MHz and +1.5 MHz) or the DFT deduced ones, −3.0 MHz and +2.8 MHz.

Obviously, acceptable agreement between the DFT deduced hyperfine couplings and the experimental dimer couplings and the worse agreement of the experimental monomer and experimental dimer couplings for the methine protons and the ethylidene group indicates that the triplet excitation of the dimer must differ at the electronic level from that of the monomer. As compared to the triplet state of the monomer, the triplet state of the dimer apparently differs in such a way, that more spin density is present at the ethylidene group in case of BChl *b* and less spin density is present at the carbon atoms at the *meso* positions. Inspection of the HOMO and LUMO orbitals of the ^{3}BChl *b*, [37], reveals that the HOMO has a large wavefunction coefficient at the ethylidene group and only small coefficients at the *meso* carbons. A pure HOMO → LUMO excitation for the dimer as compared to only 50% for the monomer would increase the contribution of the HOMO to the triplet spin density and would thus increase the hyperfine coupling constants of the protons of the ethylidene group and decrease those of the methine protons. Comparing the experimental couplings of $^3P_{865}$ and $^3P_{960}$ with values derived from DFT I calculation on monomer in pure HOMO → LUMO excitation, shows good agreement for the methine protons. Also, the disagreement for the ethylidene group in $^3P_{960}$ is reduced, although a correct description of the spin density on this group is still not obtained. Possible reasons will be discussed in the next section.

Lastly, it is interesting to compare the triplet state of the dimer with the monomeric cation and anion radicals. In the cation radical, the HOMO is singly occupied, in the anion radical the LUMO is singly occupied. Thus, in case of a symmetrically delocalized HOMO → LUMO based triplet state at the dimer, the hyperfine couplings of the dimer must equal 25 % of the sum of the couplings of the cation and anion radical.[38-42, 58] These cation and anion derived values are also included in table 7.2. The values for the methyl groups 2^1 and 12^1 from the cation and anion data are in approximate agreement with those for the triplet state of

the dimer. Indeed, the couplings for the methine protons 5, 10 and 20 in case of the cation and anion radical are much smaller than those of the monomer triplet state. The values for the dimer are actually in between those of the monomer triplet state and the average of the radical cation and anion states and mostly close to theoretically derived values from DFT I calculations on the monomer.[37]

Ethylidene group in $^3P_{960}$

Comparison of the experimental coupling constants of the ethylidene group in $^3P_{960}$, −6.6 MHz and +8.2 MHz, *cf.* table 7.2, with the experimentally or theoretically derived data sets from the monomer study,[37] reveals that the experimentally observed couplings in $^3P_{960}$ are significantly larger. The signals have nevertheless been assigned with certainty to the ethylidene group, since they are present in $^3P_{960}$ and absent in $^3P_{865}$ and all other signals are essentially identical. Moreover, the discrepancy of a factor of almost two is observed for both bands [1] and [8], corroborating the assignment. Though the origin of the discrepancy can presently not be established with certainty, some structural elements that may be responsible are investigated in this section.

One possibility could be the admixture of other orbitals to the triplet wavefunction. Obviously, the HOMO LUMO excitation results in too little spin density at the carbon 8^1, and thereby too small hyperfine couplings for methyl group 8^2 and methine proton 8^1. Upon inspection of the orbitals for monomeric ^{3}BChl *b*,[37] orbital LUMO+1 has large wavefunction coefficients at carbon 8^1 .

Geometric effects may also play a role. The amino acids surrounding the ethylidene groups may cause an increase of the spin density and thus an increase of the hyperfine coupling constants either by hydrogen bonding or by electrostatic effects. Advanced quantum mechanics/molecular mechanics calculations are necessary for taking these effects in account, which is at present not possible for the primary donor.

Another possibility concerns a perturbation of the geometry of the ethylidene group, upon excitation to the triplet state. Upon excitation of the π system, *e.g.*, in the case of π-π* transitions, bonds with double-bond character may acquire single bond character and *vice versa*. The influence of these perturbations has been investigated in a series of calculations on monomeric ^{3}BChl *b* with slightly perturbed geometry. First, the distance between C_{81} and C_{82} has been changed from 1.48 Å to 1.38 Å with steps of 0.02 Å Secondly, the distance between C_8 and C_{81} has been changed from 1.38 Å to 1.44 Å with steps of 0.02 Å (Fig. 7.1C). Larger hyperfine coupling constants have been obtained for small C_{81}–C_{82} distances and larger C_8–C_{81}

distances that virtually exchange the single bond in C_{81}–C_{82} to a double bond and *vice versa* for C_8–C_{81}. The hyperfine coupling constants from a calculation with shortened C_{81}–C_{82} distance from 1.48 Å to 1.38 Å and increased C_8–C_{81} distance from 1.38 Å to 1.44 Å raise up by 70 % and are estimated to be +4.9 MHz for methyl group 8^2 and −5.1 MHz for methine proton 8^1.

In summary, the experimentally found hyperfine coupling constants for $^3P_{865}$ and $^3P_{960}$ are in qualitative agreement with the hyperfine coupling constants derived from DFT calculations on BChl. The bands with negative coupling constants are assigned to the methine protons of the bacteriochlorin base. The bands [6] and [7] with positive coupling constants are assigned with the methyl protons of the groups 2^1 and 12^1. The bands [4] and [5] cannot be assigned with certainty, since the small couplings indicate that they may belong to β protons or protons located far away from the bulk spin density. Bands [1] and [8] are only present for $^3P_{960}$, and are thus assigned to the methine and methyl protons of the ethylidene groups.

The orientation of the ZFS axes

Knowledge of the directions of the principal axes of the ZFS tensor is necessary for the analysis of the anisotropy of the hyperfine couplings. The directions of the principal axes of the ZFS tensor for ^{3}BChl *a* are known from magnetophotoselection experiments.[59] Since the triplet spin density seems to be almost evenly distributed over two dimer halves, the orientation of the principal axes of the ZFS tensor of $^3P_{865}$ and $^3P_{960}$ can be found using simple symmetry considerations, without knowledge of the exact admixture of HOMO−1 LUMO excitation into the triplet wavefunction. The orientations of the ZFS axes must be such that the X-axis coincides with the C_2 symmetry axis of the dimer and the Z axis is perpendicular to the average P_L/P_M plane (Fig. 7.5, blue axis). This is corroborated by single crystal EPR studies on bRCs of *Rb. sphaeroides*[56, 57] where a symmetrically delocalized triplet state of $^3P_{865}$ has been observed.

For methyl groups 2^1, 12^1 and 8^2 the direction that corresponds to the maximum absolute hyperfine coupling essentially points along the C(pyrrole)-C(methyl) bond. This direction for methyl groups 2^1 both in $^3P_{865}$ and in $^3P_{960}$ is intermediate between the X and Y principal axes. The angle between the C_2 axis and the direction of maximum hyperfine coupling amounts to 45±5° both for $^3P_{865}$ and $^3P_{960}$. The field-frequency plot (Fig. 7.4) for methyl groups 2^1 indeed displays a broad maximum of the hyperfine coupling between X_{II} and Y_{II}. The angle between the C_2 axis and the principal hyperfine axis of maximum coupling for methyl groups 12^1 amounts to 50±5°. The field-frequency plot for band [7] indeed also

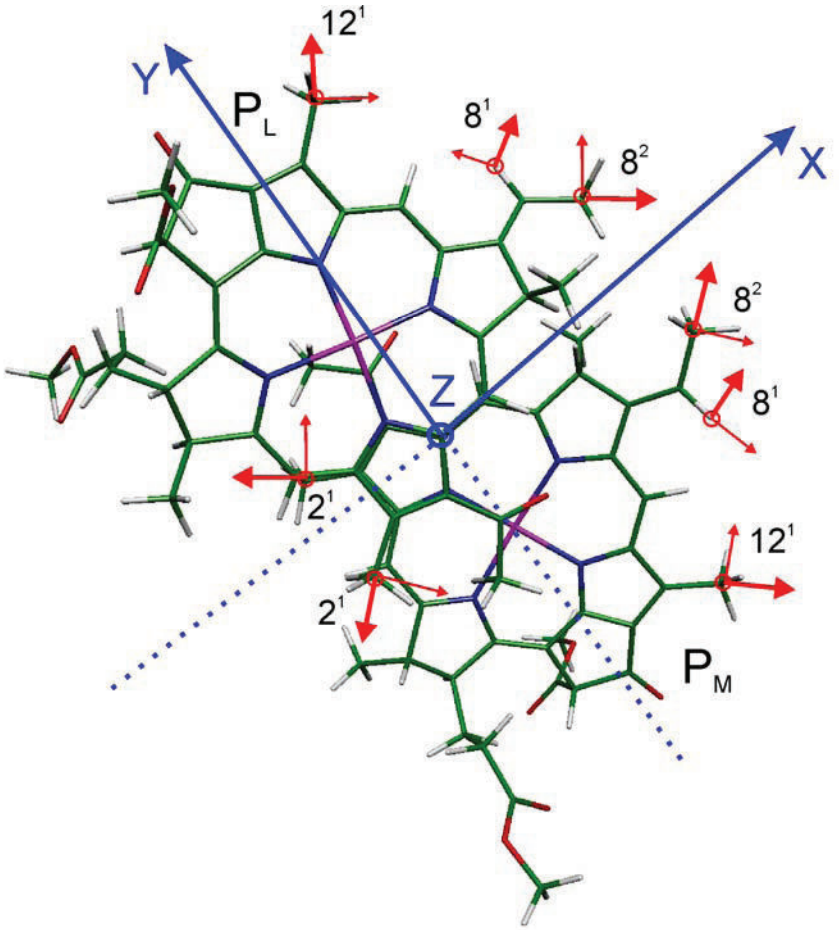

Figure 7.5. Orientation of the principal axes of the ZFS tensor for $^3P_{960}$ (blue). They correspond to principal values of the ZFS tensor of –0.0095 cm^{-1} (X), –0.0013 cm^{-1} (Y) and +0.0107 cm^{-1} (Z). The orientations of the principal axes of the hyperfine tensor are shown in red for the methyl groups 2^1, 12^1, 8^2 and the methine protons 8^1. The directions of maximum hyperfine coupling are indicated in bold.

displays a broad range in which the maximum coupling occurs between X_{II} and Y_{II}. The direction of maximum coupling for methyl groups 8^2 in $^3P_{960}$ amounts to 29±3°. In line with these simple geometric arguments, the maximum hyperfine coupling for band [8] is attained near the X_{II} canonical orientation.

7.5 Conclusions

In this work a systematic study of the triplet state of the primary donor $^3P_{865}$ in bacterial reaction centers of *Rb. sphaeroides* and $^3P_{960}$ in *Bl. viridis* has been presented. ENDOR spectroscopy at 34 GHz with laser excitation on frozen solutions allowed

determination of hyperfine coupling constants, which have been assigned to protons of the bacteriochlorin macrocycle. Given that the system is large and complex and that the nature of the triplet excitation may differ when comparing the BChl dimer with the monomer, only qualitative agreement has been found between experimental results for the dimer and the monomer.[37] Still, based on comparison of $^3P_{865}$ and $^3P_{960}$ with each other and with data for the respective BChl *a* and BChl *b* monomers, either in the triplet state or as cation and anion radicals, a number of relevant aspects about the electronic structure of the triplet state has been revealed. First, the electron spin density distribution in the triplet state of $^3P_{865}$ and $^3P_{960}$ is found to be similar. Differences are present for position 8, where an ethyl group is present in $^3P_{865}$ and an ethylidene group in $^3P_{960}$. Accordingly, in the ENDOR spectra of $^3P_{960}$ two large additional couplings are present; a positive coupling stems from the methyl groups at 8^2, a negative coupling stems from methine protons at 8^1.

The electron spin density in the triplet state is distributed almost evenly over the dimer halves. This conclusion is based on the observation that the number of bands in the spectra of the dimer equals the number of bands in the spectra of the monomer. A minor splitting is observed for the bands of $^3P_{960}$, indicating a slight asymmetry. Moreover, the hyperfine coupling constants of methyl groups 2^1 and 12^1 of the dimer equal about half of those of the monomer and half of the DFT -derived coupling of the monomer. Third, the experimentally determined directions of the ZFS principal axes from single crystal EPR studies[57] also support a symmetrically delocalized triplet state, since the predicted field-frequency behaviour of ENDOR signals is in agreement with those observed in this work. Comparison of hyperfine couplings of $^3P_{865}$ and $^3P_{960}$ and hyperfine couplings of the triplet state[37] and radical cation and radical anion of bacteriochlorophyll monomer[38-42, 58] shows that the triplet state in the primary donor largely derives from a HOMO $\rightarrow$ LUMO excitation. Minor contributions from other orbitals can, however, not be excluded.

The ENDOR study of the triplet state allowed investigation of both frontiers HOMO and LUMO orbitals in the primary donor. The electron spin density distribution in HOMO orbital has also been directly investigated in studies of the radical cation of P_{865} in *Rb. sphaeroides*[44] and of P_{960} in *Bl. viridis*.[43, 60] In both cases, an asymmetric spin density distribution has been found, with a ratio 2:1 of electron spin density on P_L and P_M. The 2:1 asymmetry in the *charged* radical cation state is most likely determined by amino acids surrounding, *e.g.* perturbation of the H-bonding due to the electrostatic interactions acting on the dimer. Furthermore in the case of the radical cation, a detergent molecule LDAO, can be incorporated into the bRC during purification process, can also cause a shift of the spin

density distribution.[61] The singly occupied orbitals in the neutral triplet state seem to be less susceptible to the electrostatic surrounding

The photosynthetic charge separation starts from the LUMO orbital of P. Since the triplet state ^{3}P has the same electronic configuration as the singlet excited state P*, the LUMO orbital of ^{3}P is arguably the best model for the LUMO orbital of P*. The evenly delocalized LUMO orbital found here indicates that asymmetry of photosynthetic charge separation with respect to the A and B branches of cofactors is *not* related to internal asymmetry of the electronic structure of the primary donor and most likely indeed stems from differences in the hydrogen-bonding network of both branches, causing different site energies ΔG[62] for the two branches.

Further investigation should include ENDOR studies on the mutants with perturbed H-bonds to the dimer and on mutants, which influence the ligation or π stacking. Moreover, a reliable calculations of spin density distribution and clear distinction between isotropic and dipolar are required. Since DFT method is not able to take in the account non-covalent π stacking and interaction of two dimer halves, more advanced calculations such as CASCF or *ab initio*,[63, 64] combined with molecular mechanics calculations, could be performed. Such experiments and calculations are underway in our laboratories.

7.6 References

(1) Blankenship, R. *Molecular mechanisms of photosynthesis;* Blackwell Science: Oxford, London, 2002.

(2) Breton, J.; Vermeglio, A. *The Photosynthetic Bacterial Reaction Center – Structure and Dynamics;* Plenum Press: New York, 1988.

(3) Breton, J.; Vermeglio, A. *The Photosynthetic Bacterial Reaction Center II;* Plenum Press: New York, 1992.

(4) Michel-Beyerle, M. E. *Reaction Centers of Photosynthetic Bacteria;* Springer Verlag: Berlin, 1990.

(5) Michel-Beyerle, M. E. *Reaction Centers of Photosynthetic Bacteria - Structure and Dynamics;* Springer Verlag: Berlin, 1996.

(6) Deisenhofer, J.; Norris, J.R. *The photosynthetic reaction center;* Academic Press: San Diego, 1993.

(7) Weber, S. Recent EPR studies on the bacterial photosynthetic reaction center. In *Electron Paramagnetic Resonance*; Gilbert, B. C., Davies, and McLauchlan, Eds.;Royal Society of Chemistry: Cambridge, 2000; pp 43-77, and references therein.

(8) Blankenship, B.; Madigan, M.; Bauer, C. *Anoxygenic Photosynthetic Bacteria;* Kluwer Academic Publishers: 1995.

(9) Hunter, C. N.; Daldal, F.; Thurnauer, M.C.; Beautty, J.T. *The purple photrophic bacteria;* Springer: Heidelberg, 2009.

(10) Allen, J. P.; Feher, G. (1984) Crystallization of Reaction Center from Rhodopseudomonas-Sphaeroides - Preliminary Characterization, *Proc. Natl. Acad. Sci. USA, 81*, 4795-4799.

(11) Allen, J. P.; Feher, G.; Yeates, T. O.; Rees, D. C.; Deisenhofer, J.; Michel, H.; Huber, R. (1986) Structural Homology of Reaction Centers from Rhodopseudomonas-Sphaeroides and Rhodopseudomonas-Viridis As Determined by X-Ray-Diffraction, *Proc. Natl. Acad. Sci. USA, 83*, 8589-8593.

(12) Allen, J. P.; Feher, G.; Yeates, T. O.; Komiya, H.; Rees, D. C. (1987) Structure of the Reaction Center from *Rhodobacter sphaeroides* R-26 - the Cofactors, *Proc. Natl. Acad. Sci. USA, 84*, 5730-5734.

(13) Allen, J. P.; Feher, G.; Yeates, T. O.; Komiya, H.; Rees, D. C. (1987) Structure of the Reaction Center from *Rhodobacter sphaeroides* R-26 - the Protein Subunits, *Proc. Natl. Acad. Sci. USA, 84*, 6162-6166.

(14) Yeates, T. O.; Komiya, H.; Rees, D. C.; Allen, J. P.; Feher, G. (1987) Structure of the Reaction Center from Rhodobacter-Sphaeroides R-26 - Membrane-Protein Interactions, *Proc. Natl. Acad. Sci. USA, 84*, 6438-6442.

(15) Allen, J. P.; Feher, G.; Yeates, T. O.; Komiya, H.; Rees, D. C. (1988) Structure of the Reaction Center from *Rhodobacter sphaeroides* R-26 - Protein Cofactor (Quinones and Fe-2+) Interactions, *Proc. Natl. Acad. Sci. USA, 85*, 8487-8491.

(16) Allen, J. P.; Feher, G.; Yeates, T. O.; Komiya, H.; Rees, D. C. Structure of the Reaction Center from Rhodobacter sphaeroides R-26 and 2.4.1. In *The Photosynthetic Bacterial Reaction Center*; Breton, J. and Vermeglio, Eds.;Plenum Press: 1988; pp 5-11.

(17) Yeates, T. O.; Komiya, H.; Chirino, A.; Rees, D. C.; Allen, J. P.; Feher, G. (1988) Structure of the Reaction Center from *Rhodobacter sphaeroides* R-26 and 2.4.1-Protein-Cofactor (Bacteriochlorophyll, Bacteriopheophytin, and Carotenoid) Interactions, *Proc. Natl. Acad. Sci. USA, 85*, 7993-7997.

(18) Feher, G.; Allen, J. P.; Okamura, M. Y.; Rees, D. C. (1989) Structure and Function of Bacterial Photosynthetic Reaction Centers, *Nature, 339*, 111-116.

(19) Michel, H. (1982) 3-Dimensional Crystals of A Membrane-Protein Complex - the Photosynthetic Reaction Center from *Rhodopseudomonas viridis*, *J. Mol. Biol., 158*, 567-572.

(20) Deisenhofer, J.; Epp, O.; Miki, K.; Huber, R.; Michel, H. (1984) X-Ray Structure-Analysis of A Membrane-Protein Complex - Electron-Density Map at 3A Resolution and A Model of the Chromophores of the Photosynthetic Reaction Center from *Rhodopseudomonas viridis*, *J. Mol. Biol., 180*, 385-398.

(21) Deisenhofer, J.; Epp, O.; Miki, K.; Huber, R.; Michel, H. (1985) Structure of the Protein Subunits in the Photosynthetic Reaction Center of Rhodopseudomonas-Viridis at 3A Resolution, *Nature, 318*, 618-624.

(22) Michel, H. The Photosynthetic Reaction Centre from the purple bacterium *Rhodopseudomonas viridis*. A Nobel lecture: 1988.

(23) Ermler, U.; Fritzsch, G.; Buchanan, S. K.; Michel, H. (1994) Structure of the Photosynthetic Reaction-Center from *Rhodobacter sphaeroides* at 2.65-Angstrom Resolution - Cofactors and Protein-Cofactor Interactions, *Structure, 2*, 925-936.

(24) Plato, M.; Möbius, K.; Michel-Beyerle, M. E.; Bixon, M.; Jortner, J. (1988) Intermolecular Electronic Interactions in the Primary Charge Separation in Bacterial Photosynthesis, *J. Am. Chem. Soc., 110*, 7279-7285.

(25) Volk, M.; Aumeier, G.; Langenbacher, T.; Feick, R.; Ogrodnik, A.; Michel-Beyerle, M. E. (1998) Energetics and mechanism of primary charge separation in bacterial photosynthesis. A comparative study on reaction centers of *Rhodobacter sphaeroides* and *Chloroflexus aurantiacus*, *J. Phys. Chem. B, 102*, 735-751.

(26) Michel-Beyerle, M. E.; Plato, M.; Deisenhofer, J.; Michel, H.; Bixon, M.; Jortner, J. (1988) Unidirectionality of Charge Separation in Reaction Centers of Photosynthetic Bacteria, *Biochim. Biophys. Acta, 932*, 52-70.

(27) Plato, M.; Möbius, K.; Lubitz, W.; Allen, J. P.; Feher, G. Magnetic resonance and molecular orbital studies of the primary donor states in bacterial reaction centers. In *Perspectives in Photosynthesis*; Jortner, J. and Pullman, Eds.;Kluwer Academic Publishers: 1990; pp 423-434.

(28) Gouterman, M. (1959) Study of the Effects of Substitution on the Absorption Spectra of Porphin, *J. Chem. Phys., 30*, 1139-1161.

(29) Gouterman, M. (1961) Spectra of Porphyrins, *J. Mol. Spectrosc., 6*, 138-163.

(30) Thurnauer, M. C. (1979) ESR study of the photoexcited triplet state in photosynthetic bacteria, *Rev. Chem. Int., 100*, 197-231.

(31) Levanon, H.; Norris, J. R. (1978) Photoexcited Triplet-State and Photosynthesis, *Chem. Rev., 78*, 185-198.

(32) Angerhofer, A. Chlorophyll triplets and radical pairs. In *Chlorophylls*; Scheer, H., Ed.;CRC Press: Boca Raton FL, 1991; pp 945-991.

(33) Lendzian, F.; Bittl, R.; Lubitz, W. (1998) Pulsed ENDOR of the photoexcited triplet states of bacteriochlorophyll a and of the primary donor P-865 in reaction centers of *Rhodobacter sphaeroides* R-26, *Photosynth. Res., 55*, 189-197.

(34) Lubitz, W.; Lendzian, F.; Bittl, R. (2002) Radicals, radical pairs and triplet states in photosynthesis, *Acc. Chem. Res., 35*, 313-320.

(35) Lendzian, F.; van Willigen, H.; Sastry, S.; Möbius, K.; Scheer, H.; Feick, R. (1985) Proton Endor Study of the Photoexcited Triplet-State Pt in Rps-Sphaeroides R-26 Photosynthetic Reaction Centers, *Chem. Phys. Let., 118*, 145-150.

(36) Marchanka, A.; Paddock, M.; Lubitz, W.; van Gastel, M. (2007) Low-temperature pulsed EPR study at 34 GHz of the Triplet states of the primary electron donor P-865 and the carotenoid in native and mutant bacterial reaction centers of Rhodobacter sphaeroides, *Biochemistry, 46*, 14782-14794.

(37) Marchanka, A.; Lubitz, W.; van Gastel, M. (2009) Spin density distribution on the excited triplet state of bacteriochlorophyll. Pulsed ENDOR and DFT studies, *J. Phys. Chem. B, 113*, 6917-6927.

(38) Lubitz, W.; Lendzian, F.; Plato, M.; Scheer, H.; Möbius, K. (1997) The bacteriochlorophyll a cation radical revisited. An ENDOR and TRIPLE resonance study, *Appl. Magn. Reson, 13*, 531-551.

(39) Borg, D. C.; Forman, A.; Fajer, J. (1976) Esr and Endor Studies of Pi-Cation Radical of Bacteriochlorophyll, *J. Am. Chem. Soc., 98*, 6889-6893.

(40) Lubitz, W.; Lendzian, F.; Möbius, K. (1981) N-14 and H-1 Electron Nuclear Multiple Resonance Experiments on Bacteriochlorophyll-A Anion Radicals in Solution, *Chem. Phys. Let., 81*, 235-241.

(41) Fajer, J.; Borg, D. C.; Forman, A.; Dolphin, D.; Felton, R. H. (1973) Anion Radical of Bacteriochlorophyll, *J. Am. Chem. Soc., 95*, 2739-2741.

(42) Davis, M. S.; Forman, A.; Hanson, L. K.; Thornber, J. P.; Fajer, J. (1979) Anion and Cation Radicals of Bacteriochlorophyll and Bacteriopheophytin-B - Their Role in the Primary Charge Separation of Rhodopseudomonas-Viridis, *J. Phys. Chem., 83*, 3325-3332.

(43) Lendzian, F.; Lubitz, W.; Scheer, H.; Hoff, A. J.; Plato, M.; Tränkle, E.; Möbius, K. (1988) Electron-Spin-Resonance, Endor and Triple Resonance Studies of the Primary Donor Radical Cation P-960+. in the Photosynthetic Bacterium Rhodopseudomonas-Viridis, *Chem. Phys. Let., 148*, 377-385.

(44) Lendzian, F.; Huber, M.; Isaacson, R. A.; Endeward, B.; Plato, M.; Bönigk, B.; Möbius, K.; Lubitz, W.; Feher, G. (1993) The Electronic-Structure of the Primary Donor Cation-Radical in Rhodobacter-Sphaeroides R-26 - Endor and Triple-Resonance Studies in Single-Crystals of Reaction Centers, *Biochim. Biophys. Acta, 1183*, 139-160.

(45) Feher, G.; Okamura, M. Y. Chemical composition and properties of reaction centers. In *The Photosynthetic Bacteria*; Clayton, R. and Sistrom, Eds.;Plenum Press: New York, 1978; pp 349-386.

(46) Trosper, T. L.; Benson, D. L.; Thornber, J. P. (1977) Isolation and Spectral Characteristics of Photochemical Reaction Center of Rhodopseudomonas-Viridis, *Biochim. Biophys. Acta, 460*, 318-330.

(47) Schweiger, A.; Jeschke, G. *Principles of Pulse Electron Paramagnetic Resonance;* Oxford University Press: 2001.

(48) Gardiner, A. T.; Zech, S. G.; MacMillan, F.; Käß, H.; Bittl, R.; Schlodder, E.; Lendzian, F.; Lubitz, W. (1999) Electron paramagnetic resonance studies of zinc-

substituted reaction centers from Rhodopseudomonas viridis, *Biochemistry, 38*, 11773-11787.

(49) Thurnauer, M. C.; Katz, J. J.; Norris, J. R. (1975) Triplet-State in Bacterial Photosynthesis - Possible Mechanisms of Primary Photo-Act, *Proc. Natl. Acad. Sci. USA, 72*, 3270-3274.

(50) Thurnauer, M. C.; Norris, J. R. (1977) Ordering of Zero-Field Triplet Spin Sub-Levels in Chlorophylls - Magneto-Photoselection Study, *Chem. Phys. Let., 47*, 100-105.

(51) Hoff, A. J.; Proskuryakov, I. I. (1985) Triplet Electron-Paramagnetic-Res Spectra of the Primary Electron-Donor in Bacterial Photosynthesis at Temperatures Between 15-K and 296-K, *Chem. Phys. Let., 115*, 303-310.

(52) Frank, H. A.; Bolt, J. D.; Costa, S. M. D. B.; Sauer, K. (1980) Electron-Paramagnetic Resonance Detection of Carotenoid Triplet-States, *J. Am. Chem. Soc., 102*, 4893-4898.

(53) Frank, H. A.; Chynwat, V.; Hartwich, G.; Meyer, M.; Katheder, I.; Scheer, H. (1993) Carotenoid Triplet-State Formation in *Rhodobacter sphaeroides* R-26 Reaction Centers Exchanged with Modified Bacteriochlorophyll Pigments and Reconstituted with Spheroidene, *Photosynth. Res., 37*, 193-203.

(54) Atherton, N. *Principles of Electron Spin Resonance;* Ellis Horwood PTR Prentice Hall: New York, 1993.

(55) Carrington, A.; McLachlan, A.D. *Introduction to magnetic resonance;* Harper & Row; John Weatherhill Inc.: New York, Evanston, London, Tokyo, 1967.

(56) Budil, D. E.; Taremi, S. S.; Gast, P.; Norris, J. R.; Frank, H. A. (1988) Single-Crystal Electron-Spin Resonance Studies of the Photochemical-Reaction Center from Rhodobacter-Sphaeroides Wild-Type Strain 2.4.1, *Isr. J. Chem., 28*, 59-66.

(57) Norris, J. R.; Budil, D. E.; Gast, P.; Chang, C. H.; Elkabbani, O.; Schiffer, M. (1989) Correlation of Paramagnetic States and Molecular-Structure in Bacterial Photosynthetic Reaction Centers - the Symmetry of the Primary Electron-Donor in Rhodopseudomonas-Viridis and Rhodobacter-Sphaeroides R-26, *Proc. Natl. Acad. Sci. USA, 86*, 4335-4339.

(58) Lubitz, W. EPR and ENDOR studies of chlorophyll cation and anion radicals. In *The Chlorophylls*; Scheer, H., Ed.;CRC Press: Boca Raton, 1991; pp 903-944.

(59) Vrieze, J.; Hoff, A. J. (1995) The Orientation of the Triplet Axes with Respect to the Optical-Transition Moments in (Bacterio)Chlorophylls, *Chem. Phys. Let., 237*, 493-501.

(60) Plato, M.; Lendzian, F.; Lubitz, W.; Tränkle, E.; Möbius, K. Molecular orbital studies on the primary donor P_{960} in reaction centers of *Rps. viridis*. In *The Photosynthetic Bacterial Reaction Center – Structure and Dynamics*; Breton, J. and Vermeglio, Eds.;Plenum Press: New York, 1988; pp 379-388.

(61) Müh, F.; Lendzian, F.; Roy, M.; Williams, J. C.; Allen, J. P.; Lubitz, W. (2002) Pigment-protein interactions in bacterial reaction centers and their influence on

oxidation potential and spin density distribution of the primary donor, *J. Phys. Chem. B, 106*, 3226-3236.

(62) Marcus, R. A.; Sutin, N. (1985) Electron Transfers in Chemistry and Biology, *Biochim. Biophys. Acta, 811*, 265-322.

(63) Szabo, A.; Ostlund, N.S. *Modern Quantum Chemistry;* Duver Publications, Inc.: New York, 1996.

(64) Koch, W.; Holthausen, M.C. *A Chemist's Guide to Density Functional Theory;* Wiley-VCH: Weinheim-New York-Torronto, 1999.

Chapter 8

B-branch electron transfer in a quadruple mutant of *Rb. sphaeroides*[*]

Abstract

The triplet state of the primary electron donor, P_{865}, in the photosynthetic bacterial reaction center of *Rb. sphaeroides* quadruple mutant, HL(M182)/GD(M203)/LH(M214)/AW(M260), has been investigated in a wide range of temperatures and at different excitation wavelengths using EPR spectroscopy at 34 GHz. At 10 K, the triplet state has been found to derive mainly from an intersystem crossing mechanism, indicating the absence of long-lived charge separated states. B-branch charge separation and formation of the triplet state $^3P_{865}$ *via* a radical pair mechanism can be induced with low yield at 10 K by direct excitation of the native and genetically introduced bacteriopheophytin in the B-branch at 537 nm. At this wavelength, charge separation most probably proceeds *via* hole transfer from bacteriopheophytin to the primary donor. The triplet state of the primary donor is found to be quenched by the carotenoid cofactor present in the reaction center.

[*] This chapter is based on publication "B-branch electron transfer in the genetically modified reaction center of *Rb. sphaeroides*" by Marchanka, A., Lubitz, W., Savitsky, A., Möbius, K., van Gastel, M.(2009), *to be submitted to Biochemistry*

8.1 Introduction

Bacterial reaction center proteins of purple photosynthetic bacteria contain two almost symmetrically arranged branches of cofactors, A and B. Each branch consists of an accessory bacteriochlorophyll, a bacteriopheophytin and a quinone (Fig. 8.1a).[1] Photosynthetic charge separation in the native system has been found to start from a singlet excited dimer of bacteriochlorophylls, called the primary donor, through a series of intermediate states that exclusively involves the accessory bacteriochlorophyll and bacteriopheophytin on the A-branch and both quinones.[2, 3] The uni-directionality of charge separation *via* the A-branch has first been detected and investigated by optical spectroscopy at cryogenic temperatures, where the Q_x bands of the bacteriopheophytins in the A and B branches in the visible absorption spectrum become resolved. After light excitation, only one Q_x band bleaches, which means that only one bacteriopheophytin is active in the charge separation.[4] Linear dichroism studies have shown that the bacteriopheophytin active in charge separation is BPheo *a* in the A-branch, H_A.[4-6] The ratio of the electron transfer *via* the B-branch and A-branch has an upper limit of one percent.[5, 7-10] The origin of the low yield of electron transfer *via* the B-branch in native bacterial reaction centers is still a question of debate. It may arise from the breaking of the two-fold symmetry at several places in the structure of the reaction center.[3] These comprise differences in the distance and mutual orientations and electronic structures of the cofactors in the A- and B-branch. These result in different electron transfer matrix elements, different reorganization energies and site energies of cofactors for the electron transfer in both branches, whose fine tuning determines the rates of the electron transfer.[2, 11]

Many studies have been performed using site directed mutagenesis to promote electron transfer through the B-branch.[7, 9, 12-16] For example, a point mutation LH(M214) introduces a histidine near the bacteriopheophytin in the A-branch, whereby the BPheo *a* converts to a BChl *a* (called *β*). In this mutated reaction center it has been found by optical techniques[17, 18] that with depleted or prereduced quinone Q_A, the lifetime of the radical pair state $P^{\bullet+}\beta^{\bullet-}$ shortens to 350 ps as compared to the lifetime of the radical pair $P^{\bullet+}H^{\bullet-}$ in native reaction centers with prereduced Q_A, which is above 10 ns.[9, 14, 15, 18, 19]

The photosynthetic activity of the B-branch can be advantageously probed by EPR spectroscopy of the paramagnetic triplet state (S = 1) of the primary donor, $^3P_{865}$. During photosynthetic charge separation in the native bacterial reaction center, the triplet state only plays a minor role. However, if the quinone cofactors are prereduced, for example by addition of sodium dithionite, the photoexcited electron cannot travel further than H_A. The

$P^{\bullet+}H_A^{\bullet-}$ radical pair state then has a lifetime long enough to convert to the triplet RP and can recombine to yield $^3P_{865}$.[20] Since the radical pair state is initially present as a singlet state, it exclusively forms a triplet radical pair state in the $M_S = 0$ triplet sublevel in about 10 ns at cryogenic temperatures.[20, 21] Within this radical pair (RP) mechanism of triplet formation, $^3P_{865}$ is also exclusively populated in the $M_S = 0$ state and an EPR signal with a characteristic polarization pattern AEEAAE (E – emissive, A – absorptive) is observed.[22-25] Since it typically takes 10 ns to convert the singlet radical pair into a triplet radical pair, EPR spectroscopy is blind to radical pair intermediate states that recombine on a timescale shorter than ~ 10 ns.

In a recent EPR study, the triplet state of the native bacterial reaction center of *Rb. sphaeroides* and that of the carotenoidless mutant R-26.1 and two double mutants GD(M203)/AW(M260) and LH(M214)/AW(M260) have been investigated.[26] The GD(M203) mutation changes the H-bonding network and local charge distribution near the accessory bacteriochlorophyll and makes the electron transport over the A-branch energetically less favourable. The mutation AW(M260) introduces a tryptophan in the binding pocket of Q_A, which blocks the access for the quinone to its native position.[16, 27] In *Rb. sphaeroides* 2.4.1, R-26.1 and mutant GD(M203)/AW(M260), an AEEAAE polarization pattern is observed, which indicates the presence of a long-lived radical pair and a radical pair (RP) mechanism of triplet formation. In the mutant LH(M214)/AW(M260) a triplet state with the same ZFS splitting parameters, but with a different polarization pattern (EEEAAA) and with strongly reduced EPR signal intensity has been observed.[26] This polarization pattern can only be explained by a spin flip of one of the unpaired electrons of P* and a direct formation of $^3P_{865}$ without radical pair intermediate states. In this intersystem crossing (ISC) mechanism the principal spin-dependent interactions are responsible for the spin flip are spin-orbit (SO) coupling and spin-spin (SS) interaction.[28] The observation of an ISC triplet state with EEEAAA polarization indicates that a long-lived radical pair state is absent in both branches.[26] Thus, even when long-lived (> 10 ns) charge separated states at the A-branch are knocked out by the LH(M214) and AW(M260) mutations, it was found that long-lived charge separation in the B-branch still does not occur.[26]

The polarization pattern of the triplet state $^3P_{865}$ thus gives important information about the presence of long-lived precursor radical pair states in the A and B branches. Moreover, in the bacterial reaction center of *Rb. sphaeroides*, the triplet state $^3P_{865}$ is taken over by the carotenoid cofactor.[29-31] The triplet-triplet transfer occurs only at temperatures above 30 K and proceeds *via* the accessory bacteriochlorophyll in the B-branch.[31-34] Since the

sign of the ZFS parameter *D* of ^{3}Car is opposite to that of $^3P_{865}$, the spectrum of ^{3}Car has an inversed polarization pattern compared to that of $^3P_{865}$, EAAEEA for the RP formed triplet state.[26] For the ISC triplet state, the polarization pattern of ^{3}Car also depends on the relative orientations of the ZFS tensors of $^3P_{865}$ and ^{3}Car. Thus, also the polarization pattern of ^{3}Car contains information about the presence or absence of long-lived radical pair states at either the A or the B branch.

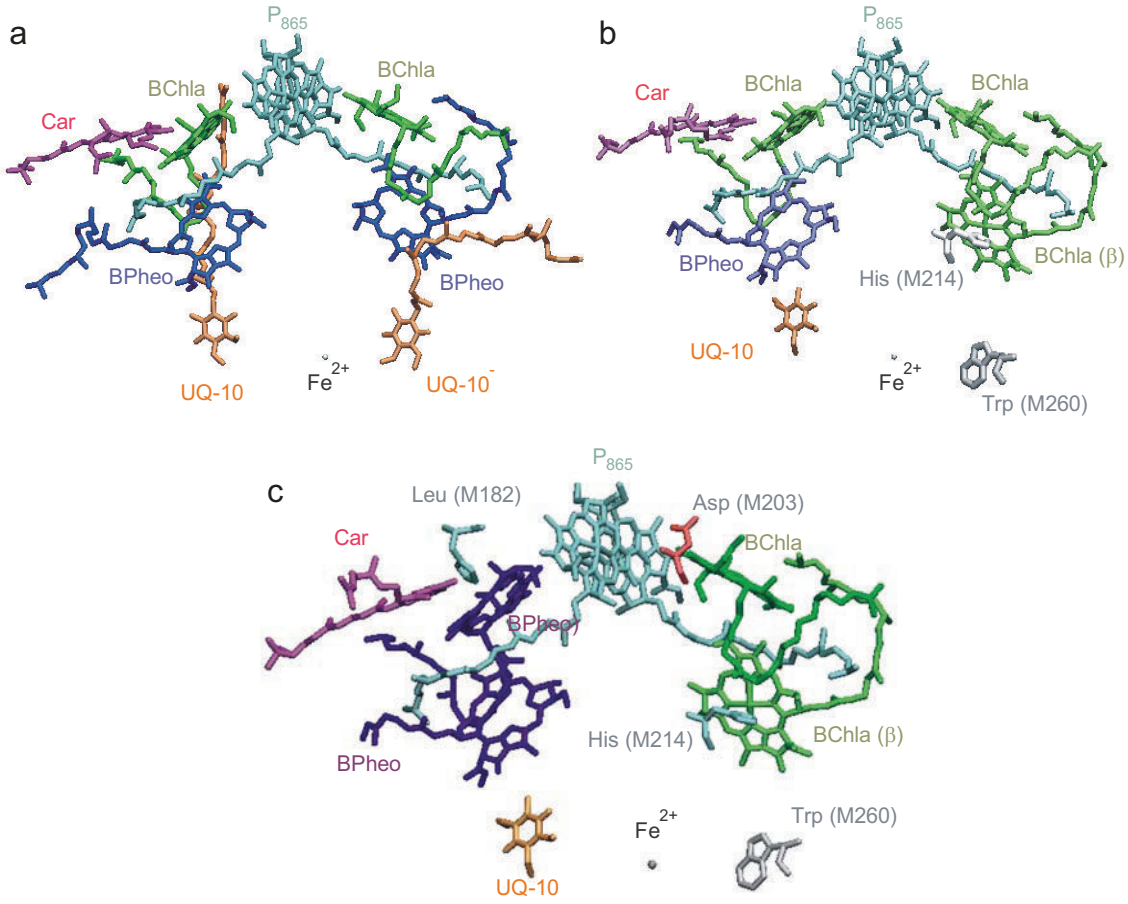

Figure 8.1. Cofactor arrangement in the bacterial reaction centers of (a) *Rb. sphaeroides* 2.4.1 (PDB code: 4rcr), (b) *Rb. sphaeroides* double mutant LH(M214)/AW(M260), and (c) *Rb. sphaeroides* LDHW quadruple mutant HL(M182)/GD(M203)/LH(M214)/AW(M260).[14] The mutation HL(M182) replaces the histidine ligand to B_B by leucine by which the accessory bacteriochlorophyll B_B is changed to a bacteriopheophytin, Φ_B; the GD(M203) mutation changes the H-bonding network and local charge distribution near the accessory bacteriochlorophyll and makes the electron transport over the A-branch energetically less favourable; the mutation LH(M214) introduces a histidine near the bacteriopheophytin H_A in the A-branch, whereby the BPheo *a* converts to a BChl *a*; the mutation AW(M260) depletes the quinone Q_A from its binding pocket.

Here, a quadruple mutant[14] of *Rhodobacter (Rb.) sphaeroides*, called HL(M182)/GD(M203)/LH(M214)/AW(M260) (LDHW), is investigated. The cofactor arrangement and the mutations are shown in Fig. 8.1c. For comparison, the cofactors in *Rb.*

sphaeroides wild type (Fig. 8.1a) and *Rb. sphaeroides* LH(M214)/AW(M260) double mutant (Fig. 8.1b) are also shown. Three of four mutations, GD(M203), LH(M214) and AW(M260) are identical to those of the afore mentioned mutants. The fourth mutation HL(M182) is the replacement of the histidine ligand to B_B by leucine by which the accessory bacteriochlorophyll B_B is changed to a bacteriopheophytin, Φ_B. It has been reported that the presence of Φ_B leads to an increased B-branch electron transfer,[12, 13, 35] a yield of up to 40 % at room temperature has been suggested.[14] Moreover, both bacteriopheophytins in the B-branch have been found to participate in the charge separation process.[14] The recombination times of the radical pairs $P^{\bullet+}H_B^{\bullet-}$ and $P^{\bullet+}\Phi_B^{\bullet-}$ at 10 K were found to be similar and below 1 ns.[14] This time constant is larger than that of the *Rb. sphaeroides* single mutant HL(M182),[12] where a time constant for recombination of 200 ps at room temperature has been observed.

The aim of this study is to detect long-lived charge separated states at the B-branch using the triplet state $^3P_{865}$ as a probe. Triplet EPR spectra have been recorded at different wavelengths, that either excite P_{865}, BChl *a* or BPheo *a*. Since, a carotenoid is present in the LDHW mutant, also the kinetics of triplet formation and decay of $^3P_{865}$ and ^{3}Car have been investigated. No significant long-lived radical pair states of the B-branch at 10 K have been detected when the primary donor P_{865} is directly excited. However, long-lived B-branch radical pair formation could be observed at low yield by direct excitation of the bacteriopheophytins with a wavelength of 537 nm. This radical pair formation is also observable at elevated temperatures.

8.2 Materials and methods

Sample preparation

Rb. sphaeroides mutant LDHW was expressed and purified according to de Boer *et al*.[14] In this work, the mutagenesis system originally developed by Paddock *et al*[36] has been used. Measurements were performed on samples containing the herbicide terbutryn, which blocks the Q_B site and thus prevents the formation of the long-lived radical pair $P^{\bullet+}Q_B^{\bullet-}$. For the triplet EPR investigations, samples have been frozen in liquid nitrogen in the dark. The optical density of the samples was 50 at 865 nm. The purity of the samples was verified by UV/VIS measurements at room temperature.

Pulsed EPR

Electron spin echo (ESE) detected EPR spectra were recorded on a Bruker Q-band Elexsys E580 FT pulse EPR spectrometer with pulsed laser excitation as described previously.[26, 37] Excitation at 537 nm has been performed with 9 mJ/pulse, at 590 nm with 7.5 mJ/pulse and at 865 nm with 3.0 mJ/pulse. Since the absorption maximum of the primary donor dimer band depends on the temperature, the excitation wavelength was optimized around 865 nm to obtain maximum intensity of the EPR signal. The EPR experiments have been performed in the temperature range of 10 K to 150 K. The two-pulse EPR and delay-after-flash (DAF)-EPR schemes consist of a laser pulse followed by two microwave pulses and followed by detection *via* a Hahn echo.[38] In the ESE-detected EPR experiments the magnetic field is swept. In DAF-EPR, the magnetic field is fixed and the delay time between laser pulse and the first microwave pulse is swept. Pulse lengths and delay times have been described elsewhere.[26] The accumulation time was typically 0.5 - 2 hours for an EPR spectrum depending on the temperature, at which the measurements have been performed.

8.3 Results and discussion

EPR spectra at 10 K using excitation at 865 nm, 590 nm or 537 nm

A transient EPR spectrum of the RP-formed $^3P_{865}$ of wild type and of the ISC-formed $^3P_{865}$ of the LH(M214)/AW(M260) mutant recorded at 34 GHz and 10 K are shown in Fig. 8.2a, top and middle, respectively. Additionally, an ESE detected EPR spectrum of RP-formed ^{3}Car is shown in Fig. 8.2a, bottom.

Q-band ESE-detected EPR spectra of a dark-frozen sample of reaction centers of the *Rb. sphaeroides* quadruple mutant LDHW at 10 K, excited at 537 nm, 590 nm, and 865 nm are shown in Fig. 8.2b. The triplet EPR spectra are characterized by polarization patterns EAEEAAEA with excitation at 537 and 590 nm, and EEEEAAAA at 865 nm (Fig. 8.2b). A polarization pattern with more than six canonical orientations indicates the presence of multiple species. The *D* and *E* values read from the spectra agree with those of $^3P_{865}$ and ^{3}Car of *Rb. sphaeroides* wild type.[26] Since the time constants of formation and decay of $^3P_{865}$ and ^{3}Car are different (see below), EPR spectra have been recorded at different time intervals between light excitation and detection (delay after flash (DAF) spectra) in order to assign the signals in the spectra to $^3P_{865}$ and ^{3}Car. The assignment of the bands is included in Fig. 8.2b. The EPR spectrum displays significantly smaller amplitudes at the absorptive transitions of

the canonical orientations X_I, Y_I, Z_I as compared to the emissive transitions, see Fig. 8.2b. This feature seems to be characteristic for $^3P_{865}$ at low temperatures using pulsed EPR at Q-band and can be explained by the ESEEM effect.[26]

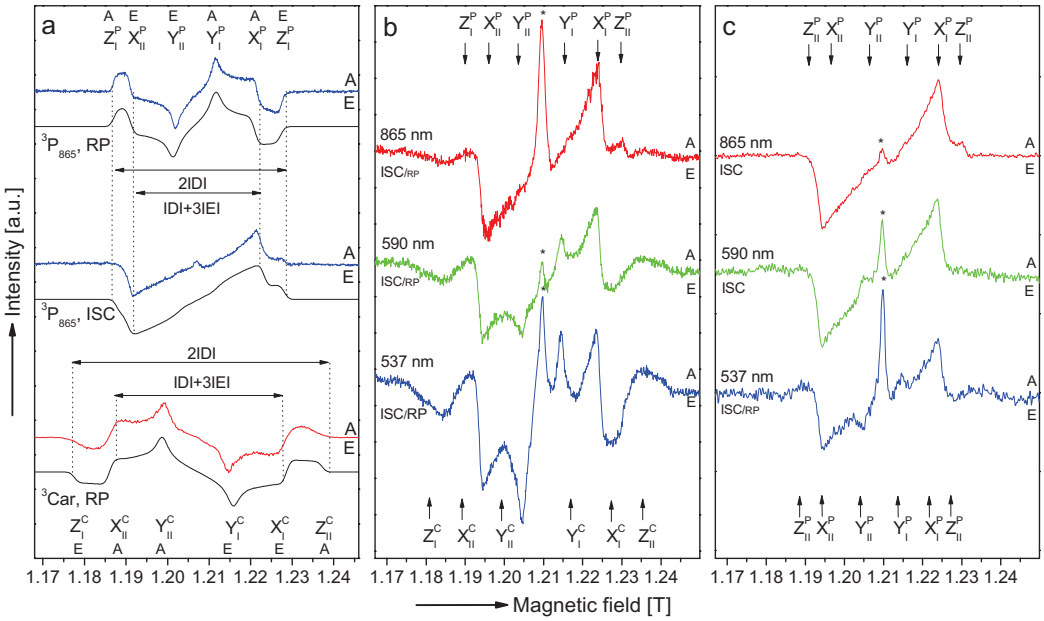

Figure 8.2. (a) (upper) transient EPR spectrum and simulation of the RP formed triplet state $^3P_{865}$ in *Rb. sphaeroides* wild type; (middle) ESE detected spectrum and simulation of the ISC formed triplet state $^3P_{865}$ in the LH(M214)/AW(M260) double mutant;[26] (bottom) ESE detected EPR spectrum and simulation of the RP formed triplet state ^{3}Car in *Rb. sphaeroides* wild type. Also depicted are the ZFS parameters *D* and *E,* the canonical orientations X, Y and Z for $^3P_{865}$ (^{P}) and ^{3}Car (^{C}) and the polarization patterns (A - absorptive, E - emissive), see text for details. (b) ESE detected EPR spectra for the LDHW mutant at 10 K and excitation wavelength of 865 nm, 590 nm, and 537 nm. (c) ESE detected EPR spectra LH(M214)/AW(M260) double mutant at 10 K and excitation wavelength of 865 nm, 590 nm, and 537 nm. The radical pair signal in the center of spectra marked with an asterisk stems from Q_B, which was not completely blocked by terbutryn.

A comparison of the EPR spectra of the bacterial reaction center in the *Rb. sphaeroides* LDHW quadruple mutant with that of *Rb. sphaeroides* wild type and LH(M214)/AW(M260)[26] is given in Fig. 8.2b,c. The EPR spectrum of the LDHW mutant with excitation at 537 nm (Fig. 8.2b) is similar to that of *Rb. sphaeroides* wild type at 10 K (Fig. 8.2a, top).[22, 25, 26] The amount of RP formed triplet state is estimated to be equal to the amount of the ISC formed triplet state in the LDHW quadruple mutant, whereas in the LH(M214)/AW(M260) double mutant, only a minor contribution of a RP-formed triplet state was observed at 537 nm excitation (Fig. 8.2c). At 590 nm, the amplitudes of all EPR signals

decrease. The amplitudes at the Y_I and Y_{II} canonical orientations decrease even more than those at X_I and X_{II}. Since the RP mechanism induces strong signals at Y_I and Y_{II} (*cf.* Fig. 8.2a), the absence thereof indicates that less long-lived radical pairs have been formed at this excitation wavelength. In the LH(M214)/AW(M260) double mutant, excitation at 590 nm yields a triplet state, which is almost completely derived from an ISC mechanism (Fig. 8.2c). At 865 nm excitation the EPR spectrum of the LDHW mutant (Fig. 8.2b) is similar to the EPR spectrum of *Rb. sphaeroides* LH(M214)/AW(M260) double mutant (Fig. 8.2a, middle, 2c) and almost exclusively displays ISC character, indicating that virtually no long-lived radical pair states are present in both branches. Apparently, direct excitation of P_{865} at 865 nm in the LDHW mutant does not induce long-lived radical pair precursor states, whereas excitation at 590 nm or 537 nm does.

It is interesting that in the LDHW mutant, the carotenoid is able to take over the triplet state already at 10 K (Fig. 8.2b, all wavelengths). In the native system and mutant, an activation barrier of 30 K was found.[32, 33] The amplitude of the signal from ^{3}Car also displays a dependence on the excitation wavelength (Fig. 8.2b). Since ^{3}Car has a larger *D* parameter than $^3P_{865}$, the presence of ^{3}Car is easily recognized at the low-field and high-field edges of the EPR spectrum. As is seen in Fig. 8.2b, significantly more ^{3}Car triplet signal is observed with excitation at 537 nm and 590 nm than at 865 nm. This observation may be related to the fact that the RP mechanism induces maximum spin polarization, where only the $M_S = 0$ sublevel is populated and the other levels are not, whereas population according to the ISC mechanism leads to a distribution over all triplet sublevel, and then to smaller spin polarization.

EPR spectra at elevated temperatures

Triplet EPR spectra of the LDHW mutant at 30 K, excited at 537 nm, 590 nm, and 865 nm are shown in Fig 8.3a, those at 50 K in Fig. 8.3b. As compared to the spectra at 10 K (Fig. 8.2b), the signals in the spectra at 30 K have become less intense. The EPR spectrum recorded with excitation at 865 nm now has increased amplitudes at Y_I and Y_{II}. Thus, with excitation at 865 nm, the triplet EPR spectra obtain more RP character at elevated temperatures. At 50 K, the EPR signals become very weak. The spectra are largely similar to those recorded at 30 K. The contribution of ^{3}Car has increased by about 10 % relative to the signal of $^3P_{865}$, which indicates that the carotenoid takes over the triplet state faster at elevated temperatures. The triplet excitation transfer to ^{3}Car observed here for the LDHW mutant is slower than that for the LH(M214)/AW(M260) mutant, where a complete quenching of the $^3P_{865}$ signal has been

observed at 50 K.[26] Nevertheless, in the LDHW mutant ^{3}Car signals have been observed at 10 K (Fig. 8.2b, all wavelengths), indicating that triplet excitation transfer to ^{3}Car seems to occur already at this temperature.

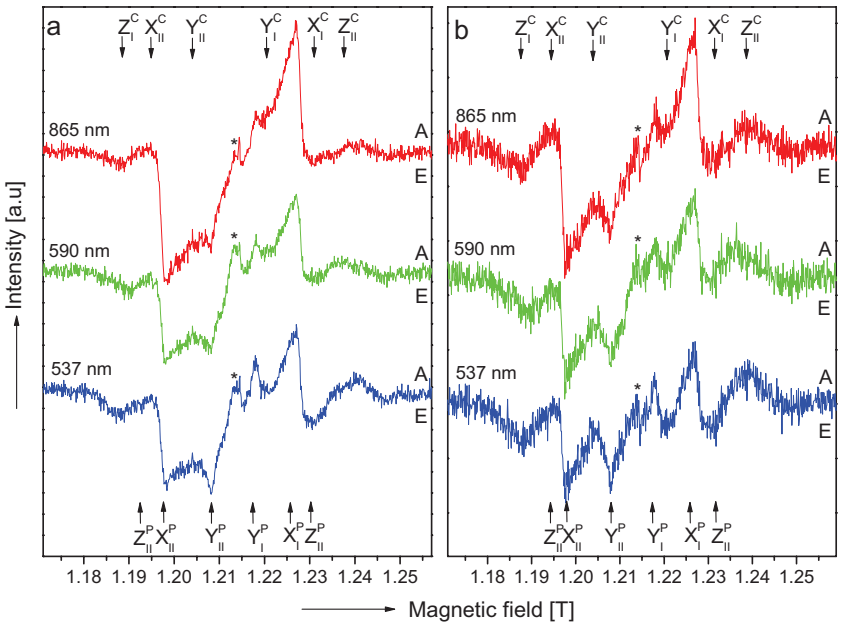

Figure 8.3. Q-band ESE detected EPR spectra the LDHW mutant at (a) 30 K and (b) 50 K recorded at excitation wavelengths of 537 nm, 590 nm, and 865 nm.

EPR measurements have also been performed at 100 K and 150 K (see Appendix D). At these temperatures the signals become even weaker and the spectra show a low signal-to-noise ratio. At 100 K, the shape of the spectra becomes excitation-wavelength independent and attains more RP character. In the spectra at 100 K, a residual amount of $^3P_{865}$ could still be detected, at 150 K only the signals from ^{3}Car are present. Though the amount of information extracted from these spectra is limited given the small signal-to-noise ratio, apparently, long-lived radical pair states are present at elevated temperatures and independent of the excitation wavelength.

Kinetics

The decay kinetics of the EPR signals from of $^3P_{865}$ and ^{3}Car have been investigated at different temperatures. The $^3P_{865}$ and ^{3}Car signals can be distinguished by DAF-EPR experiments, since the time constants for growth and decay of the $^3P_{865}$ and ^{3}Car signals are very different. The $^3P_{865}$ signals in the LDHW quadruple mutant have decay time constants of about 80 μs, which are identical to those obtained in the study on *Rb. sphaeroides* wild type

and the GD(M203)/AW(M260) mutant.[26] However, the carotenoid shows a strongly decreased decay constant (2.5-3.0 μs) at the Y canonical orientation, which is faster by a factor of four as compared to the decay constant in *Rb. sphaeroides* wild type and the LH(M214)/AW(M260) and GD(M203)/AW(M260) double mutants (15 μs).[26] The decay constants of ^{3}Car at the Z and X canonical orientations (8 μs and 27 μs) are also somewhat smaller than those for *Rb. sphaeroides* wild type (15 μs and 47 μs), see also Appendix D. Since the only mutation near the carotenoid involves the exchange of B_B to Φ_B, it is tempting to speculate that the faster decay of the ^{3}Car signals is caused by a distortion of the binding pocket and increased dynamics of the carotenoid cofactor.

8.4 Conclusions

In the LDHW mutant, the A-branch comprises two BChl *a* cofactors, the B-branch two BPheo *a* cofactors. This configuration of cofactors has been advantageously used to selectively investigate the presence of long-lived (> 10 ns) charge separated intermediate states at either of the two branches. At 10 K and excitation at 865 nm the excited state P* does not give rise to a significant amount of long-lived charge separated intermediate states at both branches, and a triplet state almost exclusively derived from the ISC triplet state mechanism is observed (Fig. 8.4a). The same observation is made for the double mutant LH(M214)/AW(M260),[26] indicating that the B-branch is not active at these temperatures even when charge separated states at the A-branch become short lived owing to mutations.

Selective excitation of the bacteriopheophytins H_B and Φ_B in the B-branch at 537 nm does, however, lead to the presence of RP based triplet EPR signals. The singlet excited states H_B* and Φ_B* have one unpaired electron in the HOMO and one in the LUMO, or alternatively, one hole in these orbitals. The radical pair states $P^{\bullet+}H_B^{\bullet-}$ and $P^{\bullet+}\Phi_B^{\bullet-}$ must then be formed by hole transfer in the HOMO orbital from H_B and Φ_B to P_{865} (Fig. 8.4b), see also Fig. 5.9 in chapter 5 for details. Selective excitation of the bacteriochlorophylls B_B and β in the A-branch at 590 nm also leads to long-lived radical pairs, but to a lesser extent than upon excitation of the bacteriopheophytins.

At elevated temperatures the wavelength dependence of the EPR spectra diminishes, which points to a higher yield of long-lived radical pairs formed directly from P_{865}^*. Simultaneously the carotenoid more efficiently takes over the triplet state, which leads to an overall decreased amplitude of the EPR signal of $^3P_{865}$ and an increased amplitude of ^{3}Car.

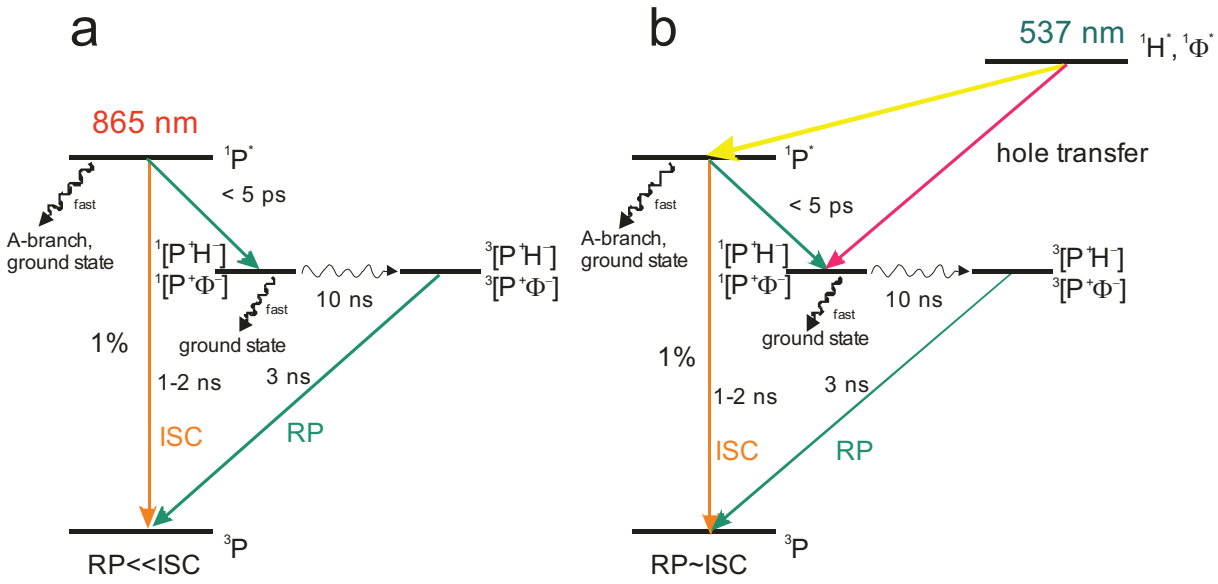

Figure 8.4. Proposed mechanism of the energy and electron transfer and charge separation in the B-branch of *Rb. sphaeroides* quadruple mutant at (a) 865 nm excitation and (b) at 537 nm excitation. The yellow arrow depicts fast energy transfer from bacteriopheophytins towards the primary donor, the magenta arrow shows the hole transfer mechanism involved in the RP-formation. The orange arrow concerns the ISC formed triplet state and the green arrow indicates the pathways for the RP formed triplet state. Also pathways of dissipation of the excitation energy are shown. See text for details.

Though it should be stressed again that EPR spectroscopy of $^3P_{865}$ is not able to detect radical pairs with recombination times shorter than 10 ns, it is the longer-lived radical pairs with long recombination times that are important for forward electron transfer. The observation that HOMO based electron or hole transfer does lead to long-lived radical pairs at 10 K when the LUMO based electron transfer from P^* is knocked out by mutation and the observation that both mechanisms are operative at elevated temperatures in the LDHW mutant, also suggests that HOMO and LUMO based charge separation likely plays a role in parallel in native reaction centers at ambient temperatures. Apparently the cofactor arrangement in the bacterial reaction center has been optimized to such an extent that the complete wavelength range covered by P_{865}, BChl *a* and BPheo *a* leads to photosynthetic charge separation, either by LUMO or HOMO based mechanisms.

8.4 References

(1) Allen, J. P., Feher, G., Yeates, T. O., Komiya, H., Rees, D. C. (1987) Structure of the Reaction Center from *Rhodobacter sphaeroides* R-26 - the Cofactors, *Proc. Natl. Acad. Sci. USA, 84*, 5730-5734.

(2) Michel-Beyerle, M. E., Plato, M., Deisenhofer, J., Michel, H., Bixon, M., Jortner, J. (1988) Unidirectionality of Charge Separation in Reaction Centers of Photosynthetic Bacteria, *Biochim. Biophys. Acta, 932*, 52-70.

(3) Feher, G., Allen, J. P., Okamura, M. Y., Rees, D. C. (1989) Structure and Function of Bacterial Photosynthetic Reaction Centers, *Nature, 339*, 111-116.

(4) Kirmaier, C., Holten, D. (1987) Primary Photochemistry of Reaction Centers from the Photosynthetic Purple Bacteria, *Photosynth. Res., 13*, 225-260.

(5) Kirmaier, C., Holten, D., Parson, W. W. (1985) Temperature and Detection-Wavelength Dependence of the Picosecond Electron-Transfer Kinetics Measured in Rhodopseudomonas-Sphaeroides Reaction Centers - Resolution of New Spectral and Kinetic Components in the Primary Charge-Separation Process, *Biochim. Biophys. Acta, 810*, 33-48.

(6) Kirmaier, C., Holten, D., Parson, W. W. (1985) Picosecond-Photodichroism Studies of the Transient States in Rhodopseudomonas-Sphaeroides Reaction Centers at 5-K - Effects of Electron-Transfer on the 6 Bacteriochlorin Pigments, *Biochim. Biophys. Acta, 810*, 49-61.

(7) Woodbury, N.; Allen, J. P. The Pathway, Kinetics and Thermodynamics of Electron Transfer in Wild Type and Mutant Reaction Centres of Purple Nonsulfur Bacteria. In *Anoxygenic photosynthetic bacteria*; Blankenship, R., Madigan, and Bauer, Eds.;Kluwer Academic Publishers: Dordrecht, Netherlands, 1995; pp 527-557.

(8) Bixon, M., Jortner, J., Michel-Beyerle, M. E., Ogrodnik, A. (1989) A Superexchange Mechanism for the Primary Charge Separation in Photosynthetic Reaction Centers, *Biochim. Biophys. Acta, 977*, 273-286.

(9) Heller, B. A., Holten, D., Kirmaier, C. (1995) Control of Electron-Transfer Between the L-Side and M-Side of Photosynthetic Reaction Centers, *Science, 269*, 940-945.

(10) Kellogg, E. C., Kolaczkowski, S., Wasielewski, M. R., Tiede, D. M. (1989) Measurement of the Extent of Electron-Transfer to the Bacteriopheophytin in the M-Subunit in Reaction Centers of Rhodopseudomonas-Viridis, *Photosynth. Res., 22*, 47-59.

(11) Marcus, R. A., Sutin, N. (1985) Electron Transfers in Chemistry and Biology, *Biochim. Biophys. Acta, 811*, 265-322.

(12) Katilius, E., Turanchik, T., Lin, S., Taguchi, A. K. W., Woodbury, N. W. (1999) B-side electron transfer in a Rhodobacter sphaeroides reaction center mutant in which the B-side monomer bacteriochlorophyll is replaced with bacteriopheophytin, *J. Phys. Chem. B, 103*, 7386-7389.

(13) de Boer, A. L., Neerken, S., de Wijn, R., Permentier, H. P., Gast, P., Vijgenboom, E., Hoff, A. J. (2002) B-branch electron transfer in reaction centers of *Rhodobacter sphaeroides* assessed with site-directed mutagenesis, *Photosynth. Res., 71*, 221-239.

(14) de Boer, A. L., Neerken, S., de Wijn, R., Permentier, H. P., Gast, P., Vijgenboom, E., Hoff, A. J. (2002) High yield of B-branch electron transfer in a quadruple reaction

center mutant of the photosynthetic bacterium *Rhodobacter sphaeroides*, *Biochemistry, 41*, 3081-3088.

(15) Haffa, A. L. M., Lin, S., Williams, J. C., Taguchi, A. K. W., Allen, J. P., Woodbury, N. W. (2003) High yield of long-lived B-side charge separation at room temperature in mutant bacterial reaction centers, *J. Phys. Chem. B, 107*, 12503-12510.

(16) Paddock, M. L., Chang, C., Xu, Q., Abresch, E. C., Axelrod, H. L., Feher, G., Okamura, M. Y. (2005) Quinone (Q(B)) reduction by B-branch electron transfer in mutant bacterial reaction centers from *Rhodobacter sphaeroides*: Quantum efficiency and X-ray structure, *Biochemistry, 44*, 6920-6928.

(17) Kirmaier, C., Laporte, L., Schenck, C. C., Holten, D. (1995) The Nature and Dynamics of the Charge-Separated Intermediate in Reaction Centers in Which Bacteriochlorophyll Replaces the Photoactive Bacteriopheophytin .1. Spectral Characterization of the Transient State, *J. Phys. Chem., 99*, 8903-8909.

(18) Kirmaier, C., Laporte, L., Schenck, C. C., Holten, D. (1995) The Nature and Dynamics of the Charge-Separated Intermediate in Reaction Centers in Which Bacteriochlorophyll Replaces the Photoactive Bacteriopheophytin .2. the Rates and Yields of Charge Separation and Recombination, *J. Phys. Chem., 99*, 8910-8917.

(19) Lin, S., Katilius, E., Haffa, A. L. M., Taguchi, A. K. W., Woodbury, N. W. (2001) Blue light drives B-side electron transfer in bacterial photosynthetic reaction centers, *Biochemistry, 40*, 13767-13773.

(20) Hore, P.J. Analysis of polarized EPR spectra. In *Advanced EPR in biology and biochemistry*; Hoff, A., Ed.;Elsevier: Amsterdam, 1990; pp 405-440.

(21) Frank, H. A., Friesner, R., Nairn, J. A., Dismukes, G. C., Sauer, K. (1979) Orientation of the Primary Donor in Bacterial Photosynthesis, *Biochim. Biophys. Acta, 547*, 484-501.

(22) Thurnauer, M. C. (1979) ESR study of the photoexcited triplet state in photosynthetic bacteria, *Rev. Chem. Int., 100*, 197-231.

(23) Volk, M., Aumeier, G., Langenbacher, T., Feick, R., Ogrodnik, A., Michel-Beyerle, M. E. (1998) Energetics and mechanism of primary charge separation in bacterial photosynthesis. A comparative study on reaction centers of *Rhodobacter sphaeroides* and *Chloroflexus aurantiacus*, *J. Phys. Chem. B, 102*, 735-751.

(24) Levanon, H., Norris, J. R. (1978) Photoexcited Triplet-State and Photosynthesis, *Chem. Rev., 78*, 185-198.

(25) Angerhofer, A. Chlorophyll triplets and radical pairs. In *Chlorophylls*; Scheer, H., Ed.;CRC Press: Boca Raton FL, 1991; pp 945-991.

(26) Marchanka, A., Paddock, M., Lubitz, W., van Gastel, M. (2007) Low-temperature pulsed EPR study at 34 GHz of the Triplet states of the primary electron donor P-865 and the carotenoid in native and mutant bacterial reaction centers of Rhodobacter sphaeroides, *Biochemistry, 46*, 14782-14794.

(27) Ridge, J. P., van Brederode, M. E., Goodwin, M. G., van Grondelle, R., Jones, M. R. (1999) Mutations that modify or exclude binding of the QA ubiquinone and carotenoid in the reaction center from *Rhodobacter sphaeroides*, *Photosynth. Res., 59*, 9-26.

(28) Neese, F. (2006) Importance of direct spin-spin coupling and spin-flip excitations for the zero-field splittings of transition metal complexes: A case study, *J. Am. Chem. Soc., 128*, 10213-10222.

(29) Hoff, A. J., Proskuryakov, I. I. (1985) Triplet Electron-Paramagnetic-Res Spectra of the Primary Electron-Donor in Bacterial Photosynthesis at Temperatures Between 15-K and 296-K, *Chem. Phys. Let., 115*, 303-310.

(30) McGann, W. J., Frank, H. A. (1985) Transient Electron-Spin Resonance Spectroscopy of the Carotenoid Triplet-State in *Rhodopseudomonas sphaeroides* Wild-Type, *Chem. Phys. Let., 121*, 253-261.

(31) Frank, H. A., Cogdell, R. J. (1996) Carotenoids in photosynthesis, *Photochem. Photobiol., 63*, 257-264.

(32) Frank, H. A., Chynwat, V., Hartwich, G., Meyer, M., Katheder, I., Scheer, H. (1993) Carotenoid Triplet-State Formation in *Rhodobacter sphaeroides* R-26 Reaction Centers Exchanged with Modified Bacteriochlorophyll Pigments and Reconstituted with Spheroidene, *Photosynth. Res., 37*, 193-203.

(33) Frank, H. A., Chynwat, V., Posteraro, A., Hartwich, G., Simonin, I., Scheer, H. (1996) Triplet state energy transfer between the primary donor and the carotenoid in *Rhodobacter sphaeroides* R-26.1 reaction centers exchanged with modified bacteriochlorophyll pigments and reconstituted with spheroidene, *Photochem. Photobiol., 64*, 823-831.

(34) Laible, P. D., Chynwat, V., Thurnauer, M. C., Schiffer, M., Hanson, D. K., Frank, H. A. (1998) Protein modifications affecting triplet energy transfer in bacterial photosynthetic reaction centers, *Biophys. J., 74*, 2623-2637.

(35) Kirmaier, C., Weems, D., Holten, D. (1999) M-side electron transfer in reaction center mutants with a lysine near the nonphotoactive B bacteriochlorophyll, *Biochemistry, 38*, 11516-11530.

(36) Paddock, M. L., Rongey, S. H., Feher, G., Okamura, M. Y. (1989) Pathway of Proton-Transfer in Bacterial Reaction Centers - Replacement of Glutamic-Acid 212 in the L-Subunit by Glutamine Inhibits Quinone (Secondary Acceptor) Turnover, *Proc. Natl. Acad. Sci. USA, 86*, 6602-6606.

(37) Marchanka, A., Lubitz, W., van Gastel, M. (2009) Spin density distribution on the excited triplet state of bacteriochlorophyll. Pulsed ENDOR and DFT studies, *J. Phys. Chem. B, 113*, 6917-6927.

(38) Schweiger, A.; Jeschke, G. *Principles of Pulse Electron Paramagnetic Resonance;* Oxford University Press: 2001.

Chapter 9

Summary and outlook

Photosynthesis is one of the most important processes on the earth. The primary processes of photosynthesis concern the absorption of photons, excitation energy transfer, and charge separation followed by electron transfer. Charge separation in bacterial photosynthesis occurs in reaction centers, which contain two nearly symmetric branches of cofactors. Triplet states in bacterial reaction centers can be used as an ideal tool for investigation of the electronic structure, i.e. spin density distribution, and indirectly the uni-directionality of the electron transfer *via* one branch of cofactors, since charge separation starts from the LUMO orbital of P^*, and both the HOMO and LUMO are singly occupied in ^3P. Furthermore, the triplet state of monomeric chlorophyll is interesting, since it can react with di-oxygen to form highly reactive species that are harmful to the reaction center. The investigation of the triplet state of carotenoid and of the mechanisms of the triplet energy quenching and dissipating is highly important due to the protective character of these processes against photooxidative damage. Triplet states in bacterial reaction centers of *Rhodobacter sphaeroides* and various mutants, in *Blastochloris viridis*, and in related model systems – *e.g.* bacteriochlorophylls *in vitro* - have been investigated with EPR/ENDOR spectroscopic methods and DFT calculations.

The triplet state of the primary donor $^3P_{865}$ in the bacterial reaction center of *Rb. sphaeroides* R-26.1, 2.4.1 and double mutant GD(M203)/AW(M260) at low temperature is formed *via* a radical pair mechanism that involves cofactors of the A-branch. In mutant LH(M214)/AW(M260) and the HL(M182)/GD(M203)/LH(M214)/AW(M260) (LDHW) quadruple mutant excitation at 865 nm leads to a completely different polarization pattern and triplet formation occurs mainly *via* an intersystem crossing mechanism. Long-lived radical-pair precursor states along the A-branch are inhibited by the mutation of bacteriopheophytin (H_A) to bacteriochlorophyll (B_A). Even upon inhibition of the A-branch, the native B-branch is found to be inactive in charge separation at T = 10 K. Only when the temperature is raised to about 30 K, the EPR spectrum shows contribution from a radical pair mechanism in mutant LH(M214)/AW(M260) and the quadruple mutant LDHW, indicating that the B-branch is "switching on" at these temperatures.

A triplet carotenoid EPR signal has been observed above 30 K, indicating that triplet-triplet transfer $P_{865} \rightarrow$ Car occurs. The growth rate of the ^{3}Car signal depends on the orientation of the reaction center in the magnetic field. The observed anisotropy of the growth rate can be traced back to that of the radical pair precursor state $[P_{865}^{\bullet+}H^{\bullet-}]$ that oscillates between the singlet and triplet states with a frequency that depends on the orientation of the bacterial reaction center in the magnetic field.

The simultaneous observation of B-branch electron transfer at excitation of 865 nm at elevated temperatures and the formation of the triplet state of carotenoid at elevated temperatures could be a sign that the energy barrier for both processes is related to the electronic structure of the accessory cofactor in the B-branch (BChl *a* for the native system, BPheo *a* for the LDHW quadruple mutant). The temperature barrier depends on the energy of the intermediate state $^3\Phi_B$ with respect to that of $^3P_{865}$ and ^{3}Car, which apparently is higher in the LDHW mutant. Still, a ^{3}Car signal is observed in this mutant even at 10 K. This seemingly barrierless mechanism of ^{3}Car formation in the LDHW quadruple mutant is not understood yet.

Small but significant changes in the electron-spin-echo detected EPR spectrum of mutant LH(M214)/AW(M260) at 10 K have been observed upon change of the excitation wavelength to 537 nm. At this wavelength the remaining bacteriopheophytin in the B-branch is directly excited. The observed additional signals seem to stem from $^3P_{865}$ that is induced by a radical pair mechanism. A possible explanation for this observation is the existence of HOMO-based electron transfer, or hole-transfer, in which the created hole on bacteriopheophytin is filled by an electron from P_{865} with concomitant formation of the B-branch radical pair $[P_{865}^{\bullet+}H_B^{\bullet-}]$. The same process has been observed in the LDHW quadruple mutant of *Rb. sphaeroides*, where the effect of 537 nm excitation was more pronounced due to the presence of two photoactive bacteriopheophytins in the B-branch.

All B-branch related long-lived processes observed in the EPR spectra at low temperature occur with an efficiency that is at most 1% of that of the corresponding processes in the A-branch. They are unable to take over photosynthetic activity when the A-branch is inactivated by mutations. At elevated temperatures the B-branch charge separation and transfer processes seem to become more efficient.

The electronic structure of the primary donor triplet itself has also been investigated in detail. Since the primary donor in the electron transfer process in bacterial reaction centers of *Rb. sphaeroides* and *Bl. viridis* is present as a special pair of BChl *a* and BChl *b*, respectively, first, a systematic study of the triplet state of BChl *a* and BChl *b* has been performed. Using

ENDOR spectroscopy at 34 GHz with laser excitation on frozen solutions and as supplementary method, DFT calculations, a set of proton hyperfine couplings has been obtained. They have been assigned to protons of the bacteriochlorin macrocycle. The electron spin density distribution in the triplet state for BChl *a* and BChl *b* is found to be similar. Spectral differences are detected for the structurally different position 8, where additional spin density is present in ^{3}BChl *b*.

The triplet state in bacteriochlorophylls was found to be not a simple HOMO LUMO excitation, but rather a combination of HOMO $\rightarrow$ LUMO and HOMO–1 $\rightarrow$ LUMO excitations. This electronic configuration is compatible with the experimentally determined directions of the principal axes of the hyperfine tensor for methyl groups and methine protons and also with the directions of the zero-field-splitting tensor from magnetophotoselection studies. Both the HOMO $\rightarrow$ LUMO and HOMO–1 $\rightarrow$ LUMO excitations may also be relevant for triplet states in related systems such as chlorophylls and porphyrin derivatives.

The study of monomeric bacteriochlorophylls by ENDOR spectroscopy is a prerequisite for the interpretation of the spin density distribution in the triplet state of the primary donor $^3P_{865}$ in bacterial reaction centers of *Rb. sphaeroides* and $^3P_{960}$ in *Bl. viridis*. Hyperfine coupling constants for $^3P_{865}$ and $^3P_{960}$ have been measured and assigned to protons of the bacteriochlorin macrocycle. The electron spin density distribution in the triplet state of $^3P_{865}$ and $^3P_{960}$, analogous to that of ^{3}BChl *a* and ^{3}BChl *b* is found to be similar. Furthermore, the hyperfine coupling constants for $^3P_{865}$ and $^3P_{960}$ of methyl group 2^1 and 12^1 are found to be half of the corresponding couplings for the monomer and the number of couplings is not doubled. No splitting of hyperfine couplings in $^3P_{865}$ is found and only a minor splitting of couplings can be detected for $^3P_{960}$. All these findings indicate that the spin density is delocalized almost *evenly* over the dimer halves both in $^3P_{865}$ and $^3P_{960}$. In contrast to BChl *a* and BChl *b* the triplet state in the primary donor largely derives from a simple HOMO $\rightarrow$ LUMO excitation. Small contributions from other excitations can, however, not be excluded.

The ENDOR study of the triplet state has allowed the investigation of both frontiers orbitals - HOMO and LUMO - of the primary donor. Though the singly occupied orbitals in the charged cation and anion radical states seem to partially localize, those of the neutral triplet state are almost evenly delocalized over the dimer halves.

The charge separation starts from the LUMO orbital of the diamagnetic P^*. Since the triplet state ^3P has the same electronic configuration as P^*, the LUMO orbital of ^3P is arguably the best model for the LUMO orbital of P*. The evenly delocalized LUMO orbital indicates that asymmetry of photosynthetic charge separation with respect to the A and B branches of

cofactors indeed does not stem from an internal asymmetry in the electronic structure of the bacteriochlorophyll dimer. Rather, differences in electronic structure of the cofactors and their surroundings, their distances and mutual orientations in both branches cause a variation of Marcus-theory parameters such as reorganization energy, change of the free energy in the reaction and different electron transfer matrix elements of both branches and thus results in strikingly different electron transfer rates in the A-branch and B-branch.

Though many hyperfine coupling constants measured in the ENDOR studies have been assigned to protons of the bacteriochlorin base, some signals could not be fully interpreted and for some protons, no signals could be observed. ENDOR measurements of the triplet state in single crystals of bacterial reaction centers of *Rb. sphaerodies* wild type and mutants would allow a more precise assignment of *all* hyperfine couplings to the molecular structure and would also deliver more accurate information about delocalization of the triplet state. Additionally, single crystal experiments at high magnetic field would deliver information about orientation of the g-tensor with respect to the zero-field splitting tensor. ENDOR experiments of bacteriopheophytin *a* and *b in vitro* are also highly relevant, since the electron that is excited at the primary donor ends up in the LUMO orbital of bacteriopheophytin. When the frontier orbitals of bacteriopheophytin are characterized, extended quantum mechanical and molecular mechanics (QM/MM) calculations of the primary donor and neighbouring amino acids and cofactors become feasible. A theoretical investigation of the mechanisms, which give rise to the difference between the rates of A and B-branch radical pair formation can then be performed.

Extended measurements have to be performed for the triplet states of carotenoids in the bacterial reaction centers of native systems and mutants. Though the triplet state is taken over by a carotenoid at elevated temperatures in *Rb. sphaeroides*, that of *Bl. viridis* is not. Perhaps the latter organism lives under conditions, which are more anaerobic than those of the former organism and the need for a triplet quenching mechanism is diminished. In any case, from an electronic structure point of view, it is not fully clear why the carotenoid is active in triplet quenching in *Rb sphaeroides* and not in *Bl. viridi*s. Time resolved optical measurements and transient EPR spectroscopy with improved time resolution could deliver information about the dynamics of triplet-triplet energy transfer in bacterial reaction centers, which may specify the possible mechanisms of the photoprotective triplet quenching. Since the triplet transfer towards carotenoid starts from the triplet state of the primary donor, the knowledge of the electronic structure of ^3P is important for understanding the triplet transfer and triplet decay in bacterial reaction centers. ENDOR experiments on $^3P_{865}$ in mutated

reaction centers with perturbed electronic structure of the primary donor and other cofactors, can reveal details of the highly effective *triplet-triplet* transfer towards carotenoid *via* the accessory cofactor in the B-branch at elevated temperature. Additionally, ENDOR spectroscopy of the triplet state of the carotenoid in native and mutated bacterial reaction centers combined with DFT calculations may deliver information about the electronic structure of the carotenoid in the excited triplet state, which is necessary to understand the mechanisms of the dissipation of the triplet excitation.

Appendix

Appendix A

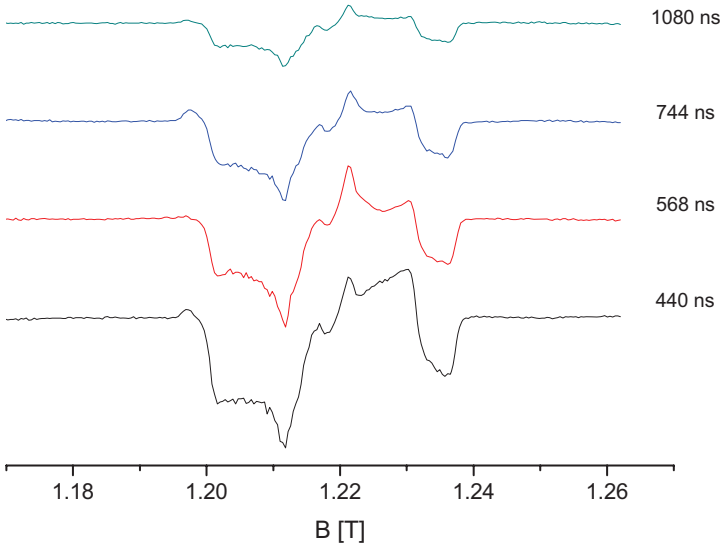

Figure A1. ESE-detected triplet EPR spectra of $^3P_{865}$ in *Rb. sphaeroides* R-26.1 at different delay time between pulses at T=10K.

Simulation of EPR spectra

The simulation program takes into account the zero-field splitting and the electron Zeeman interaction, given by the following spin Hamiltonian

$$\vec{H} = \vec{S} \cdot \vec{\vec{D}} \cdot \vec{S} + \beta_e \vec{B} \cdot \vec{\vec{g}} \cdot \vec{S} \qquad \text{(A1)}$$

Here $\vec{\vec{D}}$ is the zero-field tensor, $\vec{\vec{g}}$ is the g-tensor and β_e is the Bohr magneton. Diagonalization of the Hamiltonian gives the energy levels and the spin eigenfunctions of the triplet state. For the radical-pair (RP) mechanism, all population is present in the $M_S = 0$ level.[1, 2] For the intersystem crossing (ISC) mechanism, the population is distributed over the three triplet sublevels. Since the zero field splitting itself is also determined by(spin orbit) SO and (spin spin) SS interactions that determine the ISC rate, the equations for the populations of the triplet sublevels become

$$p_i = \sum_{u=x,y,z} c_{iu}^2 p_u \qquad \text{(A2)}$$

where $i = -1,0,+1$, p_i is the population of the $M_S = i$ sublevel, the coefficients c_{iu} represent the mixing of the zero field states in the magnetic field and p_u ($u = x, y, z$) is the population of one of the three zero-field levels. More detailed background information is available in reference.[3] The amplitude of an EPR transition is given by the population difference of the two levels involved in the transition. Since the decay of the triplet state is also mediated by ISC processes, a decay rate constant is associated with each zero-field level, according to[3, 4]

$$k_i = \sum_{u=x,y,z} c_{iu}^2 k_u \qquad \text{(A3)}$$

where k_u is the relaxation rate associated with the ZFS sublevel u. In rare cases, if the zero-field sublevels belong to the same irreducible representations of the point group of the molecule in the triplet state, interference terms may occur[5] and the equations become somewhat more complicated.

The powder spectrum is calculated by performing an orientation average in which the magnetic field direction is rotated with respect to the ZFS principal axes. Typically 100 angles were considered for the polar angle θ. Finally, the transitions are dressed with a uniform linewidth parameter. In total, nine parameters are optimized in the simulation for the RP mechanism, *i.e.*, the ZFS parameters D and E, the three g values, the three decay constants of the triplet sublevels and the linewidth parameter. For the ISC mechanism, three additional parameters describing the initial populations of the ZFS levels are needed. The $\vec{\vec{D}}$ and $\vec{\vec{g}}$ tensors are assumed to be collinear.

Simulation of triplet formation, decay and transfer kinetics

Simulation of the kinetics of the triplet carotenoid EPR signal has been performed using a model that takes into account the singlet and triplet radical-pair states, $^3P_{865}$ and ^{3}Car. The population of the singlet and triplet radical pair states oscillates back and forth with a frequency ω_{S-T_0}, which is determined by small differences in the g values and hyperfine interactions associated with both radicals.[6] The frequency is on the order of 15 MHz.[7] The triplet radical pair can decay to $^3P_{865}$, which is a process of typically 10 ns.[6] Lastly, P_{865} can transfer the triplet excitation to Car by a spin-conserving Dexter energy transfer mechanism described by an isotropic, orientation-independent time constant. Of these parameters, only the frequency ω_{S-T_0} depends on the orientation of the molecule with respect to the magnetic

field, since the hyperfine interactions and g values are anisotropic.[7] Because ω_{S-T_0} and the Dexter energy transfer rate are of similar magnitude and the other rates are faster, the anisotropy of ω_{S-T_0} of the radical pair precursor states with respect to orientation in the magnetic field is mirrored into the growth rates of the triplet EPR spectrum of ^{3}Car that are also anisotropic. Magnetophotoselection effects[8, 9] were not included since the excitation light was depolarized and largely scattered inside the cavity. The differential equations describing the dynamics of this multi-state model to fit the formation and decay of the time-trace of the ^{3}Car signals are given as a MATLAB routine.

```
function analysisp865andcarotenoid
[T,Y] = ode45(@rigid,[0 50],[1 0 0 0 0 0]);

subplot(2,1,1);
plot(T,Y(:,1),'-',T,Y(:,2),'-.',T,Y(:,5),'.');
subplot(2,1,2);
plot(T,Y(:,5),'-',T,Y(:,6),'-.');
tmY = [T, -Y];
save('temp.dat','tmY','-ASCII');

function dy = rigid(t,y)
dy = zeros(6,1);

%-------------------------------------------------------------------------
% Parameters for B || Z
%-------------------------------------------------------------------------
omega = 100;         % omega in MHz (singlet-triplet radical pair
oscillation)
kt865 = 100;         % kt865 in MHz     (triplet radical par -> P865, 10
ns)
k865car = 0.6;       % k865car in MHz   (P865 -> carotenoid, Dexter ET)
kcardecay = 0.199;   % kcardecay in MHz (carotenoid decay)
%-------------------------------------------------------------------------
% Parameters for B || X and Y
%-------------------------------------------------------------------------
omega = 13;          % omega in MHz (singlet-triplet radical pair
oscillation)
kt865 = 100;         % kt865 in MHz     (triplet radical par -> P865, 10
ns)
k865car = 0.6;       % k865car in MHz   (P865 -> carotenoid, Dexter ET)
kcardecay = 0.057;   % kcardecay in MHz (carotenoid decay)

%-------------------------------------------------------------------------
% Differential equations
%-------------------------------------------------------------------------
dy(1) = y(3);                                    % singlet radical pair
dy(2) = y(4)-kt865*y(2);                         % triplet radical pair
dy(3) = -0.5*omega*omega*(y(1)-y(2))-kt865*y(3); % singlet derivative
dy(4) = -0.5*omega*omega*(y(2)-y(1))-kt865*y(4); % triplet derivative
dy(5) = +kt865*y(2)-k865car*y(5);                % p865 population
dy(6) = +k865car*y(5)-kcardecay*y(6);            % carotenoid population
```

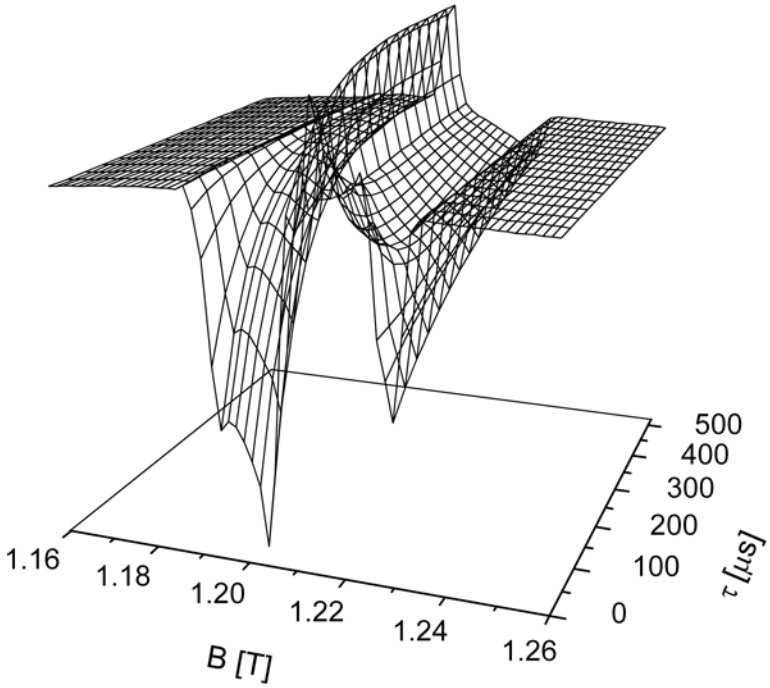

Figure A2. Two dimensional DAF EPR spectrum of $^3P_{865}$ in *Rb. sphaeroides* R-26.1 at T=10K.

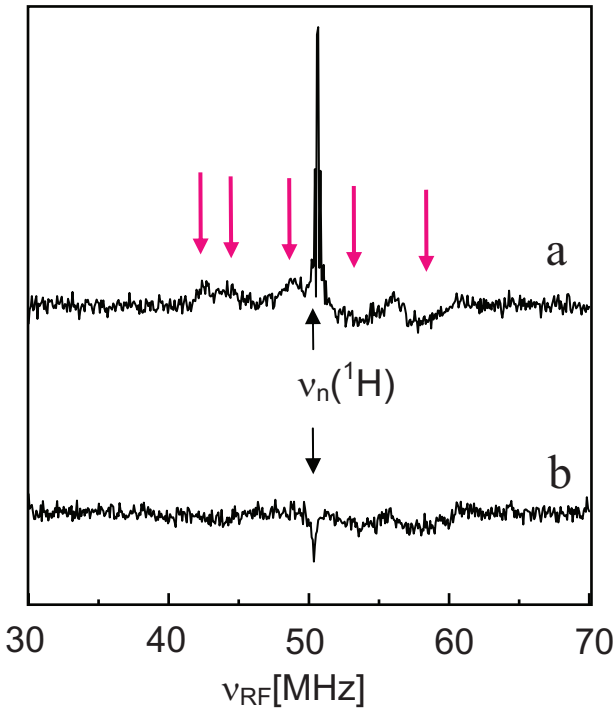

Figure A3. First triplet Davies ENDOR of ^{3}Car in bacterial reaction center of the *Rb. Sphaeroides* GD(M203)/AW(M260) double mutant at ν_{mw} = 34 GHz, T=40 K at the (a) Y_{II} and (b) Z_I canonical orientation. Up to five hyperfine couplings can be recognized.

Appendix B

Full dataset of hyperfine couplings [MHz] read from the ENDOR spectra

BChl *a*

"0 1" transition

Field, T	1	2	4	5	7	8
1.1825	–9.2	–3.4		+3.2		+8.5
1.1848	–9.4	–3.4				+8.5
1.1890	–9.4	–3.4				+8.6
1.1946						+8.9
1.2037						
1.2098	–12.6/–7.2		+1.7	+3.0	+6.7	+8.9
1.2186	–11.2/–7.4		+2.0	+3.1	+7.4	+9.6
1.2240	–7.4	–5.2			+9.0	+10.2
1.2294	–6.3					
1.2320						

"0 –1" transition

Field, T	1	2	4	5	7	8
1.1825						
1.1848	–6.4					+10.3
1.1890	–6.7	–5.2			+9.0	+10.0
1.1946	–10.6/–6.9		+1.9	+3.2	+7.2	+9.6
1.2037	–12.1/–7.5		+1.7	+2.9	+6.7	+8.9
1.2098						+8.9
1.2186						+9.0
1.2240	–8.7	–3.1				+8.7
1.2294	–9.2	–3.4		+3.0		+8.5
1.2320	-9.3	–3.4		+3.3		+8.5

BChl *b*

"0 1" transition

Field, T	1	2	3	4	6	7	8
1.1760	–9.5	–3.1	–2.3		+2.5		+8.4
1.1790	–9.3	–3.1	–2.1		+2.5		+8.5
1.1830	–9.2	–3.2	–2.0		+2.5		+8.5
1.1900							+8.8
1.1965							+8.6
1.2022	–12.5/–7.1			+1.8	+3.5	+6.4	+8.6
1.2085	–11.5/–7.1		–2.4	+1.8	+3.1	+7.2	+9.1
1.2158	–7.4			+2.0	+3.0	+8.5	+9.6
1.2200	–6.1						+10.0

1.2238

"0 –1" transition

Field, T	1	2	3	4	6	7	8
1.1760							
1.1790	–6.3						+10.2
1.1830	–6.6			+2.0	+3.1	+8.4	+10.0
1.1900	–11.0/–7.3			+1.8	+3.3	+7.3	+9.4
1.1965	–12.1/–7.6			+1.9	+3.5	+6.5	+8.7
1.2022							+8.5
1.2085							+8.9
1.2158	–8.7	–2.9	–2.0		+2.2		+8.4
1.2200	–8.7	–2.9	–2.0		+2.4		+8.4
1.2238	–8.8	–3.0	–2.1		+2.4	+6.0	+8.3

Tilting procedure

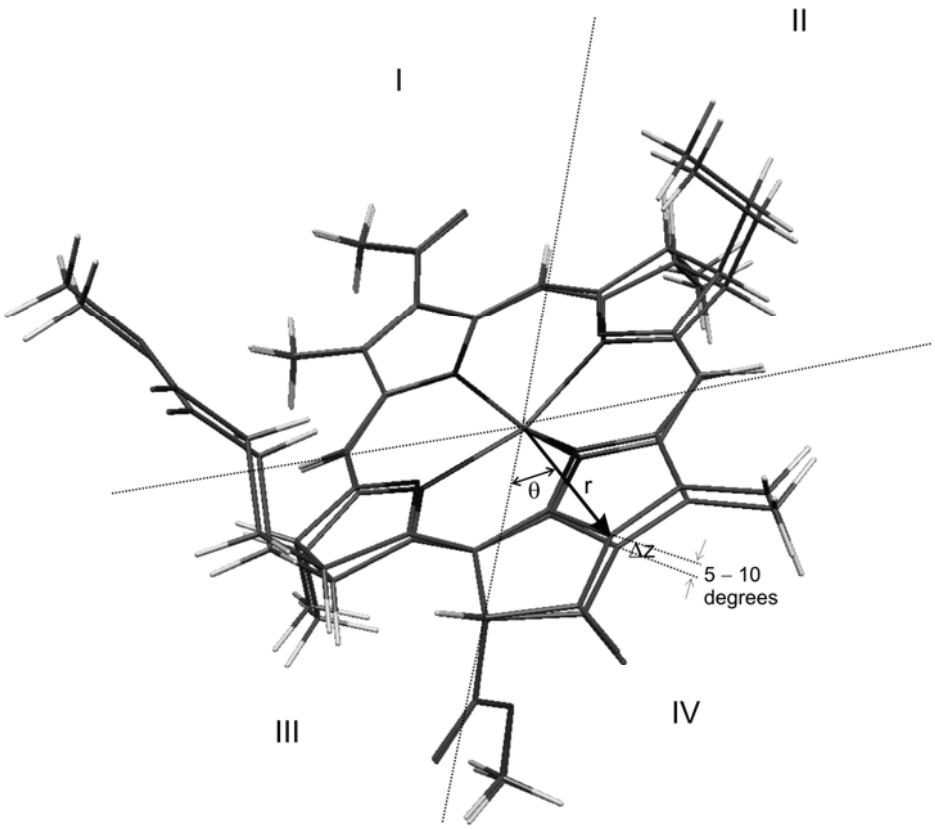

Figure B1. Bending of the porphyrin rings in BChl *a* and BChl *b* molecules in the model used for the calculation of the average hyperfine couplings and their standard deviations. The molecule was divided in four sectors and each sector is tilted according to a Lorentz function, in which the *z* coordinate of the atoms was perturbed using the equation

$$\Delta z = \frac{r \cdot \tan(bending\_angle)}{1 + \left[3 \cdot \left(\theta + 45 - 90 \cdot n\right)^2\right] / 45^2}, \qquad \text{(B1)}$$

where n varies from 0 to 3 and enumerates rings A-D; *r*, θ and Δz are depicted in the figure. In total 44 unique calculations were performed in which any combination of rings were allowed to bend either upward or downward.

Coordinates of BChl *a* and BChl *b* used for DFT calculations

BChl *a*

Mg	0.819882	-0.487853	-0.241021
C	-2.633872	-0.826116	-0.076404
C	0.377603	2.779482	-1.318915
C	4.240874	-0.052914	-0.241961
C	1.213878	-3.815656	0.613780
N	-0.870316	0.805694	-0.541715
C	-2.215770	0.459100	-0.392024
C	-3.128314	1.647434	-0.655920
C	-2.174482	2.624942	-1.386288
C	-0.795158	2.067948	-1.058926
C	-2.408461	2.622128	-2.910636
C	-3.748772	2.267691	0.627258
C	-2.633380	2.683572	1.602534
C	-3.025520	3.587483	2.753781
O	-4.056008	3.558104	3.401922
O	-2.012258	4.474404	2.967313
N	2.084861	1.092401	-0.670252
C	1.706312	2.367287	-1.043547
C	2.863801	3.236659	-1.109377
C	3.980569	2.444228	-0.778927
C	3.453900	1.097864	-0.533268
C	2.730932	4.680678	-1.410238
C	5.413849	2.807316	-0.675607
O	6.299551	1.978375	-0.420324
C	5.817734	4.246805	-0.977008
N	2.463504	-1.745753	0.051387
C	3.784171	-1.344179	-0.018819
C	4.731189	-2.514587	0.167085
C	3.790893	-3.683466	0.550954
C	2.391455	-3.075565	0.394062
C	5.553206	-2.787406	-1.104696
C	4.079489	-4.241114	1.963832
C	3.826706	-3.220228	3.084860
N	-0.404720	-2.017302	0.188006
C	-0.124141	-3.342920	0.508255
C	-1.372470	-4.090059	0.679053
C	-2.396369	-3.149591	0.448866
C	-1.748200	-1.911956	0.167898
C	-1.530639	-5.524977	1.009741
C	-3.844304	-2.956876	0.341614
O	-4.763786	-3.755338	0.449907
C	-4.052489	-1.397381	-0.014563
C	-4.829181	-1.241879	-1.321319
O	-5.978906	-0.847448	-1.398119
O	-4.063276	-1.591316	-2.395896
C	-4.663357	-1.470697	-3.701215

C	-2.123243	5.375155	4.080446
H	0.246411	3.765411	-1.792916
H	5.325389	0.128015	-0.208909
H	1.346698	-4.865405	0.926993
H	-3.963262	1.349374	-1.309701
H	-2.274463	3.652398	-0.984857
H	-1.718593	3.325119	-3.425929
H	-2.224633	1.596204	-3.294672
H	-3.461046	2.902089	-3.134351
H	-4.472897	1.559164	1.094451
H	-4.356602	3.141975	0.301621
H	-2.151807	1.765165	2.007805
H	-1.824510	3.219371	1.069093
H	3.701264	5.192415	-1.377067
H	2.057910	5.168598	-0.670624
H	2.288753	4.832068	-2.417396
H	6.910742	4.341448	-0.844639
H	5.294039	4.954290	-0.301666
H	5.535333	4.504093	-2.019241
H	5.431786	-2.276036	0.998395
H	3.904397	-4.513227	-0.181794
H	6.248178	-3.632355	-0.924742
H	6.141824	-1.894309	-1.404385
H	4.873631	-3.058299	-1.944744
H	5.139725	-4.573834	1.969584
H	3.475761	-5.160494	2.128051
H	4.062873	-3.660370	4.075315
H	4.457456	-2.311552	2.966137
H	2.765595	-2.888185	3.093173
H	-0.563899	-6.033828	1.138130
H	-2.124469	-5.639026	1.940579
H	-2.105389	-6.029862	0.206030
H	-4.704073	-0.952429	0.768784
H	-5.724920	-1.168952	-3.596852
H	-4.101153	-0.712530	-4.290776
H	-4.580502	-2.453690	-4.209586
H	-2.109984	4.808576	5.033360
H	-1.229682	6.021633	4.006694
H	-3.048391	5.987494	4.034336

BChl *b*

Mg	-0.785669	-0.172355	0.089211
C	2.615545	-1.005168	-0.243796
C	0.180640	2.922090	1.256914
C	-4.006100	0.968533	-0.420493
C	-1.577318	-3.095731	-1.735701
N	1.129906	0.788541	0.455751

C	2.404950	0.275407	0.252433
C	3.473197	1.309637	0.595273
C	2.667988	2.298332	1.482503
C	1.230121	2.022065	1.043939
C	2.862924	1.991566	2.985095
C	4.123451	1.964492	-0.654443
C	3.151374	2.658290	-1.625961
C	3.876297	3.571122	-2.606273
O	4.964737	3.354379	-3.107454
O	3.147754	4.695304	-2.853031
N	-1.755773	1.655719	0.346137
C	-1.190827	2.790066	0.890732
C	-2.188971	3.835223	1.034276
C	-3.404468	3.290354	0.557823
C	-3.084237	1.913398	0.136218
C	-1.855294	5.168573	1.583127
C	-4.751880	3.895963	0.466716
O	-5.738104	3.250787	0.080236
C	-4.971742	5.366241	0.841425
N	-2.529983	-0.969194	-0.870567
C	-3.748636	-0.321637	-0.878913
C	-4.839128	-1.227908	-1.455267
C	-4.029488	-2.414140	-1.958110
C	-2.639023	-2.190019	-1.509212
C	-5.901467	-1.591488	-0.389071
C	-4.473028	-3.464619	-2.703333
C	-5.847029	-3.683486	-3.210854
N	0.237148	-1.730662	-0.799556
C	-0.214154	-2.893622	-1.419184
C	0.907031	-3.798904	-1.701591
C	2.043442	-3.114696	-1.228154
C	1.572427	-1.866973	-0.702483
C	0.833721	-5.119162	-2.366380
C	3.500676	-3.169744	-1.084343
O	4.300175	-4.048182	-1.384305
C	3.926375	-1.780915	-0.424717
C	4.637744	-1.943732	0.917960
O	5.632310	-1.327832	1.263997
O	3.977182	-2.817519	1.720664
C	4.468934	-2.955828	3.063024
C	3.739304	5.649203	-3.752168
H	0.460152	3.852967	1.727808
H	-5.013871	1.348778	-0.499304
H	-1.824461	-4.027702	-2.244082
H	4.298044	0.843543	1.174463
H	2.944970	3.358495	1.289095
H	2.162943	2.567874	3.623700
H	2.696125	0.909609	3.182334
H	3.897122	2.229942	3.308310
H	4.711733	1.207844	-1.213193
H	4.870774	2.699036	-0.286646

H	2.597831	1.897041	-2.221555
H	2.378728	3.256371	-1.104427
H	-2.709974	5.844167	1.617693
H	-1.074986	5.661534	0.984705
H	-1.459128	5.090360	2.617068
H	-6.037551	5.596205	0.659013
H	-4.344755	6.047455	0.228493
H	-4.744596	5.579130	1.907980
H	-5.351696	-0.717020	-2.301031
H	-6.677745	-2.267062	-0.800915
H	-6.405973	-0.676160	-0.023240
H	-5.435197	-2.100567	0.481037
H	-0.196639	-5.391932	-2.638327
H	1.448058	-5.130257	-3.290808
H	1.240890	-5.925412	-1.718464
H	4.651288	-1.280288	-1.101706
H	5.574482	-2.906158	3.094213
H	4.058678	-2.146194	3.705258
H	4.111249	-3.935544	3.428277
H	3.866997	5.223185	-4.769141
H	3.041283	6.505978	-3.786886
H	4.731404	5.981936	-3.381945
H	-3.737362	-4.237988	-2.987051
H	-6.435223	-2.776726	-3.069733
H	-5.807151	-3.931718	-4.281737
H	-6.313846	-4.512895	-2.659344

Appendix C

Hyperfine couplings [MHz] for $^3P_{865}$ and $^3P_{960}$ ($0 \rightarrow -1$ transition)

$^3P_{865}$ (*Rb. sphaeroides*)								
Field	1.1833	1.1878	1.1923	1.1979	1.2076	1.2117	1.2168	1.2227
2		–3.1	–3.1	–3.1				–2.8
3		–2.2	–1.7	–1.6	–1.6			–1.2
4		+0.7	+1.0	+1.2	+0.8	+0.8	+0.6	+0.6
5		+1.6	+1.8	+2.0		+1.2	+1.4	+1.2
6		+2.7	+2.7	+3.0	+2.5	+2.5	+2.5	+2.6
7		+5.0	+4.9	+5.0	+4.7	+4.8	+4.5	+4.3
$^3P_{960}$ (*Bl. viridis*)								
Field	1.1870	1.1893	1.1980	1.2011	1.2052	1.2098	1.2169	1.2196
1		–7.1	–7.1	–7.0	–7.0	–6.9	–6.8	–6.2
2		–3.3	–3.8	–3.8			–3.6	–3.6
3		–1.6	–2.1	–2.4				-2.0
4		+1.0	+1.0	+1.1	+1.1	+0.9	+0.8	+0.8
5		+1.9	+1.6	+2.4	+1.8	+1.5	+1.5	+1.4
6.1		+2.4	+2.4	+2.9	+2.6	+2.7	+2.3	+2.1
6.2		+2.9	+3.0	+3.4	+3.1	+2.7	+2.7	+2.6
*			+4.4	+4.5				+3.5
7.1		+4.6	+5.0	+5.1	+5.0	+4.7	+4.5	+4.2
7.2		+5.1	+5.6	+5.7	+5.3	+5.2	+5.2	+4.8
8.1		+8.9	+7.7	+7.7	+7.7	+7.6	+7.3	+7.2
8.2			+8.4	+8.3				

Appendix D

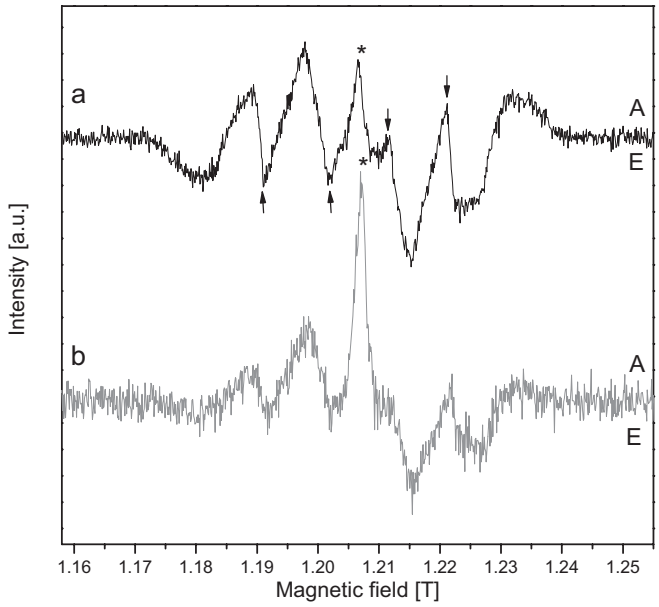

Figure D1. Q-band ESE detected EPR spectra of the LDHW mutant at (a) 100 K and (b) 150 K recorded with laser excitation of 537 nm. The residual $^3P_{865}$ signals are shown with arrows.

Table D1. Decay constants [μs] for the ^{3}Car signal in the EPR spectra of the wild type (WT) and LDHW mutant of *Rb. sphaeroides*, measured at the canonical orientations (X, Y, Z) and at variable temperatures

T, K	Decay constants, μs					
	X		Y		Z	
	WT	LDHW	WT	LDHW	WT	LDHW
10	47.3	27.0	15.3	2.5	15.3	9.6
30	25.2	9.0	9.2	2.5	9.2	7.6
50	14.7	8.1	5.6	3.0	5.6	6.0
100	11.8	8.7	3.3	3.0	3.3	7.8

References

(1) Angerhofer, A. Chlorophyll triplets and radical pairs. In *Chlorophylls*; Scheer, H., Ed.;CRC Press: Boca Raton FL, 1991; pp 945-991.

(2) Levanon, H., Norris, J. R. (1978) Photoexcited Triplet-State and Photosynthesis, *Chem. Rev., 78*, 185-198.

(3) Dauw, X. L. R., Poluektov, O. G., Warntjes, J. B. M., Bronsveld, M. V., Groenen, E. J. J. (1998) Triplet-state dynamics of C-70, *J. Phys. Chem. A, 102*, 3078-3082.

(4) Clarke, R. H., Connors, R. E., Schaafsma, T. J., Kleibeuker, J. F., Platenkamp, R. J. (1976) Triplet-State of Chlorophylls, *J. Am. Chem. Soc., 98*, 3674-3677.

(5) Schadee, R. A., Schmidt, J., van der Waals, J. H. (1976) Intersystem Crossing Into A Superposition of Spin States - System Tetramethylpyrazine in Durene, *Chem. Phys. Let., 41*, 435-439.

(6) Hore, PJ. Analysis of polarized EPR spectra. In *Advanced EPR in biology and biochemistry*; Hoff, A., Ed.;Elsevier: Amsterdam, 1990; pp 405-440.

(7) Bittl, R., van der Est, A., Kamlowski, A., Lubitz, W., Stehlik, D. (1994) Time-Resolved Epr of the Radical Pair P(865)(+)Q(A)(-) in Bacterial Reaction Centers - Observation of Transient Nutations, Quantum Beats and Envelope Modulation Effects, *Chem. Phys. Let., 226*, 349-358.

(8) Borovykh, I. V., Proskuryakov, I. I., Klenina, I. B., Gast, P., Hoff, A. J. (2000) Magnetophotoselection study of the lowest excited triplet state of the primary donor in photosynthetic bacteria, *J. Phys. Chem. B, 104*, 4222-4228.

(9) Borovykh, I. V., Klenina, I. B., Proskuryakov, I. I., Gast, P., Hoff, A. J. (2002) Magnetophotoselection study of the carotenoid triplet state in *Rhodobacter sphaeroides* reaction centers, *J. Phys. Chem. B, 106*, 4305-4312.